Deutsche Geodätische Kommission
der Bayerischen Akademie der Wissenschaften

Reihe C | Dissertationen | Heft Nr. 775

Daniel Wujanz

Terrestrial Laser Scanning for Geodetic Deformation Monitoring

München 2016

Verlag der Bayerischen Akademie der Wissenschaften
in Kommission beim Verlag C. H. Beck

ISSN 0065-5325 ISBN 978-3-7696-5187-4

Deutsche Geodätische Kommission
der Bayerischen Akademie der Wissenschaften

Reihe C Dissertationen Heft Nr. 775

Terrestrial Laser Scanning
for Geodetic Deformation Monitoring

Von der Fakultät VI – Planen Bauen Umwelt
der Technischen Universität Berlin
zur Erlangung des akademischen Grades
Doktor der Ingenieurwissenschaften (Dr.-Ing.)
genehmigte Dissertation

von

M.Sc. Daniel Wujanz
aus Bollendorf

München 2016

Verlag der Bayerischen Akademie der Wissenschaften
in Kommission beim Verlag C. H. Beck

ISSN 0065-5325 ISBN 978-3-7696-5187-4

Adresse der Deutschen Geodätischen Kommission:

DGK

Deutsche Geodätische Kommission

Alfons-Goppel-Straße 11 ● D – 80 539 München

Telefon +49 – 89 – 23 031 1113 ● Telefax +49 – 89 – 23 031 - 1283/ - 1100
e-mail post@dgk.badw.de ● http://www.dgk.badw.de

Vorsitzender: Prof. Dr.-Ing. Dr. Harald Schuh, Deutsches GeoForschungsZentrum Potsdam

Gutachter: Prof. Dr.-Ing. Frank Neitzel, Technische Universität Berlin
Prof. Dr. Roderik Lindenbergh, Delft University of Technology, Niederlande
Prof. Dr.-Ing. Ingo Neumann, Leibniz Universität Hannover

Tag der wissenschaftlichen Aussprache: 28.01.2016

Diese Dissertation ist auf dem Server der Deutschen Geodätischen Kommission unter <http://dgk.badw.de/>
sowie auf dem Dokumentenserver der Technischen Universität Berlin
unter <https://depositonce.tu-berlin.de/handle/11303/5465> elektronisch publiziert

ISSN 0065-5325 ISBN 978-3-7696-5187-4

Eidesstattliche Erklärung

Hiermit versichere ich, dass ich die vorliegende Arbeit selbstständig verfasst und keine anderen als die angegebenen Quellen und Hilfsmittel benutzt habe. Alle Ausführungen, die anderen veröffentlichten oder nicht veröffentlichten Schriften wörtlich oder sinngemäß entnommen wurden, habe ich kenntlich gemacht.

Die Arbeit hat in gleicher oder ähnlicher Fassung noch keiner anderen Prüfungsbehörde vorgelegen.

Daniel Wujanz　　　　Berlin am 08.09.2015

Summary

The determination of geometric changes within an area or object of interest by means of repetitive surveys at different points in time is referred to as geodetic deformation monitoring. Despite its development in the early years of the twentieth century the original processing chain remained identical in essence until now. It contains the choice of suitable viewpoints, observation of at least two so called epochs, transformation of all epochs into a common coordinate system and finally the actual monitoring of deformations. In order to acquire an area under investigation discrete points of interest have to be physically signalised. Thereby repetitive observations can be achieved throughout the epochs. Downsides of this approach are among others the time consuming necessity to signalise the area under investigation as well as the "blindness" against deformations that occur outside the scope of the interest points. The emergence of terrestrial laser scanners (TLS) into engineering geodesy around the turn of the millennium led to a paradigm shift that allows to observe an area under investigation in a quasi-laminar fashion without the need of signalising points within the object space. Through this, all deformations can be revealed in principle that occurred in between two epochs within the area under investigation.

Based on the already mentioned process chain of geodetic deformation monitoring the contribution at hand initially compares methodical differences as well as parallels among established approaches and terrestrial laser scanning. This results in several unsolved problems that are treated as research questions in this thesis.

A substantial preparative step for geodetic deformation monitoring is the choice of suitable viewpoints from an economic perception and under the perspective of engineering geodesy. As existing methods for this task are not directly transferable to TLS, a novel combinatorial search algorithm is proposed and exemplified. Furthermore, a stochastic model for terrestrial laser scanners is introduced that uses intensity values of the received laser signal as an input and allows to predict the theoretical precision of observations from a certain viewpoint.

A vital task in deformation monitoring under the assumption of a congruency model is the transformation into a stable reference frame. Only if this prerequisite holds, occurred deformations can be correctly identified and consequently quantified. For the case of observations onto signalised, discretely observable targets, for instance by tacheometry, several methods have been developed in the past in order to reveal sets of congruent points respectively points that were subject of deformation, so that this problem domain can be seen as solved. If one now transforms this problem to TLS then it can be established that areas where deformation occurred have to be identified and rejected from computing transformation parameters between epochs. A look at current literature on TLS based deformation monitoring shows that nearly all researchers imitate the tacheometric line of action by deploying artificial targets which have been designed for laser scanners. Through this a beneficial characteristic of TLS is neglected namely the enormous information density within the object space that can be used to compute transformation parameters. For the until then unsolved problem of automatically distinguishing stable and deformed regions in datasets which have been captured by TLS two algorithms are proposed. The performance of these implementations is tested regarding their robustness and other criteria, based on practical data.

Furthermore, a method for determination of statistically significant deformations in TLS-datasets is introduced. Through this, the subjective choice of arbitrary thresholds for quantification and visualisation of deformations is counteracted. Finally, a procedure for visualisation of deformations within the object space is presented that simplifies the now and then abstract interpretation of the outcome of deformation monitoring.

Kurzfassung

Die Bestimmung von geometrischen Veränderungen eines Untersuchungsgebietes bzw. -objektes durch wiederholte Vermessung zu verschiedenen Zeitpunkten wird als geodätische Deformationsmessung bezeichnet. Auch seit deren methodischen Entwicklung zu Beginn des zwanzigsten Jahrhunderts blieb die ursprüngliche Prozesskette im Wesentlichen unverändert und beinhaltet die Wahl von geeigneten Aufnahmestandpunkten, die Vermessung von mindestens zwei sogenannten Epochen, die Überführung der Epochen in ein gemeinsames Koordinatensystem und schließlich die eigentliche Deformationsmessung. Zur Erfassung einer Epoche wird das Untersuchungsgebiet zunächst diskretisiert, indem interessierende Punkte signalisiert werden, um so eine wiederholte Vermessung zu ermöglichen. Nachteile dieser Vorgehensweise sind unter anderem die zeitaufwändige Signalisierung, sowie die „Blindheit“ gegenüber Deformationen, die in nicht signalisierten Arealen aufgetreten sind. Mit Einzug des terrestrischen Laserscannings (TLS) in die Ingenieurgeodäsie wurde um die Jahrtausendwende ein Paradigmenwechsel eingeleitet, der nun eine quasi-flächenhafte Vermessung ohne die Einbringung von Zielmarken in den Objektraum ermöglicht. Dadurch können prinzipiell alle Deformationen aufgedeckt werden, die zwischen zwei Epochen im Untersuchungsgebiet aufgetreten sind.

Die vorliegende Arbeit vergleicht zunächst an Hand der bereits erwähnten Prozesskette der geodätischen Deformationsmessung methodische Unterschiede sowie Parallelen zwischen der etablierten Vorgehensweise und dem terrestrischen Laserscanning. Auf Grundlage der ermittelten ungelösten Probleme ergeben sich die Forschungsfragen der weiteren Kapitel.

Ein wesentlicher Schritt zur Vorbereitung von geodätischen Deformationsmessungen ist die Auswahl geeigneter Aufnahmestandpunkte unter ökonomischen und ingenieurgeodätischen Gesichtspunkten. Da bestehende Verfahren nicht direkt auf das terrestrische Laserscanning angewendet werden können, wird ein neuartiger modellbasierter Algorithmus zur kombinatorischen Suche geeigneter Aufnahmestandpunkte vorgestellt und an einem Beispiel demonstriert. Zudem wird ein stochastisches Modell für terrestrische Laserscanner vorgestellt, welches als Eingangsgrößen Intensitätswerte des reflektierten Lasersignals verwendet und somit die Berechnung der zu erwartenden Präzision der Messungen von einem vorgegebenen Standpunkt ermöglicht.

Ein entscheidender Punkt bei der Deformationsmessung unter Annahme eines Kongruenzmodells bildet die Überführung einzelner Epochen in ein stabiles Referenzkoordinatensystem. Nur wenn diese Annahme erfüllt wird, gelingt es, aufgetretene Deformationen korrekt zu identifizieren und schließlich zu quantifizieren. Liegen Beobachtungen zu signalisierten, diskret anzielbaren Zielzeichen vor, stehen zahlreiche Methoden zur Verfügung, um kongruente Punktgruppen zu ermitteln, so dass dieses Problem als gelöst angesehen werden kann. Überträgt man dieses Problem auf das terrestrische Laserscanning, so gilt es nun, flächenhafte Areale zu erkennen in denen Deformationen aufgetreten sind, und diese von der Berechnung von Transformationsparametern zwischen den Epochen auszuschließen. Ein Blick in aktuelle Publikationen zum Thema Deformationsmessung mit TLS zeigt, dass nahezu alle Ansätze die tachymetrische Herangehensweise durch Nutzung von Zielzeichen imitieren, die in den Objektraum eingebracht werden müssen. Dadurch wird ein wesentlicher Vorteil von terrestrischen Laserscannern vernachlässigt, nämlich die enorm hohe Informationsdichte im Objektraum, die zur Berechnung von Transformationsparametern genutzt werden kann. Für das bis dahin ungelöste Problem der automatischen Identifikation von stabilen und deformierten Regionen in Datensätzen aus TLS werden zwei Algorithmen vorgestellt. Die Leistungsfähigkeit der Algorithmen wird hinsichtlich der Robustheit gegenüber Deformationen und weiterer Kriterien an verschiedenen praktischen Szenarien getestet. Des Weiteren wird eine Methode zur Ermittlung von statistisch signifikanten Deformationen in TLS-Datensätzen vorgestellt, wodurch der subjektiven Wahl von frei wählbaren Schwellwerten bei der Quantifizierung und Visualisierung von Deformationen begegnet wird. Schließlich wird ein Verfahren zur Visualisierung von Deformationen im Objektraum präsentiert, welches die mitunter abstrakte Interpretation der Ergebnisse einer Deformationsmessung erleichtert.

Contents

1 Introduction

For decades the vast majority of tasks for engineering geodesists were associated to geometric monitoring of natural or manmade structures. In order to fulfil these tasks an object of interest has to be discretised based on knowledge of according experts. This means that certain parts of an object are represented by single points to which coordinates are assigned. A problem of this perception is that geometric changes can only be detected if they influence areas that are repeatedly observed. As a consequence, problems arise if unexpected or rare events occur outside of the inspected area. The development of terrestrial laser scanners (TLS) allows capturing an area under investigation in a quasi-laminar fashion without the necessity of signalisation and can hence be seen as a paradigm shift. Consequently, the emergence of TLS initiated an extension of the classical sphere of action of engineering geodesists for instance to Geomorphology, Archaeology and Cultural Heritage, Biology and Environmental Sciences where natural objects and areas are of interest. Note that the abbreviation TLS is used throughout the thesis for terrestrial laser scanners and terrestrial laser scanning in equal measure.

Despite the fact that research in the field of TLS has been vividly conducted since beginning of the new millennium only few scientists analysed or adapted the well-known processing chain of deformation monitoring within the scope of this new technology. Instead questionable methods and procedures are naively applied in research as well as in practice due to the fact that laser scanning has blossomed into a profitable business in the meantime. The thesis at hand takes a close look at all procedures that are required to derive geometric changes based on terrestrial scans and furthermore strives to reintroduce expertise that engineering geodesists thoroughly gathered within the span of more than a century.

The roots of deformation monitoring can be traced back to Ganz (1914) where the movement of Rosablanche, a summit in the Swiss Alps, has been monitored based on trigonometric observations. The applied methodology has then been used and refined to analyse the behaviour of large dams as extensively reported by Lang (1929). A review on the development of deformation monitoring can be found in Welsch (1979). Even though the origins of this problem domain have been founded in the early years of the last century its process chain remained nearly identical namely

Step 1: Network design respectively viewpoint planning in order to determine optimal viewpoints for observation,

Step 2: Data acquisition of at least two epochs,

Step 3: Transformation of all epochs into a common and stable coordinate system,

Step 4: Deformation monitoring.

It should be pointed out that throughout the thesis the term deformation monitoring is used instead of deformation analysis as causes of deformation usually have to be identified by an expert of the according problem domain and not an engineering geodesist as mentioned by Lang (1929 p. 5). Interestingly Lang (1929 p. 17) also suggests to observe an object or area of interest completely and not by just a few chosen discrete points as in classical engineering geodesy in order to being capable to entirely monitor its behaviour. An extensive description of this aspect will be given in subsection 2.1.3. Lang's argument coincides with current objectives of the German Geodetic Commission (DGK) section engineering geodesy, who state that developments in deformation monitoring should satisfy temporal and spatial continuity (Kuhlmann *et al.* 2014). Sensors that come very close to these prerequisites are terrestrial laser scanners (TLS) apart from the fact that they acquire data sequentially. Hence, data captured by TLS will be subject of this thesis.

Heunecke *et al.* (2013 p. 15) describe the subject of geodetic monitoring "*...as the acquisition of geometric changes of a measuring object...*" respectively "*...the detection of movements and deformation...*" (translation from German). The technical requirements onto a stated problem vary significantly due to the diversity of problem domains where the behaviour of an object is of interest. Typical fields of application for deformation monitoring are for instance structural monitoring of objects such as bridges, dams or towers but also wear

Table 1.1: *Model comparison for deformation monitoring* (Heunecke *et al.* 2013 p. 78)

Deformation model	Dynamic model	Static model	Kinematic model	Congruency model
Time	Deformation as a function of time and stress	Not explicitly modelled	Deformation as a function of time	Not explicitly modelled
Forces		Deformation caused by forces	Not modelled	Not modelled
Condition of object	Moves under stress	Adequately in rest during stress	In motion	Adequately in rest

of machines, crash testing and landslide or glaciers movement in the geo-scientific domain. In general, two important aspects need to be clarified in a dialogue with specialists of the according expertise namely the degree of discretisation and temporal resolution. An important boundary of the first aspect is the so called Nyquist-frequency or Nyquist interval (Shannon 1949) in imitation of an article by Nyquist (1928). It describes the required spatial frequency in order to retrieve information without loss which is referred to as aliasing in this context (Luhmann *et al.* 2011 p. 133). Assuming a case where the sampling frequency is too low in relation to the signal of interest the result leads to discretisation errors which consequently ends in misinterpretation. The second aspect concerning the required temporal resolution is highly correlated to the stated problem domain e.g. occurrence of heavy rainfalls as cause of landslides or increased production rates as a catalyst for machine wear and is usually defined within interdisciplinary exchange. In general three types of deformation can be distinguished namely (Heunecke *et al.* 2013 p. 92, Scaioni *et al.* 2013):

- Rigid body deformation - the shape of an object of interest remain stable whereas location and / or orientation change e.g. glacier detachment.
- Shape changes - for instance torsion, bending or strain due to external forces such as in crash testing.
- Deposition, degradation, wear or loss of material - e.g. soil erosion.

After data acquisition at a sufficient temporal and spatial resolution a suitable deformation model needs to be chosen. Technical literature such as Heunecke *et al.* (2013 p. 78) distinguish four different cases that are briefly discussed in the following and gathered in table 1.1. The first one, which is referred to as **dynamic model** links temporal and external forces to observed object reactions. As external forces are impossible or relatively hard to control in natural environments or on large artificial structures no use will be made in this thesis. A prerequisite of **static models** is that the object of interest needs to remain stable during measurements in order to being able to omit time as an influential factor. Furthermore the functional relationship between forces that act onto an object and its observed reaction is described. **Kinematic models** describe the time-dependent behaviour of object points for instance by polynomial or trigonometric functions. The motivation behind this approach is to being able to draw conclusions about object movements and its parameters at discrete points in time. By doing this the descriptive kinesic behaviour is monitored but not their causes. A problem that also arises in this context is the necessity of object generalisation where discrete points are chosen in order to describe an entire object. The most popular strategy for deformation monitoring which is also used in this thesis is the so called **congruency model**. This solely geometric perception considers geometric changes between two epochs for instance by comparison of coordinates. A vital assumption of the congruency model is that some portion of an observed area of interest remains geometrically stable (Neumann & Kutterer 2007).

The thesis at hand is structured in accordance to the processing chain of deformation monitoring that has already been introduced. Note that the second step of the procedure, the actual data acquisition, will not be separately discussed in this thesis. At first an overview about established geodetic methodologies as well as contemporary approaches based on TLS scans for deformation monitoring is given in chapter 2. Subsection 2.6 will assess all discussed methods based on which four research questions within the context of deformation monitoring deploying TLS data are posed. In order to support the reader in linking individual steps of the deformation monitoring processing chain to according chapters, the related design step is given in brackets in the following. A prerequisite for viewpoint planning is the availability of a suitable stochastic model while both aspects are subject of chapter 3 (Step 1). The most critical part of the above mentioned process chain concerning the outcome of deformation monitoring is the transformation into a common coordinate system which is the main topic of this thesis and can be found in chapter 4 (Step 3). A rigorous method for deformation monitoring based on point clouds captured by terrestrial laser scanners as well as a visualisation strategy of deformations on arbitrary surfaces is presented in chapter 5 (Step 4). Chapter 6 features several practical scenarios that are used to evaluate the capabilities as well as the boundaries of the most promising proposed matching algorithm from the previous section while chapter 7 concludes the thesis and gives an outlook on open questions.

2 Deformation monitoring: Past and present methodologies

This section will give an overview about all essential design steps for deformation monitoring where both established and contemporary contributions are considered. Deformation monitoring is based on frequently observing and object or area of interest which hence results in a time series of potentially different states within object space. The required frequency of documentation depends on the characteristic behaviour of the area of interest e.g. if it is of linear nature or if it is triggered by certain influences such as heavy rainfalls or increasing temperatures. After a brief introduction to the functional principle of TLS, influential impacts and calibration routines in subsection 2.1, the focus is set on stochastic models within a geodetic context. An important step when conducting measurements that have to fulfil certain requirements in terms of precision (Ghilani 2010 p. 4) is to perform viewpoint planning in order to fully deploy the potential of the sensor which will be of interest in section 2.2. Section 2.3 will introduce important aspects on referencing of point clouds which describes the central topic of this thesis. A practical analysis of commercial registration algorithms has been conducted in order to assess their suitability for deformation monitoring and will hence be extensively discussed. Furthermore the subject of outlier identification / rejection as well as the actual monitoring process are of interest in subsection 2.4, respectively 2.5. The last section of this chapter will summarise discovered problems for which several solutions are proposed in this thesis.

2.1 Fundamentals of TLS

A TLS consists of three major components namely an emitter unit, a receiver unit as well as a deflection unit (Jutzi & Stilla 2003). The essential technology that consequently allowed the development of TLS is the reflectorless distance measurement which hence can be seen as the key component and is described in the following subsection. In order to capture an area or object of interest the emitted laser beam requires deflection into different spatial directions for which several scanning principles have been developed as discussed in subsection 2.1.2. As laser scanners can be applied for acquisition of arbitrary surfaces that still have to reflect a sufficient signal numerous influences onto the outcome can occur which is subject of section 2.1.4. A prerequisite before conducting engineering surveys is to strictly apply calibrated sensors. Approaches to achieve this are discussed under subsection 2.1.5.

2.1.1 Reflectorless distance measurement approaches

The basic components for electro-optical distance measurement units are laser diodes that emit signals of the above mentioned types, optical components that ensure a potentially small beam divergence with increasing distance as well as a photosensitive diode that receives the reflected signal and provides input for signal processing (Vosselman & Maas 2010, pp. 11). In general, two reflectorless distance measurement methodologies are incorporated in TLS that are either based on continuous wave (cw) or pulsed lasers. The latter one is also referred to as time-of-flight (tof) principle and is based on the assumption that if the speed of light c as well as the refractive index n are known and the runtime τ of a signal is measured the according distance ρ between sensor and object can be computed by

$$\rho = \frac{c}{n} \cdot \frac{\tau}{2}. \tag{2.1}$$

In order to demonstrate the requirements for a tof-distance measurement unit an example is given that assumes the following parameters:

- c – speed of light in vacuum: 299792.458 km/s,
- n – refractive index: 1,
- res_{dist} – desired resolution of the distance measurement: 5 mm

while res_{temp} describes the mandatory temporal resolution. Joeckel & Stober (1999 pp. 74) name drying temperature, air pressure, partial vapour pressure as well as the coefficient of expansion of air as decisive meteorological influences onto distance measurements captured by electro-optic sensors. Based on equation (2.1) the following relation can be formed

$$res_{temp} = \frac{2}{c} \cdot res_{dist} \tag{2.2}$$

which yields to a required temporal resolution of 0.0335 ns. Joeckel & Stober (1999 pp. 21) point out that the required temporal resolution is independent to the length that should be measured. Interested readers are referred to Jutzi & Stilla (2006) for more information on the subject of reflectorless tof-distance measurement.

Another method to determine distances are phase based techniques where a continuous wave is emitted instead of pulsed signals (Vosselman & Maas 2010, pp. 7). Therefore a signal is e.g. amplitude modulated (AM) by forming a sinusoidal wave. The emitted and received signal are compared to each other in terms of waveform while the resulting phase shift yields to the time delay and hence as already introduced in equation (2.1) to the range. A downside of this method is that a low frequency f_m leads to low precision in phase detection and in consequence to inaccurate distance measurements. Usage of a higher frequency would in fact lead to a higher achievable accuracy but would amplify the second problem of the approach: the higher the frequency the smaller the range of ambiguity. In order to solve this problem various wavelengths are applied in order to ensure a potentially large ambiguity interval as well as a desirable accuracy.

As this thesis focuses on data processing and not the actual acquisition process the interested reader is referred to Wehr & Lohr (1999), Jutzi & Stilla (2003), Jutzi (2007) or Vosselman & Maas (2010, pp. 2). Comparable to other optical measuring techniques reflectorless distance measurements fail respectively produce erroneous results if the signal is subject to transmission, a substantial amount of absorption or total reflection (Stöcker 2000, pp. 375).

2.1.2 Scanning principles

In order to expand a one dimensional distance measurement unit into a laser scanner several additional components are required namely mirror(s), motors and angular detectors. The task of one or more mirrors is to deflect an emitted signal of the laser diode and to transmit the signal that is reflected of an object's surface to a collecting optical group and finally to a photodiode for signal processing. By changing the orientation of the according mirror(s) additional degrees of freedom can be measured. By emitting a signal onto a single mirror that rotates around one axis a profile in 3D-space is sampled while the use of two mirrors yields to a 3D-scanner. The current mirror orientation is determined by use of angular detectors. In order to being able to compute 3D-coordinates the following three polar elements are required (Neitzel 2006):

- Direction φ_i,
- Tilt angle λ_i,
- Spatial distance s_i as measured by the reflectorless distance measurement unit.

For precise determination of 3D-coordinates all required components need to be synchronised and calibrated as described in subsection 2.1.5. The process of scanning an environment can be achieved by various methods or combined use while figure 2.1 shows four essential approaches.

Figure 2.1 a illustrates the oscillating mirror principle which has been used in some of the first generation of laser scanners but is now still popular in aerial laser scanning systems (ALS). The basic idea is that an emitted signal is deflected by an oscillating mirror that swivels within a certain range. As the mirror is accelerating and slowing down before and after reaching the turning points a varying point density results. The combination of two orthogonally mounted mirrors that oscillate perpendicular to each other leads to so called camera-view scanners that can only capture data within a certain field-of-view. Figure 2.1 b shows the principle of the

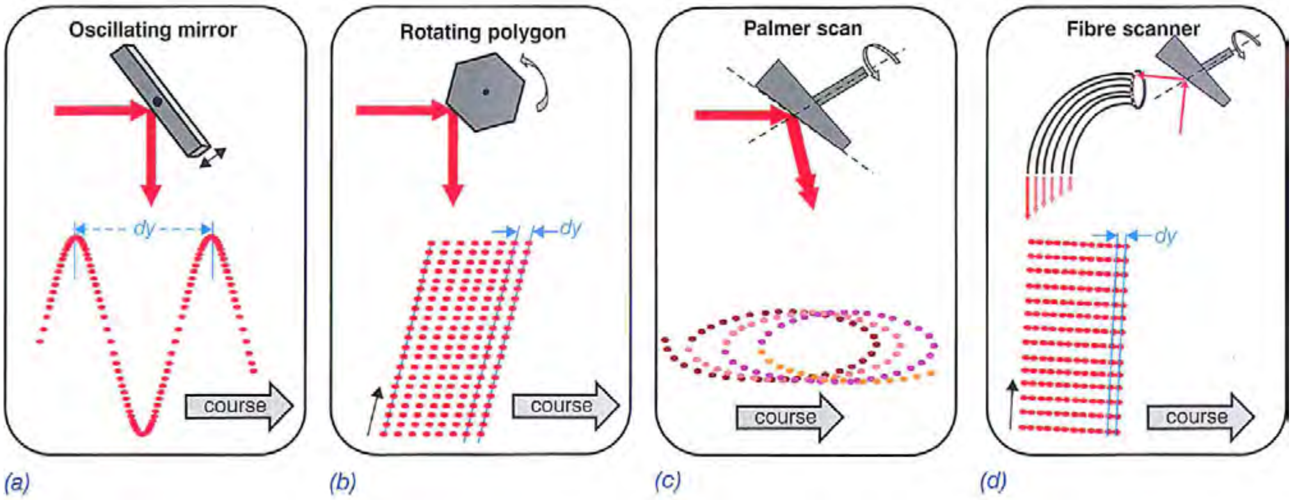

Figure 2.1: *Several scanning strategies and resulting sampling pattern in object space* (VOSSELMANN & MAAS 2010, p. 17)

rotating polygon mirror where the deflection occurs in one direction only. The deflected lines are parallel to each other which results in a far more homogeneous sampling pattern. Figure 2.1 c schematically shows the idea behind a palmer scanner that is mostly used in terrestrial laser scanners e.g. where the total station principle is applied. In order to realise such a scanner a mirror is aligned to a laser diode in an angle dissimilar to 90ř while the mirror rotation results in a circular shaped scanning pattern. The according pattern in ALS systems is of elliptic shape due to the forward motion of an aerial sensor platform. Figure 2.1 d depicts the concept of a fibre scanner where a laser pulse is sequentially fed into an array of glass fibre by a rotating mirror. As a result a fixed resolution is given leading to a homogenous ground sampling distance (VOSSELMANN & MAAS 2010, p. 16).

2.1.3 Impact of spatial sampling

Classical geodetic acquisition methods describe an object or area of interest by several discrete points that are selected by a geodesist and / or under consultation by an expert of the according field as already briefly mentioned. The major difference between this established perception and TLS is that no actual point selection is carried out in the field. Instead an object of interest is covered by a densely sampled set of discrete points - a so called point cloud. The acquisition method of TLS is referred to as being quasi-laminar throughout the thesis due to the fact that it occupies some properties of discrete strategies yet holds more laminar characteristics and hence comes close to the desired ideal of laminar data acquisition. Figure 2.2 illustrates the circumstance where an object of interest has been acquired from two slightly different viewpoints by a TLS which results consequently in a varying point distribution on the object's surface. As a consequence one could say that TLS observes non-repeatable points on an object's surface that are dependent to the sensor's position in relation to the object. Interestingly the point sampling may also differ between two scans even if the orientation and location of the TLS remained stable between two scans due to the imperfection of angular detectors. In summary it has to be established that novel thresholds respectively stochastic measures have to be derived that account for the spatial sampling of the acquisition procedure which will be covered in some of the following subsections.

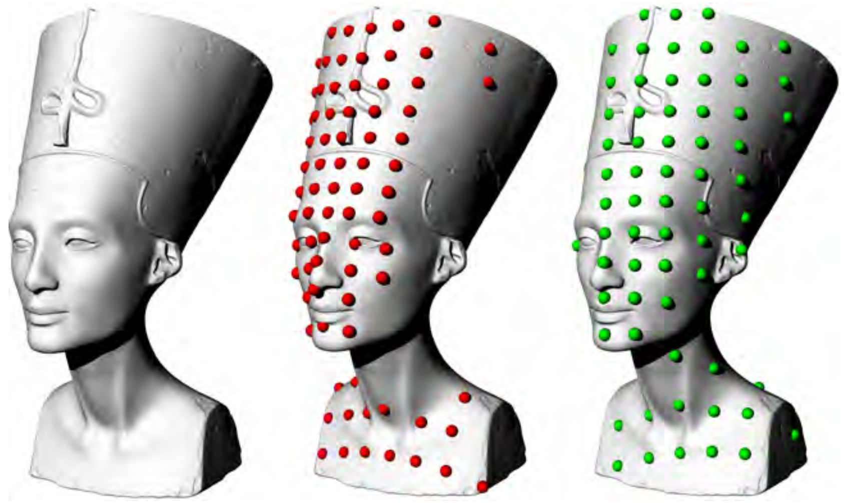

Figure 2.2: *Object of interest (left) and acquired data from two slightly different viewpoints (middle and right part). It can be seen that the point sampling on the object's surface differs between both datasets. Digitised copy of the Bust of Queen Nefertiti, New Kingdom, 18th dynasty ca. 1340 BCE, Egyptian Museum and Papyrus Collection, National Museums Berlin, Germany. Unauthorised external use is strictly prohibited.*

2.1.4 Influences onto reflectorless distance measurements

On one hand reflectorless range finders allow to observe distances without the necessity to equip a point of interest but on the other hand that means that a multiplicity of additional falsifying effects compared to classical tacheometer observations on prisms emerge. Hence, this circumstance is a relevant scientific subject starting from the early days of TLS in surveying as Lichti *et al.* (2000) demonstrate. Soudarissanane *et al.* (2011) groups the entirety of influences into the following four categories:

- Scanner mechanism which includes properties of applied hardware, calibration and settings.
- Atmospheric conditions and environmental impacts such as temperature, humidity or air pressure.
- Object properties such as roughness and reflective behaviour of the irradiated surface.
- Scanning geometry includes the relative spatial relation between object and TLS during data acquisition.

Böhler *et al.* (2003) perform accuracy and performance tests on TLS while the most significant contribution of this work can be found in the development of a 3D-version of the Siemens-star, a device that is applied to determine the resolution of a photographic system (Luhmann *et al.* 2011, pp. 130). The proposed device is referred to as Böhler-star and determines the resolution of a TLS in dependence to object distance and local spatial resolution that is defined by angular increments of the deflector unit. The highest resolution can be achieved at the distance where the spot size or foot print of the laser beam is minimal (Wujanz 2009). Staiger (2005) gives an overview about influential parameters onto the quality of point clouds and compares various TLS within practical experiments that were available on the market at the time. The behaviour of a TLS' foot print is discussed by Jacobs (2006) while Reshetyuk (2006b), Bucksch *et al.* (2007), Vögtle *et al.* (2008) and Zamecnikova *et al.* (2014) analyse influences caused by the surface reflectance respectively various materials onto the distance measurement unit. Soudarissanane *et al.* (2007, 2009, 2011) carried out extensive experiments concerning the error budget of TLS including influences caused by incidence angle and distance. An overview about influencing factors within the TLS data acquisition and post processing chain is given by Buckley *et al.* (2008) from the perspective of geological monitoring. Hejbudzka *et al.* (2010) analysed the impact of meteorological incidents onto distance measurements conducted by TLS which is to the best knowledge of the author the only article that deals with this vital subject. It has to be mentioned that this impact is extremely hard to model as laser scanners capture data in a polar fashion hence every single emitted ray is subject to effects of different degree. Pesci *et al.* (2011) theoretically and experimentally assess influences caused by a TLS' footprint as well as the chosen scan resolution.

2.1.5 Calibration of TLS

An important prerequisite of surveying instruments that needs to be satisfied is the necessity of a valid calibration which includes the distance measurement unit as well as certain conditions concerning the instruments' axes that have to be met. The aim of a calibration procedure is to minimise systematic errors which otherwise yield to falsification of an instruments' observations. Various articles have been published on the subject that can be briefly distinguished by the type of observations that serve as input for the calibration as well as the applied functional model that has been chosen for the TLS of interest. Neitzel (2006) applied Stahlberg's (1997) vectorial description of axes errors based on observation of six spheres that have been surveyed in two phases in order to calibrate a Z+F Imager 5003 TLS whose functional model is in accordance to a tacheometer. Furthermore three essential conditions are defined that have to be met by an error free instrument while the according axes are illustrated in figure 2.3:

- Rotation axis and tilting axis are normal to each other,
- Tilting axis and collimation axis are in a perpendicular relation,
- The collimation axis intersects the rotation axis.

Rietdorf *et al.* (2004) respectively Rietdorf (2005) describe a calibration procedure for estimation of axis errors that applies planar patches as observations whereas the idea has been adapted by Bae & Lichti (2007) in form of an on-site calibration routine analogue to photogrammetric solutions (Luhmann *et al.* 2011, pp. 448).

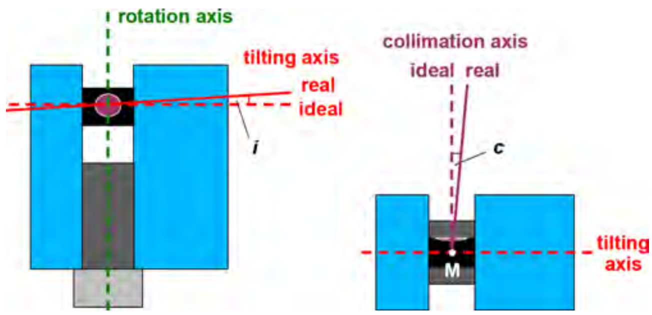

Figure 2.3: *Occurrence of a tilting axis error and collimation error* (Neitzel 2006)

Salo *et al.* (2008) presented a distance component calibration routine that has been applied to a phase-based TLS. Sound summaries on the subject are presented by Lichti & Licht (2006), Lichti (2007), Reshetyuk (2006a), Schulz (2007), Reshetyuk (2009) and Lichti (2010). In order to check a TLS in the field e.g. after a longer period where the instrument hasn't been used, after a fall or uncertain transportation a field test procedure (Gottwald 2008) should be carried out that allows the user to draw conclusions whether a re-calibration is required or not.

2.2 On stochastic models for TLS and viewpoint planning

The field of deformation monitoring can be clearly assigned to the subject of engineering geodesy where detailed knowledge about a sensor's error budget in form of stochastic models is essential to objectively and reliably draw conclusions about a stated problem. In order to fully employ the potential of an applied sensor in terms of its achievable accuracy the shape of an object of interest has to be known. This aspect is schizophrenic to some degree as the shape that is actually of interest is usually not known prior to a survey – if this would be the case data acquisition would be needless at first glance. In summary, it can be established that the survey of an object is actually an iterative process where the degree of details improves during the cause of repetitive acquisition that consequently lead to an improved set of required viewpoints. The following subsections describe the state-of-the-art of stochastic modelling and viewpoint planning at first from the traditional surveying perspective and subsequently within the context of TLS.

2.2.1 Stochastic modelling

A telling definition on stochastic models is given by Bjerhammar (1973, p. 8) who states that "*the stochastic model (random model) is used, when there is no way of making an exact prediction of the outcome (random trial)*". As this is always the case for observations as well as the fact that only the precision can be determined in the field but not the according accuracy. Furthermore stochastic models serve for weighting of individual observations during parameter estimation. Ghilani (2010 p. 165) argues that "*the weight of an observation is a measure of an observation's relative worth compared to other observation in an adjustment. Weights are used to control the sizes of corrections applied to observations in an adjustment*". In addition it has also to be mentioned that weights or *a priori* accuracies influence the quality measures of the estimated parameters due to given functional relations (Niemeier 2008 pp. 124). The relation between weights, diagonal elements, and correlations, given on the secondary diagonal, between observations is expressed by weight matrix $\mathbf{P}$ that is related to the observation vector $\mathbf{l}$. In the following representation of $\mathbf{P}$ no correlations are assumed which is expressed by zero values in the secondary diagonals

$$\mathbf{P} = (\mathbf{Q}_{ll})^{-1} = \begin{bmatrix} \sigma_0^2/\sigma_1^2 & & & 0 \\ & \sigma_0^2/\sigma_2^2 & & \\ & & \ddots & \\ 0 & & & \sigma_0^2/\sigma_n^2 \end{bmatrix}. \tag{2.3}$$

In order to express relations respectively weights between observations an unknown variance is required usually depicted by σ_0^2 which is also referred to as variance factor, standard error or variance of the unit weight. A frequently used assumption is $\sigma_0^2 = 1$ for weighting of all observations while also more advanced presuppositions can be made where individual variance factors are used for different observation groups. Apart from choosing appropriate correlations between observations the most critical part is related to determination of individual variances σ_n^2. While this circumstance is well known for tacheometric observations, where typical variances are 0.3 mgon for directions and 1 mm + 1 ppm for distances, this issue is a lot more complex for TLS measurements, as already discussed in subsection 2.1.4. This aspect may be the reason that very few studies have focused on the subject of stochastic modelling for TLS observations.

A comparison of different stochastic models for registration of point clouds captured by TLS has been conducted by Elkhrachy & Niemeier (2006). Point-to-point correspondences for computation of transformation parameters were established based on artificial tie points. Centre coordinates of the applied targets have been weighted by using three different stochastic models:

- Equal weights which leads to an identity matrix $\mathbf{P} = \mathbf{I}$.
- Weight proportional to range between scanner and target.
- Weight proportional to squared range between scanner and target.

Consequently the according weight matrices follow

$$\mathbf{A} = \begin{bmatrix} 1/s_1 & 0 & 0 & & & \\ 0 & 1/s_1 & 0 & & 0 & \\ 0 & 0 & 1/s_1 & & & \\ & & & 1/s_2 & 0 & 0 \\ & 0 & & 0 & 1/s_2 & 0 \\ & & & 0 & 0 & 1/s_2 \end{bmatrix} \tag{2.4}$$

for the second model and

$$\mathbf{B} = \begin{bmatrix} 1/s_1^2 & 0 & 0 & & & \\ 0 & 1/s_1^2 & 0 & & 0 & \\ 0 & 0 & 1/s_1^2 & & & \\ & & & 1/s_2^2 & 0 & 0 \\ & 0 & & 0 & 1/s_2^2 & 0 \\ & & & 0 & 0 & 1/s_2^2 \end{bmatrix} \tag{2.5}$$

for the third model where s_1 indicates the distance to the target centre from the origin of the TLS in the first scan while s_2 represents the according value for a second scan. It can be seen that the impact of less precise targets that are located further from the scanner receive lower weights and hence a smaller impact onto the outcome. Tests on a real world dataset revealed the last model to produce the most accurate results. Even though a stochastic model has been applied for weighting purposes a global test of the adjustment (NIEMEIER 2008 pp. 167) is not conducted. Other related articles such as SCHAER *et al.* (2007) or BAE *et al.* (2009) also derive stochastic information for airborne laser scanning respectively TLS but also do not assess the validity of the according models. Hence, the motivation arises to develop and validate a stochastic model for a TLS that is of vital importance for:

- Planning of optimal viewpoints,
- Weighting of observations e.g. for registration or estimation of geometrical parameters,
- Outlier identification,
- Deformation monitoring

which will be subject of chapter 3.

2.2.2 Geodetic viewpoint planning

A prerequisite before carrying out a classical engineering survey based on total station observations is to perform a sophisticated network design respectively network optimisation. The major aims of this task are to receive an optimal solution that satisfies homogeneity of surveyed points in terms of accuracy and reliability for instance by carefully controlling the redundancy numbers of observations. While these aspects are purely seen from an engineering perspective an economic point of view is also essential. For this sake a minimisation of the required expenditure of work needs to be undertaken which has to be smaller than a predefined value $\sum_A$. This measure can either be defined by economic means or by a client for instance at a construction site where certain other design steps can only to be interrupted for a predefined amount of time during the survey. The following equation describes this problem by

$$\sum a_j n_j \leq \sum_A \tag{2.6}$$

where a_j denotes the required effort for a single observation while n_j represents the amount of repetitions. A detailed summary on network design is for instance given by NIEMEIER (2008 pp. 331) or GHILANI (2010 pp. 455).

While the established perspective in engineering geodesy is based on chosen discrete points it is obvious that the mentioned procedure cannot be simply transferred to TLS that acquires an area of interest in a quasi-laminar fashion. First thoughts on finding optimal TLS viewpoints have been proposed by Soudarissanane *et al.* (2008) and Soudarissanane & Lindenbergh (2011) which will be discussed in this section. As an input a 2D map is derived from a given 3D-model of a scene as "*Almost all 3D indoor scene can be reduced to a 2D map by taking an horizontal cross section of the scene at for instance the height of the sensor. This approximation of the 3D surrounding as a 2D map results in less intensive computations*" (Soudarissanane & Lindenbergh 2011). In contrast to the aforementioned equation that describes the expenditure of work in laser scanning a minimum number of viewpoints is desired to cover a region of interest which still features sufficient overlap between adjacent scans for registration via e.g. fine matching algorithms that will be extensively discussed in section 2.3.2.2.2. Again a trade-off has to be found that serves both, the number of acquisitions and the required effort for registration. Furthermore the quality of all measured points should be optimal for which the following criteria need to be satisfied:

- Completeness: All edges of the 2D map should be covered by at least one viewpoint.
- Reach: All edges are captured from at least one viewpoint that is not closer as the minimum distance of a scanner d_{min} and the maximum distance between instrument and edge d_{max}.
- Incidence angle: All edges are acquired from at least one viewpoint where the according incidence angles fall below a maximum threshold α as this influence causes the largest falsifying impact according to Soudarissanane *et al.* (2011).

The problem of determining optimal viewpoints is solved by gridding the given 2D map based on predefined distances. On each grid point a simulated scan with defined settings is carried out via ray tracing. As a result, artificial point clouds are computed where the distance between individual points and scanner as well as according incidence angles on the object's surface arise. These geometric measures are then used to evaluate all viewpoints according to the above mentioned criteria. Gridding the 2D map dramatically reduces the required computational effort which can be quite high in dependence to the chosen number of potential viewpoints and angular resolution of the simulated scanner. The left part of figure 2.4 depicts an example of a visibility polygon for a complex room. The outer bound polygon $\mathbf{P}_0$ is outlined by red lines. Interior obstruction polygons $\mathbf{P}_{0j} = 1 \ldots 6$ are represented by blue areas. The interior of these polygons are not visible. A simulated viewpoint $\mathbf{O}$ is depicted by a red star. The visibility polygon $\mathbf{V}$ from this location $\mathbf{O}$ is represented by the green area. On the right a simulation of nineteen viewpoints are shown that are required to cover all the edges under range and incidence angles constraints. The resulting visibility polygons are represented by grey areas.

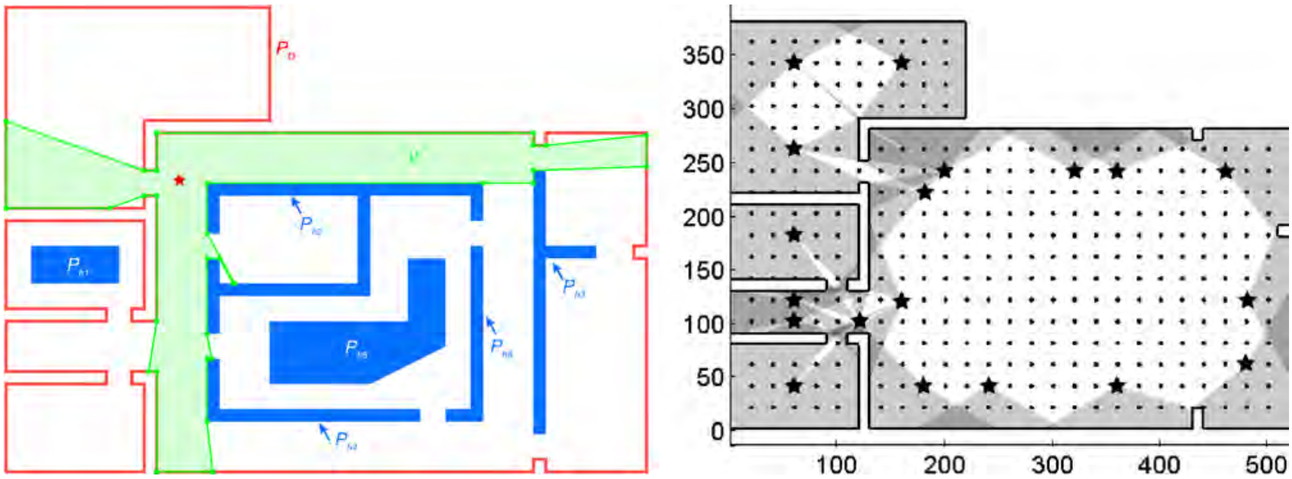

Figure 2.4: *The left part of the figure depicts an example for a visibility polygon based on a 2D map. On the right nineteen optimal viewpoints are represented by stars (both figures by* SOUDARISSANANE & LINDENBERGH 2011).

In conclusion the content of the mentioned articles have to be rated as an important and vital contribution within the context of laser scanning especially from an engineering surveying perspective. However, some aspects need to be rated critically and hence require improvement. At first it has to be said that a 2D map may be a suitable simplification for indoor scenarios but definitely not for natural scenarios outdoors. Indeed the solution provides an optimal solution regarding the stated criteria however does the user not know what that means in terms of achievable accuracy. Finally, the first criterion has to be highlighted as it states that it is sufficient to capture every edge by at least one viewpoint. This argument neglects the fact that this procedure does not ensure sufficient resolution to avoid discretisation errors. In addition a set of viewpoints may be determined that cannot be registered to a common dataset. Based on these drawbacks advanced thoughts and techniques will be presented in section 3.2.

2.3 Referencing methodologies

As already mentioned in the introduction the most influential component in the processing chain of deformation monitoring is the transformation of various captured epochs into a common reference coordinate system. In order to achieve this several approaches are applicable, that can be categorised into georeferenced and co-registration strategies and will be discussed in the following more closely. The peculiarity of the first method is that the common coordinate frame is described by a reference coordinate system which is established by additional geodetic observations (PAFFENHOLZ *et al.* 2010, RESHETYUK 2010). The second methodology, which is also referred to as registration or alignment, works solely on the captured data.

2.3.1 Georeferenced approaches

The first category of referencing approaches follow the long tradition of deformation monitoring where superior predominantly georeferenced coordinate systems serve as reference frames in order to being able to quantify geometric changes in between epochs. In order to achieve this, several approaches can be distinguished that require additional sensors or other equipment such as artificial targets, which will be of interest in the following subsection.

2.3.1.1 Use of artificial targets

The most popular methodology for the sake of registration within the context of deformation monitoring thus far is based on artificial targets which need to be placed within the area of interest. During acquisition of an according epoch all targets need to be captured in order to being able to derive transformation parameters into the desired coordinate system. In general two types of target centre detection can be distinguished namely geometrically motivated approaches and intensity based methods. The most typical form from the first mentioned group are spherical targets where the centre can be determined by adjusting a sphere through the acquired point cloud. However, other geometric arrangements are also applicable, for instance by using corner cube reflectors that are assembled by three intersecting metal sheets (Wujanz *et al.* 2013a). Georeferencing can be directly achieved by tacheometric observations or via global navigation satellite system (GNSS) and forced-centring. Intensity based target identification apply well established methods from image processing such as correlative techniques (Ackermann 1984) that use radiometric information in form of laser intensity images. A detailed description of target centre determination based on reflectance imagery is given by Abmayr *et al.* (2008), Alba *et al.* (2008b) or Chow *et al.* (2010).

Numerous downsides of this strategy are known such as the necessity to enter the area of interest, which may be prohibited, dangerous or impossible as well as the prerequisite that at least some of the attached targets have to maintain stable between epochs. Clarification of this requirement, for instance via S-Transformation (Baarda 1973), needs to be conducted before another epoch can be captured. The size of a target determines up to which distance it can be detected - the larger the distance between scanner and target, the larger the target has to be. While targets based on geometric primitives can be easily adapted to larger distances between TLS and target, radiometrically motivated targets are restricted to the minimum extent of the scanner's laser footprint. This circumstance is highly correlated to the highest achievable resolution (Böhler *et al.* 2003) which peaks at the focal point of the embedded laser's optic (Wujanz 2009). It is obvious that targets can't be scaled arbitrarily as they would be difficult to manufacture and transport as well as prone to gusts of wind that may alter their original position. Also it has to be mentioned that the distribution of targets within an investigated area has an impact onto the derived transformation parameters and hence also onto the result of the deformation monitoring itself. The biggest drawback of this strategy however is the fact that the high redundancy of TLS is not utilised.

2.3.1.2 Direct Georeferencing

The basic principle behind direct georeferencing is the determination of six degrees of freedom (6dof) by usage of external sensors such as inclinometers, compasses and GNSS antennas. Usually the last mentioned sensors also establish the superior coordinate system as a prerequisite for deformation monitoring. Early thoughts on the topic have been raised by Lichti & Gordon (2004) who investigated the error budget of the procedure for acquisition of cultural heritage. Schuhmacher & Böhm (2005) proposed several strategies for direct referencing of terrestrial laser scans including a low cost GPS-antenna and a digital compass. Due to the high demands in terms of accuracy onto the sensors - especially for scenarios with large object distances - the resulting insufficient alignment of the point clouds requires a refinement by using acquired information from the object space in order to generate the final result. Paffenholz & Kutterer (2008) propose the additional use of two GPS antennas for determination of position and orientation within a superior coordinate system. Reshetyuk (2010) presented an approach where two GPS-antennas are solely deployed. The approach follows the strategy of a traverse where the position of the scanner is determined by an attached antenna while the second antenna is mounted on a second tripod. After determination of both positions an orientation is computed where the external antenna is replaced by a cylindrical target. Paffenholz *et al.* (2010) proposed a multi sensor system consisting of a TLS, a GNSS-antenna as well as two inclinometers. An adaptive extended Kalman filter is introduced, which allows in combination with the inclinometer data to determine all desired 6dof. Figure 2.5 shows different setups of the system where the TLS is combined with different sensors: use of two GNSS-antennas (left), one GNSS antenna with two inclinometers (centre) and one antenna with one 360°-prism for assessment.

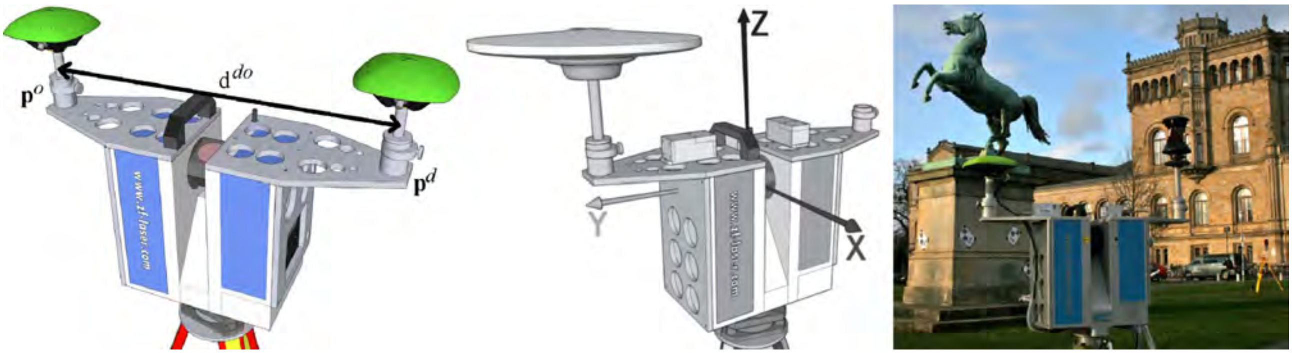

Figure 2.5: *Various configurations of the developed direct referencing system* (Paffenholz *et al.* 2010, Paffenholz 2012).

An extension of the previously mentioned approach has been published by Paffenholz & Bae (2012) where transformational and positional uncertainty is considered. Furthermore refinement of the outcome is conducted by a modified version of the iterative closest point algorithm (ICP) that will be discussed in detail in section 2.3.2.2.2. For sound summaries on the topic the reader is referred to Reshetyuk (2009) and Paffenholz (2012). As mentioned in the first section the congruency model for deformation monitoring assumes a certain part of a scene of interest to remain stable. This requirement can be overcome by usage of georeferenced approaches as the comparison of epochs is conducted within a global reference frame. This aspect has to be rated advantageous in contrast to co-registration approaches that are discussed later in this section.

2.3.1.3 Kinematic data acquisition

A disadvantage of TLS is its sequential sampling process which hence leads to temporal offsets between measured points and consequently to geometric distortion if the object of interest moves or the scanner itself moves during data acquisition. Hence, laser scanners are per se not suitable for observation of kinematic processes or acquisition of a scene by moving a TLS through object space on a movable sensor platform. The last mentioned strategy would lead to a notable acceleration of the data acquisition process in the field compared to static TLS where the instrument's viewpoint is bound to a tripod. However, if the movement of the object or sensor platform can be described by tracking its six degrees of freedom (6dof) during scanning corrections can be applied that yield to a geometric rectification and thus allows kinematic laser scanning or short k-TLS. The most prominent example of k-TLS can be seen in mobile mapping (Schwarz & El-Sheimy 2004) where a kinematic multi sensor platform moves through an area of interest. A sound overview on the history, components, processing steps and other important aspects concerning mobile mapping in a general sense are given by El-Sheimy (2005). Nevertheless several cases can also be defined that are suitable to capture kinematic scenarios whereas the object coordinate system (OCS), sensor coordinate system (SCS) and environment coordinate system (ECS) need to be introduced in this context:

- Case 1: OCS, SCS and ECS remain constant. The object of interest however changes its shape caused by dynamic influences during data acquisition.
- Case 2: OCS and ECS remain constant while the SCS moves within them (mobile mapping).
- Case 3: SCS and ECS remain constant while the OCS moves within them.
- Case 4: OCS and SCS change independently from each other within the ECS.

Since the focus of this subsection lies on systems that apply active instruments for the purpose of data acquisition, contributions that apply TLS in a kinematic sense are introduced in the following. Paffenholz *et al.* (2008) focus on problems that follow the definition of case 1 where an object deforms during the measurement and conclusions concerning its behaviour have been revealed. Neitzel *et al.* (2012) satisfy the same case by performing structural health monitoring (SHM) within a comparative study between k-TLS, accelerometers as well as ground-based radar.

The majority of scientific effort has nevertheless concentrated on problems related to or focusing on the second case. Mettenleiter *et al.* (2008) describe different possibilities and essential aspects of time synchronisation in detail on example of TLS which has been applied in this contribution. Vennegeerts *et al.* (2008) discuss soft- and hardware-based approaches for temporal synchronisation and evaluate the geometric outcome derived by both methods. Hesse (2007) uses a combination of TLS, GPS and inclinometers for a mobile mapping system which turns down usage of costly inertial measurement units. While the previous approaches applied terrestrially operating platforms Böder *et al.* (2010) installed their system including hydrographic sensors onto a vessel. An ongoing project at Jade University of Applied Sciences, Germany called “WindScan” (Grosse-Schwiep *et al.* 2013) applies a combination of TLS and photogrammetry in order to determine strain on blades of actuated wind generators. Hence, this project as well as the approach described by Wujanz *et al.* (2013c) where a ship has been captured in motion on the water follows, according to the previously stated definitions, the third case. The author is not aware of any contribution that covers the fourth mentioned case. In order to conduct kinematic laser scanning the following four steps need to be carried out:

Step 1: Transformation of all sensor coordinate systems into a common coordinate system.

Step 2: Synchronisation / temporal calibration of the system.

Step 3: Data acquisition and determination of the object’s kinematic parameters.

Step 4: Geometric rectification of the point cloud.

For further details on the subject the reader is referred to the cited literature.

2.3.2 Co-registration approaches

A downside of the previously mentioned approaches is that they require additional sensory. Thus, methods are discussed in the following subsections that solely apply data captured by TLS as an input for so called co-registration approaches. In general, a prerequisite of all approaches in order to carry out registration is that a sufficient overlap between point clouds is given. This aspect is assumed to be the case anyway as otherwise deformation monitoring can’t be conducted. A second requirement is that the data contains sufficient information which is:

- Radiometric contrast for intensity based methods: Acquired intensity values feature a heterogeneous characteristic.
- Geometric contrast for geometrically motivated approaches: The captured surface is discontinuous.

2.3.2.1 Intensity based registration

A major challenge in matching of point clouds is the enormous complexity due to the three dimensional characteristic of the stated problem. By interpreting the 3D-point cloud as a two-dimensional image computational and methodological issues can be overcome. This can be achieved by using meta-data that is stored for instance in specific formats such as Leica’s ptx-format. The header as well as the first line of such a file is given in the following. The first two lines specify the dimensions of the acquired scan which hence can be used to define the dimensions of an image. Lines three to ten can be used to store transformational information in case that the given dataset has been transformed into another coordinate system. From line eleven onwards a list that contains 797500 lines is given (number of columns multiplied by the number of rows) where each line represents a single point. The first three values represent the according coordinates while the fourth value features the intensity value which is standardised to a range between 0 and 1. This information embodies the key component of the approach as it is used to generate an image like representation. Line twelve contains a point where a distance measurement failed. Hence, default values are added to the file so that the topology of the scanned area remains stable.

```
1276                           // number of columns
625                            // number of rows
0.000 0.000 0.000              // skip
1 0 0                          // skip
-0 1 0                         // skip
0 -0 1                         // skip
1 0 0 0.0                      // skip
-0 1 0 0.0                     // skip
0 -0 1 0.0                     // skip
0.000 0.000 0.000 1.0          // skip
-0.0046 -0.0073 2.3062 0.754 // coordinates and radiometric information
0.000 0.000 0.000 0.5          // default values
// X Y Z Intensity
```

Figure 2.6 shows on the left how the image matrix is assembled where i stands for the according intensity. In addition to the intensity values the according coordinates are stored which hence also allows querying geometric information for each pixel. On the right a generated intensity image can be seen. Green coloured pixels highlight points for which the distance measurement failed.

$$\begin{pmatrix} i_{1:1} & \cdots & i_{625:1} \\ \vdots & \ddots & \vdots \\ i_{1:1276} & \cdots & i_{625:1276} \end{pmatrix}$$

Figure 2.6: *Dimensions of the image matrix (left) and generated intensity image of a point cloud (right)*

One of the first articles that applied an intensity based registration by using image processing strategies has been presented by Böhm & Becker (2007). Based on two intensity images feature points and descriptors are computed based on Lowe's (2004) scale-invariant feature transform algorithm (SIFT). A set of consistent feature matches are then identified by usage of Fischler & Bolles' (1981) random sample consensus (RANSAC) method which revealed an outlier ratio of roughly 90%. Reasons for this high amount can be found in repetitive patterns and symmetry of the object. In terms of achieved accuracy the outcome falls behind conventional methods. A comparable solution has been presented by Kang *et al.* (2009) who also apply SIFT for feature matching yet propose a sequential algorithm for rejection of mismatches. Another problem that is related to usage of input images respectively detected feature descriptors is their dependency to the sensor location. Houshiar *et al.* (2013) tackle this issue by using map projection methods for rectification of intensity images before feature matching is conducted. A supplementary approach has been proposed by Akca (2007a) which extends a previously published method (Grün & Akca 2005). Instead of using image processing techniques where features are detected and matched so called quasi-surfaces are generated based on the intensity data. The results are in terms of achieved accuracy comparable to surface based matching. A related technique has been proposed by Al-Manasir & Fraser (2006) where the exterior orientation between two TLS viewpoints is determined by photogrammetric means and usage of an integrated camera.

2.3.2.2 Surface based registration approaches

As already mentioned under subsection 2.3.2.1 the complexity of determining transformation parameters in $\mathbb{R}^3$ is an ambitious task. Hence, the registration procedure solely based on using the overlapping region of point clouds is divided into two steps: a pre-alignment which brings the datasets into a coarse arrangement and a fine matching that defines the final relative orientation and location. The first function fulfils two major tasks namely avoidance of local minima as well as reduction of the computational effort that is required within the iterative fine matching process. The following subsection will give an overview on selected matching algorithms of both types. It should be mentioned that a vast amount of contributions has been published on the subject thus only several methodically different approaches will be discussed.

2.3.2.2.1 Coarse registration algorithms

Aiger *et al.* (2008) proposed an approach called four-points-congruent-sets-algorithm (4PCS) where a quadruple of approximate coplanar points from one point cloud is matched to another randomly chosen set of the same amount. The motivation of this procedure is based on the fact that the search space of the problem dramatically decreases in comparison to triplets. A key component of the approach is described by two measures that are invariant under affine transformation. These points uniquely define 4-points set which hence allows to selectively seek for approximately congruent quadruples. Based on these matches a suitable set of transformation parameters is found by evaluating the resulting overlapping region of two point clouds in dependence to a relative congruence measure (RANSAC). According to the authors the algorithm is "robust against noise" as the quadruples are chosen as big as possible based on an overlap estimate between two datasets. Figure 2.7 illustrates the matching process between a target set of four points as well as a source set consisting of five points. A set of points is approximately congruent to each other if $e_1 \approx e_2$. In this case point set {a,b,c,d} as depicted left is congruent to {q_1, q_3, q_4, q_5} that is shown right (Aiger *et al.* 2008).

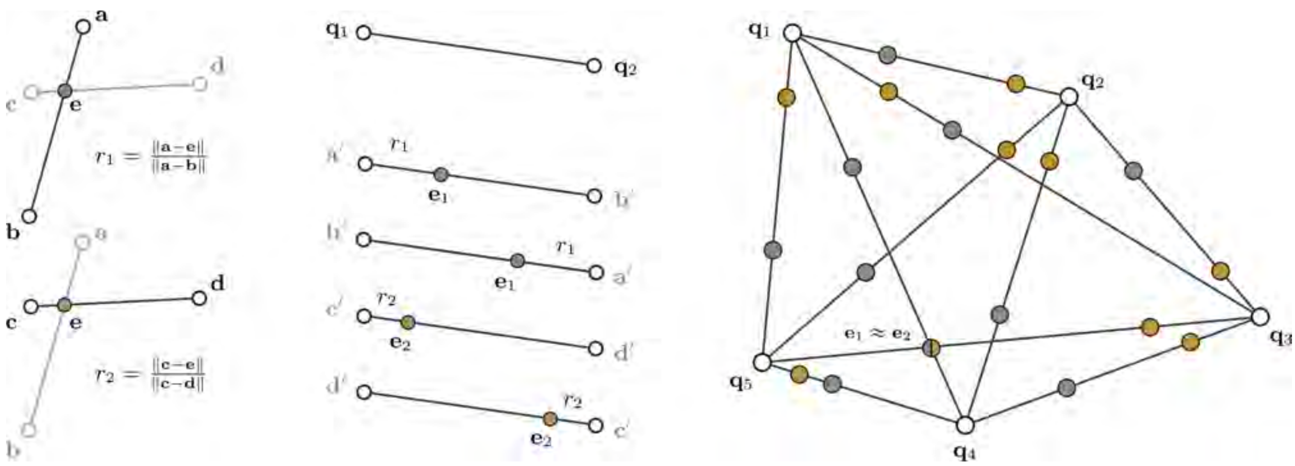

Figure 2.7: *Based on a quadruple of points two ratios can be computed which are referred to as r_1 and r_2 (left part). For every vector within a 4-point congruent subset two possible assignments of intersection e_i can be generated dependent to the definition of the vector (centre). Finally, quadruples are established from a second set of points to which the first dataset should be related. For the sake of simplification only two intermediate points e_i are shown in the right part of the figure* (Aiger *et al.* 2008).

Rusu *et al.* (2008, 2009) introduce the idea of so called persistent feature histograms which generally coincides with Lowe's (2004) methodology of descriptors for image matching that are used to precisely characterise detected features. Therefore points are analysed in a k-neighbourhood that are locally enclosed by a sphere of a predefined radius. Based on this environment a histogram is computed based on different surface normals between a point of interest (POI) and all k-neighbours which hence describes the mean surface curvature of the POI. The characterisation process applies a 16-bin histogram in which the percentage of source points within the k-neighbourhood is sorted that fall into predefined intervals. These intervals are described based on four feature types that essentially describe measures of angles between all points' normals and distances among them – thus they describe datum independent measures. In order to reduce the amount of features down to a set that adequately characterise a dataset persistence analysis is conducted. For this sake the radius of the sphere that encloses the k-neighbourhood is altered in several steps so that several histograms arise for the POI while only points are chosen that show unique characteristics. In order to establish correspondences between two point clouds the according histograms of persistent features are compared and sorted regarding their similarity. Based on the most similar entries correspondences and finally transformation parameters are obtained. As a final step an ICP-algorithm including a modified error function is conducted. Figure 2.8 illustrates persistent features on the Stanford bunny dataset over a series of varying radii as well as the final selection of persistent points. Apart from the two discussed approaches coarse alignment processes have also been proposed by Torre-Ferrero *et al.* (2012), Theiler *et al.* (2013, 2014), who applied the 4PCS-algorithm only on 3D-keypoints, Chuang & Jaw (2015) and Weber *et al.* (2015).

Figure 2.8: *Persistence over multiple radii (left to right: r_1 = 3 mm, r_2 = 4 mm, r_3 = 5 mm,) that enclose a k-neighbourhood and overall persistent points exemplified on the Stanford bunny dataset* (Rusu *et al.* 2009)

2.3.2.2.2 Fine Matching algorithms

After coarse alignment of two datasets relative to each other has been carried out as described in the previous subsection the final matching process in form of fine matching algorithms follows. The necessity of conducting coarse matching before fine matching can be explained by a convergence region in which the two point clouds need to fall into in order to avoid local minima. One of the first fine matching algorithms named iteratively closest point algorithm (ICP) has been proposed by Besl & McKay (1992) where point-to-point correspondences are established. This step has to be rated critical, as illustrated in figure 2.2, due to the fact that points are captured by TLS that are non-repeatable while this issue can be tackled by establishing point-surface correspondences (Chen & Medioni 1991). A comparable methodology has been presented by Zhang (1994).

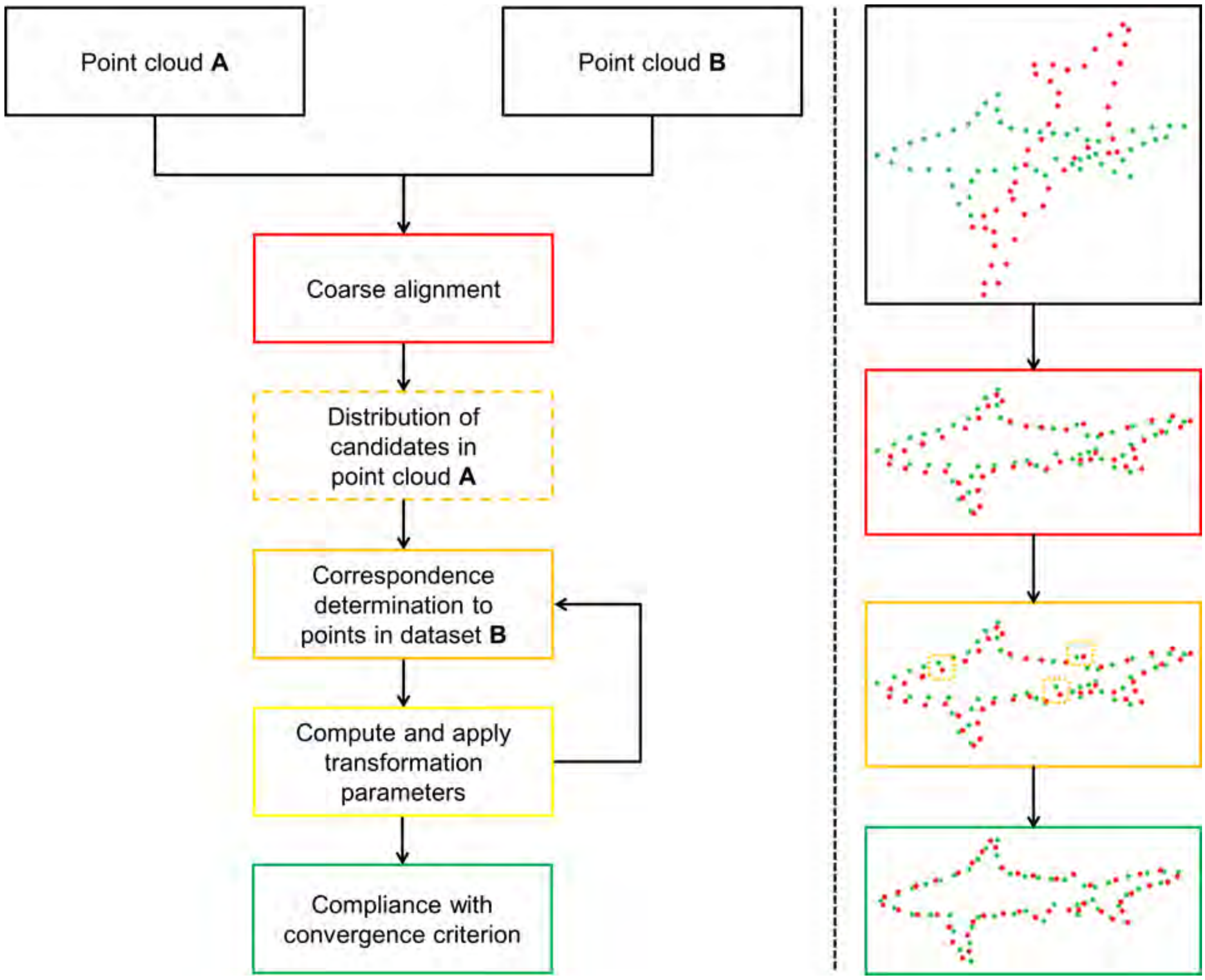

Figure 2.9: *Schematic illustration of the ICP algorithm (left part) and graphical representation of the process on the right. The depicted models are modified versions of dataset kk719 from the Squid database* (Squid 2014).

In the following the general ICP process chain should be described in detail. As a first step coarse alignment between the datasets referred to as point cloud **A** (green shark on the right of figure 2.9) and **B** (red shark) needs to be carried out which can be achieved either manually, by direct georeferencing as introduced in subsection 2.3.1.2 or coarse registration algorithms that have been subject of the previous subsection. This step respectively the outcome is highlighted by a red rectangle on the left while the result of coarse matching is accentuated on the right by using the same shape and colour. Assuming that point cloud **A**'s coordinate system has been defined as a target system a point subset of the whole is selected in order to cut down computational cost and to reduce matrix dimensions during computation of transformation parameters. This selection is referred to as candidate points or candidates and is determined only once during the algorithm. Now that candidates have been sampled the ICP's task is to iteratively determine correspondences between the datasets. This is carried out either by determining the closest point (for instance Besl & McKay 1992, Zhang 1994) in **B** to a candidate of point cloud **A** or the closest triangle (e.g. Chen & Medioni 1991). In order to avoid implausible matches correspondences need to lie within a certain radius and a certain search window that is defined around the face normal of a candidate (Rusinkiewicz & Levoy 2001). It has also to be mentioned that the search of correspondence is a computationally demanding procedure which can be tackled more efficient by using spatial structures such as *k*-*d*-trees (Bentley 1975). This crucial step is highlighted by a large orange rectangle on the right in the figure in which correspondences based on the shortest distance between **A** and **B** are surrounded by dashed rectangles. Note that established correspondences iteratively change during the algorithm while the relative alignment gradually improves. This circumstance is necessary as no correspondences are known before the start of the algorithm. The iterative part of the ICP is repeated until a convergence criterion is satisfied as depicted by the green rectangles in the illustration. Several strategies are applicable while the one that comes to mind at first has its origin in adjustment calculation. In order to solve a non-linear adjustment problem an iterative strategy is applied. Starting with an approximate parameter vector $\mathbf{X}^0$ parameters are iteratively estimated where the current solution vector $\hat{\mathbf{X}}_i$ serves as a new approximate parameter vector $\mathbf{X}_i^0$. This procedure is repeated until $\hat{\mathbf{X}}_i$ falls below a predefined threshold. Depending on the functional model different units and types may be stored in the solution vector $\hat{\mathbf{X}}_i$ hence Akca (2007b) introduces separate thresholds for rotational and translational components. Chen & Medioni's (1991) strategy compares the average squared error of residuals between two sets of correspondences within two adjacent iterations to a set threshold. Grant (2013) determines the root mean square error (RMS) of transformed points between two iterations and a threshold. As divergence may occur between datasets due to insufficient geometric contrast a maximum number of iterations is also defined.

After a general description of the ICP has been given several extensions and variants are discussed in the following. As measurements in general are always subject to uncertainty a certain positional accuracy results for the case of laser scanners. In order to address this issue Bae & Lichti (2008) proposed a weighted variant of the Chen & Medioni's (1991) algorithm for which geometric characteristics are derived namely change of curvature, estimated surface normals vectors and the variance of angular changes of normals (Bae 2005). Furthermore a method for accuracy assessment of the resulting registration error is proposed based on the computed spatial variance. In order to eliminate outliers from the computation of transformation parameters Fischler & Bolles' (1981) random sample consensus (RANSAC) method has been applied. An extensive summary of the procedure can be found in Bae (2006). An overview about several variations of the ICP can be found in Rusinkiewicz & Levoy (2001) while Nüchter *et al.* (2010) focus on different parameterisations of rigid body transformations for registration of point clouds. An approach that is conceptually very similar to the ICP is the so called *least squares matching* (LSM) approach as published by Grün & Akca (2005) and Akca (2007b). Transformation parameters are estimated by use of a generalised Gauss-Markoff-model where the squared Euclidian distance between two surfaces is minimised. The theoretical fundaments of least squares matching have been developed amongst others by Ackermann (1984), Förstner (1982, 1984), Grün (1984, 1985), Gülch (1984) and Pertl (1984). Instead of trying to iteratively find corresponding points search surfaces are matched to template patches. It should be mentioned that LSM can also be used to solve other correspondence issues for instance matching of a 3D-space curve to a 3D-surface. Grant *et al.* (2012a, 2012b, 2013) introduced the idea of symmetric correspondence where point-to-plane correspondences are established on both scans that are to be co-registered. Hence, the methodology describes an extension to Chen & Medioni's (1991) approach where correspondences are determined between a point a from point cloud $\mathbf{A}$ and a triangle derived from point cloud $\mathbf{B}$ and vice versa. Another noteworthy extension is the computation of stochastic measures of all face normals that are used to assemble a full weight matrix. The critical procedure of outlier removal is conducted by definition of a threshold value comparable to Bae (2006) whereas a closer look at this subject will be given under subsection 4.3. Even though a stochastic model has been applied for weighting purposes a global test of the adjustment (Niemeier 2008 pp. 167) is not conducted. In case that more than two point clouds need to be registered at a time a so called global registration problem has to be solved as discussed by Pulli (1999) or Williams & Bennamoun (2001). Non-rigid registration methods have been proposed by Li *et al.* (2008a, 2009) e.g. for motion reconstruction or matching of objects that changed their shape between scans.

2.3.2.3 Registration based upon geometric primitives

An essential problem of TLS is the fact that captured points are usually not repeatedly observed during a successive scan. Hence, point-to-point correspondences cannot be formed as it is the case in classical geodesy e.g. for computation of transformation parameters or determination of deformation vectors. An established and often used technique to overcome this issue is the identification and use of geometric primitives within scenes such as cylinders, planes or spheres. While the latter one is mostly brought into a scene of interest in form of artificial targets the previously mentioned shapes are very likely to be found in urban areas such as houses or roads for the case of planar shapes while cylindrically shaped objects are for instance pipes in industrial facilities or lamp posts. Two central advantages of using geometric primitives for registration purposes should be highlighted while the first one is that reproducible parameters can be derived for instances discrete points (e.g. centre of a sphere) or normals / axes as for the case of cylinders and spheres. In addition the amount of storable data reduces dramatically as only geometric parameters of all detected primitives need to be stored and not the entire point cloud. Figure 2.10 illustrates the circumstance of independence against sampling where an artificial target is depicted by a grey sphere which has been captured from two different viewpoints at a varying sampling rate (green and red spheres on the left respectively right). It can be seen that the approximated centre of the sphere that is represented by a blue sphere remains the same. The second one is that the accuracy of the geometric parameters is higher compared to solely measured TLS points due to the use of highly redundant observations.

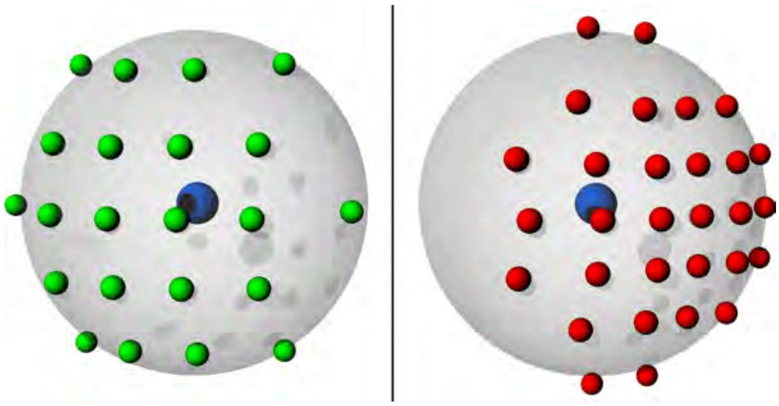

Figure 2.10: *Impact of varying sampling and scan position onto the centre of a spherical target (grey transparent sphere). It can be seen that the centre of the sphere (blue sphere) remains equal despite the fact that acquired points are different.*

A method that applies straight lines respectively axes of cylinders has been proposed by Lichtenstein & Benning (2009, 2010) respectively Lichtenstein (2011) predominantly for matching of industrial facilities as well as buildings. As a first step edges or cylinders need to be identified within the datasets that should be matched. Subsequently correspondences between straight lines need to be established for which four characteristic states namely skew, parallelism respectively identical or intersecting lines can be distinguished. Distances and angles between pairs of straight lines serve as discriminative measures for correspondence determination based on a correspondence matrix. After determination of an approximate rotation (Schwermann 1995) all straight line pairs are aligned nearly parallel. Subsequently exact transformation parameters are estimated based on corresponding centre points between the shortest distance of two line pairs as depicted in figure 2.11. A contribution by von Hansen *et al.* (2008) applies extracted straight lines in order to register aerial and terrestrial point clouds.

A far more popular procedure obtains planes instead of straight lines and bears the highest accuracy potential due to the very high redundancy of planes e.g. that are typically available in urban environments. Several scientific articles have been published on the subject (e.g. Dold 2005, He 2005, von Hansen 2006, von Hansen *et al.* 2006, Dold & Brenner 2006, Pathak *et al.* 2009) while one commercial implementation called SCANTRA is available on the market (Technet 2014) that correlates to the contributions of Rietdorf (2005) and Gielsdorf *et al.* (2008). Rabbani & van den Heuvel (2005) proposed an algorithm that detects planes, cylinders and spheres within an industrial environment for registration purposes. A sound description of the general methodology for plane based matching is given by Dold (2010). The first step of the procedure converts given point clouds into a raster-wise representation where the periodical sampling process of laser scanners is deployed that leads to a matrix where each element contains a 3D point. Subsequently a filter

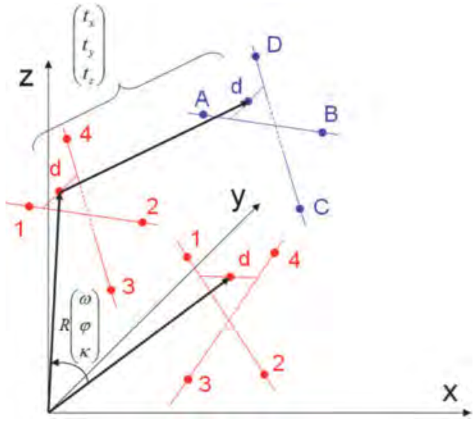

Figure 2.11: *Sequential determination of transformation parameters between two datasets based on straight lines. After coarse rotation of lines 1-2 and 3-4 the distance d between the centre points (red and blue circle) is minimised* (Lichtenstein & Benning 2010).

mask is run over the matrix as in image processing where local plane fitting is conducted. Based on the standard deviation of each plane a decision is drawn whether a planar region has been detected or not. Then a region growing algorithm is applied that automatically sets seed points and determines connected planar regions as depicted in the left part of figure 2.12. Optionally, characteristic properties can be assigned to each detected planar segment in order to simplify the process of correspondence search. In order to avoid perspective falsification of characteristic properties in dependence to the chosen viewpoint during data acquisition geometric conversion is undertaken as illustrates in figure 2.12 on the right.

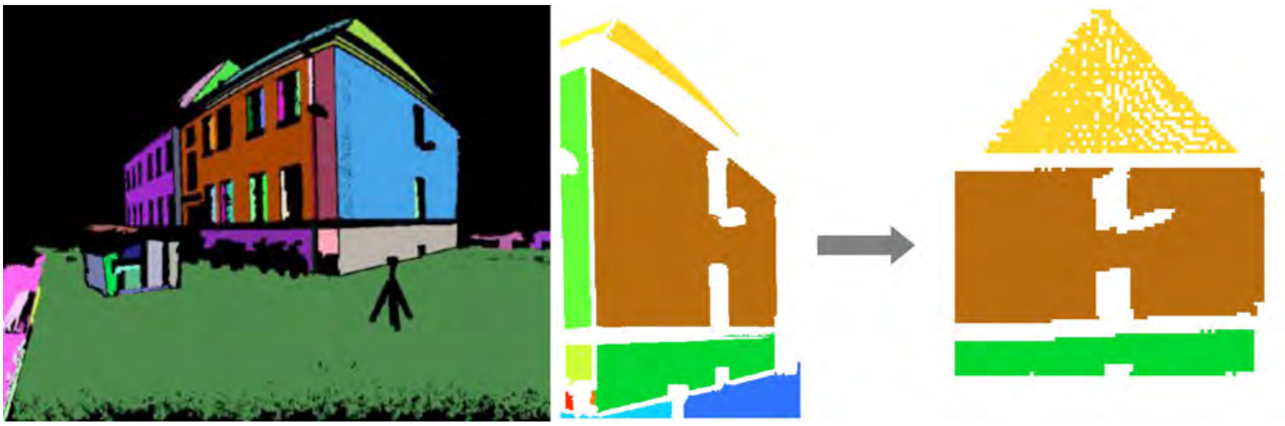

Figure 2.12: *Outcome of the plane segmentation process (left) and geometric conversion of extracted planes (right) for feature characterisation* (Dold 2010 pp. 61)

Therefore planes are rotated in a way that the according face normals coincide with one axis of an arbitrary coordinate system. Then properties are computed that help to discriminate segmented patches such as:

- Circumference of a convex hull around a segment.
- Encircling rectangle.
- Area of a planar patch.
- Average intensity value of segmented points.
- Optionally: Average value of RGB values in case that a point cloud is textured.

Now that planes as well as descriptive properties have been computed correspondences need to be established which describes the most sophisticated part of the approach. Hence, the reader is referred to DOLD (2010 pp. 73) where several techniques are extensively discussed.

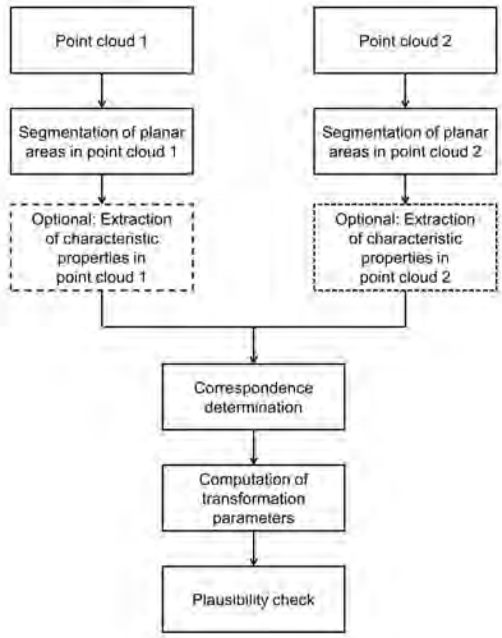

Figure 2.13: *Schematic description of plane based matching* (*based on* DOLD 2010)

The problem of finding transformation parameters based on now known correspondences between planes from different datasets is conducted in a sequential fashion – first determination and application of rotation, then translation, as approximate values including an iterative process would be elsewise required. The determination of rotational transformation parameters is conducted based on the planes' face normals for which several approaches can be applied e.g. SANSO (1973), HORN (1987) or EGGERT *et al.* (1997). After application of rotation onto one dataset translation components need to be calculated. Therefore at least three planar segments are required that assemble a space in order to solve translational fractions in three directions. Additionally the assumption is made that after application of rotation corresponding planes have identical face normal apart from slight deviations caused by the measurement process. Finally, the distances between corresponding planes is minimised within a least squares adjustment. A schematic description of the procedure is illustrated in figure 2.13.

2.3.3 Assessment and categorisation of (Geo-) referencing and matching procedures

Several procedures for co-registration and georeferencing of point clouds have already been discussed in subsection 2.3 hence a comparison and assessment should reveal the most suitable one for the stated problem of carrying out deformation monitoring based on TLS observations. Important aspects for the evaluation are the following prerequisites that are respectively aren't required by the according methods where the first key word is used as an abbreviation in table 2.1 that gathers the outcome:

- Sensors: Additional sensors are needed for geo-referencing.
- Access: The area of interest needs to be entered.
- Content: The scenery has to contain certain information.

The outer left column of the table below contains all methodologies of interest which are coarsely structured into georeferenced approaches abbreviated by (GEO) and co-registration approaches (CR).

Table 2.1: *Assessment of referencing methods*

Methodology	Sensors	Access	Content
GEO: Use of artificial targets	Yes	Yes	Artificial targets
GEO: Direct Georeferencing	Yes	No	None
GEO: Kinematic data acquisition	Yes	Yes	None
CR: Intensity based registration	No	No	Radiometric contrast: e.g. features on a surface
CR: Surface based registration	No	No	Geometric contrast: local geometric variations
CR: Use of geometric primitives	No	No	Geometric primitives: urban scenarios

As the motivation in this thesis is to develop a potentially versatile approach georeferenced approaches are ruled out as additional sensors and / or access of the area of interest is required. Furthermore the accuracy of the required referencing sensors acts accumulatively in context with the TLS and hence decreases the achievable quality. Hence, co-registration methods bear the bigger potential for the stated problem. However intensity based registration requires existence of unique and distinguishable features a prerequisite which may not be satisfied in natural areas. The same argument can be applied for registration methods that apply geometric primitives as an input which are well suited for use in artificial scenes. Thus, these strategies are not versatile enough to be used in various cases of deformation monitoring which is why surface based registration is applied in this thesis. However it has be mentioned that a perfect co-registration algorithm should be capable to process all possible forms of information as an input in order to establish an integrated matching approach. This procedure may also incorporate several additional radiometric information layers in the future that prospective instruments such as multi spectral laser scanners provide (Hemmleb *et al.* 2005, Wujanz 2009, Hakala *et al.* 2012).

2.3.4 Comparative analysis of several registration algorithms

In this subsection different algorithms and commercial products have been compared concerning their capabilities in terms of their implemented quality assurance measures as well as their behaviour against deformed areas namely Raindrop Geomagic, Leica Cyclone, GFaI Final Surface and the academic 4PCS-algorithm. Therefore two point clouds with nearly complete overlap featuring non-rigid body deformation which is subsequently denoted as “snow” have been employed. The “snow” dataset features two epochs of a roof section, see figure 2.14. A snow mantle of roughly 16 cm can be found on the roof in the first dataset while most of the snow has melted when the second point cloud has been captured. In order to provide a reference set of transformation parameters all “deformed” areas that are covered by snow have been removed before the registration process has been started in Final Surface. The matching error of the reference set added up to 3.9 mm based on 2509 points which represented the best 50% of the matching points. Table 2.2 shows the reference values for the second dataset below where t_x, t_y, t_z denote translations in three cardinal directions and r_x, r_y, r_z three Euler rotations around the according axes. The major aim of this experiment is to determine the stability of all algorithms against datasets that contain outliers in form of deformation. Hence, the “snow” scene has been processed including the snow cover to provoke potential effects. Furthermore the impact of tunable parameters onto the final result respectively their quality measures should be determined if possible. Note that parts of this subsection have been published in Wujanz (2012).

Table 2.2: *Reference transformation parameters*

t_x[m]	t_y[m]	t_z[m]	r_x[°]	r_y[°]	r_z[°]
-0.007	0.046	0.125	0.203	-0.145	10.633

2.3.4.1 Raindrop Geomagic Studio 12

Raindrop's Geomagic Studio is able to perform transformations by using geometric primitives and a surface based matching algorithm. The only implemented quality measure is the average distance between two datasets while a colour coded inspection map can be computed if one of the point clouds has been converted into a meshed surface representation. The outcome of the surface based matching can be influenced by the sample size and a maximum tolerance setting. It is worth mentioning that no initial alignment of the datasets is needed which works in most cases. Figure 2.14 shows a colour coded visualisation of computed deformations where the units of the colour bar are given in metres. It can notably be seen that the dataset on the left side, which has been computed by applying the reference parameters, shows only deformations on the roof (blue shades) caused by the snow as expected. The yellow patterns in the windows are affected by blinds that have been lowered in between epochs. A look on the right half of the image would lead to the conclusion that the wall as well as the roof would lean forward as indicated by the colour coding.

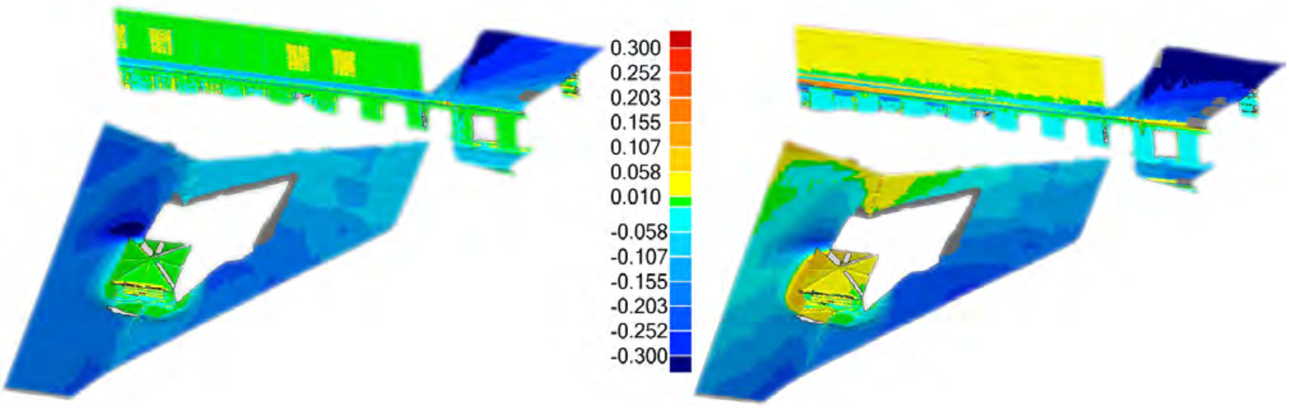

Figure 2.14: *Colour coded visualisation of deformations* [m]*: Based on reference transformation parameters and Result 2 derived by Geomagic (right)*

Table 2.3 gathers all produced results where the first column depicts the according results. Result 1 has been derived with default settings, whereas result 2 has been processed by applying an implemented "automatic deviator eliminator" that marginally reduced the average error. After setting the deviator eliminator down to 0, which actually means that only points are used that perfectly satisfy the current set of transformation parameters, the computed average error was oddly enough larger than the deviations computed by applying default settings as depicted by result 3.

Table 2.3: *Transformation parameters computed with Geomagic*

Result	t_x [m]	t_y [m]	t_z [m]	r_x [°]	r_y [°]	r_z [°]	**Average error**
1	-0.067	-0.193	0.138	-0.087	0.029	10.912	72.9
2	-0.001	0.006	0.205	0.345	0.042	10.641	71.2
3	-0.071	-0.220	0.130	-0.065	-0.005	10.903	73.6

2.3.4.2 Leica Cyclone 7.1

Leica's Cyclone software is capable of performing target based registrations, surface based registrations, using geometric primitives as well as a combination of all mentioned approaches. Implemented quality measures are a histogram depicting the deviations, a function to colour the registered point clouds differently in order to check the result manually as well as a report that gathers transformation parameters and a statistical description of the residuals. Control parameters of the programme are the number of points that are used to compute the transformation parameters whose default setting is 3% of the points within the overlapping area as well as a maximum search distance. Figure 2.15 illustrates the impact of the maximum search distance (horizontal axis) onto the average deviations and their according root mean squares (RMS). Expectedly both measures decreased in general with declining search distance.

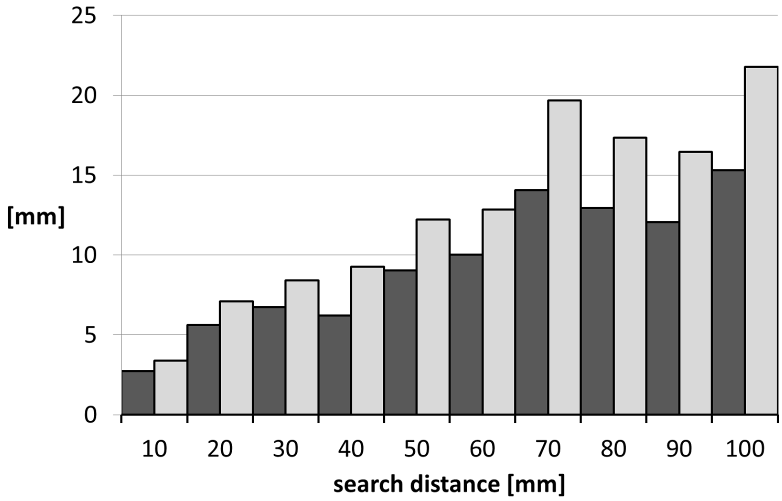

Figure 2.15: *Influence of maximum search distance onto average deviations (dark grey) and their according RMS (light grey)*

Table 2.4 gathers the according transformation parameters for three selected settings where the first column depicts the search radius and the last one the average error both in mm. Nevertheless is the allegedly most accurate result not the closest one to the set of reference parameters. In fact one can't draw conclusions about a whole set of transformation parameters in this table but only for its single components hence none of the computed sets can be regarded as being the best result.

Table 2.4: *Transformation parameters calculated with Cyclone*

Result	t_x[m]	t_y[m]	t_z[m]	r_x[°]	r_y[°]	r_z[°]	**Average error**
10	0.001	0.009	0.019	0.105	0.006	10.622	2.73
50	0.013	0.034	0.020	0.069	-0.034	10.712	9.0
100	0.027	0.051	0.160	0.261	-0.255	10.562	15.3

2.3.4.3 GFaI Final Surface 3.0.5

Final Surface is a software package that has mainly been developed for being used in the field of mechanical engineering. Figure 2.16 illustrates a colour coded visualisation of 500 points that were used to compute a set of transformation parameters. Small deviations are coloured blue; shades of green describe the medium section while yellow to red represent the large end of the spectrum. It can clearly be seen that the distribution of points is quite heterogeneous. The sampling of points is as usually determined by a random component within the implementation. Nevertheless the likelihood for points of being selected is higher for points that have been captured in areas with high point density which occurs very likely close to the TLS's viewpoint as visible in figure 2.16. The colour coding represents the residuals after registration while the colour bar is given in metres.

An established approach in surveying to draw meaningful conclusions about the calculated transformation parameters is a regular sampling of tie points in order to ensure verification within a whole dataset as already pointed out by Dold & Brenner (2008) while Rusinkiewicz & Levoy (2001) propose an approach where the variation of normals is as large as possible. A close look at the roof reveals small deviations within the densely covered foreground while the sparse sampled area shows larger deviances.

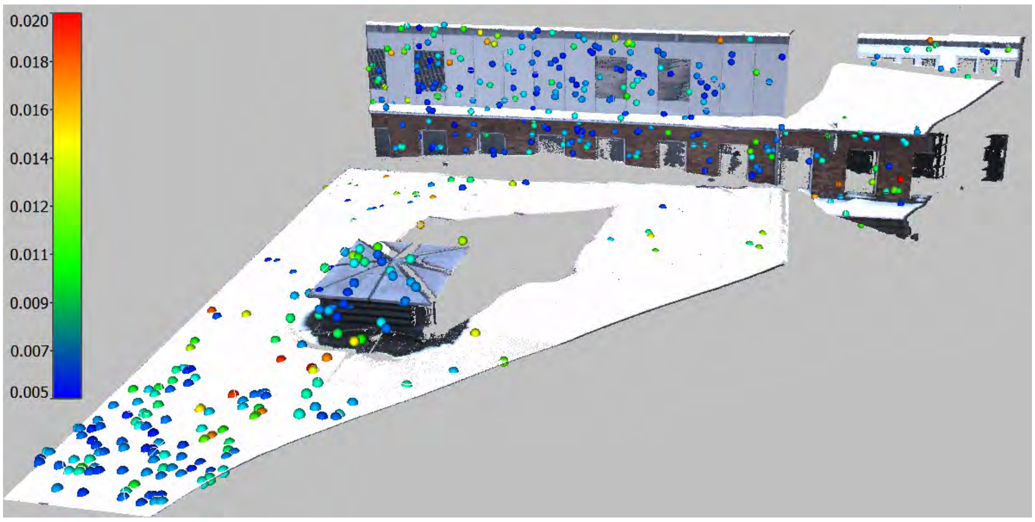

Figure 2.16: *Colour coded visualisation of all applied tie points*

Table 2.5 gathers results based on 5000 points. Result 1 used the best matching 90% of these points while result 2 applied a margin of 50% leading to an applied amount of 2500 points. It is noteworthy that the individual transformation parameters only slightly change while the average error implies a significant enhancement of the results.

Table 2.5: *Transformation parameters computed with Final Surface*

Result	t_x[m]	t_y[m]	t_z[m]	r_x[°]	r_y[°]	r_z[°]	Average error
1	-0.012	-0.036	0.196	0.304	-0.033	10.657	19.6
2	-0.009	-0.024	0.189	0.315	-0.015	10.634	5.3

2.3.4.4 4-Points Congruent Sets Algorithm

The academic 4PCS-algorithm, which was applied with default settings, detected four congruent planes within the deformed scene while 559 points have been used to verify the computed transformation parameters. As 476 points satisfied the acceptable margin of error a quality measure of 85.1% has been computed while table 2.6 depicts the according transformation parameters. Even though the individual transformation parameters show large deviations to the reference values the result was good enough as an initial alignment for the ICP.

Table 2.6: *Transformation parameters calculated by the 4PCS-algorithm*

Result	t_x[m]	t_y[m]	t_z[m]	r_x[°]	r_y[°]	r_z[°]	Average error
1	0.009	-0.057	0.061	0.898	0.083	10.349	92.5

2.3.4.5 Interpretation of the results

The previous sections showed that significantly different results have been generated by all solutions. None of the implementations was able to cope with the “snow” dataset that has been captured with a compensator equipped (accuracy 0.0004°) TLS namely a Leica ScanStation C10 (Leica 2013). This can be constituted by significant rotational deviations from 0 in x and y-direction as well as large translational variations in vertical direction caused by contamination of outliers. None of the implemented quality measures led to the conclusion that a point cloud was subject of deformation. Hence, the explanatory power of the quality measures can be questioned.

2.4 Identification / Rejection of outliers

As already introduced in the first section the most popular model for deformation monitoring is the so called congruency model that identifies geometric changes between epochs. A crucial prerequisite of this procedure is to transform all acquired epochs into a common coordinate frame based only on stable areas. If this precondition is not satisfied erroneous results arise due to falsification by outliers and hence wrong conclusions are drawn as shown in the previous subsection. Thus, outliers respectively deformation must be rejected from the process of computing transformation parameters. This necessity is mentioned by Besl & McKay (1992) who state concerning prerequisites of their approach that "*the algorithm requires no extracted features, no curve or surface derivatives, and no pre-processing of 3D-data, **except for the removal of statistical outliers**.*" This statement can be justified by the so called breakdown point which describes the percentaged fraction of outliers that an adjustment method is capable to cope with (Niemeier 2008, pp. 218). The breakdown point of the L_2-norm amounts to 0% in principle which becomes obvious if one considers the target function of least squares parameter estimation

$$\sum_{i=1}^{n} v_i^T v_i \rightarrow \min \tag{2.7}$$

as proposed by Legendre (1805) respectively Gauss (1809, 1823). It can be seen that the squared sum of all residuals is minimised. Thus, every erroneous observation influences the outcome.

Despite the fact that the term outlier has been used frequently in this thesis a sound definition hasn't been given yet. Hence, this logical gap should be bridged in the following. Ferguson (1961) and Niemeier (2008, pp. 9) define an outlier to be an observation that deviates notably to the mean while the probability for its occurrence is very low considering a normal distribution. While these definitions are indisputable from a probabilistic perspective a wider description has to be used in the context of parameter estimation. Petrovic (2003, pp. 1) states in this context, that it is impossible to completely model reality due to its complexity. If one then assumes that an at least sufficient functional model has been defined, the result of a parameter estimation can be biased by probabilistic and systematic errors whose occurrence is unpredictable. Furthermore observations may be present that do not fit to the assumed functional model e.g. a circle has been observed yet several points have been mistakenly acquired on a straight line. Hence, the following definition is used in this thesis:

An observation is considered to be an outlier if it is subject of systematic and / or probabilistic errors and / or ulterior influences that falsify the estimation of parameters under the assumption of a correct mathematical model.

It has to be explicitly mentioned that various sources can act as outliers while it is not always possible to identify the actual cause. In the context of transformation parameter estimation by usage of surface based information several influences are mentioned in section 4.3. Several techniques will be discussed in this section to cope with outliers while Lehmann (2010) states that "*... all strategies and approaches for the treatment of outliers need to solve an immanent trade-off: They have to avoid that outliers falsify the outcome. Simultaneously no suitable measurements should get lost or if no outliers are present the result shouldn't deviate much to the optimal solution*".

A popular method to eliminate outliers from a set of observations is so called data snooping (Baarda 1968). This method eliminates an observation that shows the biggest normalised residual $|w_i| > c$ where c denotes the according threshold which is also referred to as critical value. Geodetic standard works argue that this value is usually defined by $2.5 \leq c \leq 4$ while LEHMANN (2010) computes the largest acceptable critical value by Monte-Carlo-simulation (METROPOLIS & ULAM 1949).

The iterative process chain of data snooping follows:

1. Adjustment calculation by means of least squares.
2. Global test of the adjustment (subject of 4.3). If the null hypothesis of the test is accepted the procedure ends.
3. Computation of normalised residuals.
4. Verification if the largest normalised residual is smaller than c. If this is the case the according observation is assumed to be an outlier and rejection from the procedure which starts from step 1.
5. The procedure ends as soon as no outliers can be identified.

In order to compute normalised residuals w_i as required in the third step the following basic relationship is used (NIEMEIER 2008, pp. 293)

$$w_i = \frac{v_i}{\sigma_{v_i}} \tag{2.8}$$

where v_i is the residual of an observation while σ_{v_i} represents the according precision. It is noteworthy to point out that this methodology is only successful if the amount of outliers in relation to the observations is comparatively low. If the amount of 3-5% of outliers (in dependency to the geometry) is exceeded (NIEMEIER 2008, pp. 218) the method cannot determine the parameters of interest due to known numerical "smearing". This issue can be related to equation (2.7) where the residuals of all observations are influenced by e.g. a single erroneous observation. Due to the fact that data snooping is an iterative procedure its performance is decreasing with increasing datasets. If the degree of outlier contamination increases the approach rapidly reaches its functional boundaries. The author states that "*Because of the random character of observations it is impossible to signalize {gross} errors with certainty. At the best only statements having a certain probability of success, can be made*" (BAARDA 1968, p. 5). Furthermore he remarks that "*It must be emphasized that the procedure (data snooping) does not give any certainty only a supposition (for identification of gross errors). Data snooping will therefore always be a risky activity* (BAARDA 1968 p. 28)". While the previously mentioned arguments all refer to the problem of identifying erroneous observations and hence the enumerator of equation (2.8), LEHMANN (2013) raises the question related to the denominator of the mentioned equation: Which effects are caused by various test statistics? Also related to this issue is a contribution by POPE (1976) who introduces the *a posteriori* variance factor for the case that no reliable *a priori* information is known. Numerous publications reported failure of outlier removal by usage of data snooping which is why the procedure is not considered in this thesis e.g. HEKIMOGLU & KOCH (2000), NEITZEL (2004, pp. 99), XU (2005) or BASELGA (2011).

Another method to eliminate outliers from a dataset is represented by pre-processing with resistant and robust estimation procedures where the impact of erroneous observations onto the estimated parameters should be kept preferably low. STAUDTE & SHEATHER (1990, pp. 92) define an estimate to be *resistant* if small changes in all of the data (such as round errors) or large changes in a small proportion of the data do not affect the estimate very much. According to CASPARY (1996) resistant estimates are applied only for the sake of data analysis and diagnostic reasons while typical approaches are Median and L_1-norm estimators.

CASPARY (1996) also states that *robust* estimators are *resistant* and fulfil theoretically justified estimation criteria such as efficiency, consistency and asymptotic normal distribution. The development of robust estimators tries to satisfy three main goals:

1. The influence of individual observations onto the estimated parameters should be restricted.
2. The estimator should have a high efficiency concerning the parametric model which has been assigned to the inliers.

3. The estimator should have a high breakdown point in order to withstand even many outliers.

In 1964 Huber introduced the first robust method named **M**aximum-likelihood-estimator or short M-estimator. Based on this original methodology several modifications arose such as HAMPEL (1968) or WICKI's (1999) BIBER estimator (**b**ounded **i**nfluence **b**y standardiz**e**d **r**esiduals) that is used in context of geodetic networks. For a sound overview on robust estimation theory the reader is referred to ROUSSEEUW & LEROY (1987), KOCH (1996), NIEMEIER (2008 pp. 210), HAMPEL *et al.* (2011) or HUBER (2011).

Another related approach is ROUSSEEUW's (1984) **l**east **m**edian **s**quares estimator (LMS) that tries to find a subset under minimal configuration. After computation of parameters squared residuals are calculated from which the Median is determined. A repetition of this procedure is repeated for all possible combinations which leads to enormous computational effort in dependence to the size of the problem. A detailed discussion can be found in subsection 4.5.1.

In summary *resistant* estimators are diagnostic tools to reveal deviations to previously made assumptions while *robust* estimators try to "protect the outcome" against incomplete functional models. CASPARY (1996) concludes his article with the following statement "*Diagnostic tools should not be used for parameter estimation in any case*". Furthermore it has to be stated that the breakdown point of M-estimators decreases in relation to the complexity of the applied functional model, the degree of outlier contamination, the magnitude of outliers and the geometry of the stated problem (HEKIMOGLU 2005). Application of robust estimators in geodesy can for instance be found for blunder detection in close range photogrammetry (FAIG & OWOLABI 1988), transformations (KANANI 2000) or point cloud segmentation captured by TLS (NURUNNABI *et al.* 2012, 2014).

Table 2.7 gives an overview concerning target functions and breakdown points of various estimators. It is rather astonishing to see that the breakdown point for least squares-, M- and L-estimators is equal: namely 0% (ROUSSEEUW & LEROY 1987 p. 10, 149, KOCH 1996). ROUSSEEUW & LEROY (1987 p. 10, p. 149) argue that the breakdown point of the last two mentioned robust procedures is dependent to the geometry of a stated problem "*... because of their vulnerability to leverage points...*".

Concerning the LMS-estimator ROUSSEEUW & LEROY (1987 p. 120) claim that "*... it can be said that the classical LS has a breakdown point of 0%, whereas the breakdown point of the LMS technique is as high as 50%, the best that can be expected. Indeed, 50% is the highest possible value for the breakdown point, since for larger amounts of contamination it becomes impossible to distinguish between the good and the bad parts of the sample*". At first glance the LMS-estimator appears to be most promising methodology and hence a potential solution for the stated problem of deformation monitoring. However a study by HEKIMOGLU (2001) revealed critical aspects that speak against usage of this approach: "*LMS method fails to identify all outliers in some critical cases although it has high breakdown point. There is no guarantee to identify all possible outliers especially if they have small magnitudes. The local reliability is not so high as its breakdown point. In addition, the LMS method may produce outliers in some cases when the observations do not have any outliers*".

Table 2.7: *Overview on several estimators*

Estimator	Target function	Breakdown point
Least squares (L_2-norm)	$\sum_{i=1}^{n} v_i^T v_i \rightarrow \min$	0% (Koch 1996)
Least squares (L_2-norm) + data snooping	$\sum_{i=1}^{n} v_i^T v_i \rightarrow \min$	3-5% (NIEMEIER 2008 pp. 210)
Maximum-likelihood-method (M-estimators)	$\sum_{i=1}^{n} \sigma(v_i) \rightarrow \min$	0% (ROUSSEEUW & LEROY 1987 p. 149, KOCH 1996)
L-estimators (L_1-norm)	$\sum_{i=1}^{n} \lvert v_i \rvert \rightarrow \min$	0% (ROUSSEEUW & LEROY 1987 p. 10, KOCH 1996)
LMS-estimators	$\text{median}\left(v_i^2\right) \rightarrow \min$	50% (ROUSSEEUW & LEROY 1987 p. 120)

In summary it has to be stated that the highest achievable break down point of 50% is eventually still too low to cope with deformation rates that occur in natural scenarios e.g. on glaciers or landslides (Oppikofer *et al.* 2008). Apart from different robust estimators the RANSAC paradigm is often used in the context of outlier contaminated data. A downside of RANSAC is that a threshold has to be defined which decides whether an observation is considered to be an inlier or an outlier. In addition an assumed portion of outliers can be optionally set that clarifies if a valid solution has been found or not. As the degree of deformation can vary significantly in between epochs this task has to be rated as not trivial. Due to the fact that RANSAC tries to randomly find solutions within a certain number of iterations results may arise that are not optimal. In summary it can be stated that RANSAC is unreliable due to its random characteristic and its parameter dependence. Hence, an alternative approach originally proposed by Neitzel (2004) will be used that is subject of subsection 4.5.1 due to its breakdown point beyond the 50% margin.

2.5 On TLS-based deformation monitoring

After identification of congruent respectively stable areas transformation parameters can be computed based on which deformations can be measured. Again similar problems as in registration of point clouds occur as no point-to-point-correspondences can be established. This subsection will give an overview about various fields of application while subsequently the focus is set on different methodologies for computation of deformations. Finally, different strategies are assessed in terms of suitability for different tasks and regarding critical aspects. It has to be highlighted that this section is strictly focussing on deformation monitoring in a geodetic sense where occurring geometric changes are detected and quantified. Another field that is related yet not of interest can be found under the term change detection where the question is posed from a binary perspective namely have notable changes occurred or not (Vosselman & Maas 2010, pp. 237, Lindenbergh & Pietrzyk 2015).

2.5.1 Related work: Fields of application

Numerous contributions have been published on the problem of deformation monitoring based on TLS observations. However they can be categorised by means of referencing and computation of geometrical change which will be done under section 2.5.2. Shortly after the first TLS systems emerged on the market engineering geodesists quickly noticed the potential for extensive deformation monitoring e.g. in the field of structural monitoring respectively civil engineering. Gordon *et al.* (2004) performed a comparative study between TLS and close range photogrammetry in order to determine deflections during loading tests of different beams and a timber bridge. Observations of the beam scenarios have been carried out from one viewpoint while vertical deflections were computed based on a given functional deflection model as well as TLS point clouds.

Schäfer *et al.* (2004) applied TLS on a hydropower station where a lock chamber has been surveyed at different water levels. Data has been acquired from one viewpoint in all epochs while geometric changes have been derived as differences between interpolated grids based on the original point clouds. Hence, deformation can only be detected in one dimension which was suitable for this case. Lindenbergh & Pfeifer (2005) also apply TLS on a lock. The major difference however lies in computing deformation. Each planar lock segment is at first detected in the point cloud. As all segments appear to not entirely satisfy a planar description they are subdivided into smaller equally sized parts which are then approximated by planes. Within a plane adjustment statistical values have been derived for all estimated plane parameters which finally are tested on significant change between epochs. A point cloud of a cooling tower has been compared to a non-uniform rational basis spline (NURBS) model in Ioannidis' *et al.* (2006) contribution. Schneider (2006) applied a long range laser scanner to monitor the bending line of a television tower. Therefore the point cloud has been segmented by generating several slices of the conic tower. Each slice was approximated by a circle where the centre point was of interest and has finally been mapped over time. The seasonal behaviour of a dam was of interest in Alba *et al.* (2006). Fifteen ground control points have been distributed around the dam and then surveyed by a total station in order to establish a stable reference network. For the actual transformation into a common coordinate system of epochs only 9 to 10 points were used. Deformation monitoring was conducted by different methods namely distance between points to a resampled mesh, a polynomial surface and a resampled polynomial mesh. The use of TLS for wear monitoring of material handling systems such as mills has been proposed by Franke *et al.* (2006), Toor *et al.* (2011) and Franke *et al.* (2013).

Lovas *et al.* (2008) as well as Berényi *et al.* (2009) apply TLS for monitoring purposes on bridges. A system for data acquisition in tunnels as well as deformation monitoring based on captured data is proposed by Chmelina *et al.* (2012) while a previous study by van Gosliga *et al.* (2006) focussed on monitoring for the same type of object. Neitzel & Johannes (2009) apply TLS-based deformation monitoring on a historic building by comparing parameters of planar segments. Holst *et al.* (2012, 2015) mounted a TLS on a sub-reflector of a 100 m radio telescope in order to analyse gravity evoked variations of its focal length. Recent developments have shown that the connection between finite element modelling (FEM) and TLS measurements is a promising field of research which can be used for model update and verification (Zaczek-Peplinska & Popielski 2013). A comparison of TLS, accelerometers and ground based RADAR for the sake of structural health monitoring (SHM) has been presented by Neitzel *et al.* (2012). In this contribution kinematic measurements of an externally exited bridge in shape of geometric deflections are used to conduct analysis of the structure in the frequency domain. Alba *et al.* (2008a) and Gikas (2012) apply interferometric techniques based on terrestrial RADAR measurements. In order to avoid potentially existing ambiguities of this relative measurement approach the idea was raised to combine ground based RADAR with TLS which has been implemented for the first time by Wujanz *et al.* (2013a).

However, the field of application where TLS based deformation monitoring is most popular is in sciences where geomorphological processes such as landslides, rockfall and lava, debris or glacier flow is studied. Alba *et al.* (2009) compare different methods of registration as a prerequisite of deformation monitoring. Furthermore a procedure for removal of vegetation from the acquired point clouds is proposed where an infrared camera is conducted. Abellan *et al.* (2009) detect millimetric changes by nearest neighbour averaging of TLS measurements. A case study for rockfall monitoring on a basaltic formation was presented by Abellan *et al.* (2011). An approach for identification of planar segments within a rock face has been presented by Alba & Scaioni (2010) respectively Scaioni & Alba (2010) or Scaioni *et al.* (2013). Statistical tests were carried out to identify only areas where statistically significant changes occurred. Avian *et al.* (2009) carry out deformation monitoring on a rock glacier in the Austrian Alps. For registration purposes five targets have been distributed around the scanner however at rather close distances of 30 m to 75 m. James *et al.* (2009) apply thermal photos which have been mapped on point clouds to study the flow of active lava flow fields while Nguyen *et al.* (2011) monitored volcanic rock slopes. Wang *et al.* (2011) present an integrated approach where continuous Global Positioning System (GPS) measurements have been combined with TLS observations for landslide monitoring. A combination of aerial and terrestrial laser scanning, UAV imagery and geodetic measurements have been used by Roncat *et al.* (2013) to analyse the behaviour of a landslide. A rather untypical case study has been presented by Esme *et al.* (2009) where a TLS has been used to monitor two epochs of a female patient before and after cosmetic breast augmentation.

2.5.2 Related work: Methodologies

This subsection revisits some of the already mentioned methodologies that were subject of section 2.5.1 and other approaches while the focus is now set on the procedural differences and critical assessment.

Cignoni *et al.* (1998) presented probably the first algorithm for point to surface inspection, nowadays mostly referred to as cloud-to-mesh (C2M) or cloud-to-model if a comparison to an *a priori* known shape is made. As a first step a reference point cloud is triangulated while subsequently points are assigned to triangles based on which distances are computed. In a final step points can be colourised based on their distance to the reference surface. This procedure is the most popular approach for generating colour coded inspection maps and is hence implemented in nearly every commercially available point cloud processing software. A close look at the procedure reveals a parallel to Chen & Medioni's (1991) method for registration of point clouds. Lane *et al.*

(2003) present a method which is a common method for deformation monitoring in earth sciences. Therefore two point clouds are converted into gridded digital elevation models (DEM) while a pixel-wise comparison is carried out.

Girardeau-Montaut *et al.* (2005) present three approaches for deformation monitoring. The key component of all methods is an octree structure (Meagher 1982) that will be discussed in detail later on under section 4.2. In brief this method subdivides a point cloud in several cubes of equal size and performs computational operations within all cells which is very efficient in terms of computational demand. As a prerequisite both point clouds must already be registered so that corresponding octree cells should contain data of the same area. The approaches can be found in the list below and will be discussed in detail in the following:

Strategy 1: Average distance within octree cells.

Strategy 2: Comparison of tilt angles based on planar patches.

Strategy 3: Computation of the Hausdorff-distance.

The first strategy calculates average distances between octree cells of two epochs. This is achieved by computing all distances between closest points within all octree cells and by generating the mean value. Areas where change occurred should be identifiable as their average distance is unequal to zero. The second strategy approximates all points within a cell by a planar patch. Subsequently the same is done for the second epoch while tilt angles are computed between planes. The last method computes the so called Hausdorff-distance (Hausdorff 1927 pp. 290) for all points which is defined as the shortest distance between a point in one epoch to one of the adjacent dataset. A similar approach has been proposed by Little (2006) where coordinates respectively distances are compared to repeated observations. This approach is hence a vectorial comparison in relation to the scanner's coordinate system. All proposed approaches can be rated as visualisation techniques for the identification of geometric changes as they do not allow drawing certain conclusions whether deformation occurred or not. Girardeau-Montaut *et al.* (2005) first strategy is dependent to spatial sampling while it would have been cunning to average all points within a cell to form a centroid and to compare it to the one of the other epoch. In strategy 2 shifts of planes were surprisingly not of interest despite the fact that they are a vital source of information even though they could have been easily displayed in an additional visualisation. The third strategy features the highest spatial resolution however is also dependent to spatial sampling.

Methods that are comparable to strategy 1 of Girardeau-Montaut *et al.* (2005) have been proposed by Eling (2009) respectively Wujanz *et al.* (2013). However the major difference is that points within octree cells have been averaged before computation which leads to a higher accuracy of the resulting centroid due to point redundancy. In the following the approach of Eling (2009) is described in detail where a dam was monitored. Registration of epochs is conducted based on artificial targets that surround the scene while all points are assigned to cubes of equal size which is similar to the concept of octrees apart from the fact that the shape of this spatial structure adapts itself to the form of the acquired dam (left part of figure 2.17). Subsequently planes are adjusted based on the points within each cell. Then an average point is computed which represents the spatial centre of each cell. Subsequently this point is projected onto the adjusted plane in parallel direction to the according face normal as depicted in the right part of figure 2.17. An extended version of this procedure is demonstrated by Wang *et al.* (2012).

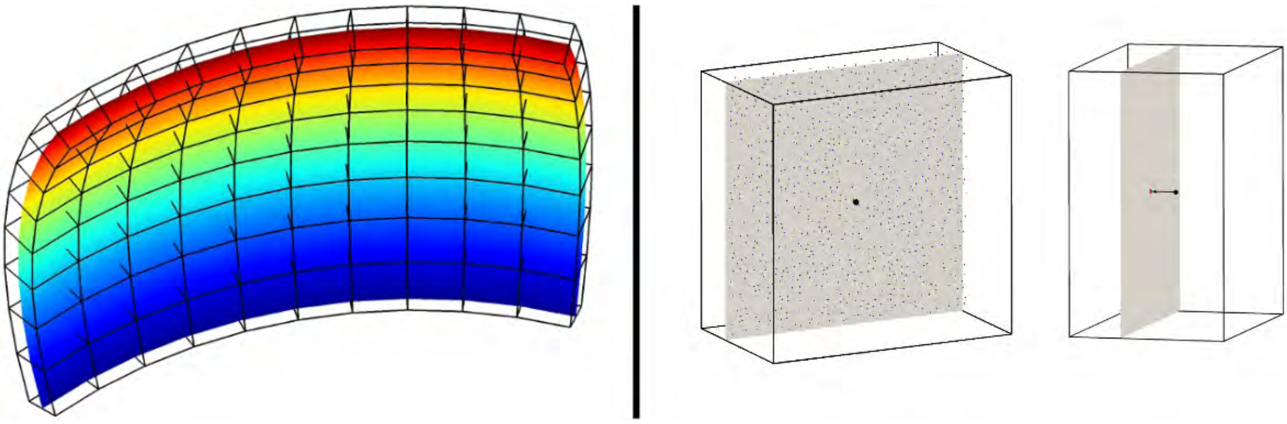

Figure 2.17: *Data structure of the procedure (left), adjustment of a plane through all points in a cell (right) and projection of centroid to the plane* (Eling 2009)

According to Eling (2009) this concept comprises the following advantages:

- Derivation of reproducible object points for multi-temporal comparison of point clouds.
- Increase of the inner accuracy (precision) for every locally filtered point using least squares plane adjustments.
- High spatial discretisation of the structure of interest without usage of artificial markers. Thereby the expressiveness of the results increase while simultaneously costs for targeting and maintenance decrease.
- Locally derived points can also be used for additional analysis such as bending lines.

Teza *et al.* (2007, 2008) also apply the idea of a spatial data structure on already registered point clouds captured in several epochs. The point clouds are sorted into an octree while the ICP is subsequently locally conducted an idea that is also applied in chapter 4 however for a different purpose. In case that no deformation occurred between the datasets no noteworthy transformation vector will result from the ICP-algorithm. However if geometric change occurred in between epochs transformation vectors will result that are interpreted as displacement vectors. Teza *et al.* (2007) state: "*A new method for the automatic calculation of a landslide displacement field is presented here. It is based on a piecewise application of the ICP algorithm and is made possible by the robustness of this algorithm against noise and small morphological modifications.*" This aspect is not correct as the ICP is neither robust against noise nor against geometric changes as demonstrated in section 2.3.4. If this would be the case the proposed approach would only be applicable to datasets where the percentaged change would be beyond the margin of 50%: all other areas would be declared as stable! A comparable approach to Teza's *et al.* (2007, 2008) strategy has been used by Monserrat & Crosetto (2008) while Grün & Akca's (2005) approach was applied for local matching and that deformed regions require manual identification which has to be critically assessed and subjective as it heavily influences the outcome.

Lague *et al.* (2013) developed at strategy, referred to as Multiscale Model to Model Cloud Comparison (M3C2), which derives stochastic measures based on the according local characteristic of the data and does not require triangulation of point clouds. As the procedure is quite sophisticated the reader is advised to have a look at the original contribution. Nevertheless a brief summary of the algorithm is given. The first step of the procedure generates face normals within a sub-sampled environment referred to as core point which is described in detail by Brodu & Lague (2012). In addition this approach can be used to remove vegetation based on a segmentation procedure which would falsify the outcome. A difference to other approaches is the option to generate face normals by using data of the reference epoch, based on the successive epoch or on both. Based on the previously computed normals distances between core points are generated. Subsequently a spatially variable confidence interval is derived which then decides whether deformation occurred in between epochs or not. A closer look at some statements that are given in the article will be discussed later on. Barnhart & Crosby (2013) compared two methods for change detection namely C2M and M3C2. For sound summaries on deformation monitoring the reader is referred to Jaboyedoff *et al.* (2012), Lague *et al.* (2013) or Lindenbergh & Pietrzyk (2015).

Now that several approaches have been introduced a categorisation is conducted based on several characteristic properties. The first attribute of interest is the deformation model for TLS observations while Ohlmann-Lauber & Schäfer (2011) define five cases which are discussed in detail under subsection 2.5.3:

- Point based strategies (PB),
- Point cloud based models (PC),
- Surface based approaches respectively cloud to mesh / model (C2M),
- Geometry based methods (GB),
- Parameter based procedures (PRB).

Furthermore the potential field of usage is of interest where three cases can be discerned:

- Natural, arbitrarily shaped surfaces (NAT),
- Artificial (mostly planar) shapes such as structures or buildings (ART),
- Versatile approaches which can be used for any type of data (VER).

Also the outcome of the monitoring procedure is rated where three potential products can be distinguished namely (Lague *et al.* 2013):

- Displacement vector fields (DVF) based on corresponding points or areas,
- Distance measurements between two epochs usually represented by so called colour coded inspection maps (CCIM),
- Statistically significant difference of geometric parameters (DOP);

as well as the execution of a statistic test.

Table 2.8: *Categorisation of selected approaches for deformation monitoring*

Publications	Deformation model	Usability	Outcome	Statistic test
Cignoni *et al.* (1998)	C2M	VER	CCIM	No
Girardeau-Montaut *et al.* (2005)	PC	VER	CCIM	No
Holst *et al.* (2012)	GB: rotational paraboloid	ART	CCIM	No
Ioannidis *et al.* (2006)	PRB: NURBS	ART	CCIM	No
Lague *et al.* (2013)	PC	VER	CCIM	Yes
Lindenbergh & Pfeifer (2005)	GB: Planes	ART	DOP	Yes
Little (2006)	PB	NAT	CCIM	No
Monserrat & Crosetto (2008), Teza *et al.* (2007)	C2M	NAT	DVF	No
Schneider (2006)	GB: Circle	ART	DOP	No

2.5.3 Procedure assessment

A close look at the mentioned articles in subsection 2.5.1 and 2.5.2 reveals the fact that only very few authors address the necessity of registering point clouds that have been captured at different epochs solely based on stable areas e.g. Lindenbergh & Pfeifer (2005), Monserrat & Crosetto (2008), Scaioni & Alba (2010) or Grant *et al.* (2012a). It can only be assumed that all other authors rate this fact as a matter of course or are not aware of the erroneous impact of geometric changes in between epochs onto the outcome of deformation monitoring, as discussed under section 2.3.4. Another aspect that should be mentioned is the extensive use of C2M in geo-scientific or topographic deformation monitoring while methods based on geometric primitives or parametric surface descriptions are rather dominant in structural monitoring. The reason for using the last mentioned procedures can be found in the higher accuracy that is achieved by redundant parameter estimation.

Based on the categorisation gathered in table 2.8 an assessment will be carried out throughout this subsection that will expose advantages and critical aspects of all procedures. The most important choice to make when conducting deformation monitoring is the selection of an appropriate deformation model. Point based approaches require a fixed instrument location as well as a constant setting of sampling while geometric changes are detected by comparison of distances or coordinates for each point. Hence, this method can be interpreted as a comparison of vector bundles whose origin coincides with the one of the TLS. The biggest drawback of this method is the assumption that previously acquired points can be re-measured in a successive epoch which untruly assumes perfect observation of angular increments. As point cloud based approaches also work on the original point clouds usage of a stochastic model would open the chance to apply statistic tests in order to check for statistically significant change. A major drawback of this model is the direct dependence to the local spatial resolution which is most critical in moving terrain. The last mentioned effect has been addressed in surface based methods where a reference dataset is triangulated before deformation monitoring can be conducted. However discretisation errors are still an influencing factor onto the outcome which can be tackled by providing suitable local spatial resolution. Due to their versatile nature this method is the most popular deformation model in scientific and commercial software. Special cases of C2M approaches have been proposed by Teza *et al.* (2007) and Monserrat & Crosetto (2008) who use co-registration methods to derive displacement vector fields. While the derivation of displacement vector fields is a desirable product especially for e.g. geo-scientific or civil engineering applications the proposed methods have some essential drawbacks that need to be tackled in prospective implementations. The first issue is that correct displacement vectors can only be derived if the object whose location and alignment has changed can be precisely segmented which describes a very challenging task. Furthermore the use of octrees in this context has to be seen critical as the content of a cell influences length and direction of a displacement vector due to the fact that not only the object of interest is featured. Parameter based approaches are mostly used in artificial environments or on manmade objects. Usually processing is carried out by using commercial software packages. This strategy can be compared to C2M-approaches apart from the fact that an ideal parametric state is generated as a reference. A downside of this technique is its complexity as multiple parameters influence the reference model so that the outcome is highly dependent to the processor. In summary it is surprising that very few publications, e.g. Lindenbergh & Pfeifer (2005) or Lague *et al.* (2013), apply or even discuss the necessity of a statistic test in order to satisfy this vital aspect of engineering geodesy that rules out the subjective usage of thresholds and in addition causes a dependence of the outcome to the processor. A prerequisite for statistical testing is of course meaningful stochastic information that Lague *et al.* (2013) categorises as follows and will be discussed in detail under chapter 5:

- Position uncertainty of point clouds: Scanner related influences,
- Registration uncertainty,
- Surface roughness related errors.

2.6 Concluding remarks

This section featured essential fundamentals as well as contemporary approaches for TLS based deformation monitoring. In contrast to other well established geodetic sensors no meaningful stochastic models are available for TLS up to now which describes a vital prerequisite for viewpoint planning, weighting of observations or statistical testing. After discussion of various registration strategies a practical test on data that contained deformation revealed that none of the tested commercial matching algorithms was capable to cope with the stated problem. Consequently all tested products are not suitable for automated deformation monitoring or applications where movement of objects can't be ruled out. The only option to determine stable areas by using commercial matching software is to perform this step manually. As this procedure has to be classified as subjective and very time consuming new automated approaches have to be developed that automatically identify deformation and remove the according point correspondences from the computation of transformation parameters. Furthermore it has been shown that barely no solution for point cloud based deformation monitoring conducts a statistical test for decision making whether deformation has occurred or not. In summary four essential problems which have been revealed in this section are addressed throughout the course of this thesis and hence serve as research questions namely:

1. Development of a stochastic model for TLS.
2. A viewpoint planning algorithm for terrestrial laser scanners.
3. Implementation of diagnostic algorithms for identification and rejection of deformation prior to computation of transformation parameters.
4. A statistical testing procedure for C2M-algorithms.

3 On viewpoint planning based on an intensity based stochastic model for TLS

The previous section has extensively outlined fundamentals as well as current scientific efforts related to established approaches and contemporary TLS-based methods for deformation monitoring while several drawbacks have been reported. This section will propose strategies in order to tackle two of them namely:

- Derivation of a meaningful stochastic model for TLS,
- Model-based viewpoint planning.

and hence complies with step 1 of the deformation monitoring processing chain. Consideration of these aspects is inevitable before an engineering survey is conducted.

3.1 An intensity based stochastic model for TLS

A close look at various programmes of scientific conferences and journal publications shows that a key aspect in the context of TLS was related to accuracy analysis respectively comparison of different scanners. Even though this subject has extensively been analysed the favoured concept still remained untouched until today (e.g. Böhler *et al.* 2003, Kersten *et al.* 2009, Lindstaedt *et al.* 2012) and can uncouthly be summarised as follows: *Take a TLS and measure various targets. Then compare the outcome to known values or to the ones captured from other scanners.* This strategy contains several drawbacks that should be exposed in the following. At first it should be repeated that TLS are assembled of different parts whose key component is the reflectorless distance measurement unit. Moreover TLS is not capable to acquire discrete points repeatedly which is why artificial targets are mostly used for calibration and accuracy analysis of the distance measurement unit. Finally, erroneous effects onto the distance measurements are associated to various geometric influences that are modelled while other sources of falsification are left out as no information about them can be gathered. A parameter that is influenced by nearly all sources of falsification is the intensity value. Thus it is capable to reflect the quality of the received signal and consequently the quality of the derived distance measurement. Based on the mentioned disadvantages a novel approach for stochastic modelling of a TLS is introduced in the following that postulates the following hypotheses:

- If one wants to describe the stochastic behaviour of a distance measurement unit (1D) one should measure only in one dimension and not in 3D.
- The intensity value can be used for precision estimation prior to a survey or weighting of observations as it gathers information about a signal's quality.

The first mentioned aspect is theoretically justified by two arguments. The first one is that comparable measures respectively spatial distances between targets derived by 3D-measurements contain not only influences by the distance measurement unit but also by the deflection unit. Hence its contribution to the outcome should be precluded. Secondly, spatial distances between targets are influenced by the type of target itself, the applied sampling rate as well as the algorithm or method to detect the according centre. The second aspect is motivated by the fact that several influencing factors onto the reflectorless distance measurement are known, as discussed in subsection 2.1.4, yet these impacts can't be separately modelled and hence require observations before being considered within a stochastic model. Before a stochastic model for an applied Zoller & Fröhlich Imager 5006 h laser scanner is proposed the relation between signal strength (intensity) and variance of a distance measurement is of interest.

3.1.1 Experimental determination of stochastic measures

In order to proof the hypothesis that the intensity value can be used for precision estimation of reflectorless distance measurements an experiment has been conducted under controlled circumstances within the range of approximately 8 to 32 m between an object of interest and the applied scanner. In steps of 8 metres a device has been set-up to which only the distance has been observed under varying incidence angles namely 0°, 30°, 60° and 80°. In order to accurately determine the incidence angle a device has been built that consists of an aluminium beam which allows to attach two total station prisms as well as an artificial target for laser scanning. The device is depicted on the left of figure 3.1, is referred to as “Moose of Berlin” and is hence abbreviated by MOB in the following. The experimental set-up of the procedure is illustrated in the right part of figure 3.1 where the blue box depicts the scanner on a tripod and several positions of MOB. Before distances are observed by the scanner the incidence angle has to be determined. Therefore the TLS is replaced by a total station under forced centring so that the origins of both instruments comply. Subsequently the distances to both prisms are measured. For e.g. a normal alignment between scanner and object of interest the distances have to be equal. Before the analysis of the distance measurement unit can be initiated the centre of the artificial target has to be determined. Therefore a 3D-scan is carried out based on which the target centre can be detected by using an integrated function of the scanner control software Z+F Laser Control V8.4.2. Afterwards the centre coordinates of the target that are given in Cartesian coordinates have to be converted into polar ones. The resulting two angles are then used to align the scan head as well as the deflective mirror so that they aim at the centre of the target. Afterwards all preparative steps are completed and the actual measurements can be deployed. For this a Kodak grey-card with a quotient of reflection of 18% within the visible spectrum has been placed over the centre of the artificial target (see left part of figure 3.1) to simulate a quasi Lambertian scatterer (Stöcker 2000 p. 372). To simulate the behaviour of various materials other samples such as e.g. sandpaper or black carton can be placed on the target instead.

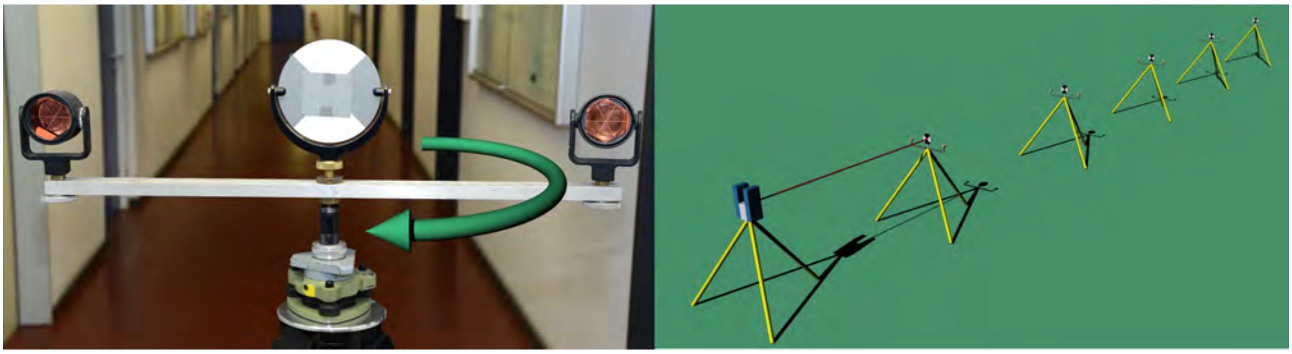

Figure 3.1: *Prototypical implementation of MOB (left) and experimental set-up to examine the stochastic behaviour of a TLS (right)*

Before the results of the experiments are discussed it has to be mentioned that the applied scanner is capable to use different filter frequencies as illustrated in table 3.1 (Zoller & Fröhlich 2010 p. 51, 82). These frequencies determine whether if respectively how often distances measurements are repeated by the instrument. The left column represents a filter index that has been defined by the manufacturer; the centre column shows all available frequencies while the last one contains the amount of distances that are used to compute the mean value. One can see that the frequency with the index 0 represents the basic acquisition rate that is used to capture the data. All filters are subsequently applied onto the captured distance measurements. According to variance-covariance propagation the standard deviation of an observation drops by an increasing amount of repetitions. All results presented in this chapter assume that a filter frequency of 254182 Hz has been applied which means that the distance that is needed to compute the coordinates of a 3D-point has been derived based on the average of four observations.

Table 3.1: *Filter frequencies and number of measured distances for a Z+F Imager 5006h TLS*

Filter index	Frequency [Hz]	Average of n distances
0	1016727	0
1	508364	2
2	254182	4
3	127091	8
4	63545	16
5	31773	32

In total 16 different scenarios have been captured under varying geometric configurations, as described at the beginning of this subsection, of the MOB. For each one of them data has been collected for 10 seconds as a running-in characteristic has been reported by the manufacturer. As a consequence the stochastic model has been derived based on the last 0.1% of the collected data that corresponds to about 10000 distance measurements. The according average intensities as well as the standard deviations of the distance measurements serve as input for the stochastic model that are denoted by black dots in figure 3.2. The horizontal axis illustrates the observed intensities for all scenarios while the according standard deviations of distance measurements, given in metres, are plotted in vertical direction. Due to illustrative reasons only a part of the observations are depicted.

The section has been chosen in accordance to the intensity range that is used in the following subsection. A notable dependence from the signal strength onto the precision of the distances with exponential characteristics can be seen. Especially the part of the graph that features a significant increase of the stochastic measures provoked by a comparatively low intensity is of interest as it is obvious that observations with low intensity should be avoided. As a consequence the demonstrated relationship can be used to describe the theoretical precision of a distance measurement of a TLS within a stochastic model. For this sake the following equation, which has been obtained by fitting, expresses the relation

$$\sigma_s = 0.450 \cdot \left(0.1307 \cdot e^{-1.609 \cdot 10^{-4} \cdot I} - 9.994 \cdot 10^{-9} \cdot I + 0.003587\right) \tag{3.1}$$

where I denotes the observed intensity and σ_s the estimated precision of an observed distance. The coefficient of determination R^2 for the estimation of this function sums up to 97.29%. The green line represents the estimated exponential function described in equation (3.1).

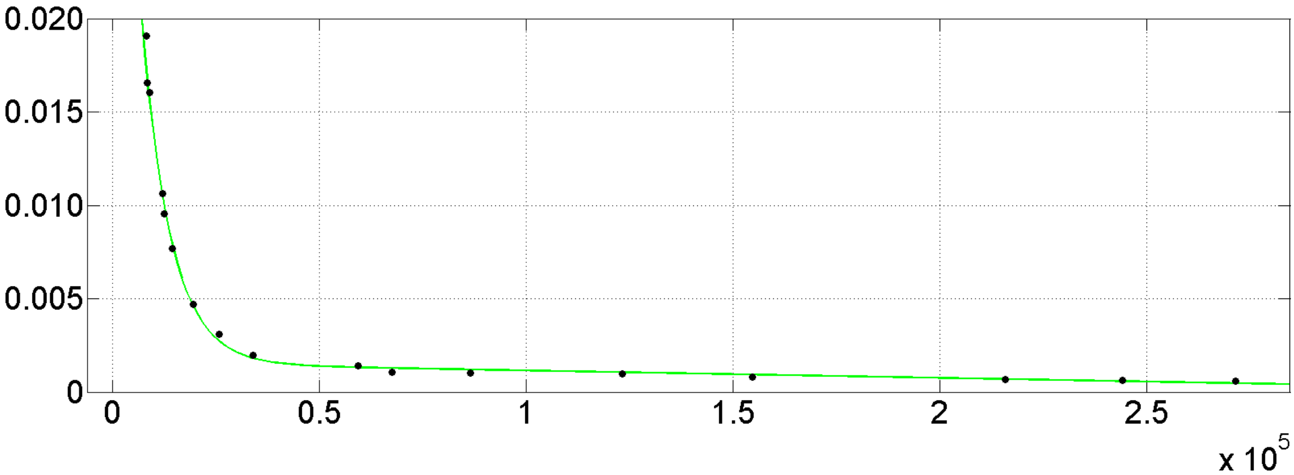

Figure 3.2: *Precision of distance measurements* [m] *in dependence to the observed intensity.*

As the outcome of equation (3.1) is now solely dependent to the observed intensity its variation under different geometric configurations during data acquisition has to be considered. Note that not all manufacturers allow exporting the observed intensity within their respective software but only corrected data instead. As a consequence the assumed stochastic behaviour of observations would be false. Changing the instrument's viewpoint in relation to the object of interest causes a loss of intensity e.g. by increasing distance or by decreasing incidence angles. The physical properties of the object's surface such as roughness and quotient of reflection remain constant yet influence the observed intensity. Note that the roughness of a surface can be described by a scheme of the German National Standard (DIN 4760) that defines six categories of geometrical characteristics. In the context of this experiment category three and four apply that specifies amongst others grooves and rills in surfaces that are within the range of some to several μm. Furthermore it has to be mentioned that the quotient of reflection is influenced by the applied wavelength of the laser scanner as well as the roughness of the test object (Stöcker 2000 p. 374). As the physical properties of the object's surface are considered of being constant the two mentioned geometric influences are investigated in the following as they can be derived from the laser scanner's observations. Therefore data from the above mentioned experiments has been used which corresponds to a data-driven intensity approach as defined by Höfle & Pfeifer (2007). The loss of intensity I_{dist} caused by an increasing object distance d follows

$$I_{dist} = 21.036 \cdot d^3 - 1722.996 \cdot d^2 + 50544.679 \cdot d - 305928.802 \tag{3.2}$$

while the coefficient of determination R^2 sums up to 99.80%. Note that the distance has to be entered in metres. Finally, the signal loss I_{angle} caused by a decreasing incidence angle δ has been modelled by a linear function that follows

$$I_{angle} = 0.0083 \cdot \delta + 0.0327. \tag{3.3}$$

The parameter angle has to be entered in degrees while the coefficient of determination R^2 for the estimated function sums up to 98.40%. In summary the signal dependence onto geometric influences can be expressed by

$$I_{geom} = (I - I_{dist}) \cdot I_{angle} \tag{3.4}$$

where I_{geom} describes the intensity where the according loss has been applied. These geometrically provoked influences onto the intensity are of interest within the scope of viewpoint planning and will be subject of section 3.2.5.

3.1.2 Assessment of the stochastic model

After the stochastic behaviour of the applied laser scanner has been modelled its validity is assessed in the following. Therefore a so called global test of the adjustment is conducted (Niemeier 2008 pp. 167) that decides if the chosen functional and stochastic models of an adjustment are appropriate. Alternatively the term overall model test is used by Teunissen (2000 pp. 93). The general idea is to estimate parameters of geometric primitives based on several datasets where it can be assumed that the functional model holds. Therefore three datasets have been used that contain planar shapes. The first one has been captured under controlled conditions referred to as Door in the following as well as two that were acquired in the field that are named Sandstone. The first dataset features a wooden door with a height of 2 m, a width of 0.80 m and a thickness of 40 mm. This object has been chosen as doors have to meet well defined quality measures in terms of planarity. According to the European norm EN 1530 the captured door falls into planarity tolerance class II. This means that the maximum deviations to a perfectly planar surface have to be less than 0.4 mm. As a consequence this measure falls below the expected precision of the scanner under investigation so that the functional model has to be considered as true. Thus, the noise within the acquired point clouds should be mainly caused by the applied scanner so that its stochastic behaviour can be assessed. The remaining datasets feature planar parts of redecorated sandstone claddings and also assumedly fall below the achievable precision of the applied sensor in terms of planarity.

Table 3.2 gathers characteristic properties of the datasets. In total three variants of the Door dataset have been captured while the initial incidence angle at the centre of the door sums up to approximately 2.3°. Subsequently the door has been opened at varying angles. It can be seen that the mean intensity of the object's surface decreases notably and as a consequence the estimated precision of observed distances, too. As all scans have been captured with the same setting in terms of resolution the amount of points on the door's surface decreases due to the influence of perspective. In general, it can be established that the bandwidth of average intensities spans over 181970 values so that the according theoretical mean precision of distances ranges from 0.64 mm to 1.67 mm. A description of how the theoretical precision of distances has been computed will be given in the following.

Table 3.2: *Overview about the applied data sets*

	Mean intensity	Mean theoretical precision of distances [mm]	Distance to object centre [m]	Incidence angle at object's centre [°]	Points	Approximate dimensions [m]
Door 1	217640	0.64	27.034	2.28	21150	2.00 x 0.80
Door 2	44947	1.46	27.254	34.69	17475	2.00 x 0.80
Door 3	35670	1.67	27.264	46.90	15340	2.00 x 0.80
Sandstone 1	176490	0.82	29.27	2.17	9945	0.91 x 0.58
Sandstone 2	95302	1.18	26.06	19.65	1682	2.31 x 1.32

In order to assign stochastic information to each point cloud the given Cartesian coordinates x_i, y_i, z_i in the instrument's coordinate system have to be converted into the polar elements φ_i, that denotes the direction around the rotation axis of the scanner, λ_i that represents the angle around the deflection axis and the spatial distance s_i. This step is necessary as polar elements are the observations of a TLS that consequently are subject of stochastic processes. For this the following equations apply:

$$x_i = s_i \cdot \cos(\varphi_i) \cdot \cos(\lambda_i) \tag{3.5}$$

$$y_i = s_i \cdot \sin(\varphi_i) \cdot \cos(\lambda_i) \tag{3.6}$$

$$z_i = s_i \cdot \cos(\lambda_i) \,. \tag{3.7}$$

Subsequently variance-covariance propagation is conducted where as a start the Jacobian matrix $\mathbf{F}$ including all partial derivatives of the unknowns can be assembled as follows

$$\mathbf{F} = \begin{bmatrix} \frac{\partial x_i}{\partial \varphi_i} & \frac{\partial x_i}{\partial \lambda_i} & \frac{\partial x_i}{\partial s_i} \\ \frac{\partial y_i}{\partial \varphi_i} & \frac{\partial y_i}{\partial \lambda_i} & \frac{\partial y_i}{\partial s_i} \\ \frac{\partial z_i}{\partial \varphi_i} & \frac{\partial z_i}{\partial \lambda_i} & \frac{\partial z_i}{\partial s_i} \end{bmatrix} . \tag{3.8}$$

The according stochastic information for all observations is gathered in covariance matrix $\mathbf{\Sigma}_{ll}$ that is structured in the following way

$$\mathbf{\Sigma}_{ll} = \begin{bmatrix} \sigma_{\varphi_i} & \cdots & 0 \\ \vdots & \sigma_{\lambda_i} & \vdots \\ 0 & \cdots & \sigma_{s_i} \end{bmatrix} . \tag{3.9}$$

The required stochastic information for the directional observations σ_{φ_i} and σ_{λ_i} sums up to 0.007° according to the manufacturer of the scanner (Zoller & Fröhlich 2010) while the theoretical precision of the distance measurement σ_{s_i} is computed based on the stochastic model introduced in subsection 3.1.1. After computation of the cofactor matrix of unknowns $\mathbf{\Sigma}_{ff}$

$$\mathbf{\Sigma}_{ff} = \mathbf{F}\, \mathbf{\Sigma_{ll}}\, \mathbf{F}^T \tag{3.10}$$

the desired values σ_{x_i}, σ_{y_i}, σ_{z_i} can be extracted from the diagonal of the matrix. Finally, the precision of all directional components σ_{x_i}, σ_{y_i}, σ_{z_i} can be merged into a spatial measure by computing

$$\sigma_{xyz_i} = \sqrt{\sigma_{x_i}^2 + \sigma_{y_i}^2 + \sigma_{z_i}^2}. \tag{3.11}$$

After the above mentioned procedure has been applied to all datasets the Cartesian coordinates x_i, y_i, z_i as well as their according stochastic measures σ_{x_i}, σ_{y_i}, σ_{z_i} computed by variance-covariance propagation are used to estimate plane parameters for all datasets. Note that equation (3.10) only describes a linear approximation of the given non-linear functional relationship. Nevertheless this line of action describes a standard procedure in adjustment calculation by means of least squares within the process of error estimation. This circumstance remains inconsiderable if the functional relationship of the stated problem can be fittingly expressed by a linear approximation. According to Jeudy (1988) or Teunissen (1989) this assumption can be rarely stressed in Geodesy so that their proposed approaches or alternatively heuristic methods such as Monte-Carlo-simulation (Metropolis & Ulam 1949) may be applied.

In the following characteristics of the parameter estimation are listed according to Neitzel & Petrovic (2008):

- Definition of the task:
  - Observations: x_i, y_i, z_i under the assumption that only uncorrelated random errors occur.
  - Unknown parameters: Components of the normal vector n_x, n_y, n_z as well as the perpendicular distance d_i from the estimated plane to the origin of the scanner's local coordinate system.
- Functional model: The functional relationship for the estimation of plane parameters follows $n_{x_i} \cdot x_i + n_{y_i} \cdot y_i + n_{z_i} \cdot z_i - d_i = 0$ which leads to

  $$\color{green}{n_{x_i}} \cdot (\color{red}{x_i} + \color{blue}{v_{x_i}}) + \color{green}{n_{y_i}} \cdot (\color{red}{y_i} + \color{blue}{v_{y_i}}) + \color{green}{n_{z_i}} \cdot (\color{red}{z_i} + \color{blue}{v_{z_i}}) - \color{green}{d_i} = 0$$

  after introduction of residuals $v_{x_i}, v_{y_i}, v_{z_i}$. Note that unknown parameters are highlighted in green, observations in red and according residuals in blue.
- Stochastic model: $\mathbf{P} = \begin{bmatrix} \sigma_0^2/\sigma_{x_i}^2 & \cdots & 0 \\ \vdots & \sigma_0^2/\sigma_{y_i}^2 & \vdots \\ 0 & \cdots & \sigma_0^2/\sigma_{z_i}^2 \end{bmatrix}$.
  For the adjustment the variance of the unit weight σ_0^2 has been set to 1.
- Choice of an adjustment method: Method of least squares with the target function

  $$\mathbf{v}^T\mathbf{P}\mathbf{v} \rightarrow min$$

- Selection of an adjustment model: Non-linear Gauss-Helmert model (Helmert 1872, Lenzmann & Lenzmann 2004, Niemeier 2008 pp. 172) with restrictions between the parameters namely $\sqrt{n_{x_i}^2 + n_{y_i}^2 + n_{z_i}^2} - 1 = 0$.

A single measure that assesses the outcome of an adjustment is the so called variance factor σ_0^2 (Niemeier 2008 pp. 167) that is compared to its adjusted *a posteriori* value s_0^2. The general assumption is that s_0^2 should be close to σ_0^2 within its probabilistic boundaries if the stochastic as well as the functional model are valid which is referred to as global test of the adjustment. This decision is established by usage of a χ^2-test (Ghilani 2010 pp. 76-79). In order to conduct a global test of the adjustment the unknown parameters $\hat{\mathbf{x}}$ as well as the residual vector $\mathbf{v}$ have to be computed based on the adjustment described before. The actual test (Niemeier 2008 pp. 170) is conducted by computing

$$P\left\{\frac{\mathbf{v}^T\mathbf{P}\mathbf{v}}{\sigma_0^2} > \chi^2_{\mathbf{f},1-\alpha} \middle| \mathbf{H}_0\right\} = \alpha \tag{3.12}$$

where $\chi^2_{f,1-\alpha}$ denotes the quantile of the χ^2-distribution, usually assuming α to be 5% and a noncentrality parameter λ of 0, while H_0 represents the null hypothesis that assumes that both the chosen stochastic and the functional model can be stressed.

If the ratio between $\mathbf{v}^T\mathbf{P}\mathbf{v}$ and σ_0^2 is larger than 1, the estimated precision based on the stochastic model is too optimistic, if it is smaller than 1 then it can be interpreted as too pessimistic. However, this test is only suitable for problems with a redundancy lower than 20 due to the fact that the probability of error notably increases (Niemeier 2008 pp. 304). As the redundancy for the given case is significantly higher a criterion is used for verification of the test's outcome that is established in practice. The empirical boundaries (Neitzel 2015) that declare the aforementioned ratio as acceptable are +/- 20% under the assumption that standard deviation of the unit weight has been defined as 1.

Table 3.3 contains an overview about the computed stochastic measures as well as the outcome of the plane adjustments. For the door example it can be seen that the theoretical spatial precision σ_{xyz_i}, given in millimetres, notably increases corresponding to the loss of intensity as depicted in Table 3.2. The according empirical standard deviations for this example are depicted in the second column of the table and do not cross the 20%-margin so that the outcome has to be positively rated. It has to be mentioned that the specified angular precision of 0.007° lead to very pessimistic results so that this value has been set to the resolution of 0.0018° as published by the manufacturer. After this adaption the results lead to a much higher degree of accordance in terms of the empirical standard deviation s_0.

Table 3.3: *Overview about the estimated parameters and their stochastics*

	Mean of σ_{xyz_i}	s_0 *a post.*	$n_x \mid \sigma_{n_x}$	$n_y \mid \sigma_{n_y}$	$n_z \mid \sigma_{n_z}$	$d \mid \sigma_d$ [m|mm]
Door 1	1.40	0.856	0.543 | $2.15 \cdot 10^{-3}$	-0.840 | $3.34 \cdot 10^{-3}$	$1.485 \cdot 10^{-3}$| $1.00 \cdot 10^{-5}$	27.016 | 107.26
Door 2	1.90	1.105	0.940 | $4.10 \cdot 10^{-3}$	-0.342 | $1.49 \cdot 10^{-3}$	$-1.638 \cdot 10^{-4}$| $1.63 \cdot 10^{-5}$	22.413 | 97.89
Door 3	2.07	1.029	0.992 | $4.62 \cdot 10^{-3}$	-0.128 | $1.49 \cdot 10^{-3}$	$5.313 \cdot 10^{-4}$ | $1.72 \cdot 10^{-5}$	18.541 | 86.43
Sandstone 1	0.87	0.858	-0.998 | $5.79 \cdot 10^{-3}$	-0.018 | $1.10 \cdot 10^{-4}$	0.003 | $5.31 \cdot 10^{-5}$	29.240 | 169.29
Sandstone 2	1.66	0.840	0.714 | $6.634 \cdot 10^{-3}$	0.699 | $6.501 \cdot 10^{-3}$	$2.058 \cdot 10^{-3}$ | $2.833 \cdot 10^{-5}$	8.839 | 82.11

3.2 Viewpoint planning for TLS

A look into geodetic standard literature on the subject of planning and viewpoint configuration reveals parallels between several acquisition methods such as for instance tacheometry (Niemeier 2008 pp. 331) and photogrammetry (Luhmann 2003 pp. 498). Common properties of both techniques include the compliance of predefined criteria concerning accuracy and reliability yet within acceptable economic boundaries (Rehr *et al.* 2011). A direct transition of the described procedures onto TLS is not applicable as both cases assume discrete, repeatedly observable points in object space while only the acquisition configuration is optimised. This case is not given in terrestrial laser scanning as the point sampling on the object's surface is directly dependent to the chosen viewpoint. Consequently observations have to be simulated for all potential viewpoints under consideration of predefined settings – this procedure is referred to as ray casting (Appel 1968). Economic aspects in the context of viewpoint planning will be subject of subsection 3.2.4 where only geometric information serves as input data. Viewpoint planning for the use in engineering surveying is discussed under subsection 3.2.5 where the previously proposed stochastic model is deployed.

Hence, two essential sets of information are needed at most in order to carry out viewpoint planning for TLS namely a suitable stochastic model as suggested in the previous subsection as well as a closed surface representation of the object under investigation as a minimum input. This information is often available prior to a survey for instance in form of blueprints, previously generated 3D-models at a lower resolution from other sources or any kind of CAD-models. Alternatively scans can be acquired and triangulated in order to receive the required input. Before several different strategies for determination of optimal viewpoints under varying considerations will be proposed a suitable formulation for the required expenditure of work (EOW) is suggested. While equation (2.6) is dependent to the required effort for a single observation and its repetitions within the context of total station surveys this circumstance is now transferred for usage with TLS and follows

$$\sum \mathrm{VP}(\mathrm{HFOV},\mathrm{Res},\mathrm{Filter}) \leq \sum_{\mathrm{A}} . \tag{3.13}$$

This adaption of the original equation had to be made as the time of a single observation with a TLS can be conducted in split seconds as denoted in table 3.4. Concerning equation (3.13) it can be seen that the expenditure of work is a function of the required number of viewpoints VP as well as the current settings of the scanner and should be as large respectively smaller than the maximum expenditure of work $\sum_A$. It has to be emphasised that the amount of viewpoints VP should be minimal due to the fact that changing the scanner's position is the most time consuming part in comparison to the mentioned scanner settings. The settings of the scanner include the horizontal field of view HFOV, the chosen resolution Res and eventually filter frequency Filter where distance measurements can be repeated respectively filtered multiple times. In summary these settings influence the acquisition time carried out from one particular viewpoint. The horizontal field of view has been chosen in this context as it substantially influences the time of acquisition due to the fact that the revolution of the scan head around the rotation axis is significantly slower as the one of the deflection mirror. Table 3.4 gathers the scanner performance of a Z+F Imager 5006 h (Zoller & Fröhlich 2010 p. 51, 82) in dependence to various scanner settings. The outer left column gathers several settings of the scanner that influences the angular increment (see second column from the left) and consequently the spatial sampling (third column from the left). The remaining columns contain information that controls the noise of the distance measurement unit and will be discussed in detail in the latter. Each cell contains three values where the first indicates the rotation speed of the deflection mirror that is given in rotations per second (rps). Note that the scan duration is given for a panorama scan. The second value depicts the filter frequency as already gathered in table 3.1 where the units are kHz respectively MHz while the last value represents the scan durations in minutes and seconds. A comparative look at different scan settings reveals a large span of scan durations which hence directly influences the expenditure of work. As a consequence a setting has to be chosen by the user that requires the shortest length of stay on one viewpoint where the resolution is still high enough not to cause unacceptable discretisation errors. For the remainder of this subsection it is assumed that an appropriate setting has been chosen.

The proposed methodology works in several stages and will be briefly described before detailed considerations are made. At first potential viewpoints need to be defined by the user, which is usually done in form of a grid or another different systematic distribution, that surrounds the model of interest and restricts the computational effort of the solution. On each grid point ray casting is conducted based on predefined settings of a simulated scanner. This process leads to simulated point clouds whereas stochastic information for each point can be computed optionally via variance covariance propagation. For this stochastic information of angles as published by the manufacturer of the simulated scanner as well as the proposed stochastic model is used which yields to the according 3D precision of every point. Finally, all simulated viewpoints are evaluated based on different attributes that are proposed in the following. In summary it can be established that this subsection closes methodical gaps of Soudarissanane *et al.* (2008) as well as Soudarissanane & Lindenbergh's (2011) previous work and focuses on two major disadvantages of their proposed strategies and thus introduces:

Table 3.4: *Scanner performance of a Zoller & Fröhlich Imager 5006h in dependence to various settings*

Resolution	**Angular increment** [°]	**Resolution at 25 m distance [mm]**	**Quality low**	**Quality normal**	**Quality high**
Preview	0.288	125.7	-	25 rps 31.25 kHz 13 s	-
Middle	0.072	31.4	50 rps 250 kHz 51 s	25 rps 125 kHz 1 min. 41 s	12.5 rps 62.5 kHz 3 min. 22 s
High	0.036	15.7	50 rps 500 kHz 1 min. 41 s	25 rps 250 kHz 3 min. 22 s	12.5 rps 125 kHz 6 min. 44 s
Super high	0.018	7.9	50 rps 1 MHz 3 min. 22 s	25 rps 500 kHz 6 min. 44 s	12.5 rps 250 kHz 13 min. 28 s

- A 3D-viewpoint planning algorithm for TLS,
- Different strategies for economic data acquisition and engineering surveys.

The issue that has to be solved for viewpoint planning is referred to as *set cover* and belongs to the group of so called NP-completeness problems as defined by Karp (1972). As it is not possible to determine an analytic solution a deterministic strategy has to be chosen as briefly mentioned before.

Let GS be a ground set assembled by z elements for which the smallest possible number of sets has to be found that entirely covers GS. Bear in mind that for the stated task of viewpoint planning GS would be represented by a 3D-model - the problem however remains the same. A solution to solve the stated problem is the so called greedy algorithm (Chvatal 1979) who's functionality is described by Slavik (1996) as follows "*. . . at each step choose the unused set which covers the largest number of remaining elements*" and "*. . . delete(s) these elements from the remaining covering sets and repeat(s) this process until the ground set is covered*". This sequential strategy is also referred to as next best view method and bears the drawback of being dependent to the chosen starting point. That means that different solutions arise if the problem is approached from varying starting points.

As in practice complete coverage can usually not be achieved due to obstacles or restrictions in terms of perspective compromises have to be made. This can be done by setting a threshold that describes an acceptable solution and will be subject of the next subsection.

3.2.1 On discretisation errors and captured surfaces

Due to the fact that TLS discretise an object of interest the occurrence of discretisation errors arises. This outcome emerges likely in case of flat incidence angles, complex unsteady geometries or with increasing distance between scanned area and instrument. This effect should be avoided as it would otherwise lead to falsification for instance of ICP-based registration or deformations if epochs are compared against each other even though no geometric alteration occurred within object space. In consequence the occurrence of discretisation errors between a given model and a simulated laser scan will be quantified and finally used as part of an assessment scheme. For this sake the proposed procedure allows to define a maximum discretisation error de_{max}. The discretisation error is defined in this context as a perpendicular distance between a point from a simulated laser scan and a corresponding triangle in the model dataset (Cignoni *et al.* 1998) that is larger than de_{max}. It should be mentioned that a detailed model of the object of interest has to be known beforehand to reliably determine de_{max} which for instance can be generated by scanning an object at the highest possible resolution from many viewpoints.

The first quality measure to evaluate one or many simulated viewpoints is the so called coverage cov [%] that follows

$$cov = \frac{surface_{acquired}}{surface_{total}} \cdot 100 \tag{3.14}$$

and hence describes the ratio between captured surface $surface_{acquired}$ and the entire surface of the given model $surface_{total}$. For the sake of clarity it should be remarked that the terms surface and area are used in this thesis synonymical to surface area. In order to compute $surface_{acquired}$ every current simulated point cloud is triangulated. Then all triangles are analysed in order to check which one have already been acquired from different viewpoints and if discretisation errors larger than de_{max} are existent. If the last mentioned aspect is the case according edges are deleted so that only triangles are considered in cov that are not subject of critical discretisation errors. As the procedure contains several steps it is demonstrated in detail on an example in the following.

A model of a statue, that is referred to as Nefertiti in the following, is given that features an unsteady and hence rather complex surface. The input model $Model_{Original}$ is a scaled version of the dataset illustrated in figure 2.2 which leads to a width of 1.95 m, a depth of 2.47 m and a height of 4.78 m. The scaled dataset is depicted on the left of figure 3.3 with the author of this thesis for comparative reasons. The scaling has been done in order to simulate acquisition of a larger statue. The right half of figure 3.3 schematically exemplifies the chosen concept for computing discretisation errors in two dimensions based on the silhouette of the Nefertiti model. Based on the original model a buffer buf is computed (Rossignac & Requicha 1986, Chen *et al.* 2005) whose thickness complies to the largest acceptable discretisation error. The large grey area corresponds to $Model_{Original} - buf$. Hence a buffer towards the centroid of the original model while the black area depicts the positive buffer that is computed by $Model_{Original} + buf$. As a consequence areas acquired by simulated scans have to be located in the black region which are highlighted by green colour. Discretisation errors are shown in red colour that are caused by an insufficient local sampling rate.

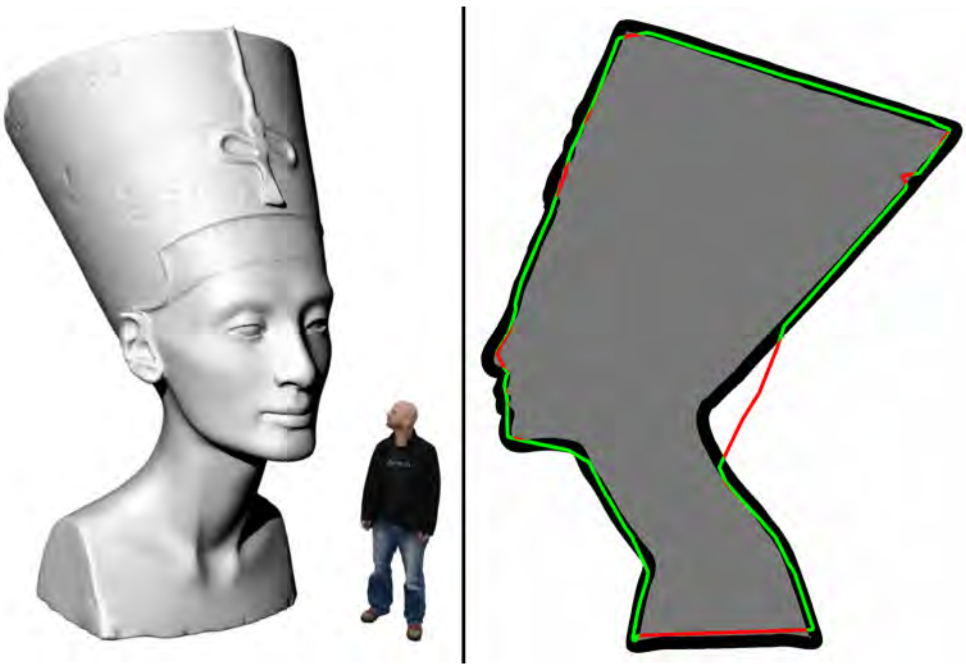

Figure 3.3: *Object of interest in relation to the author's height (left). Exemplary visualisation of discretisation errors (right).*

Assuming that the statue is located at a planar horizontally aligned plaza and that all simulated scanner viewpoints are positioned 1.60 m above the ground a total surface of 29.94 m^2 is visible. As the focus of this subsection is set onto quantification of discretisation errors only one viewpoint is simulated however at two varying resolutions. The maximum discretisation error de_{max} should be no larger than 1.5 cm. At first two modified versions $Model_{modified}$ are generated based on the original dataset with parallel offsets of +/- 1.5 cm to the original dataset. Subsequently a point cloud $PC_{simulated}$ is simulated with a set resolution that leads to a comparatively low amount of 77 points. A visualisation of the given model and simulated TLS points, depicted by purple spheres, is illustrated in figure 3.4 a. The resulting dataset is then triangulated, as depicted in figure 3.4 b, which is referred to as $PC_{triangulated}$ and spans over a surface of 8.78 m^2. The next step is to analyse if and most importantly where discretisation errors occurred for which the triangulated simulated scan as well as the two modified copies of the original dataset are used. For that purpose Boolean operations (named by its creator the English Mathematician George Boole 1815 - 1864) are sequentially conducted to identify intersections (Lauther 1981, Martinez *et al.* 2009) between $PC_{triangulated}$ and the two buffered modified models $Model_{modified}$. The result of this procedure is exemplified in figure 3.4 c. Red lines highlight intersections between buffered models and the simulated triangulated point cloud and hence show where discretisation errors larger than the predefined threshold occurred. In consequence these areas require to be scanned at a higher resolution. As a result of the intersection process the surface has been reduced to 5.92 m^2 yet it is not the final outcome. Finally, all triangles have to be removed that abut on areas that are subject of discretisation errors. The outcome is depicted in figure 3.4 d and covers only 1.93 m^2. In summary the outcome has to be rated as being to sparsely sampled which leads to a low *cov* value of 6.4%. Furthermore it can be seen that no connected region results which also has to be rated negatively. Subsequently results of a second run of the procedure are presented where the sampling resolution has been significantly increased.

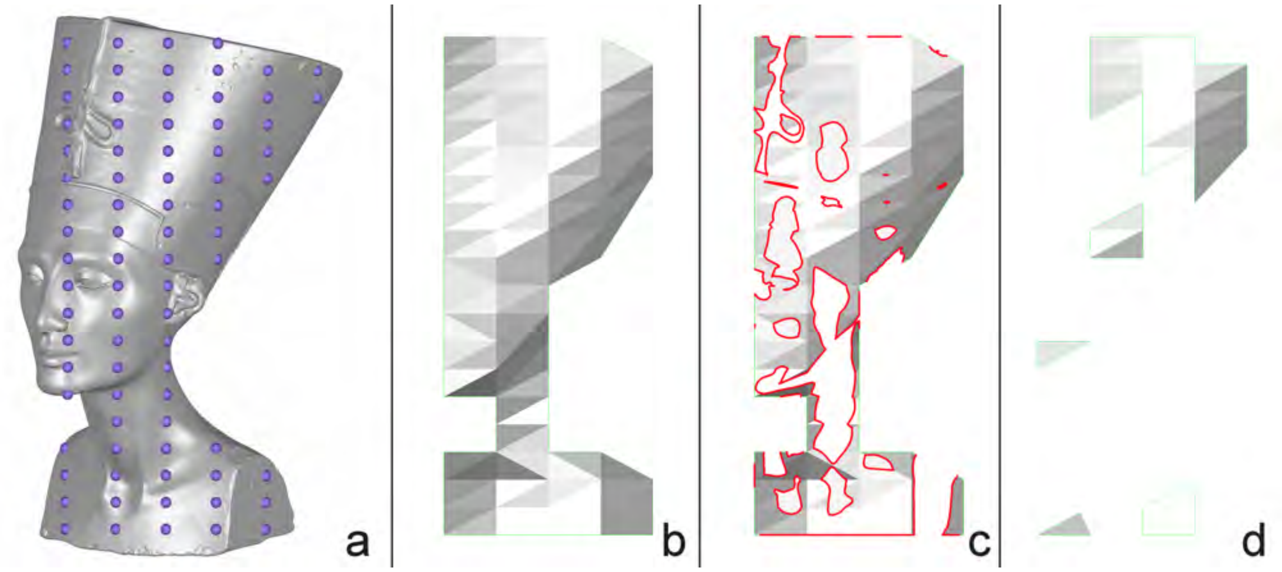

Figure 3.4: *Model with simulated TLS points (a), triangulated point cloud (b), outcome of Boolean operations (c) and valid surface without discretisation errors (d).*

For the second example the discretisation error de_{max} has been set to a stricter +/- 5 mm while now 4473 simulated points covered the surface of the statue from the exact same position as before. The resulting surface of the triangulated point cloud adds up to 12.41 m^2 as shown on the left of figure 3.5. After conducting the described Boolean operations areas arise where discretisation errors occur. The surface of this intermediate step measures 11.92 m^2. Again these regions are highlighted by red lines. It can be seen that the area is sufficient enough for steady areas such as helmet, neck or the forehead but not for more complex parts as nose, ears and eyes. In order to overcome this, an even higher sampling resolution would be required. After all undersampled regions have been removed a region of 9.55 m^2 results while the according *cov* value adds up to 31.9%.

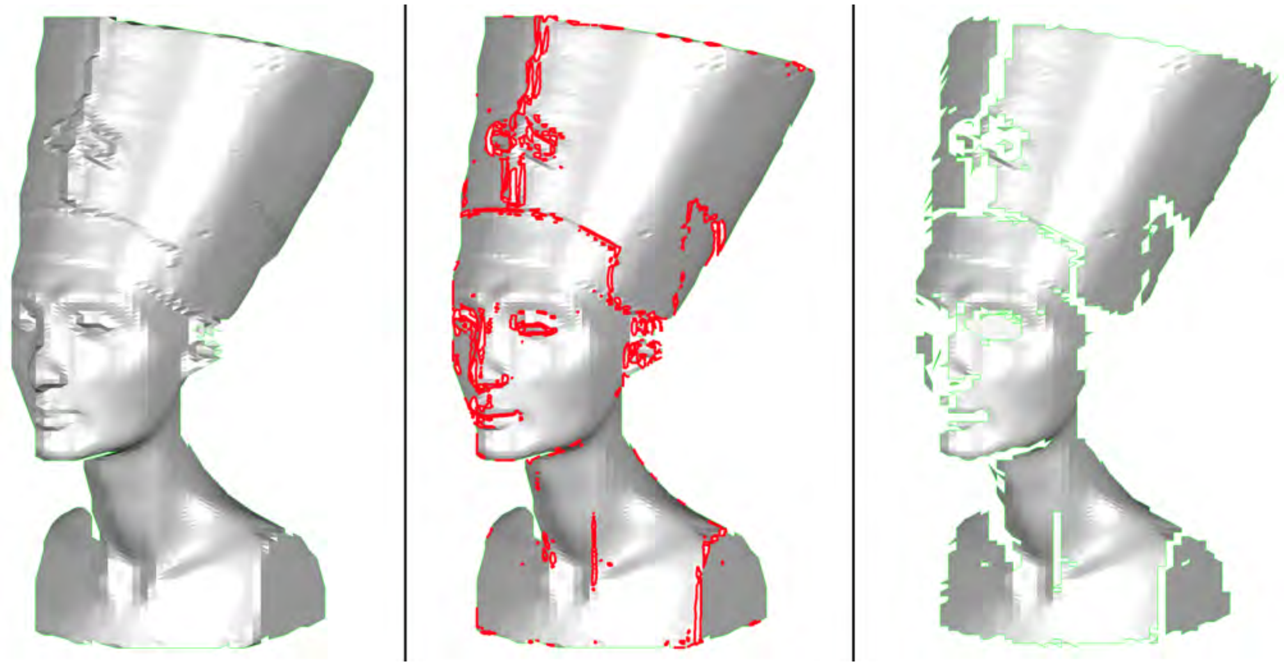

Figure 3.5: *Simulated and triangulated scan (left), identified areas with discretisation errors (centre) and cleaned dataset for evaluation of a viewpoint (right)*

A close look at the examples reveals the importance of considering the discretisation error. Assuming a naive perception onto the stated problem one could come to the conclusion that the first outcome is more economic as is covers 29.3% of the entire surface while requiring only scanning of 77 points. Hence this could be seen as an enormous gain of time in contrast to more than 4000 points scanned points that assembled the second dataset. However, this narrow perspective can easily been invalidated by comparing the triangulated simulated point cloud which adds up to 8.78 m^2 and the acceptable captured surface $surface_{acquired}$ that amounts to a slim 1.93 m^2. Thus only 22% of the acquired data are capable to sufficiently describe the given geometry. In summary it can be established that the chosen resolution of TLS is an underestimated source of falsification. Thorough planning and considerations prior to a survey are hence required even though it is mandatory to generate a detailed model for the sake of planning. While this step appears to be very tedious at first glance it should be pointed out that this information is capable to save time when carrying out frequent measurements, which is for instance the case for many tasks in engineering surveying, at a sufficient sampling rate. Even though the described procedure is used to evaluate single simulated viewpoints it should be carried out for all potential viewpoints in order to receive a telling measure for the achieved coverage.

3.2.2 An economic planning strategy

Depending on a stated task different strategies may be applied for viewpoint planning which hence requires different assessment procedures. This subsection will propose an economic strategy where the surface of a given object has to be captured to a certain degree. Therefore the variable completeness *comp* is introduced that serves as a quality measure respectively abort criterion of the planning algorithm. Hence *comp* can be interpreted as a threshold that specifies a required degree of completeness and is compared against a current set of *cov*. As it is usually impossible to capture an object of interest entirely *comp* is chosen smaller than the sum of all surfaces *cov* which have been captured from different viewpoints without the according overlapping regions.

Assuming that *comp* has been set as 0.9 the algorithm will try to find suitable viewpoints until the ratio between acquired and entire surface area lies above 90%. Furthermore the parameter *overlap-surface* [m^2] and *overlap* [%] are introduced that quantify the common area respectively the percentaged amount between two or more point clouds as already mentioned by Wujanz (2012). The last mentioned parameter is described by the quotient between the entire surface area *ESA* [m^2] that is covered by two scans and the overlapping surface area *overlap-surface* [m^2] of the two point clouds

$$overlap = \frac{overlap\text{-}surface}{ESA} \cdot 100 \tag{3.15}$$

Figure 3.6 illustrates the above mentioned parameters on a simple example. The outer grey shape depicts the area of interest *aoi*, the yellow area denotes the overlapping region *overlap-surface* between shape A and B while the orange form represents the overlap of contours B and C.

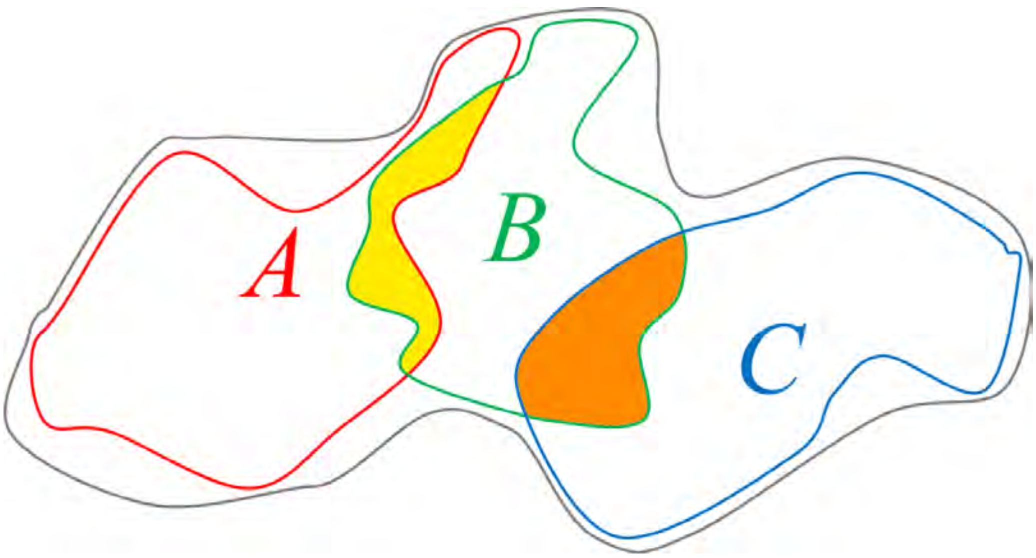

Figure 3.6: *Three datasets with two overlapping regions*

For the given example several measures were computed. The acquired surface $surface_{acquired}$ and the resulting coverage *cov* are gathered in table 3.5. It can be seen that shape C features the largest coverage with 32% of the total area in comparison to the area of interest *aoi*. Table 3.6 contains information about the acquired surface (lower green toned diagonal matrix) as well as the overlapping regions (upper blue coloured diagonal matrix) between shapes.

Table 3.5: *Surface and cov of the given example*

	surface **[m²]**	***cov*** **[%]**
aoi	235	100
A	70	30
B	59	25
C	74	32

Table 3.6: *Acquired surface and overlap*

Overlap	***A*** [m²|%]	***B*** [m²|%]	***C***[m²|%]
A		11 | 8	0 | 0
B	129 | 55		17 | 11
C	144 | 61	133 | 57	

Now that all required parameters are introduced several desired aims should be defined for this economic planning strategy:

1. The number of viewpoints should be minimal: $\sum \mathrm{VP} \rightarrow \min$.
2. Coverage *cov* should be at a maximum but at least larger than a preset boundary: $cov \rightarrow max$ with $cov \geq comp$.

In order to satisfy the above mentioned criteria usage of a greedy type of algorithm as introduced in subsection 3.2 appears to be a suitable solution to the problem of finding an optimal set of TLS viewpoints. A downside of greedy algorithms is that they determine the solution in a sequential fashion which may be efficient from a computational point of view but not optimal. An optimal result can only be determined by considering all potential solutions from the solution space, for which a combinatorial approach will be proposed in the following. Furthermore it has to be mentioned that the desired aim for the algorithm have to be converted into a target function. For an economic solution the following relations apply:

$$comp < cov \text{ with } cov = \frac{\sum(surface_{acquired} - overlap)}{surface_{total}} \cdot 100. \tag{3.16}$$

In the following a combinatorial approach for finding an economic set of suitable viewpoints is proposed for which pseudo code is used. The economic nature of the algorithm can be found in line 13 where the amount of potential viewpoints is only increased if the predefined completeness *comp* is not satisfied – as a consequence a solution with a minimum number of viewpoints results.

```
1  % An economic combinatorial algorithm for TLS viewpoint planning
2  % Input: Information on the surface of a given model as well as enclosed areas of
3  % simulated laser scans
4   Index int i=1;
5   if i = 1 then
6   loop 1
7   s = (surface acquired(i)/surface total)*100
8   if (comp < s) then return s
9   end loop 1
10  else
11
12  loop 2
13  i = i + 1
14  loop 3
15  compute all possible combinations c
16  of i TLS viewpoints
17  s = (surface acquired (c) - overlap(c))/surface total)*100
18  if (comp < s) then store s(i)
19  end loop 2
20  determine largest entry s(i) from line 13
21  end loop 3
```

In order to exemplify the algorithm it is assumed that *comp* has been set to 60%. A comparison with the outer column of table 3.5 shows that no viewpoint is solely larger than *comp*. Hence the algorithm proceeds with loop 2 and 3 and terminates for $i = 2$ which leads to the following results based on the output of line 17 of the pseudo code listed before:

1. Combination AB: 70 m^2 + 59 m^2 - 8 m^2 = 121 m^2 yields to 52%,
2. Combination AC: 70 m^2 + 74 m^2 - 0 m^2 = 144 m^2 yields to 61%,
3. Combination BC: 59 m^2 + 74 m^2 - 13 m^2 = 120 m^2 yields to 51%.

The colours of the list above denote whether false (red) or true (green) results have been computed. Hence combination AC consisting of the two viewpoints A and C yields to the only acceptable result which covers 61% in relation to the entire surface.

3.2.3 Data preparation

Before the algorithm can be applied to 3D-data some preparatory steps are required. As already mentioned under subsection 3.2 ray casting is conducted at first which will be described in detail in the following. Required information for the ray casting process are angular increments that consequently control the resulting resolution of the simulated laser scanner. Based on the set angular increments a set of spherical vectors is created around all defined potential viewpoints as already discussed under section 2.2.2. Subsequently intersection points between model and vectors are determined. The first intersection point between each vector and the model finally yields to simulated point clouds as depicted in figure 3.7 a. An additional scanner parameter that may be used for filtering is the maximum reach that removes points from the simulated point cloud if the distance between instrument and object point lies above the scanner's capability.

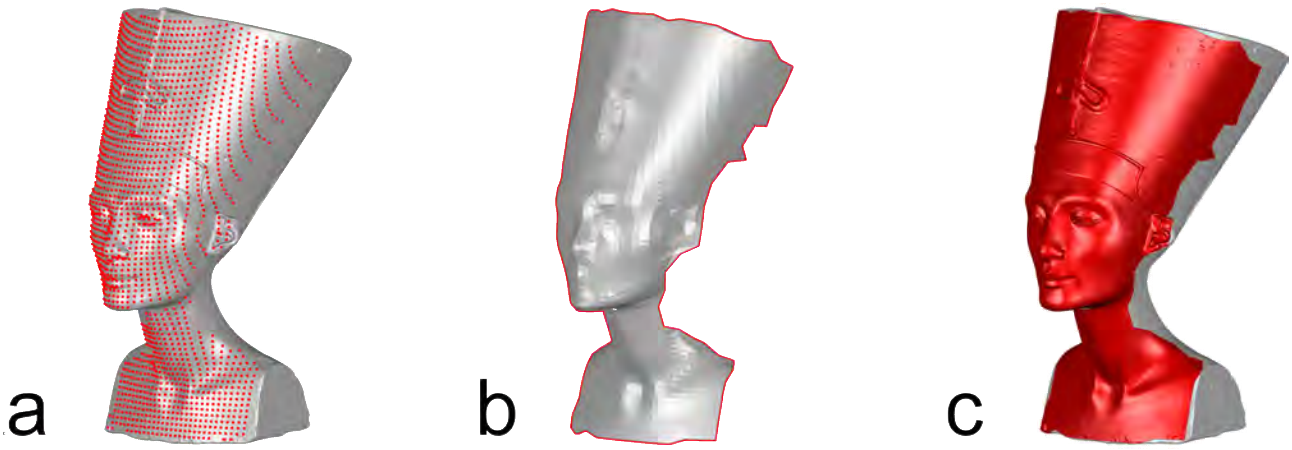

Figure 3.7: *Simulated point cloud (a), triangulated point cloud with outer boundary (b) and projection of the boundary onto the object of interest (c)*

As laser scanners capture information in a quasi-laminar fashion yet describe surfaces the simulated point clouds are converted into a surface representation by applying Delaunay-triangulation (Delaunay 1934) as illustrated in figure 3.7 b. These closed surface representations in form of meshes are then used to determine overlapping regions and the covered surface, as this process would be quite demanding in computational terms under usage of Boolean algebra an alternative approach is proposed in this contribution. Therefore the boundaries of all meshes, represented by the red line in figure 3.7 b, are projected onto copies of the model surface which is highlighted by the red coloured surface in figure 3.7 c. Subsequently areas outside of the projected boundaries are deleted so that only the captured area from the current viewpoint remains. As a consequence the acquired surfaces from all viewpoints are transferred onto the model surface. Hence overlapping regions can be determined quite easily as the geometric information is identical if overlap between two datasets exists.

In order to achieve this all datasets have to be transferred into a common numbering system as every file contains its own system for vertices and triangles. It is obvious that the projected boundaries of all simulated scans onto a common geometry are very helpful in this context. The chosen file format for this sake was the obj-format (Fileformat 2015) that is assembled by two basic lists. One that contains all vertices in the file and one that gathers all triangles. An individual identifier helps to distinguish all vertices. Note that every file features its own numbering system so that equal triangles may be described by varying identifiers. The list below shows an excerpt from an obj-file while the first part contains the vertex list. Each vertex receives an individual identifier based on its position in the list.

```
# Number of geometric vertices: 5165

v -1.17251563072 0.22867621481 2.76873922348
v -1.22034883499 0.06214559451 2.71739578247
v -1.20730364323 0.14652410150 2.75031471252
...
```

An extract of the second list, as depicted below, contains the topological relations of the triangulated point clouds. Each line contains a single triangle while the three featured numbers refer to the vertex identifiers from the first list.

```
# Number of triangles: 8862

f 790 3233 4167
f 3233 790 4351
f 3233 1150 4167
...
```

Hence a common numbering system has got to be created that allows to identify redundant information respectively overlap. For this purpose the vertices from all files are added to one list while redundant coordinate triples need to be removed so that only unique entries result. These revised entries then receive novel identifiers after which the numbering of all triangles is updated. The procedure is demonstrated in figure 3.8 on a simple example with two datasets. Figure 3.8 a and b show meshes that are both assembled of two triangles that feature four vertices. Triangle identifiers are highlighted by coloured numbers that are placed close to the centre of each triangle while vertex identifiers are located in proximity to their according vertex. It can easily be seen that the identifiers do not allow identifying common information namely the red triangle. After all datasets received superior identifiers for vertices and triangles the content of figure 3.8 c emerges. If one now updates the identifiers of the meshes in the figure below based on the superior numbering system the following outcome arises:

- Figure 3.8 a contains triangles 2 and 3.
- Figure 3.8 b contains triangles 1 and 2.

Subsequently all triangles are added to a list which leads to 1, 2, 2, 3. As triangle 2 was listed twice it is describing an overlap between the two meshes. For computation of the according surface the vertex identifiers for this triangle respectively their coordinates have to be retrieved.

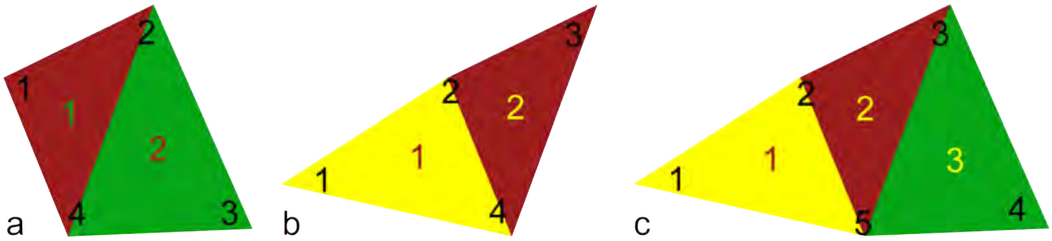

Figure 3.8: *Mesh 1 with according numbering (a), second mesh with own numbering of triangles and vertices (b) and combined datasets with superior numbering for determination of overlap and surface computation (c)*

Figure 3.9 illustrates a flow chart of the preparation that contains the two major phases simulation of observations and data preparation. Note that the optional filters highlighted by dashed lines in the data preparation stage require stochastic information which is not the case for the remaining options.

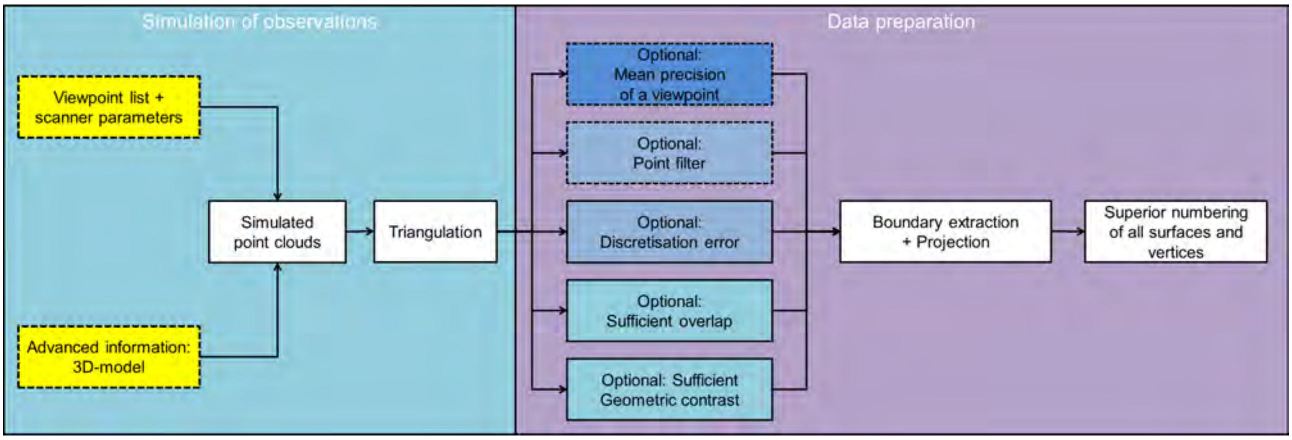

Figure 3.9: *Flow chart of the data preparation process*

3.2.4 Viewpoint planning by geometric means

In order to illustrate the capability of the proposed procedure the Nefertiti dataset has been processed. Therefore ten viewpoints have been circularly distributed around the dataset with a radius of 20 m. The angular resolution has been set to 0.18° so that four million vectors that simulated observations by a laser scanner from each viewpoint resulted. In terms of height all viewpoints were located about 1.6 m above the lowest point of the bust. The surface of interest measures 29.94 [m^2] and covers the bust without the top part of the helmet as this region is not visible from any viewpoint. A summary about the data acquired from all simulated viewpoints is given in table 3.7. Note that the colours mentioned in the first row are used for colour coding in the following illustrations. The first row denotes all viewpoints VP while the second row gathers the area A for all datasets without the consideration of discretisation errors. The third row accounts for the last mentioned discretisation error of 10 mm which yields to A' as discussed under section 3.2.1. The resulting decrease in captured surface can be found in the fourth row which have been converted into percentaged values ΔA. The horizontal field of view HFOV can be found in the last row and denotes the horizontal angle that encloses the object of interest from a certain viewpoint.

Table 3.7: *Overview about the simulated viewpoints*

VP	1 dark grey	2 red	3 orange	4 light green	5 cyan	6 pink	7 yellow	8 dark green	9 blue	10 lavender
A [m^2]	11.04	11.28	10.52	11.36	10.45	11.02	12.22	11.56	12.17	10.63
A' [m^2]	9.90	10.21	9.28	9.66	7.88	10.38	11.74	11.06	10.85	8.42
ΔA [%]	10.33	9.49	11.79	14.96	24.59	5.81	3.93	4.33	10.85	20.79
HFOV [°]	17.19	17.46	21.84	22.71	23.20	18.38	18.98	23.27	22.03	21.26

Figure 3.10 illustrates all possible viewpoints shaded according to the above mentioned colour code. In the following several results are presented that have been generated based on the basic algorithm. For the first

Figure 3.10: *All potential viewpoints (spheres), triangulated simulated point clouds (coloured mesh segments of the bust) and and input model (light grey bust in the centre of the scene)*

example a combination of viewpoints with an assumed coverage of at least 95% should be detected by the algorithm. The computation time for this problem took 404 s by using a 3.07 GHz quad core processor and 12 GB of RAM. In total 165 combinations and the ten viewpoints solely have been checked while a solution consisting of three viewpoints, namely 2 (red data), 5 (cyan datasets) and 9 (blue objects) as depicted in figure 3.11, was found covering 96.21% of the model's surface. The overlap between all viewpoints sums up to 29.54% of the entire surface.

In order to demonstrate the increasing computational demand for a growing number of combinations the desired ratio of coverage has been set to 99%. The computation time slowed down enormously to 5509 s while 837 combinations of different viewpoints have been tested. A coverage of 99.12% was found for viewpoints 2, 3, 5, 7, 8 and 9 as depicted in figure 3.12. The overlap between the meshes sums up to 92.92%.

Figure 3.11: *Outcome of the algorithm for a level of completeness of at least 95% without consideration of the discretisation error*

Figure 3.12: *Outcome of the algorithm for a level of completeness of at least 99% without consideration of the discretisation error*

While the previous scenarios didn't take the existence of discretisation errors into consideration this will be done in the following. The proposed algorithm for determination of optimal viewpoints remains unmodified yet the input data is subject of modification. As a consequence areas that are subject of insufficient spatial resolution will be removed. Hence the coverage of each simulated scan will decrease in comparison to its original version. For this example a maximum discretisation error of 10 mm has been assumed with a minimum coverage of 95%. As an outcome of the algorithms viewpoints 2, 3, 4, 7, 9 and 10 have been chosen leading to a coverage of 96.85% with an overlap of 80.89%.

3.2.4.1 Consideration of sufficient overlap between viewpoints

The previously processed scenarios revealed a significant computational increase due to the chosen combinatorial strategy – an increase of the minimum coverage setting from 95% to 99% multiplied the computational effort by a factor of more than 13. Hence it is obvious that additional criteria have to be introduced that reduce the amount of possible combinations. The previous implementation was designed to find a combination where the number of viewpoints was at a minimum while the coverage should be possibly large. As a consequence the overlap between adjacent point clouds was fairly small which eventually does not allow to carry out surface based registration which eventually makes it impossible to create a continuous complete 3D-model of the object of interest.

Figure 3.13: *Outcome of the algorithm for a level of completeness of at least 95% with consideration of a discretisation error of at maximum 10 mm*

Thus the criteria of the basic algorithm are extended in a way that ensures a sufficient overlap of point clouds, as introduced in section 3.2.3, for the sake of registration:

1. The number of viewpoints should be minimal: $\sum \mathrm{VP} \rightarrow \min$.
2. Coverage *comp* should be at a maximum but at least larger than a preset boundary: $comp \rightarrow max$ with $cov \geq comp$.
3. A minimum overlap *overlap* [%] between point clouds has to be given.

The pseudo code below contains a simplified version of the modified algorithm. A detailed look at how the algorithm identifies sufficient overlap will be given in the following.

```
% A combinatorial algorithm for viewpoint planning:
% Consideration of overlap
% Input: Information on the surface of a given model as well as enclosed areas of
% simulated laser scans
  Index int i=1;
  if i = 1 then
  loop 1
  s = (surface acquired(i)/surface total)*100
  if (comp < s) then return s
  end loop 1
  else

  loop 2
  i = i + 1
  if (i == 2)
  Compute and store overlap between point clouds
  loop 3
  compute all possible combinations c
  i TLS viewpoints
  if (overlap > threshold)
  s = (surface acquired (c) - overlap(c))/surface total)*100
  if (comp < s) then store s(i)
  end loop 2
  determine largest entry s(i) from line 16
  end loop 3
```

The motivation for this extension was to ensure that combinations of point clouds can always be registered based solely on their overlap. In addition this aspect allows cutting down the computational cost as now the algorithm only calculates surface and overlap among point clouds, as shown in line 20 and 21 of the according pseudo code, if sufficient overlap is present. Thus, the according query is described in detail in the following. At first all combinations that feature two point clouds are stored as shown in line 16. Combinations that feature more overlap than a predefined threshold are marked by a tag. As soon as i >= 3 combinations of two point clouds are established based on the current combination. For e.g. A-B-C the combinations A-B, A-C and B-C have to be established. Afterwards all combinations are tested for sufficient overlap. As a consequence the question arises how this circumstance can be tested.

A versatile tool for this purpose are so called incidence matrices that are widely used in geodesy to express topological relations e.g. within a geodetic network. The use of these matrices that have their roots in graph theory will be extensively discussed in subsection 4.5.1.5 within the context of deformation monitoring respectively identification of congruent regions. An introduction on the subject can be found in Gründig (1988) and Linkwitz (1999) exemplified on geodetic problems. Figure 3.14 illustrates two scenarios on which this method is demonstrated. The one on the top features five datasets that are arranged continuously where every point cloud is connected to its adjacent one. This case will be referred to as scenario A in the following. The lower part of the figure, referred to as scenario B, depicts datasets that are divided into two clusters yet they are connected amongst each other as highlighted by red dotted lines. The incidence matrix **C** depicted in table

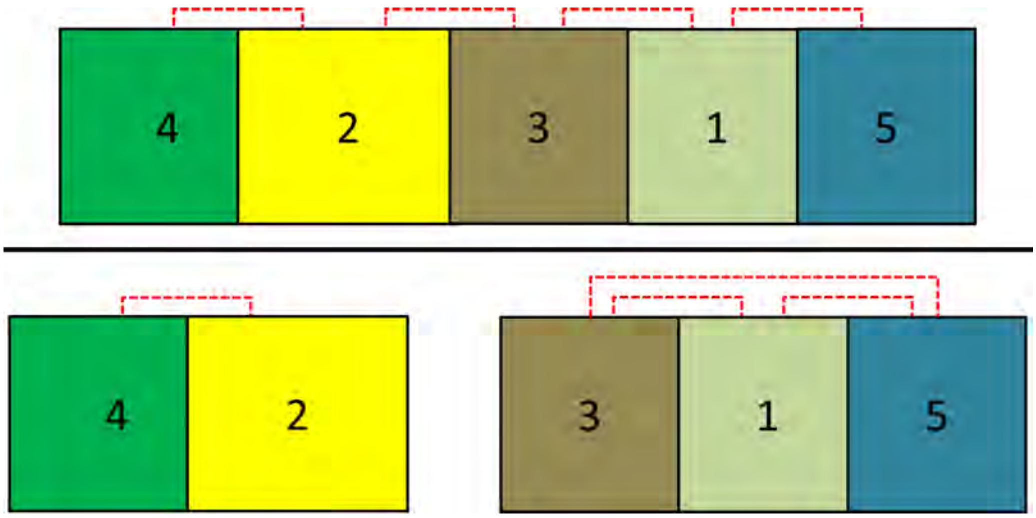

Figure 3.14: *Cluster with continuous arrangement (top) and one of disconnected datasets (bottom)*

3.8 is based on scenario A. The number of rows is equal to the amount of possible combinations of two while the number of columns is defined by the current amount of viewpoints i. It can be seen that valid connections are highlighted by 1 and -1. A positive sign denotes the starting point of a connection while a negative sign describes its end. In this example any given overlap is interpreted as sufficient. If there is no sufficient overlap between two point clouds the entire row is filled with zeros.

Subsequently the adjacency matrix $\bar{\mathbf{C}} = \mathbf{C}^T\mathbf{C}$ can be computed as illustrated in table 3.9. The upper green tinted part is associated to the upper half of figure 3.14 while the blue coloured one represent the adjacency matrix of the lower half. An interesting piece of information is located on the diagonal of the matrix, which is highlighted in grey, where the according number represents the amount of overlapping datasets. It can immediately be seen that the values on the diagonal are equal even though the arrangement varies. The distribution of values is dependent to the topology as well as the definition of identifiers for individual files hence the sole consideration of the diagonal is not a suitable measure for the identification of continuous point clouds.

Table 3.8: *Incidence matrix for scenario A depicted in figure 3.14*

Dataset / Combination	**1**	**2**	**3**	**4**	**5**
1-2	0	0	0	0	0
1-3	1	0	-1	0	0
1-4	0	0	0	0	0
1-5	1	0	0	0	-1
2-3	0	1	-1	0	0
2-4	0	1	0	-1	0
2-5	0	0	0	0	0
3-4	0	0	0	0	0
3-5	0	0	0	0	0
4-5	0	0	0	0	0

Table 3.9: *Adjacency matrices for scenario A (green) and B (blue)*

	1	**2**	**3**	**4**	**5**
1	2	0	-1	0	-1
2	0	2	-1	-1	0
3	-1	-1	2	0	0
4	0	-1	0	1	0
5	-1	0	0	0	1

1	2	0	-1	0	-1
2	0	1	0	-1	0
3	-1	0	2	0	-1
4	0	-1	0	1	0
5	-1	0	-1	0	2

As a consequence other information from the adjacency matrix is used namely the secondary diagonal. The minimum requirement for the stated problem is that all point clouds are connected among each other at least once. Thus, this formulation accepts combinations that describe an open traverse. For the identification process, which will be exemplified on the two scenarios depicted in figure 3.14, all values that contain a valid connection are extracted. For scenario A the following connections are highlighted by -1 in the secondary diagonal which is referred to connection list in the following:

- viewpoints 1-3,
- viewpoints 1-5,
- viewpoints 2-3,
- viewpoints 2-4.

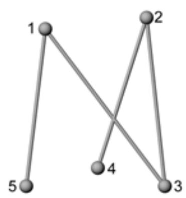

In the previously depicted network graph potential viewpoints are represented by spheres. Edges between these vertices signify sufficient overlap among the point clouds captured from the according viewpoints. Since all viewpoints have to be connected among each other a concatenation has to be found that has the same length as the amount of potential candidates. The following procedure applies three lists that contain the following information:

- Candidate list: Contains candidates to which associable viewpoints are added.
  → At the start of the procedure this list contains one arbitrary combination of two viewpoints. It is replaced by the concatenation list if other viewpoints can be connected to one of the entries.
- Connection list: All valid connections between two viewpoints.
  → This list decreases in length during the procedure.
- Concatenation list: All viewpoints that describe a continuous arrangement.
  → This list increases in size if other viewpoints can be associated to it.

For the given problem this length has to be five. In order to check if this prerequisite is given the first double of viewpoints is added to the candidate list that hence contains viewpoint 1 and 3. Subsequently the remaining viewpoints from the connection list are analysed if they contain at least one member from the candidate list. For the given case viewpoints 1-5 are connected to viewpoint 1 while viewpoints 2-3 are connected to viewpoint 3. As a consequence the concatenation among viewpoints looks as follows where the current candidates are highlighted in green: 5-1-1-3-3-2. Note that the order of viewpoints has been arranged so that direct connections become immediately visible. Subsequently this concatenation list is ordered leading to 1-1-2-3-3-5, while redundant entries are deleted. This list is now interpreted as the current candidate list that contains 1-2-3-5. Again the remainder of the connection list, that now only contains viewpoints 2-4 is analysed whether valid connections are given to one of the entries from the candidate list. As this is the case for viewpoint 2 the concatenation list follows 5-1-1-3-3-2-2-4 where the current members of the candidate list are again tinted in green. If one now reverses the order of the sequence and removes redundant entries the following list emerges: 4-2-3-1-5 – which is exactly the order in which the viewpoints are arranged in scenario A. After sorting the concatenation list and removal of repetitive entries the final candidate list appears that contains the following viewpoints 1-2-3-4-5. As the list contains five entries which is equal to the amount of viewpoints that have to be connected among each other the outcome has to be rated as valid.

Now the procedure is applied to scenario B. The resulting network graph is depicted in the following while the connection list contains:

- viewpoints 1-3,
- viewpoints 1-5,
- viewpoints 2-4,
- viewpoints 3-5.

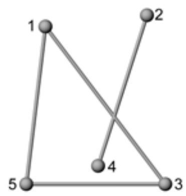

The first entry of the connection list is interpreted as the first pair of candidates containing viewpoints 1 and 3. Subsequently the connection list is queried for valid links which are viewpoints 1-5 and viewpoints 3-5. Hence the concatenation list contains 5-1-1-3-3-5. It has to be pointed out that all viewpoints can be found twice in the list which means that all of them are connected to each other. After ordering and removing redundant entries the candidate list contains three entries namely 1-3-5. The only remaining entry in the connection list features viewpoints 2 and 4 which are not part of the candidate list. Hence there is no valid connection to the previously assembled cluster of three viewpoints. As the size of the candidate list is three and hence smaller than 5 this combination has to be rated as invalid so that no further calculations are conducted.

Now that the extended algorithm has been introduced the given test case is now processed with the following settings:

- Completeness *comp* of at least 90%.
- Overlap *overlap* of at least 10% between point clouds.

From 45 combinations that were assembled of two point clouds 29 (64%) satisfied the stated criterion for sufficient overlap. After 287 seconds a valid solution, namely 2-3-6-9, has been found assembled by viewpoints that feature a level of completeness of 93.06%. The adjacency matrix is assembled as follows:

$$\begin{matrix} 2 & -1 & 0 & -1 \\ -1 & 2 & -1 & 0 \\ 0 & -1 & 2 & -1 \\ -1 & 0 & -1 & 2. \end{matrix}$$

Hence each viewpoint has got two connections which means that a combination has been found that describes a closed traverse. Figure 3.15 illustrates the result generated by the extended algorithm.

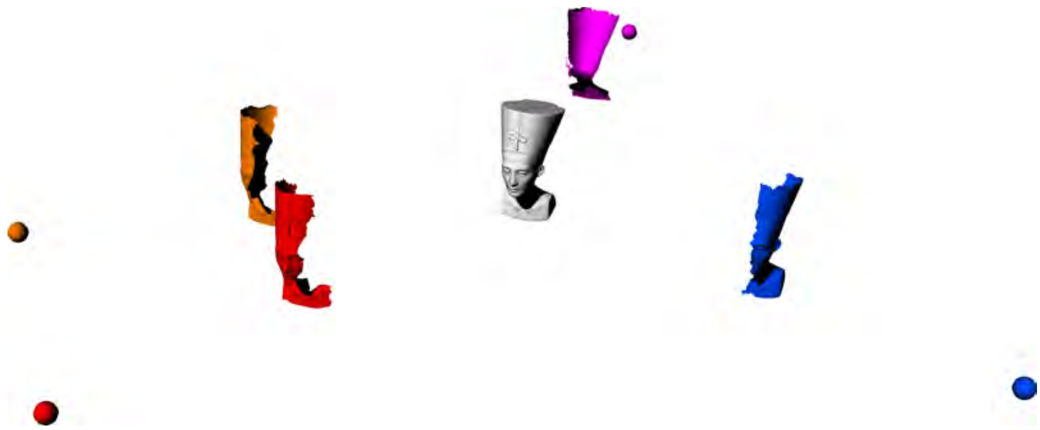

Figure 3.15: *Outcome of the algorithm for a level of completeness of at least 90% with consideration of sufficient overlap*

In order to demonstrate the increased performance of the algorithm the required level of completeness was set to 95% with a minimum overlap of 30%. The result has been computed in 321 seconds, is assembled by six viewpoints (3-4-5-8-9-10) and describes an open traverse. The computation of a solution with the mentioned settings containing all viewpoints took 392.26 seconds for which 127 combinations were analysed. The naive computation required to analyse 1013 combinations in total of which four combinations fulfilled the level of completeness criterion of 95%. On average the analysis of one combination took about 6.57 seconds so that 6658 seconds of computation were required. Another option to decrease the computational cost is to define an upper margin respectively a range of overlap. Again the completeness criterion has been set to 95% while now the overlap between two point clouds has to be beyond 10% and not larger than 30%. The outcome consisted of six viewpoints and has been computed in 95.77 seconds.

3.2.4.2 Consideration of sufficient overlap and geometric contrast between viewpoints

Even though the previously proposed extension of the original algorithm considers if sufficient overlap between point clouds is given it does not analyse the geometric contrast in this region. The term geometric contrast denotes a sufficient distribution of spatial information within the overlapping area of two or more point clouds in all cardinal directions, that is required to carry out surface based registration. For clarification this circumstance should be exemplified in the following. It is assumed that two point clouds overlap by 90% yet the common region contains a planar surface. As a consequence the geometric information within the overlapping region is not sufficient to solve all degrees of freedom in 3D space within the context of a surface based registration. Hence an additional extension is proposed that computes numeric values which describe and characterise the geometric properties of the overlapping region among point clouds. Analogous to the extension proposed in subsection 3.2.4.1 the crucial line of code in the algorithm can be found in line 20. A detailed description of how the according values for the evaluation process are computed will be given in the following. This evaluation procedure has to satisfy the requirement of being independent to the chosen coordinate system so that its numerical outcome solely expresses the characteristics of the local geometry. In summary the algorithm has to fulfil the following requirements:

1. The number of viewpoints should be minimal: $\sum \mathrm{VP} \rightarrow min$.
2. Coverage *comp* should be at a maximum but at least larger than a preset boundary: $comp \rightarrow max$ with $cov \geq comp$.
3. A minimum overlap *overlap* [%] between point clouds has to be given.
4. A sufficient geometric contrast [%] within the overlapping region has to be given. Note that a detailed description of this parameter will be given throughout this section.

```
% A combinatorial algorithm for TLS viewpoint planning:
% Consideration of overlap and sufficient geometric contrast
% Input: Information on the surface of a given model as well as enclosed areas of
% simulated laser scans
 Index int i=1;
 if i = 1 then
 loop 1
 s = (surface acquired(i)/surface total)*100
 if (comp < s) then return s
 end loop 1
 else

 loop 2
 i = i + 1
 if (i == 2)
 Compute and store overlap between point clouds
 loop 3
 compute all possible combinations c
 of i TLS viewpoints
 if (overlap > threshold AND geometric contrast > threshold)
 s = (surface acquired (c) - overlap(c))/surface total)*100
 if (comp < s) then store s(i)
 end loop 2
 determine largest entry s(i) from line 16
 end loop 3
```

A prerequisite for computation of transformation parameters is of course that point to point correspondences are known or more general that parts within the region of interest have been acquired redundantly. In addition the overlapping region has to contain enough geometric information to solve all transformation parameters. This aspect should be demonstrated on some examples. If one assumes that the parameterisation of a spatial transformation in $\mathbb{R}^3$ is described by three translations t_x, t_y, t_z as well as three Euler rotations r_x, r_y, r_z and that the face normals of the known correspondences are aligned parallel to the z-axis of the coordinate system then it can be established that only three degrees of freedom can be determined. As a consequence the normal equation matrix during the least squares adjustment for determination of transformation parameters has a rank deficiency. Even if the face normals are located on two perpendicular aligned planes one degree of freedom cannot be determined namely the translation along the intersection line of the planes. Hence the desirable distribution of correspondences within the overlapping region that allows determining all six degrees of freedom would be established if the triple product of face normals equals to one. Based on this thought a procedure is proposed in the following that evaluates the overlapping region based on the distribution of face normals.

As a first step face normals of all triangles within the overlapping region need to be computed. As an outcome Cartesian coordinates arise that are converted into polar elements while only the directional components α and β are used. In order to assess the distribution of face normals a spherical grid is defined within a unit sphere that is bounded by equally sampled vectors that are all d degrees apart from each other. Then all polar components are sorted into the spherical grid while the according mean of all polar elements within a cell is computed. Furthermore the amount of containing entries within a cell is used as a measure for characterisation. This is achieved by interpreting the amount of entries within a cell as the length of a vector while the directional components are defined by the mean polar elements of the according grid element. Subsequently the cell with the most entries is determined which is referred to as the most dominant direction (MDD). In other words the MDD expresses in which direction most of the face normals within the region of overlap are oriented. In addition this strategy achieves the desired independence against the choice of coordinate system. After the MDD has been computed all entries within the spherical grid are normalised by it. The left part of figure 3.16 shows the spherical grid with the normal vectors of the overlapping region. The largest entry, the MDD is highlighted in green.

Based on the desired distribution of face normals that was subject of the previous subsection all remaining normal vectors are set into relation to the MDD. Therefore a plane is computed whose normal vector is described by the MDD and starts in the origin of the coordinate system. Subsequently all normal vectors are projected onto this plane while the largest entry is determined which will be referred to as second dominant direction (SDD). As MDD and SDD are perpendicular to each other and because all normal vectors have been normalised this procedure assesses the relation between the two vectors. A view that is aligned parallel to the MDD is depicted in the centre of figure 3.16 while the resulting SDD is coloured in red. At last a vector is computed by the cross product of the MDD and SDD, as depicted in the right part of figure 3.16, to which all normal vectors are projected. Note that the resulting vector highlighted in yellow has been increased in length for demonstrative purposes only. Analogous to the other dominant directions the largest projected vector is determined which is referred to as the third dominant direction (TDD) and is coloured in pink. The desired relation among all dominant directions should be MDD = 1, SDD = 1 and TDD = 1 which would mean that they are all perpendicular to each other. Hence the proposed procedure allows to numerically assess the geometrical characteristics of an overlapping region. The previously mentioned scenario consisting solely of two perpendicular planes would quality measures of MDD = 1, SDD = 1 and TDD = 0. As a consequence the geometrical content of the overlapping region has to be rated as insufficient for surface based registration.

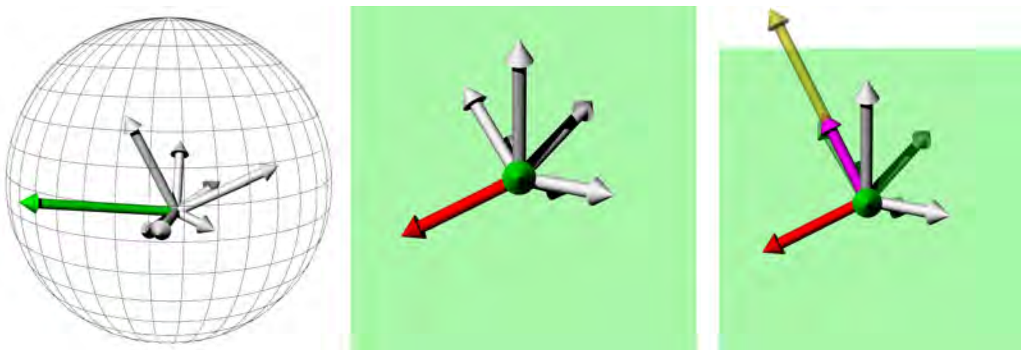

Figure 3.16: *Spherical grid with normal vectors of an overlapping region (left). The vector colourised in green depicts the most dominant direction. A view parallel to the MDD is depicted in the centre of the figure. The red vector denotes the SDD. The pink vector highlights the TDD as illustrated on the right.*

In the following the procedure is demonstrated on the overlapping region between viewpoint 1 and 2 as illustrated in figure 3.17. The red dataset has been acquired from viewpoint two while the dark grey mesh was observed from viewpoint 1. After computing the overlap, which spans over 6.19 m^2, between these two triangular meshes the light grey bust emerges. It can be seen that the boundaries of the overlapping region can be found in this resulting dataset e.g. the characteristic shape of the right boundary from viewpoint 2. In addition the resulting maximum geometric contrast is illustrated by three colour coded vectors. The MDD amounts per definition to 100% while the SDD represents 54.4% and the TDD to a slim 2.51%.

It has to be mentioned that the bandwidth of normal directions for each simulated viewpoint of this dataset never exceeds 180° as a closed object with a convex characteristic is acquired. If for instance the interior of a

Figure 3.17: *Datasets acquired from viewpoint 2 (red) and viewpoint 1 (dark grey). The overlapping region of these two scans, as depicted in the centre, is coloured in light grey.*

Table 3.10: *Overview about adjacent viewpoints in terms of overlap and geometric contrast*

Combination / Parameter	1-2	2-3	3-4	4-5	5-6	6-7	7-8	8-9	9-10	1-10
MDD [%]	100	100	100	100	100	100	100	100	100	100
SDD [%]	65.22	54.62	43.15	43.42	53.17	71.91	42.27	40.58	79.09	51.55
TDD [%]	2.51	1.65	0.01	0.05	15.23	13.32	13.38	0.03	0.01	0.13
Overlap [%]	42.89	53.01	53.16	63.92	58.62	55.67	65.51	56.03	66.73	7.09
Covered surface [m^2]	14.43	14.05	14.44	14.19	13.82	13.57	13.61	14.50	13.31	13.80

building has been captured the potential bandwidth of normals increases to 360°. Hence the ratio of MDD, SDD and TDD may be more favourable than in this example. Table 3.10 gathers an excerpt from all combinations that are assembled of two viewpoints. In this case only adjacent viewpoints are exemplarily listed where the first row depicts the current combination. Rows two to four contain MDD, SDD and TDD in percent. It can be seen that the geometric contrast appears to be weak in most cases apart from the overlapping region between viewpoint 6 and 7. The last two rows contain information about the extent of the overlapping region in percent as well as the entire covered surface in m^2.

Another test has been conducted based on the final extended algorithm where the following settings were defined:

- Completeness *comp* of at least 95%.
- Overlap *overlap* of at least 10% between point clouds.
- The geometric contrast has to satisfy at least the following requirements: MDD = 100%, SDD, = 10% and TDD = 1%.
- Division of a normal sphere into 24 horizontal and vertical sectors.

A solution with the above mentioned settings has been found after 169.16 seconds which is depicted in figure 3.18. In total a coverage of 95.13% has been achieved for which six viewpoints, namely 2-3-6-7-8-10, would have to be observed.

2	-1	0	0	0	-1
1	2	-1	0	0	0
0	-1	3	-1	-1	0
0	0	-1	2	-1	0
0	0	-1	-1	2	0
-1	0	0	0	0	1.

Figure 3.18: *Outcome of the algorithm that considers sufficient overlap and geometric contrast*

3.2.4.3 Reduction of computational costs: Estimating the minimum amount of viewpoints

A drawback of the chosen combinatorial approach for viewpoint planning is that search space enormously grows with an increasing amount of viewpoints. Hence a good estimate of how many viewpoints are required to fulfil certain criteria have to derived and / or the amount of viewpoints should be restricted if possible, which will be done in the following.

While various criteria for an optimal solution based on a selection of several viewpoints have been presented in subsection 3.2.4 novel aspects should be proposed in the following that assess single viewpoints. Therefore the term efficiency is suggested in the following while two different interpretations are discussed. The basic idea behind this measure is to evaluate the amount of data from one viewpoint that fulfils certain criteria. A measure that can be computed based on table 3.7 is $\mathit{Eff}\cdot_{disc.}$ that sets the acquired surface without discretisation errors in relation to the entire captured surface

$$\mathit{Eff}\cdot_{disc.} = \frac{A'}{A} \cdot 100. \tag{3.17}$$

This circumstance is illustrated in figure 3.5 a) and c). According to table 3.7 area A captured by viewpoint 1 spans over 11.04 m^2 and decreases to 9.90 m^2 after rejection of undersampled areas that yield to discretisation errors. Hence $\mathit{Eff}\cdot_{disc.}$ for viewpoint 1 can be computed by ${}^{9.9\,\mathrm{m}^2}/_{11.04\,\mathrm{m}^2} \cdot 100$ which leads to the conclusion that 89.7% of the acquired data can be used for post processing. This measure can be used to reject viewpoints from the entirety of potential viewpoints which will be exemplified on table 3.7. Therefore a threshold is defined according to which $\mathit{Eff}\cdot_{disc.}$ has to be smaller than for instance 88%. As a consequence the entirety of potential viewpoints is reduced from ten to six. Another interpretation of the efficiency measure will be proposed in subsection 3.2.5.

The problem of estimating a good entry point to the combinatorial viewpoint planning algorithm is crucial to avoid unacceptable computations. This aspect is necessary of being considered in the future as the proposed algorithm sequentially increases the number of viewpoints starting from a minimum of two viewpoints. If we assume that for instance a certain coverage can only be reached based on five viewpoints onwards out of ten then the required computational cost for sets of 2, 3 or 4 viewpoints is obsolete.

3.2.4.4 Comparison of the expenditure of work

After several variants of the original algorithm have been proposed the expenditure of work is computed for all presented results. For this purpose it is assumed that one operator is capable to carry a tripod as well as a stand-alone scanner at 1.5 m/s respectively 5.4 km/h. The distance that the operator has to carry the scanner and other required equipment is defined by the direct connection between chosen viewpoints as long as they don't intersect the object. It is assumed that it takes 120 seconds per viewpoint to set up the sensor and another 60 seconds that the scanner requires for initialisation and acquisition of a pre-scan. The setting for data acquisition has been defined as "middle", as listed in table 3.4, while a panorama-scan takes 101 seconds. In order to determine the time that is required for scanning the last column of table 3.7 is used in which the horizontal field of view for every viewpoint is listed. For every found solution the sum of all according HFOV's is computed that is then set into relation with the time that is needed to capture a panorama scan. For explanatory reasons a simple example will be given in the following where data from viewpoints 1, 2 and 3 are captured. Figure 3.19 illustrates the scenario where all related elements are coloured in accordance to the viewpoint's tones: viewpoint 1 (dark grey), viewpoint 2 (red) and viewpoint 3 (orange). The circular segments originating from the according viewpoints (spheres) depict the horizontal field of view that sum up to 17.19° for viewpoint 1, 17.46° for viewpoint 2 and 21.84° for viewpoint 3. The cylindrical connections among viewpoints denote the path that an operator has to travel in order to capture the scenario.

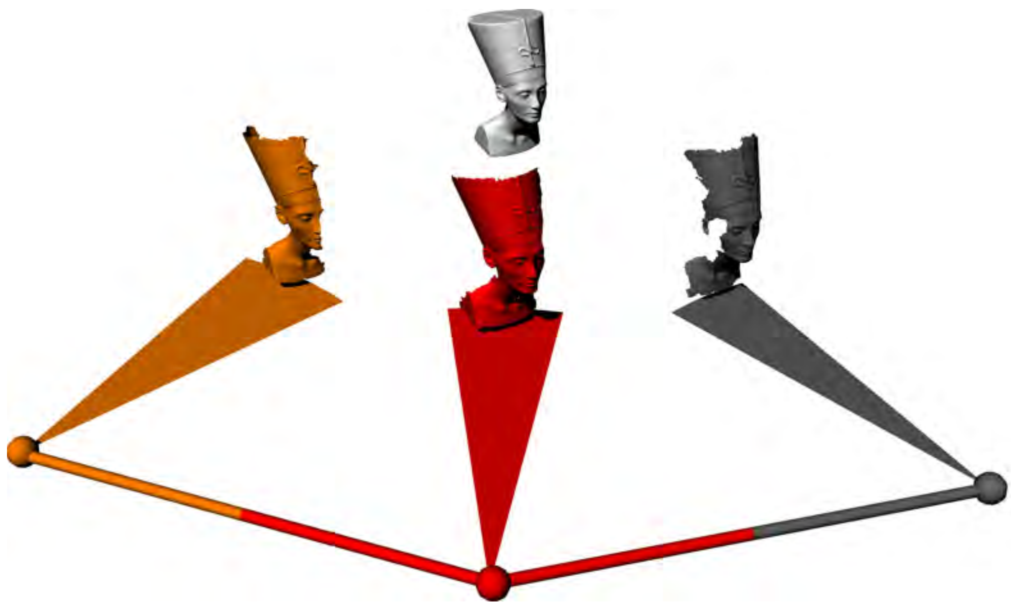

Figure 3.19: *Acquired data from viewpoint 1 (grey), viewpoint 2 (red) and viewpoints 3 (orange) with object of interest in the background*

In total 56.49° have to be scanned in horizontal direction so that the time of scanning will take $({}^{56.49°}/_{180°}) \cdot 101\,\mathrm{s} = 31.70\,\mathrm{s}$. As data will be captured from three viewpoints preparation of the scanner will take $3 \cdot 120$ s $= 360$ s while the initialisation phase of the scanner adds up to $3 \cdot 60$ s $= 180$ s. Finally, the time of transportation has to be taken into consideration. For this the direct distance between viewpoints of 27.72 m is considered.

Table 3.11: *Comparison of the expenditure of work for all computed results*

Min. coverage [%] |overlap [%]	$\sum$ HFOV [°]	Computed coverage [%]	View-points	Distance [m]	Combi-nations	EOW [s]
95 | 0	62.69	96.21	3	70.40	165	622.11
99 | 0	126.78	99.12	6	84.11	837	1207.21
95 | 10	134.31	96.84	6	81.80	127	1209.90
max | min	206.32	98.52	10	111.25	1013	818.25

As mentioned earlier a speed of 1.5 m/s is assumed so that this task will take $(27.72\,\mathrm{m}/1.5\,\frac{\mathrm{m}}{\mathrm{s}}) = 18.48\,\mathrm{s}$. In total the expenditure of work adds up to 31.70 s + 360 s + 180 s + 18.48 s = 590.18 s for this example. A comparison of the expenditure of work and required information for several scenarios is given in table 3.11. It can be seen that the expenditure of work is mainly influenced by the amount of viewpoints. The proposed restriction of sufficient overlap among simulated point clouds shows a significant decrease of required computations in order to determine an optimal set of viewpoints.

3.2.5 Viewpoint planning considering stochastic information

The previous subsection presented a planning algorithm that exclusively used geometric information without considering stochastic information. By doing this an optimal solution can only be found in economic terms but not from an engineering surveying point of view as the user does not receive any numerical information concerning the estimated theoretical precision that can be expected from a viewpoint. Thus this subsection makes use of the proposed stochastic model for TLS as described under subsection 3.1. The theoretical precision of a reflectorless distance measurement is dependent to the signal strength respectively the intensity which is influenced by three factors:

- Physical properties of the object's local surface.
- Signal loss by increasing object distance.
- Signal loss caused by decreasing incidence angle.

While the first factor is bound to the local characteristic of an object, the remaining two are dependent to the acquisition configuration. The aim of the planning strategy proposed in this section is to find a single viewpoint with optimal properties for the use in engineering surveying.

3.2.5.1 Exemplification of the procedure on a simple example

Hence a simple example is presented in the following to demonstrate the stochastic behaviour of the investigated scanner. The object of interest consists of a 5 m by 5 m large plane with an assumed degree of reflection of 25% for the wavelength of the applied scanner. The assigned radiometric properties correspond to a dark grey appearance if observed in the visible spectrum. Subsequently 35 potential viewpoints have been defined which have been arranged parallel to the face normal of the plane and approximately 8 m to 24 m located from the horizontal centre of the plane. From each viewpoint a scan has been simulated via ray casting which lead to roughly 10000 points per scan. Subsequently the distance between scanner to each object point as well as its according incidence angle has been computed to determine the intensity loss caused by the geometric configuration. Based on the resulting intensity the theoretical precision of each distance measurement σ_s is computed by applying equation (3.1). Subsequently stochastic measures are calculated for all simulated TLS points by conducting variance-covariance propagation as described in subsection 3.1.2.

Figure 3.20 illustrates the outcome of the above mentioned example. The spheres on the bottom of the figure depict all 35 simulated viewpoints where the colour coding depicts the mean spatial precision. Note that the colour bar on the right is given in millimetres. The colour coded surface on the left represents the spatial precision of approximately 10000 simulated points. These points have been virtually captured from the viewpoint with the highest precision on average – in this case the closest one to the plane - which hence describes the best solution. Based on the colour coding of the viewpoints it can be seen that the mean precision increases with decreasing distance to the object. The reason for this is caused by the fact that the distance has got a larger impact onto the signal loss than the incidence angle. However it should be mentioned that this may not be case for unsteady and rather complex geometries. The according histogram that displays the distribution of theoretical precision for the best viewpoint is displayed right next to the colour bar. Concerning the stochastic characteristics of the simulated point cloud it can be seen that the precision drops in a circular fashion to the outer boundaries of the object due to a decrease of the incidence angle which results in an intensity loss. The results generated in this subsection allow to numerically analyse and assess varying acquisition configuration. Through this, requirements and perceptions from the field of engineering surveying can be satisfied for the first time.

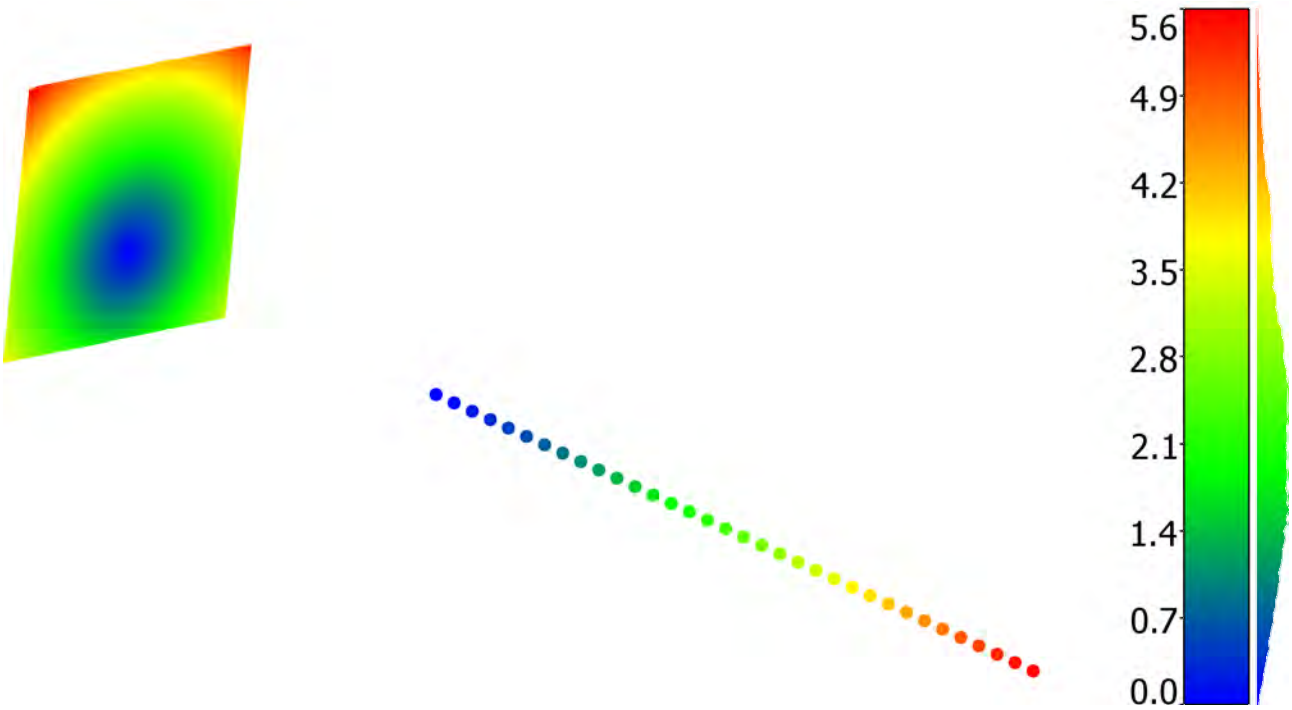

Figure 3.20: *Average spatial precision for each simulated viewpoint (colour coded spheres). Spatial single point precision for simulated scanner points based on the best viewpoint (left surface). Note that the scale of the colour bar is given in millimetres.*

3.2.5.2 Exemplification of the procedure on a complex example

As the previous example featured the simplest geometric characteristic possible a second more challenging case will be analysed in the following for which the scaled Nefertiti data has been used just as in the previous subsections. The radiometric properties of the dataset have been defined to be constant while assuming a quotient of reflection of 25% as for the previous example. Through this, effects provoked solely by the geometric configuration should become visible. In total ten viewpoints have been simulated within a range of 8 to 24 m where the distance to the object increased in steps of approximately 1.78 m. Again the height of the collimation axis has been set to 1.60 m. The first two columns of table 3.12 from the left denote the horizontal (HFOV) as well as the vertical field (VFOV) of view in degrees which is required to capture the object of interest. The

Table 3.12: *Overview about the chosen setting of the example*

HFOV [°]	VFOV [°]	Object distance [m]	Angular increment [°]	Resolution	Assumed number of points
18.10	36.88	8.00	0.072	middle	129276
14.64	30.04	9.78	0.072	middle	85272
12.27	25.29	11.56	0.036	high	239723
10.55	21.81	13.33	0.036	high	178164
9.25	19.16	15.11	0.036	high	136981
8.42	17.07	16.89	0.036	high	111150
7.42	15.39	18.67	0.036	high	88596
6.75	14.01	20.44	0.018	ultra-high	292125
6.19	12.86	22.22	0.018	ultra-high	245960
5.72	11.88	24.00	0.018	ultra-high	209880

third column from the left contains the distance between simulated scanner viewpoint and object of interest. Column four from the left contains the angular increment in degrees that has been used for ray casting the object while column five shows the designation of the resolution according to the manufacturer of the simulated scanner. It can be seen that the angular resolution has been increased with growing object distance in order to ensure a sufficient resolution on the object's surface. The column on the outer right represents the estimated number of points for which it is assumed that the field of view is entirely filled. As this is not the case for the Nefertiti dataset a lower amount of simulated points will result from the ray casting process.

For the computation of the spatial precision two restrictions have been introduced namely that only points should be considered where the incidence angle is smaller than 80° and that the remaining intensity after subtraction of geometric influences has to be larger than 20000 which corresponds to a precision of 13.88 mm for the reflectorless distance measurement. Figure 3.21 illustrates the result where each simulated viewpoint is depicted by a sphere while its according colour denotes the average spatial theoretical precision in millimetres.

It can be seen that the average spatial theoretical precision grows with increasing object distance apart from the most remote viewpoint. The reason for this will be discussed in the following while a measure is introduced that rejects this viewpoint from the solution space. Subsection 3.2.4.3 introduced the efficiency measure $\mathit{Eff}._{disc.}$ where only viewpoints were considered as a valid solution that featured a minimum ratio between acquired surface and the surface that was free of discretisation errors. The idea behind this measure is now adapted to datasets that feature stochastic information. For that purpose the measure $\mathit{Eff}._{precision}$ is introduced where only points are considered that lie above a preset precision. The computation of this efficiency measure follows

$$\mathit{Eff}._{precision} = \frac{N_{precision}}{N} \cdot 100 \tag{3.18}$$

where $N_{precision}$ is the amount of points that fulfil a defined criterion concerning its spatial theoretical precision and N that denotes the quantity of all simulated points. In order to find an optimal viewpoint two criteria have to be fulfilled:

- Minimum intensity of 20000 for all simulated observations which corresponds to a distance precision of 13.88 mm.

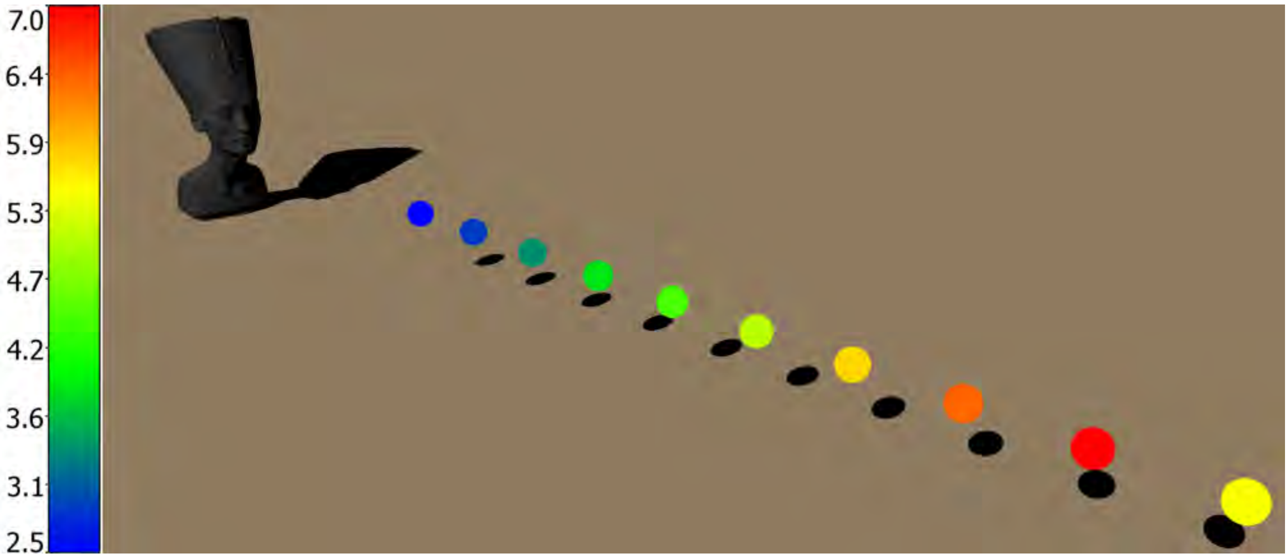

Figure 3.21: *Average spatial variance in millimetres (colour coded spheres) in dependence to object distance. The radiometric properties of the object's surface are assumed to be constant.*

- Minimum $Eff._{precision}$ of 80%.

Table 3.13 gathers the numerical outcome that is already depicted in figure 3.21. It can be seen the average spatial precision for each viewpoint decreases with increasing distance apart for viewpoint 10 as reported earlier. A look at the efficiency measure $Eff._{precision}$ reveals that viewpoints 1 to 9 lie above the predefined threshold while viewpoint 10 considerably falls below 80%. The reason for this can be found in the fact that a considerable part of simulated points falls below the minimum intensity margin of 20000 between viewpoint 9 and 10. For viewpoint 10 $Eff._{precision}$ amounts to 42.346% which means that the majority of acquired points wouldn't be usable. In other words 57.654% of the time that is required to capture data in the field would be wasted. The optimal viewpoint to capture this scenario is viewpoint 1 with a mean spatial precision of 2.54 mm.

Table 3.13: *Overview about spatial precision and efficiency*

Viewpoint	1	2	3	4	5	6	7	8	9	10
Object distance	8.00	9.78	11.56	13.33	15.11	16.89	18.67	20.44	22.22	24.00
Average spatial precision [mm]	2.541	2.893	3.383	3.878	4.425	5.080	5.719	6.351	6.953	5.437
Efficiency[%]	98.477	99.978	98.170	99.969	99.996	99.967	99.977	99.781	99.937	42.346

Figure 3.22 a) shows a depth map of the Nefertiti dataset simulated from viewpoint 1 where the unit is given in metres. It can be seen that the face is the closest part to the scanner as denoted by blue tones, followed by the chest and the central part of the helmet which are coloured in green and yellow tones while the upper, outer area of the helmet is the most remote portion. Figure 3.22 b) depicts the incidence angles of the bust in degrees. Nearly normal incidence angles can be found on the central part of the chest as well as on the chin, brows and eyes. Moderate angles of incidence are located on the outer parts of chest and shoulders as well as in the centre of face and helmet. Unfavourable steep incidence angles can be found on the outer boundaries of the object as well as on jaw, nose and ears. The outcome of ray casting and following variance-covariance propagation leads to the inspection map illustrated in figure 3.22 c) where the unit is given in millimetres. As expected the result shows characteristic patterns provoked by a combination of both geometric influences. The majority of points fall below a theoretical precision of 2.5 mm while the precision drops with increasing altitude especially on the helmet as well as on the outer boundaries of chest and shoulders. A low precision is located on the outer parts of the helmet.

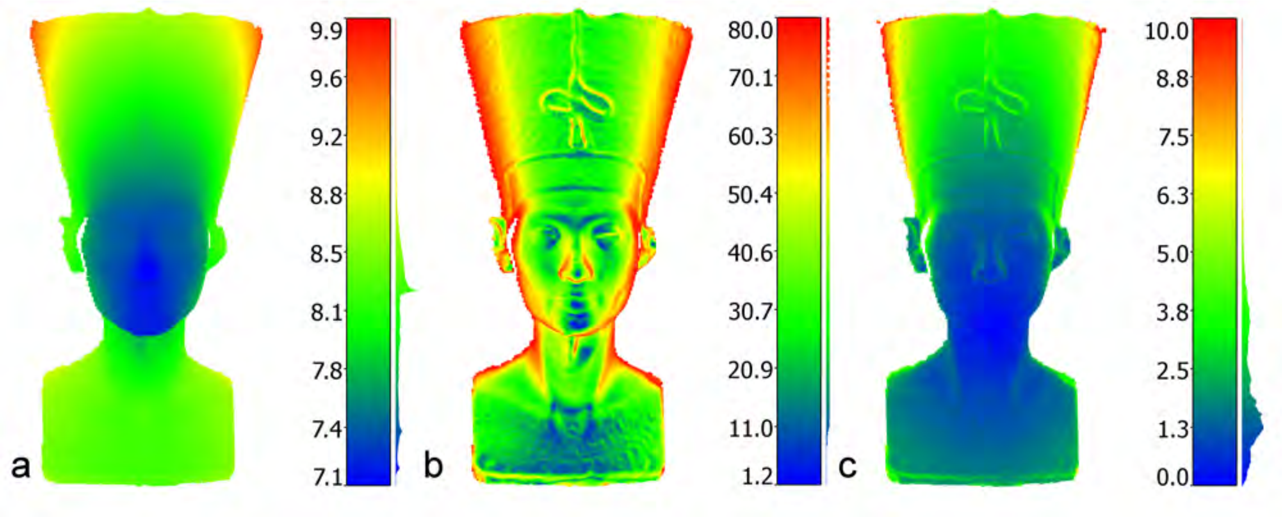

Figure 3.22: *Depth map in metres (a), incidence angle in degrees (b) and spatial theoretical precision in millimetres (c)*

3.2.5.3 Exemplification of the procedure on a complex example using radiometric information

While the previous examples assumed the radiometric properties of an object's surface to be constant it is now demonstrated in detail how this information can be captured and applied for the estimation of stochastic properties. It is assumed that a 3D-model including radiometric information of the object of interest is given which can for instance be captured by using photogrammetry (Luhmann 2003) or multi view stereo (Hartley & Zisserman 2010) which applies uncalibrated cameras or preferably a pre-scan with the TLS of choice. The procedure is now demonstrated on the Nefertiti dataset which has also been scaled as in the earlier part of this chapter. The input data consists of a meshed and textured 3D-model, as depicted in figure 3.23 a, which has been generated based on photographs captured of the bust's replica. The yellow sphere denotes the viewpoint from which the TLS is simulated. Before a laser scan observation can be deployed two tuneable parameters need to be defined namely the region of interest as well as the angular resolution which influences the resulting spatial sampling on the object's surface. In order to define the region of interest the bounding box of the object is computed as depicted by the yellow semi-translucent box. Based on the bounding box the horizontal and vertical field of view is defined which is represented in figure 3.23 b by a red respectively a green surface originating from the viewpoint. Subsequently the ray casting process itself can be conducted which leads to a simulated point cloud as signified by small green spheres on the object's surface (Figure 3.23 c).

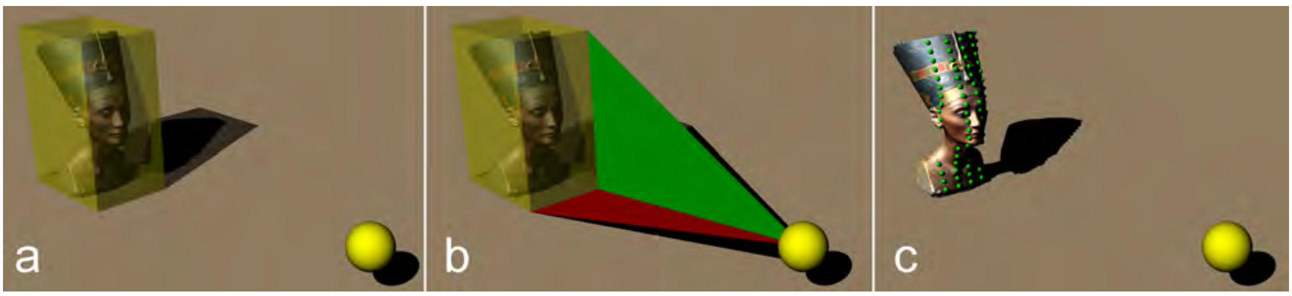

Figure 3.23: *a: Textured 3D-model of the object of interest with bounding box and simulated viewpoint (yellow sphere). b: Horizontal (red surface) and vertical field of view (green surface) that encloses the bounding box. c: Simulated TLS-points (green spheres on the object's surface).*

The outcome is then used to compute the distance between the simulated scanner and each point on the object as well as their incidence angles. Thus this information can be used to calculate the intensity loss which is caused by the given geometric acquisition configuration. However, the information that is still missing is the intensity that can be associated to a simulated point. An aspect that has to be emphasised is that the given radiometric information of the 3D-model is dependent to the radiometric sensitivity of the applied camera. While TLS capture radiometric information within several nanometres cameras are sensitive to wider spectrums of the light which are separated into channels – usually red, green and blue (LUHMANN 2003 p. 192). Due to this spectral discrepancy among the sensors, the dependence of camera acquired intensities to the lighting conditions and the fact that cameras capture the required information in a laminar fashion while laser scanners discretise the object space point wise it is only possible to receive approximate values. Therefore the spectral channel of the camera is used that is in closest radiometric proximity to the applied TLS. For the simulated scanner, a Z+F Imager 5006 h, the wavelength is specified with 690 nm (LI *et al.* 2008b) and hence can be associated to the red channel of an RGB image. As mentioned before the ray casting process yields to which ray of the simulated scanner intersects a certain triangle. The radiometric information that is associated to each vertex of the triangle is now used to assign spectral data to the intersection point which will be exemplified in the following. Figure 3.24 illustrates three vertices that assemble a triangle of the given surface model. The according eight bit coded greyscale values of the red channel are:

- Vertex 1: 190,
- Vertex 2: 105,
- Vertex 3: 60.

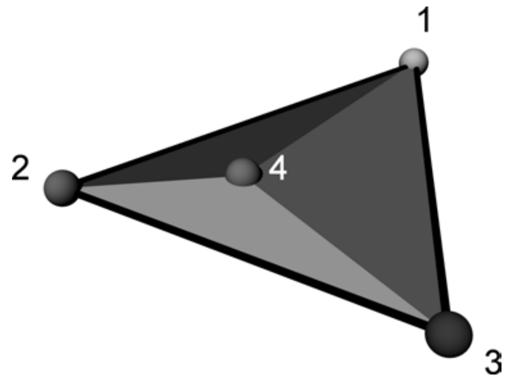

Figure 3.24: *Example for intensity interpolation within a triangle*

As a next step radiometric information is computed for the intersection point g_i by deploying barycentric interpolation (GRIEGER 2013 p. 229). This procedure follows

$$g_i = (g_1 \cdot A_1 + g_2 \cdot A_2 + g_3 \cdot A_3) / A \tag{3.19}$$

where g_{1-3} denotes the greyscale values for the three observed vertices. The surfaces of the opposing triangles of all vertices are represented by A_{1-3} while Asignifies the surface that is described by the observed vertices. At first A is computed which is assembled by vertices 1-2-3 and sums up to 64.36 mm^2. Subsequently the triangle surfaces A_1 (triangle 2-3-4), A_2 (triangle 1-3-4) and A_3 (triangle 1-2-4) are calculated that measure 15.64 mm^2, 33.15 mm^2 and 15.81 mm^2. As a next step the interpolation itself is initiated for which the greyscale values of all observed vertices are weighted by the opposing surface. Then the sum of all weighted observations is divided by the surface 1-2-3 which yields to the greyscale value of the intersection point

$$g_4 = (190 \cdot 15.65 + 105 \cdot 33.15 + 60 \cdot 15.81)/64.36 = 115.$$

As a final step this greyscale value which has been captured by a camera is converted into an observed intensity by the applied TLS. For this purpose the maximum greyscale value of 255 is associated to an intensity value of 1000000.

The search for an optimal viewpoint has been conducted as in the previous subsection. Therefore only viewpoints are considered as valid where $Eff._{precision}$ is larger than 80% and where the intensity of single points has to lie above 20000. Figure 3.25 illustrates the outcome where each simulated viewpoint is depicted by a sphere while its according colour denotes the average spatial theoretical precision in millimetres. In analogy to figure 3.21 the average spatial precision decreases with increasing object distance.

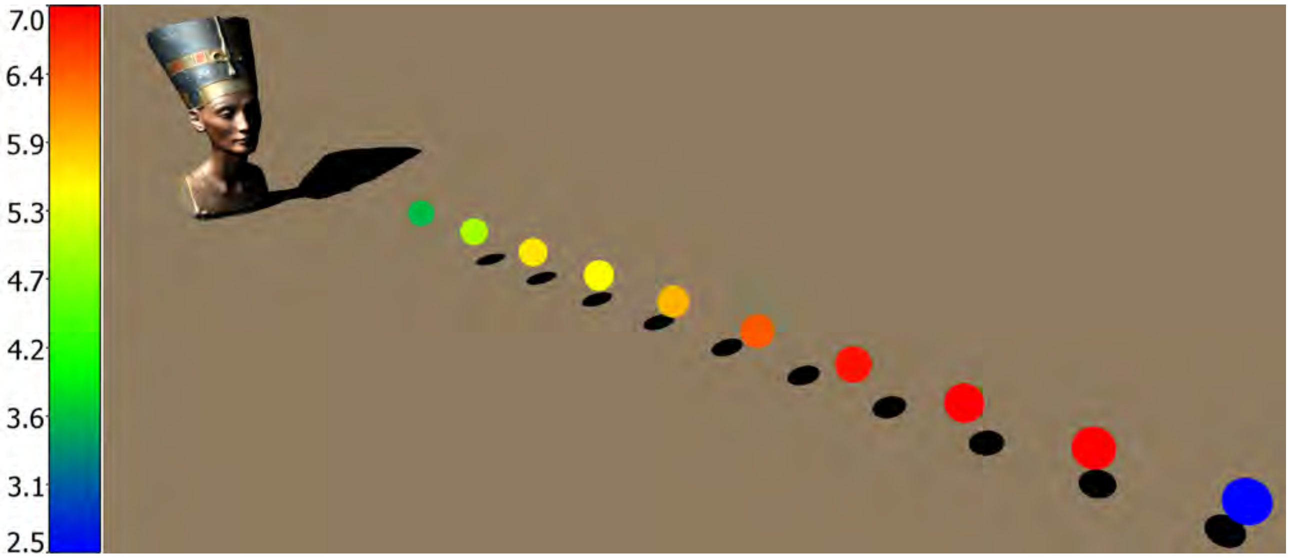

Figure 3.25: *Average spatial variance in millimetres (colour coded spheres) in dependence to object distance. Detailed radiometric properties have been assigned to the object's surface.*

As viewpoint 10 appears to be the most precise on average and hence optimal viewpoint $Eff._{precision}$ values are computed in order to see if a valid optimal solution has been found. Table 3.14 gathers the basic data. A look at the last row of the table shows that viewpoints 8 to 10 fall below the required minimum efficiency measure and are hence invalid. From the entirety of valid viewpoints the closest one to the object is the optimal viewpoint.

Table 3.14: *Overview about spatial precision and efficiency*

Viewpoint	1	2	3	4	5	6	7	8	9	10
Object distance	8.00	9.78	11.56	13.33	15.11	16.89	18.67	20.44	22.22	24.00
Average spatial precision [mm]	3.232	3.883	4.194	4.133	4.333	4.574	4.763	4.825	4.822	2.722
Efficiency[%]	98.153	98.629	92.679	89.539	86.225	82.964	80.014	76.720	74.024	34.905

Figure 3.26 illustrates the used 3D-model including its radiometric information on the left. On the right side the spatial precision for all simulated points captured from viewpoint 1 is colour coded where the colour bar is given in millimetres. It can be seen that the influence of the local radiometric properties are superior to the geometric influences apart from the outer parts of the helmet where unfavourable incidence angles and a low quotient of reflection significantly dampens the signal notably.

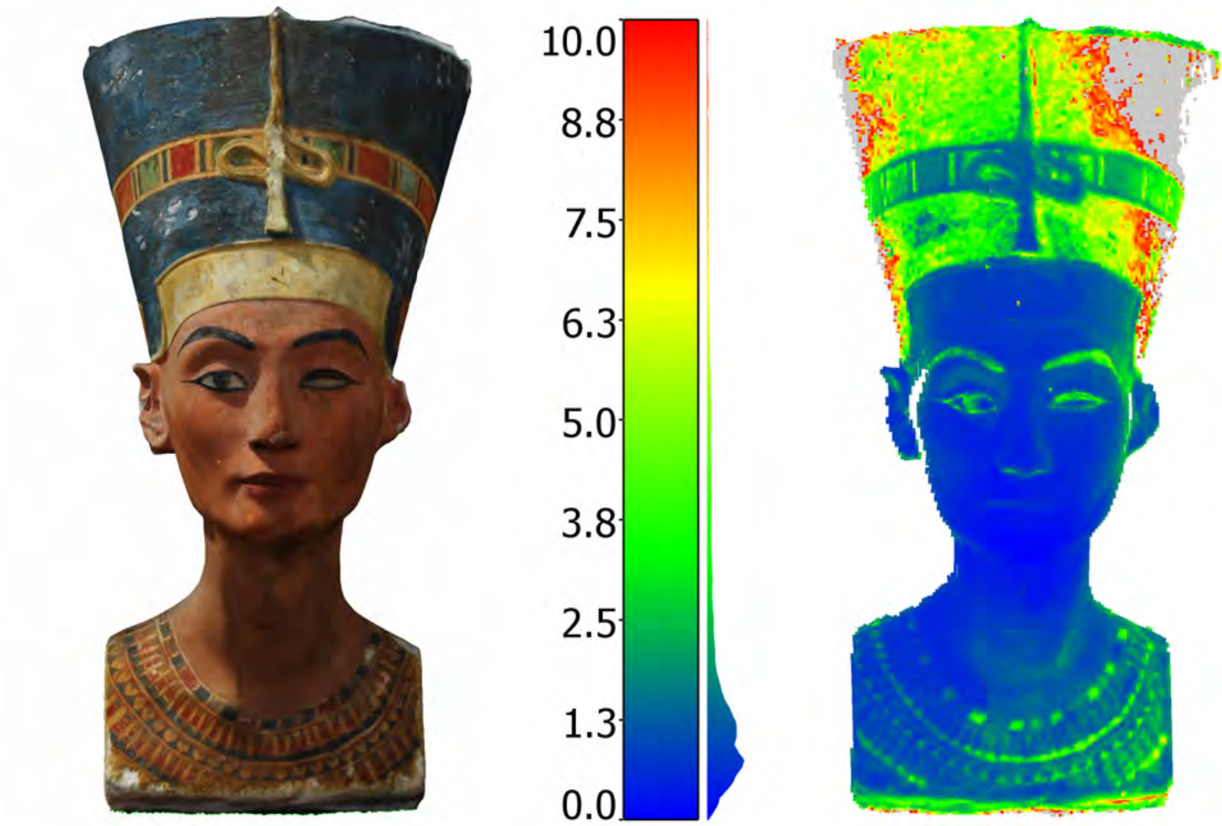

Figure 3.26: *Illustration of the RGB-coded input model (left) and colour-coded inspection map that displays the spatial variance in millimetres (right).*

3.3 Conclusion

This chapter proposed an intensity based stochastic model for TLS while geometric influences provoked by incidence and object distance have been shown. Thus far various researchers explained the stochastic behaviour of TLS simply by the influence of acquisition geometry. The author of the thesis argues that the observed intensity value not only reflects geometric influences onto the distance measurement of TLS but also the radiometric properties of the object of interest which are superior in terms of signal impact. Furthermore a combinatorial viewpoint planning algorithm has been proposed based on a given 3D-model. Besides a basic implementation geometric restrictions can be defined that yield to a certain overlap among simulated point cloud for the sake of surface based registration. The introduction of a measure for the geometric contrast ensures that the overlapping region of two point clouds can be used for registration. Based on several computed viewpoint plans the required expenditure of work is estimated in order to capture a scene in the field which is vital for the preparation of field trips, expeditions or other survey campaigns. By usage of the proposed intensity based stochastic model viewpoint planning has been conducted from the perspective of engineering surveying. It is now possible to fully capitalise the potential of a deployed TLS in terms of achievable precision by determining an optimal viewpoint. A procedure that has to be refined in the future is the process of simulating TLS-observations which is very time consuming.

4 Registration of point clouds based on stable areas for deformation monitoring

A key element of the deformation monitoring process chain is the transformation of several epochs into a common coordinate system based on stable areas which allows identifying deformation. As the outcome of this task, which complies to step 3 of the deformation monitoring processing chain, is substantially influenced by outliers respectively deformation that occurred in between epochs, diagnostic methods have to be developed that allow to identify these regions within the datasets and to reject them from the computation of transformation parameters. In this section data preparation is discussed at first as it plays a major role in the latter. Subsequently several methods for identification of stable areas are proposed and critically evaluated while two algorithms will be introduced, tested and compared. Before technical details of both algorithms are illuminated a general description is given. Both algorithms consist of three essential phases that are introduced in the following and specified in the latter:

Phase 1: Local matching of data sets.

Phase 2: Identification of stable areas.

Phase 3: Computation of transformation parameters based on stable areas.

The aim of the first phase is to orientate two arbitrary aligned point clouds, respectively to determine correspondences, by applying the ICP algorithm which is conducted within every local segment:

Step 1: Coarse alignment of point clouds.

Step 2: Segmentation of the point clouds' overlapping area, see section 4.2 for details.

Step 3: Determination of correspondences via ICP and transformation of local segments.

Step 4: Repetition of the previous step until the average of squared errors is smaller than a predefined threshold.

The first step of the first phase, the coarse alignment of two point clouds, is conducted by applying the four-points-congruent-sets-algorithm (4PCS) as proposed by Aiger *et al.* (2008). After this phase point correspondences and transformation parameters emerge for each cell as a direct outcome of a locally applied ICP. The objective of the second phase, that distinguishes the two algorithms, is to identify deformations within the scene and to exclude them from processing as already mentioned before:

Step 1: Calculation of comparative values,

Step 2: Computation of stochastic measures respectively uncertainty for diagnostic purposes,

Step 3: Identification of congruent clusters,

Step 4: Selection of the largest congruent and hence stable cluster.

Within the previously mentioned steps the largest stable region between two epochs should be determined. By fulfilling this goal all pre-conditions for the last phase, namely determination of transformation parameters for deformation monitoring, are satisfied. The innovative moment of this chapter is described by step 2 of phase 2 that considers the varying spatial sampling of terrestrial laser scanners. The general idea behind both algorithms in this context is to generate uncertainty measures under the assumption that no geometric changes occurred in comparison to the reference epoch.

4.1 Introduction of the test case

In order to test all developed algorithms and procedures a standard test case will be used throughout this thesis which has been captured on a brim within a quarry. Blasted material has been removed from the area while a scan has been acquired before and after removal. The viewpoint of the scanner was constant for both scans so that reference values for transformation parameters are given. In order to simulate data acquisition in different epochs the coordinate system of the second dataset has been modified so that the point clouds didn't overlap anymore. The captured area extends 15 m in width, 11 m in length with a height of 10 m. The deformation between epochs caused by removal of material covers about 34% of 224 m^2 while the maximum deformation amounts to approximately 80 cm. Figure 4.1 depicts the area under investigation during material transport (left) while the right part of the figure shows the captured point cloud after evacuation.

Figure 4.1: *Brim during material withdrawal (left) and point cloud after evacuation (right)*

4.2 Data preparation

After the first step of phase 1 has been deployed preparatory measures for fine matching via ICP are conducted. Therefore an octree structure (Meagher 1982) is generated that divides the point clouds into spatially equally large segments and contains dataset **B** that describes the target coordinate system and ancillary point cloud **A**. By finding suitable transformation parameters, **A** should be transformed into the coordinate system of **B**. This is achieved by minimising the distance d_i between corresponding points b_i and a_i. Within the presented solution an octree can be defined by either defining a desired depth which is a common definition in computer sciences or a metric measure that describes the required size sz of each octree cell c_i. Note that a metrically defined octree is usually larger in extent than its relatively scaled counterpart due to the fact that these cells are arbitrarily scaled. The octree is furthermore used for uniform sampling of so called candidates in each cell of the reference coordinate system that is defined by one of the point clouds system in order to avoid random candidate sampling that can be noted in classical ICP implementations. In addition this data filtering step allows to efficiently co-register very large point clouds. Therefore a certain number of points nop per cell c_i are defined. For each candidate in **B** the ICP will later on seek a corresponding point in **A**. The algorithm then subdivides each cell c_i of size sz into nop equally dimensioned fragments and chooses the respectively closest point to each cell's centre. If a subset does not contain any points or not enough to solve the stated problem the respective cell is dismissed. The outcome of the point filtering process leads to similar distances between adjacent candidates. The left part of figure 4.2 illustrates sampling of candidates on the ISPRS reference dataset of the golden Buddha statue. The size of each octree cell has been set to 1 m including 6 points per segment on average. Black dots represent the original point cloud, blue points depict candidates while red lines highlight octree cells in the right half of the figure.

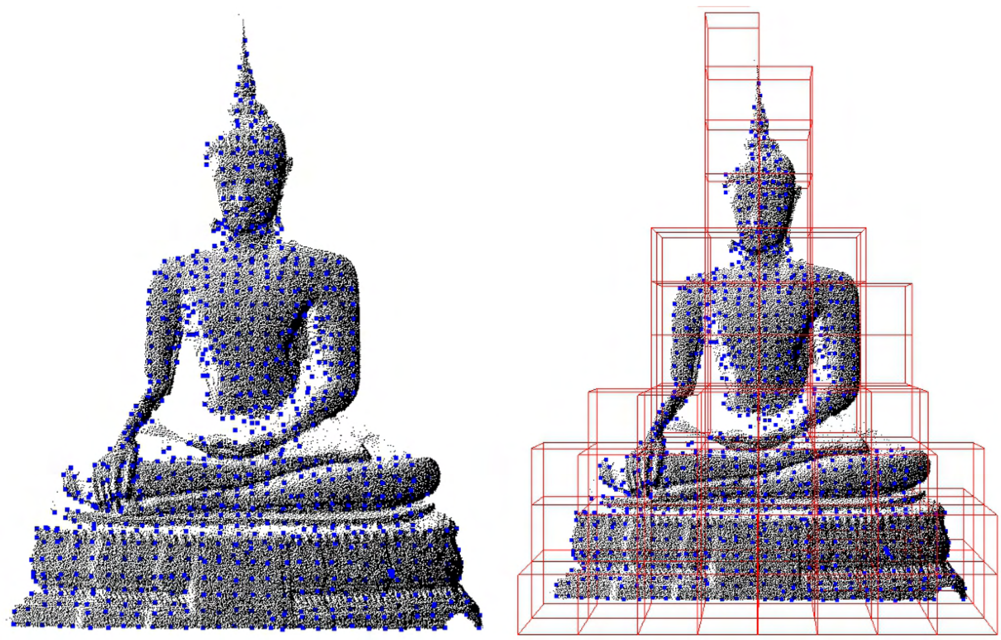

Figure 4.2: *Candidate sampling (left) and visualisation of according octree (right)*

The general assumption of the stated approach is that transformation parameters derived by subsets of the point clouds are equal to parameters computed based on the ensemble. That means on the other hand that areas that have been subject to deformation should be identifiable through deviations of individual transformation parameters. As candidates and consequently correspondences are uniformly sampled by applying the mentioned data structure topological consistency is given where transformation parameters can only be computed based on a set of adjacent tie points.

4.3 Identification of stable areas

A crucial component for the identification process of stable areas respectively deformation is the choice of suitable comparable values. In the following several approaches are introduced and discussed while finally a comparison summarises the section. As input of the procedure octree-cell wise application of the ICP-algorithm provides point correspondences and transformation parameters. In general three essential impacts falsify the outcome of all comparable values mentioned below namely:

- Statistical outliers of a measurement,
- Regions that were subject of deformation between epochs,
- Insufficient spatial resolution during data acquisition (discretisation error).

As a consequence wrong correspondences are established that bias the estimation of transformation parameters.

Comparison of transformation parameters: By segmented application of the ICP transformation parameters are a direct outcome for each cell. In principle transformation parameters are suitable measures for comparative purposes however the stochastic measures for all parameters are datum dependent even if discrete point to point correspondences have been established as e.g. in total station observations. It has to be noted that the term datum dependence denotes the distance of points to the origin of the coordinate system in this context.

Comparison of difference vectors: Instead of analysing several parameters as described before it is desirable to compare only one which can be achieved by introducing distances as comparative values. Therefore the magnitudes of vectors are compared that are established by points before application of transformation parameters (as illustrated by green circles in figure 4.3) and the same points after application of the transformation parameters as depicted by red circles in the same illustration. For the given example it is assumed that no deformation occurred and that correspondences are known. The mentioned vectors are referred to as difference vectors and are highlighted by grey lines between points e.g. from 1 to 1'. In this example a 45° rotation around the origin of the coordinate system has been conducted. As a result it can notably be seen that these quantities derived from transformation parameters are also datum dependent and thus are not used as comparable values in this thesis.

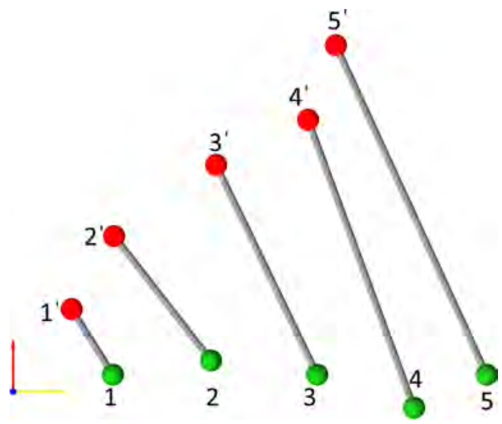

Figure 4.3: *Visualisation of transformation vectors and its datum dependency*

Global test of the adjustment: An established procedure in adjustment calculation is the so called global test of the adjustment (Niemeier 2008 pp. 167) which is also referred to as overall model test. This test clarifies if a previously known variance factor σ_0^2 is in accordance to the adjusted *a posteriori* value s_0^2 within its probabilistic boundaries. This decision is established by usage of a χ^2-test (Ghilani 2010 pp. 76-79). If the test reveals a statistically significant deviation Niemeier (2008 p. 170) points out three potential reasons:

- The functional model is **not** appropriate.
- The stochastic model is **not** suitable provoked by coarse or systematic errors, wrong weighting between observation groups or neglected correlations.
- σ_0^2 is **not** valid for the actual measuring conditions.

If the functional model is assumed to be appropriate the latter reasons have to be watched closely. Until now many studies tried to model the stochastic behaviour of the key component of TLS' which is the reflectorless distance measurement unit (see section 2.2.1) while in summary the outcome could not be stressed from a geodetic perspective. Hence the second reason has to be considered as true which consequently rules out the global test of the adjustment as a comparative measure. In addition the third aspect also has to be assessed as true as laser scanners capture points in a quasi-laminar way as discussed in section 2.1.3. Therefore the last reason has to be rated as true even if meaningful stochastic models for laser scanners would exist. If one assumes that all required prerequisites for this strategy are fulfilled another flaw has to be mentioned which can be interpreted as some sort of invisibility against rigid body transformations as illustrated in figure 4.4. The scenario includes a car in front of a building that altered location and orientation relative to the building in between two scans as illustrated by the pink coloured transformation vector as well as the object's coordinate system. If one now conducts ICP based matching within all octree cells separately notably different transformation vectors would arise. As this procedure only describes how well observations respectively two datasets fit together the previously derived information would simply vanish a circumstance that may occur e.g. in geosciences where parts of a glacier or rock faces separate from one another. In summary the discussed procedure is also not suitable for identification of stable areas respectively deformation.

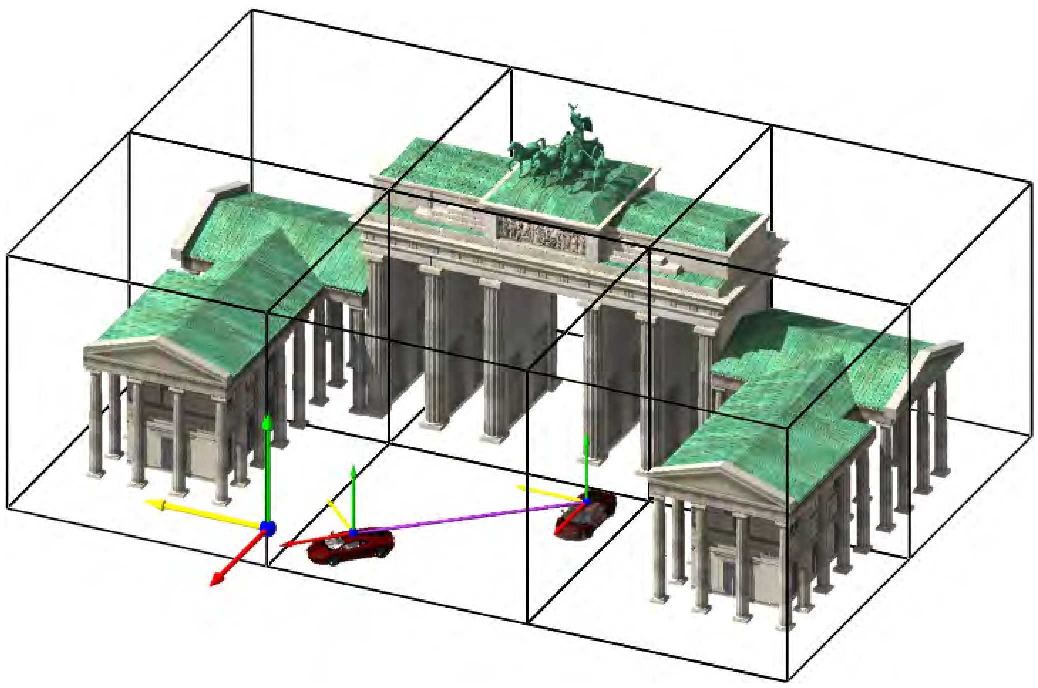

Figure 4.4: *Illustration of a scenario where geometric changes occurred (3D models courtesy of tf3dm.com)*

Comparison of spans between transformed points: One outcome of the ICP are point to point correspondences between datasets which are determined iteratively. In contrast to the first two approaches which are subject to datum dependence a comparison of distances between corresponding points before and after application of locally derived transformation parameters is proposed in this subsection. Figure 4.5 illustrates the same scenario as in figure 4.3. Green circles denote points in their original position while grey lines represent distances between adjacent ones. Red circles depict points after transformation parameters have been applied. It can be seen that the distances between points remain the same regardless of the applied transformation. However two problems need to be critically assessed: the computational effort increases with a rising amount of correspondences as well as the question of how to generate meaningful thresholds for comparative purposes. An implementation of this strategy has been presented in WUJANZ *et al.* (2013b).

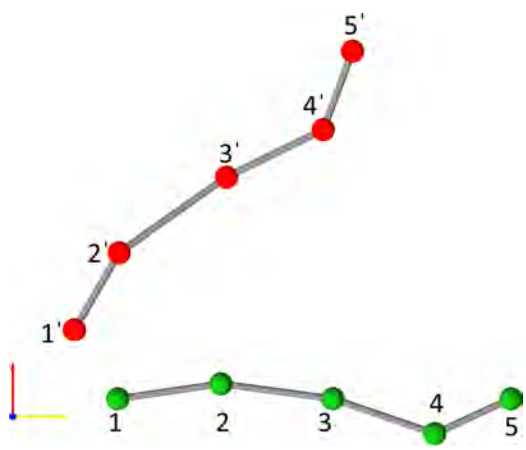

Figure 4.5: *Distance comparison between corresponding points of two datasets*

In order to overcome the issue of vast complexity an approach is proposed that generates comparable values per octree cell. Therefore the second outcome of the ICP namely a set of locally determined transformation parameters for each octree cell is used. In case that deformation occurred within a cell between two epochs the correspondences as well as the arising transformation parameters are falsified. This effect allows identification of the according cells as the transformation parameters for all stable cells should be more or less equal. These sets of transformation parameters are then applied to the respective centre of gravity based on all candidate points within the according octree cells. Then the distance between cells is compared before and after transformation of the focal points.

Now that several approaches for discrimination of stable and deformed areas have been introduced it is obvious that only two of them, namely comparison of spans between transformed points and the global test of the adjustment, are independent against a chosen geodetic datum. As the global test of the adjustment is not applicable for various reasons the approach where spans between transformed points are compared has been implemented and will be discussed in the following. Table 4.1 gathers important properties of all discussed procedures. A crucial aspect that requires additional remarks is the fact that all comparable values as well as its stochastic properties are dependent to the spatial sampling of terrestrial laser scanners as discussed in subsection 2.1.3.

Table 4.1: *Comparison of properties from all comparable values*

	Parameter	**Stochastic information**
Transformation parameters	Datum dependent and dependent to sampling	Dependent to datum and sampling
Transformation vectors	Datum dependent and dependent to sampling	Dependent to datum and sampling
Global test of the adjustment	Datum independent but dependent to sampling	Datum independent but dependent to sampling
Spans between transformed points	Datum independent but dependent to sampling	Datum independent but dependent to sampling

4.4 DefoScan++: Identification of deformation via comparison of spans between transformed points

The following section describes the first proposed algorithm in detail where spans between corresponding points before and after application of locally determined transformation parameters serve as comparable values for the identification of deformation. A prototypical implementation has been conducted in Final Surface (GFaI 2015), a commercial software by a co-operation partner of TU Berlin. Note that parts of this subsection have already been published in Wujanz *et al.* (2013b).

4.4.1 Identification of deformation via comparison of corresponding points

A central aspect of the contribution at hand is to distinguish stable and deformed regions within point clouds that have been captured in different epochs. Hence this subsection presents criteria for the identification of deformation. Therefore distances between corresponding points within the two original point clouds are compared which have been determined earlier by local application of the ICP inside each octree cell. At first consistent cells have to be found that are subsequently clustered by comparing distances between segments and are referred to as collaborating cells. As already mentioned transformation parameters are determined based solely on points from the biggest consistent cluster as this region of the point clouds is assumed to be geometrically stable.

An important issue to solve in order to test on consistency is to develop a suitable threshold. Since TLS discretises the surface of an object in a quasi-laminar manner, as discussed in subsection 2.1.3, and hence no identical points are measured in two scans the single point precision can't be used as a suitable measure particularly as no manufacturer provides suitable stochastic models for this purpose. Thus three criteria are introduced in the following that are used to derive suitable thresholds and consider local properties of point clouds:

1. A point from **B** (green sphere in figure 4.6 a) needs to be located within the area that is described by its corresponding point and its adjacent points from **A** (white spheres in figure 4.6 a and b). Note that the mentioned figures only illustrate the two closest points for the sake of simplification. In order to ensure compliance a statistical test (t-Test) by using the according single point accuracies can be used. A simplified approach has been chosen in this contribution where the 3σ-rule (also referred to as 68–95–99.7-rule) is executed in combination with the equally weighted single point accuracies of the applied TLS as published by the manufacturer. The 3σ-rule (PUKELSHEIM 1994) assumes that 99.7% of all observations lie within three standard deviations to the mean in a Gaussian distribution and is based on CHEBYSHEV's inequality (CHEBYSHEV 1867).

2. A corresponding point *has to lie on the surface* (Figure 4.6 c) that has been described in the previous step. As all measurements are subject of a certain variance it has to be tested if the perpendicular distance between a point and the previously mentioned surface is acceptable. Therefore variance-covariance propagation needs to be conducted in order to assign stochastic measures to individual points. Subsequently the variance of a dropped perpendicular foot and thus the variance of the span between point and plane can be determined. Again, for the sake of simplification the 3σ-rule has been applied.

3. At last a corresponding point needs *to be located within a partial area* (Figure 4.6 d) that has been derived from the area described by the first criterion. The mentioned partial area defines the region in which a corresponding point can be located and is hence used to compute the required thresholds. Therefore the closest perpendicular bisectors to a corresponding point are computed and intersected. This procedure is an extension of the first criterion and is applied as a last step in order to increase efficiency of data processing.

If all criteria are satisfied thresholds can be computed that are valid for two corresponding points of point cloud **B**. Therefore distances are computed in all combinations between corner points of the according partial areas where the longest and shortest span (Figure 4.6 e) define valid thresholds. Hence the comparative length of **A** needs to lie within the distances of **B** as derived by the third criterion. As mentioned earlier the accuracy of the applied TLS can be used in combination with the computed thresholds as a statistical measure to test on compliance of compared distances. For simplification in this first implementation it has solely been tested if the distance from **A** lies within the shortest and longest distance of **B**. A close look at the third criterion reveals the fact that the local resolution of the point clouds relevantly limits the acceptable size of potentially existing deformation. In other words: the coarser the resolution of a point cloud the less sensitive is the proposed method against larger deformations.

By applying the introduced criteria comparisons between all corresponding points can be conducted. For organisation purposes of this comparative approach three different attributes can be assigned to each octree cell:

1. Cell is valid / invalid,
2. Cell is consistent / inconsistent,
3. Cell i collaborates with cell $j \dots n$.

The first attribute labels if an octree cell is valid and hence decides if a segment is used for further processing. The attribute *invalid* is set if a cell contains less than the predefined quorum or if the determination of transformation parameters failed for instance due to a diverging adjustment. A cell receives the attribute *consistent* if less than

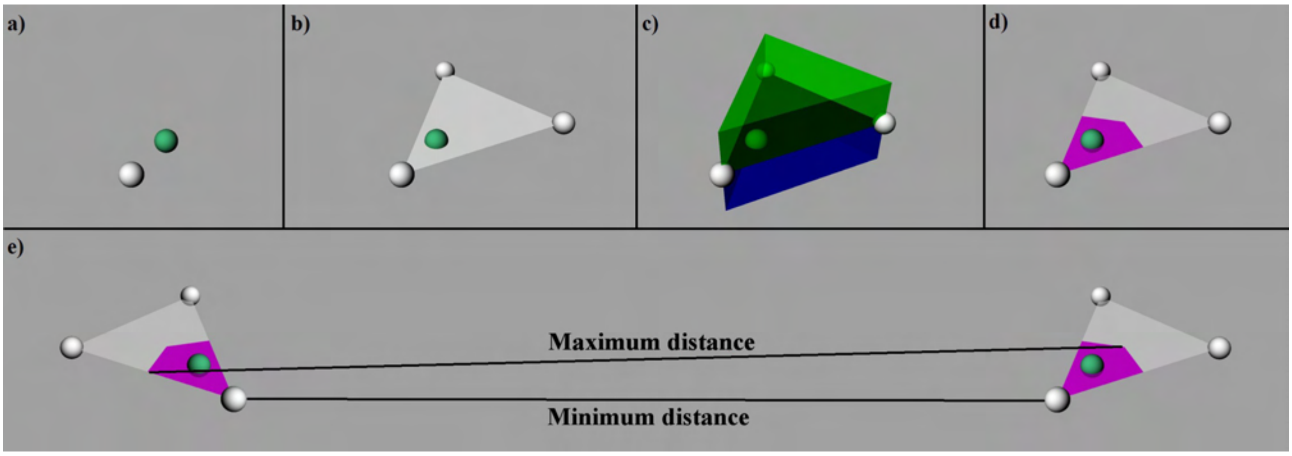

Figure 4.6: *a) Corresponding points b) Area criterion c) Maximum span to area d) Area in which a correspondence can be located e) Distance tolerance for consistency testing*

15% of all comparisons of distances exceed the range of tolerance as introduced afore. This empirical value has been used to generate all results presented in this section. Comparisons of distances are executed between all corresponding points within a cell apart to themselves or in reverse order. Points which have been classified as invalid are rejected, including their correspondence, from further processing.

Within the last step of the algorithm consistent octree cells are merged to clusters which is achieved by comparing distances between different octree cells. This step is carried out analogue to the determination of consistency within segments. Cells that have been set as *collaborating* are added to a cluster list. The cluster, respectively the correspondences inside the cluster, with the most entries is used to compute transformation parameters – all other corresponding points within the remaining octree cells are regarded as outliers and are hence rejected from the computation.

4.4.2 Application of the procedure

For coarse registration of both scans that were discussed in subsection 4.1 the 4PCS-algorithm (see section 2.3.2.2.1 for details) has been used that brought the point clouds into a sufficient pre-alignment despite the existence of deformation. Subsequently the proposed algorithm has been applied for fine registration whereupon deformation monitoring should be performed. The edge lengths of the octree were chosen with 3 m while 10 corresponding points should be within each cell on average. This led to 598 corresponding points that are organised in 51 octree cells. Figure 4.7 illustrates the outcome of the clustering process by using the described settings.

White coloured points describe invalid cells while highlighted points in red mark inconsistent areas which are assumed to contain deformation. Orange coloured points mark the second biggest cluster and yellow the remaining collaborating clusters. Green points denote the cells that assemble the biggest cluster and are hence used to compute transformation parameters. The average of absolute residuals computed by 116 correspondences amounted to 14 mm. A comparison with the right part of figure 4.8 reveals that the region that contained deformation has been omitted which leads to the conclusion that the result can be evaluated positively.

A critical aspect when using algorithms is the interaction between outcome and tunable parameters. For the proposed algorithm the decisive parameter is the size of the octree cells. A varying number of correspondences per cell did not lead to significantly different results. Apart from the already introduced results derived with edge lengths of 3 m additional versions have been computed with 2 m and 1.5 m. Another attempt with a setting of 1 m failed due to lack of “geometric contrast” within the cells. A close look at figure 4.7 reveals a dependency of the result to the chosen size of the according octree. It can nevertheless be established that the majority of deformation has been rejected from the computation of transformation parameters.

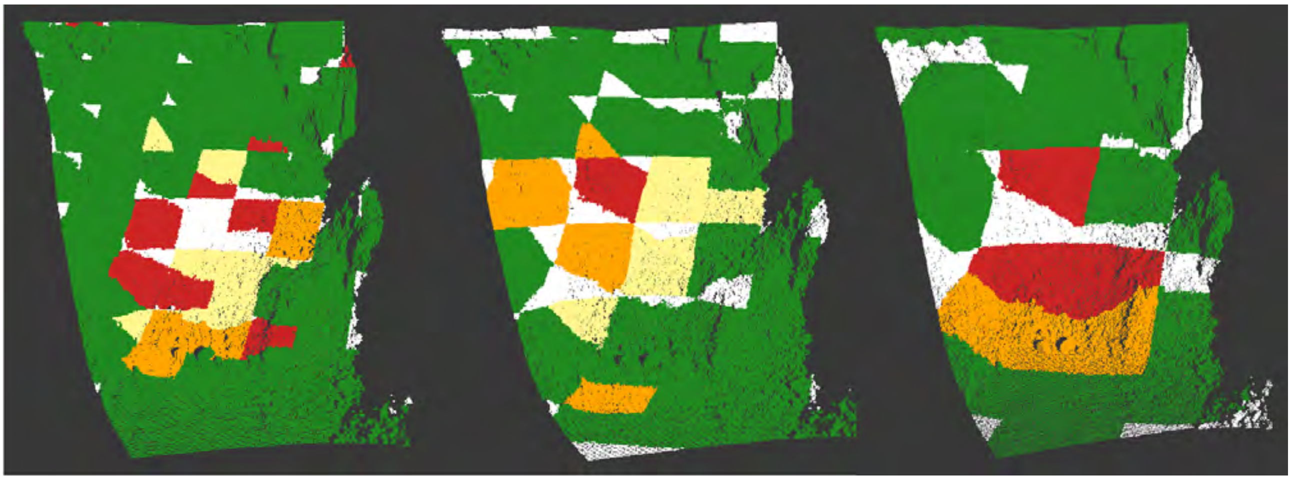

Figure 4.7: *Results of the clustering process in dependence to the edge lengths of the respective octrees: 1.5 m (left), 2 m (centre) and 3 m (right)*

Figure 4.8 depicts the result of deformation monitoring between the epochs as a colour coded inspection map. The left part illustrates the reference as measured from one viewpoint. The right part shows the outcome of DefoScan++ which has been derived fully automatic with an octree size of 2 m. At first glance the results are barely distinguishable which is why a comparison between the transformed data to the original ones has been carried out. Slight differences are noticeable if average deviations between reference and transformed data are computed which leads to 9 mm / -6 mm for a cell size of 1.5 m, 6 mm / -5 mm for size of 2 m and 9 mm / -4 mm for an octree setting of 3 m. The prefixes denote if points are located above or below the reference data.

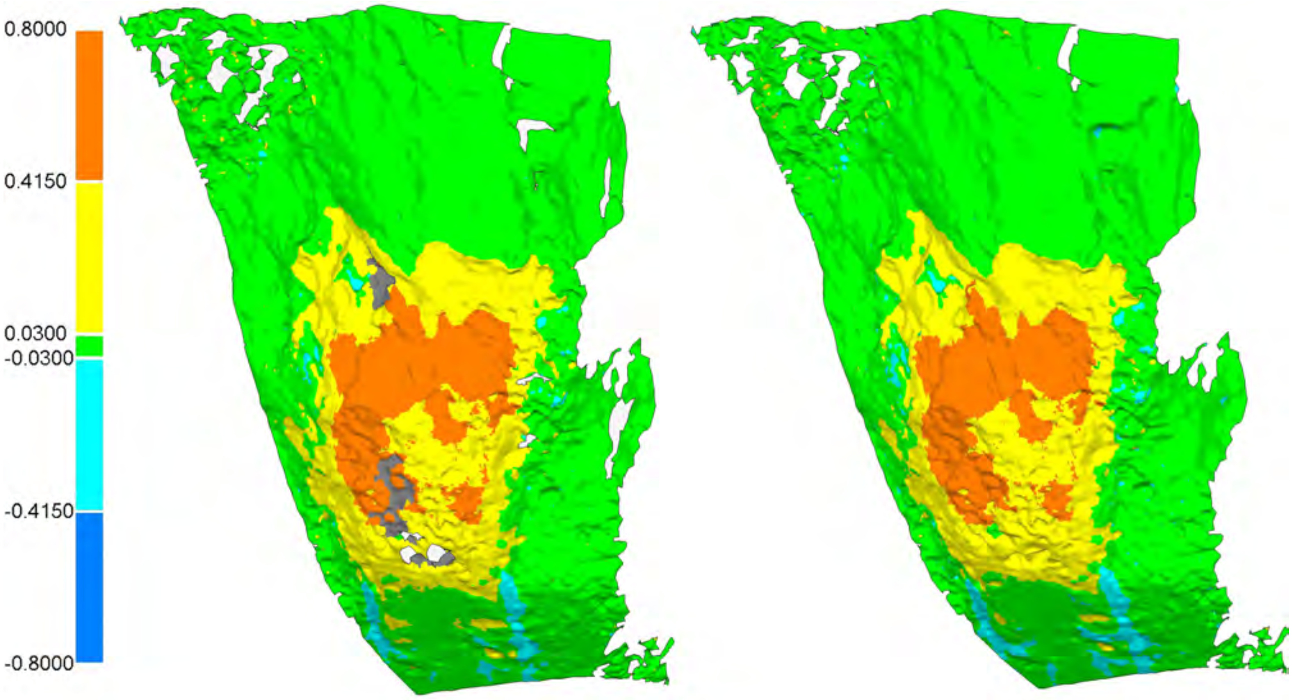

Figure 4.8: *Colour coded inspection map based on original datasets (left) and modified coordinate system after matching with DefoScan++ (right). The unit of the colour bar is metres*

4.4.3 Results and discussion

This section introduced a novel procedure for registration of point clouds that identifies existing deformations within datasets by comparison of distances between corresponding points and finally rejecting them during computation of transformation parameters. The combination of 4PCS and DefoScan++ describes a two-tiered procedure for fully automatic deformation monitoring. The capability of the approach has been demonstrated on a practical dataset while the achieved results have been verified by comparison to a reference dataset. Dependencies of the outcome to the octree cell size have been established while the area that contained deformation was identified in all cases. Declining spatial resolution during data acquisition increases the insensitivity against potentially existing smaller deformation. A downside of the approach in its current implementation is that entire octree cells are rejected in case that they've been classified as inconsistent even though they may contain consistent corresponding point pairs.

Even though the proposed approach produced usable results several aspects have to be seen critical. The first one is the use of an empiric threshold that determines how many invalid connections between corresponding points are acceptable. Furthermore the method is in computational terms very demanding as it calculates not only distances between all corresponding points within an octree cell in all combinations but also between octree segments. However, the step of the procedure that comprehends the biggest risk in terms of generating erroneous results is the sequential clustering process. An example of potential negative effects is illustrated in figure 4.9. A network of five points is represented by grey vertices and lines. Two epochs are simulated where all points remained stable apart from the blue vertex which corresponds to the upper right point in the first epoch. It is assumed that green lines and vertices have already been declared as being stable. The given task is now to sequentially determine if the upper two points have remained stable in between epochs. Therefore the upper sequence of the figure shall be examined. At first the distance between the lower right and the upper left point is compared. As a sequential approach has been chosen, only the scalar is considered which is visually represented by a circle with the radius of the distance between the two mentioned points in the first epoch. The accepted range precision for all measurements is depicted by the thickness of the circle which is assumed to be identical for all distances. As the inspected point lies on the circle within the accepted range it is considered of having remained stable. Subsequently the distances between the two upper points are analysed as represented by the white circle in the figure on the upper second left. Since the blue point lies outside the boundaries of the circle it is presumed to not being part of the stable set assembled by four vertices which is highlighted by red colour. If one now examines the lower sequence of the figure it can be seen that the deformed point (blue vertex) is now part of the stable area while the upper left point has been interpreted as being subject of deformation. Hence it is obvious that the previously applied sequential clustering respectively outlier removal strategy, which is still the most popular approach for this task, is dependent to the sequential arrangement of the inspection. Hence another algorithm should overcome the mentioned critical aspects of DefoScan++ that will be introduced in the next section.

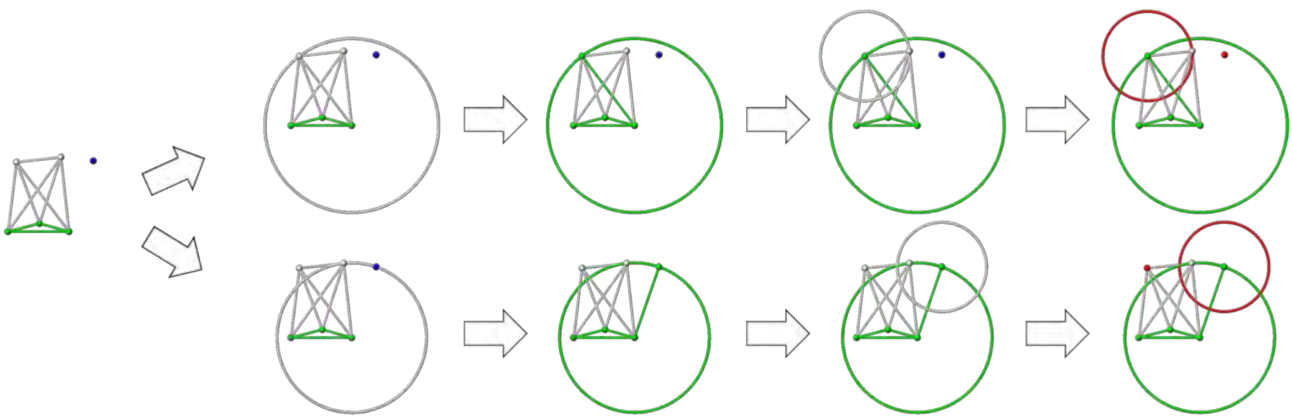

Figure 4.9: *Potential problems in sequential clustering processes exemplified on a network based on five points.*

4.5 The ICProx-algorithm: Identification of deformation based on comparison of spans between focal points

As shown in section 4.4.3 two crucial aspects of the previously proposed algorithm have to be rated critical and hence need to be substituted namely: sequential outlier removal respectively clustering as well as testing all correspondences within an octree cell which is very demanding in computational terms. In order to identify outliers by using the entire information within an octree element comparison of spans between transformed focal points are applied as described in section 4.3. Table 4.2 gathers differences and important properties of both implementations.

Table 4.2: *Comparison of fundamental properties of both algorithms*

Workflow	**DefoScan++**	**ICProx**
Coarse alignment of datasets	4PCS (Aiger *et al.* 2008)	4PCS (Aiger *et al.* 2008)
Segmentation of the object space	Octree	Octree
Local matching	ICP	ICP
Comparable values	Comparison of spans between corresponding points	Comparison of spans between transformed focal points
Determination of thresholds / uncertainty for congruency analysis	Threshold based on geometric criteria as described under 4.4.1	ICProx
Congruency analysis	Sequential clustering	Maximum subsample method

4.5.1 The maximum subsample method

The maximum subsample (MSS) method has been originally published in 2004 by Neitzel however only in German language which is why important parts of this thesis are translated and gathered in this section as it is used in the latter. The aim to eliminate outliers from acquired data so that acceptable residuals emerge after a least squares adjustment is an essential problem when analysing geodetic observations. As this problem can neither be solved by successive removal of single observations after a least squares adjustment nor by usage of resistant or robust estimation procedures in all cases, as shown in subsection 2.4, the question arises how this issue can be tackled. A close look at alternative estimation procedures reveals the fact that the least median squares estimator (LMS), in contrast to all other approaches, tries to find a solution by combinatorial means. The advantage of this strategy is its independence against the geometry of the stated adjustment problem including so called leverage points (Niemeier 2008 pp. 215). As this method only determines a solution under minimum configuration implausible results may result. The basic concept to solve adjustment problems by combinatorial means is kept in the following. Furthermore a novel strategy should be developed which allows to directly solve the actual problem namely to identify the maximum subsample of consistent data.

“MSS” describes a method in the following that conducts a combinatorial search for the maximum subsample within the entirety of a dataset that yields to a compliant result of a least squares adjustment.

The following subsections describe the basic concept for determination of such a subset while subsequently a special strategy for congruency analysis of geodetic networks is proposed.

4.5.1.1 Basic concept

While subsection 2.4 already extensively covered various methods and aspects on outlier identification respectively resistant or robust estimators this section will focus on a combinatorial approach to cope with the given problem. The basic concept of the MSS is to compute *all* potential subsets of observations within the entirety and to compute individual least squares adjustments. Hence, the aim to identify the biggest consistent subset for which all observations satisfy $|w_i| \leq c$ can be solved by combinatorial techniques which are not very widespread in Geodesy. The only method that applies combinatorial search is the already mentioned LMS-estimator whose application in geodetic problems has been presented by Kanani (2000).

Congruency analysis of geodetic networks describes a special case of the general aim where displaced points provoke the hypothesis of congruency to be rejected. Established methods usually try to identify stable points in a sequential fashion while Neitzel (2004, pp. 99) proved that this approach may lead to wrong results. Hence, the determination of congruent subsets is conducted by combinatorial means in the following.

4.5.1.2 Direct solution of the MSS-problem

An adjustment problem with n observations and m unknowns is given. A "brute force" approach to try all combinations of observations is not feasible even when considering modern computers. The reason for this can be easily shown by an equation system of n equations with i unknowns which leads to

$$K = \sum_{i=1}^{r} \binom{n}{n-i} = \sum_{i=1}^{r} \frac{n!}{(n-i)!i!} \qquad \text{where } r \text{ is the redundancy} \tag{4.1}$$

possible combinations in order to find a solution. Assuming a set of 50 equations and 10 unknowns 1.02722781e+10 adjustments would have to be computed. It is obvious that the computational effort is not justifiable. Hence a strategy needs to be developed that drastically reduces the sample space and allows to determine a solution at an reasonable amount of time.

4.5.1.3 Randomised selection of combinations

A general limitation of combinations can be achieved by not considering all combinations, but a predefined number of subsets which have been randomly selected an approach that complies with e.g. Fischler & Bolles' (1981) **ran**dom **sa**mple **c**onsensus. However, it can't be guaranteed that the factual maximum subsample has been found. In order to antagonise this circumstance all observations that are not considered should be eliminated from the adjustment by setting their according weights to zero. Through this dodge, these observations do not influence the outcome of the parameter estimation but however receive residuals which can be used for assessment purposes in order to clarify whether an observation can be adjoined to the group of compliant data.

4.5.1.4 Preliminary inspection

In order to drastically reduce the sample space several measures can be carried out. As an input direct observations or parameters that may be interpreted as such can be used, for instance distances. For explanatory reasons a network of points that has been surveyed in two epochs shall be assumed. After application of a free network adjustment a global test on the adjustment model (Niemeier 2008, pp. 167) can be carried out. This test clarifies if the variance factor s_0^2 coincides (within probabilistic boundaries) with a computed *a priori* value.

If this is not the case as significant deviations result three reasons can be responsible for this:

- The chosen variance factor s_0^2 is not valid for the measuring conditions,
- The functional model is not appropriate,
- The stochastic model is not correct while outliers or systematic errors, erroneous weighting of observations or neglected correlations have not been considered as a potential source of error.

In case that the first two mentioned factors can be considered as being correct point displacements may be existent. Thus the maximum subsample of stable points has to be identified from the entirety of points. To avoid computing all combinations only points should be examined that have the potential to being part of a stable group. For this purpose a strategy is proposed which applies datum-invariant measures (distances) for preliminary inspection. At first all possible distances need to be computed between the points in both epochs. Based on these measures deviations d_{li} can be computed which allow a first assessment of occurring deformations. This information needs to be prepared in a way that "impossible" combinations can be eliminated from the search procedure.

At first all distances $\hat{\mathbf{l}}_\mathrm{i}$ are computed based on adjusted coordinates in epoch 1 and 2 including their cofactor matrices $\mathbf{Q}_{\mathrm{l_i l_i}}$

$$\hat{\mathbf{l}}_1 = \mathbf{F}_1\hat{\mathbf{x}}_1,\ \mathbf{Q}_{l_1 l_1} = \mathbf{F}_1\mathbf{Q}_{\hat{x}_1\hat{x}_1}\mathbf{F}_1^\mathrm{T} \quad \text{and} \quad \hat{\mathbf{l}}_2 = \mathbf{F}_2\hat{\mathbf{x}}_2,\ \mathbf{Q}_{l_2 l_2} = \mathbf{F}_2\mathbf{Q}_{\hat{x}_2\hat{x}_2}\mathbf{F}_2^\mathrm{T} \tag{4.2}$$

where $\mathbf{F}_\mathrm{i}$ denotes the linearised functional relationship for the computation of distances. Subsequently the difference vector and its according cofactor matrix can be computed which follows

$$\mathbf{dl}{=}\hat{\mathbf{l}}_2 - \hat{\mathbf{l}}_1,\ \mathbf{Q}_{\mathrm{dl}} = \mathbf{Q}_{\mathrm{l_1 l_1}} + \mathbf{Q}_{\mathrm{l_2 l_2}} \tag{4.3}$$

Based on these values conclusions can be drawn whether the differences d_{li} lie above a certain threshold or not. In general three procedures can be applied which define such a threshold:

- Assessment by empirical data: e.g. comparison of manufacturer's data or empiric information with a 3σ-criterion,
- Assessment by signal-to-noise-ratio (S/N): the difference between two distances is compared and interpreted as a "signal" while the empirical standard deviation is seen as "noise". If the ratio exceeds 5 a significant deviation can be assumed (Niemeier 1976),
- Assessment based on a multiple t-test (Student 2008) where single elements d_{li} of $\mathbf{dl}$ can be evaluated.

4.5.1.5 Topological matrix of congruent subsets

Usage of graphs are widespread in the field of Geodesy reaching from routing, where Dijkstra's (1959) algorithm is applied, to the work of Gründig (1988) and Linkwitz (1999) who describe its use for problems in the field of Engineering Geodesy. As geodetic networks which consist of points and lines can be interpreted as graphs that are assembled of vertices and edges methods from graph theory can be adopted for the identification of congruent sets respectively deformation monitoring. A suitable tool for this task are so called incidence matrices that are capable to express topological relations within a graph where vertices are connected by edges.

Within the context of the previous subsection improper deviations d_{li} between distances need to be rejected from the process of estimating transformation parameters. In order to achieve this topological relations can be used to identify congruent point sets based on the remaining distances. Therefore an incidence matrix $\mathbf{C}$ has to be assembled that assigns observed distances to according edges and hence embodies topological relationships. A graph of five points in which distances have been measured in all combinations is depicted in figure 4.10 while its incidence matrix is shown in table 4.3.

$\mathbf{C}$ contains the i^{th} observation of the j^{th} vertex while the following definition holds:

c_{ij} = 1, if the i^{th} observation originates from the j^{th} vertex,

c_{ij} = -1, if the i^{th} observation ends at the j^{th} vertex,

c_{ij} = 0, in all other cases.

Note that the sign of c_{ij} may only be of relevance for diagnostic purposes for instance of tacheometric observations where some vertices were instrument viewpoints during data acquisition. Hence the use of signed entries helps to reproduce which observations have been conducted from where.

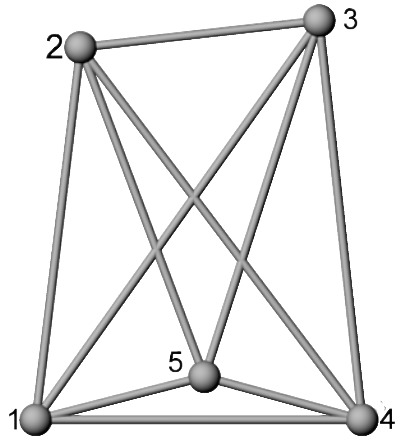

Figure 4.10: *Sample network consisting of five points*

Table 4.3: *Incidence matrix of the figure depicted in figure 4.10*

	Pt. 1	Pt. 2	Pt. 3	Pt. 4	Pt. 5
$s_{1,2}$	1	-1	0	0	0
$s_{1,3}$	1	0	-1	0	0
$s_{1,4}$	1	0	0	-1	0
$s_{1,5}$	1	0	0	0	-1
$s_{2,3}$	0	1	-1	0	0
$s_{2,4}$	0	1	0	-1	0
$s_{2,5}$	0	1	0	0	-1
$s_{3,4}$	0	0	1	-1	0
$s_{3,5}$	0	0	1	0	-1
$s_{4,5}$	0	0	0	1	-1

Based on the incidence matrix the adjacency matrix $\bar{\mathbf{C}}= \mathbf{C}^{\mathrm{T}}\mathbf{C}$ can be computed which is illustrated in table 4.4.

Table 4.4: *Adjacency matrix of the network graph of figure 4.10*

	Point 1	Point 2	Point 3	Point 4	Point 5
Point 1	4	-1	-1	-1	-1
Point 2	-1	4	-1	-1	-1
Point 3	-1	-1	4	-1	-1
Point 4	-1	-1	-1	4	-1
Point 5	-1	-1	-1	-1	4

The elements of $\bar{\mathbf{C}}$ can be interpreted as follows:

$\bar{C}_{ii}$= Degree of vertex i,

$\bar{C}_{ij}$= -1 if there is a connection between i and j,

$\bar{C}_{ij}$= 0, if there is no connection between i and j.

Note that the degree of a vertex signifies the amount of edges that is incident to it. In order to identify all potential congruent point groups within the network, distances are computed in all combinations for both epochs. After analysis of distance deviations only valid distances are assembled in incidence matrix **C**.

Subsequently the adjacency matrix $\bar{\mathbf{C}}$ is calculated where the identification of congruent point sets is conducted as follows:

1. Find the maximum element of $\bar{\mathbf{C}}$ on the diagonal matrix so that $\bar{C}_{ii} = max$.
2. Determine the amount n of vertices in $\bar{\mathbf{C}}$ whose degree is $\bar{C}_{ii} \geq max$. The existence of $n \geq max + 1$ suggests that point groups with $max + 1$ elements may be present.
3. If the amount of detected points n is equal to $max + 1$ it has to be tested if valid connections are existent between all according points. If this is the case this group can be seen as a candidate for a potential congruent point set.
4. If $n > max + 1$ combinations between all detected points have been found it has to be clarified if acceptable distance deviations between epochs are present. If this is the case then valid edges between according vertices are existent. Point sets for which all edges are present are candidates for congruent point sets.
5. Candidates which may represent a congruent point group are tested by using a global test (Niemeier 2008, pp. 167) which can only be conducted for discrete measurements under the assumption that a valid functional and stochastic model is given. The formulation of a hypothesis is carried out by usage of datum-invariant elements (distances). If a stable group has been detected according rows and columns need to be deleted from $\bar{\mathbf{C}}$ assuming that different congruent sets do not share common points. Subsequently the quest can be continued by restarting at the first step.
6. If no congruent set of points has been identified the procedure is started at step 2 with $max = max - 1$.

4.5.1.6 Exemplification of the procedure

In order to demonstrate functionality and performance of the MSS a simple example will be processed featuring the dataset of figure 4.10. At first computation of distances between points in every epoch has to be carried out in all combinations while differences between according distances will arise. Assessment of acceptable deviations is conducted by using the signal-to-noise-ratio as introduced in 4.5.1.4. The according test statistics are listed in arranged order in table 4.5 while the network graph is depicted in figure 4.11. Accepted deviations are characterised by grey lines.

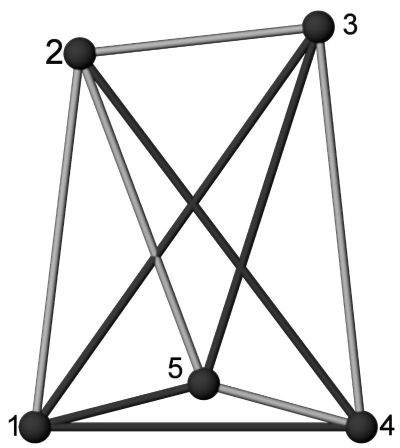

Figure 4.11: *Network from figure 4.10 where accepted deviations are highlighted by dark grey lines*

Table 4.5: *Test statistic q for all distances of the network*

i	Test statistic
1	$q_{dl_{2,5}} = 6.8$
2	$q_{dl_{1,2}} = 5.9$
3	$q_{dl_{2,3}} = 5.5$
4	$q_{dl_{4,5}} = 5.4$
5	$q_{dl_{3,4}} = 5.2$
6	$q_{dl_{1,4}} = 1.7$
7	$q_{dl_{3,5}} = 1.3$
8	$q_{dl_{1,3}} = 1.1$
9	$q_{dl_{2,4}} = 0.9$
10	$q_{dl_{1,5}} = 0.4$

As the first five values lie above a threshold of $q > 5$ the search for the maximum size of a stable point set is narrowed down from line 6 to 10. Only these values are added to the incidence matrix $\mathbf{C}$ as depicted in table 4.6. The according adjacency matrix $\bar{\mathbf{C}}$ is illustrated in table 4.7.

Table 4.6: *Incidence matrix $\boldsymbol{C}$ that contains only accepted distances*

	Pt. 1	Pt. 2	Pt. 3	Pt. 4	Pt. 5
$s_{1,3}$	1	0	-1	0	0
$s_{1,4}$	1	0	0	-1	0
$s_{1,5}$	1	0	0	0	-1
$s_{2,4}$	0	1	0	-1	0
$s_{3,5}$	0	0	1	0	-1

Table 4.7: *Adjacency matrix $\bar{\mathbf{C}}$ of the network*

	Pt. 1	Pt. 2	Pt. 3	Pt. 4	Pt. 5
Pt. 1	3	0	-1	-1	-1
Pt. 2	0	1	0	-1	0
Pt. 3	-1	0	2	0	-1
Pt. 4	-1	-1	0	2	0
Pt. 5	-1	0	-1	0	2

Localising potentially congruent point groups based on the adjacency matrix $\bar{\mathbf{C}}$ is conducted for this example as follows:

- The largest element on the main diagonal is $\bar{C}_{11} = max = 3$ which leads to the conclusion that a quadrangle may be existent as three edges converge in every corner point.
- As n=1 which means that only one element is equal to $\bar{C}_{ii} = max$ no quadrangle can be present.
- Set $max = max - 1 = 2$.
- As $n = 4$ elements are existing that hold for $\bar{C}_{ii} \geq max$ several triangles may be present.
- Based on the detected points 1, 3, 4 and 5 the following triangles can be arranged: 1/3/4, 1/3/5, 1/4/5, 3/4/5. Finally an assessment has to be carried out in order to clarify if a triangle is present that possesses all connections which equates in analysing the adjacency matrix from table 4.7.

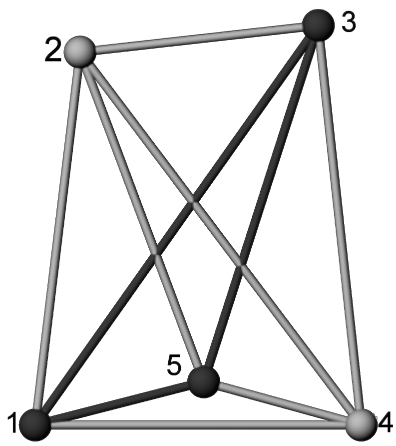

Figure 4.12: *Maximum subsample of the given network.*

Table 4.8: *Adjacency matrices in all combinations based on valid vertices*

	Pt. 1	Pt. 3	Pt. 4
Pt. 1	3	-1	-1
Pt. 3	-1	2	0
Pt. 4	-1	0	2

	Pt. 1	Pt. 3	Pt. 5
Pt. 1	3	-1	-1
Pt. 3	-1	2	-1
Pt. 5	-1	-1	2

	Pt. 1	Pt. 4	Pt. 5
Pt. 1	3	-1	-1
Pt. 4	-1	2	0
Pt. 5	-1	0	2

	Pt. 3	Pt. 4	Pt. 5
Pt. 3	2	0	-1
Pt. 4	0	2	0
Pt. 5	-1	0	2

As adjacency matrix $\bar{\mathbf{C}}$ is symmetrical, elements above the main diagonal can be used to clarify whether all connections between vertices are present. This is only the case for the depicted triangle in figure 4.12 which is assembled by points 1, 3, and 5, as highlighted by green elements in table 4.8, so that a congruent set may be present. This hypothesis can be tested by applying a global test that contains only these points. In the present example it is assumed that the null-hypothesis of congruency can be accepted.

If one tries to analyse if other congruent sets are detectable the according rows and columns of points 1, 3 and 5 need to be deleted from the original adjacency matrix $\bar{\mathbf{C}}$. Then the procedure as described above needs to be conducted repeatedly.

The required computational effort by combinatorial means can be calculated in analogy to equation (4.1)

$$K = \sum_{c}^{n} \binom{n}{n-c} = \sum_{c}^{n} \frac{n!}{(n-c)!c!} \tag{4.4}$$

where c depicts the size of the largest congruent set and n the amount of points within the network. A look at the given example in order to reveal the maximum subsample shows that

$$K = \binom{5}{5} + \binom{5}{4} + \binom{5}{3} = 16$$

adjustments would have to be computed. On the other hand a very effective approach in terms of computational effort has been proposed based on compilation and analysis of topological matrices where only one adjustment needs to be conducted in order to inspect the identified subset. The proposed techniques for preliminary inspection drastically reduce computing time which allows applying combinatorial search in larger networks. Furthermore it has to be mentioned that compilation of topological matrices and the search of potential point sets can be easily implemented and integrated into existing software.

4.5.2 The ICProx-algorithm

As spans between transformed focal points are used in this approach as distinctive measures the question arises how meaningful and objective decision variables can be derived. Since laser scanners discretise extensive areas in a way that previously surveyed points will usually not be acquired within a consecutive scan – as illustrated in figure 2.2 - new methods need to be introduced that consider not only the precision of measurements but also the variation of the data acquisition process itself. A summary of this problem is stated within the **g**uide to the expression of **u**ncertainty of **m**easurement (GUM) which has been published by the international organisation for standardisation (ISO 2008). A problem that arises due to the quasi-laminar acquisition method of TLS within the context of point cloud registration is the dependence of residuals to the local point resolution. An algorithm that is particularly error-prone to the local point density is the ICP (Besl & McKay, 1992) since point to point correspondences are established. This issue is tackled by introducing point surface relations as presented by Chen & Medioni (1991) which is also applied within the registration algorithm in this section. The remaining downside of applying the previously mentioned correspondences is that discretisation errors may lead to classification as outliers. Since correspondences between surfaces and points are valid as long as a point can be projected to the introduced surface a new approach that models the uncertainty of the data acquisition process respectively the matching procedure rather than applying the theoretical single point precision has been developed named the iterative closest proximity algorithm (ICProx). The ICProx uses the triangulated reference epoch as an input and is assembled of three stages:

1. Uniform sampling of candidates in the reference epoch for determination of local transformation parameters within all octree cells,
2. Determination of direct neighbours where a corresponding point can be located in relation to a candidate,
3. Derivation of uncertainty measures for each octree cell based on so called virtual transformations.

The procedure is demonstrated on example of a single octree cell in the following as illustrated in figure 4.13. Note that the point cloud within the octree cell has been triangulated only for illustrative purposes as depicted in the figures below.

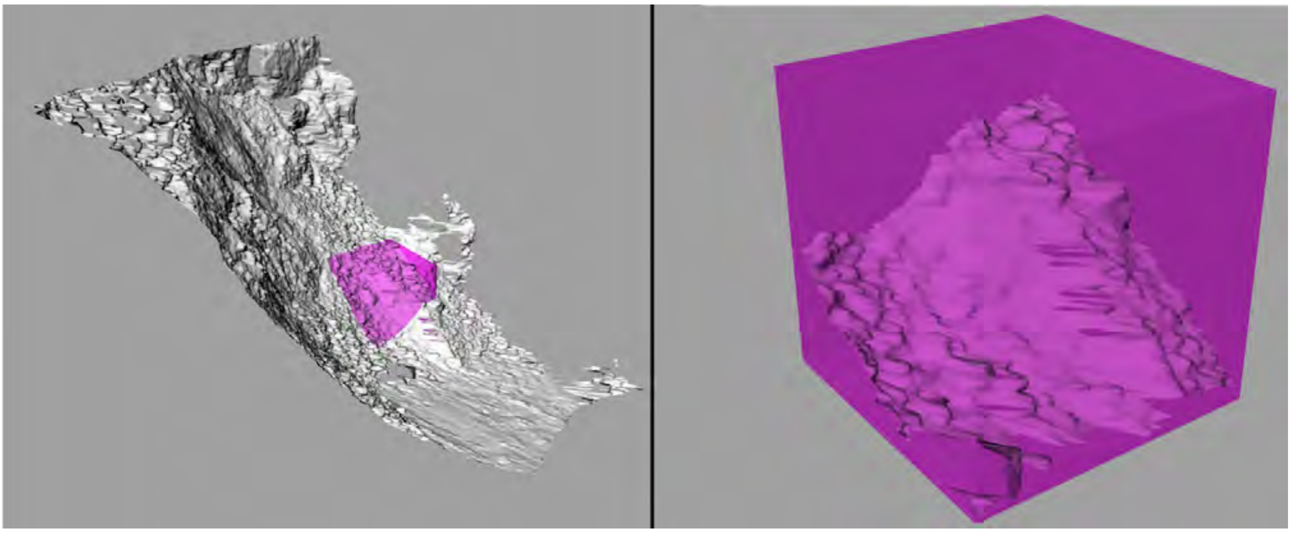

Figure 4.13: *Triangulated reference epoch (left) and single octree cell (right)*

As a first step candidates (yellow spheres in the following figure) are selected from the reference epoch so that the distances amongst them are somewhat equally as discussed under subsection 4.2 and depicted in the left part of figure 4.14. This procedure corresponds to stage 1 from the above mentioned list. Subsequently direct neighbours to all candidates need to be detected (stage 2) as illustrated by the red rectangle on the left respectively the green area in the centre part of the figure. After determination of direct neighbours the area needs to be computed in which a corresponding point can be located after a second scan has been acquired. In order to achieve this median lines between a candidate and all direct neighbours are computed and connected from which the dark green area results as illustrated on the right of figure 4.14 – the habitat. Note that this practice coincides with Voronoi diagrams which have been proposed by Dirichlet (1850) for the two- and three dimensional case and later on Voronoi (1908) who extended it to the n-dimensional case. An extensive presentation on the subject was made by Lindenbergh (2002).

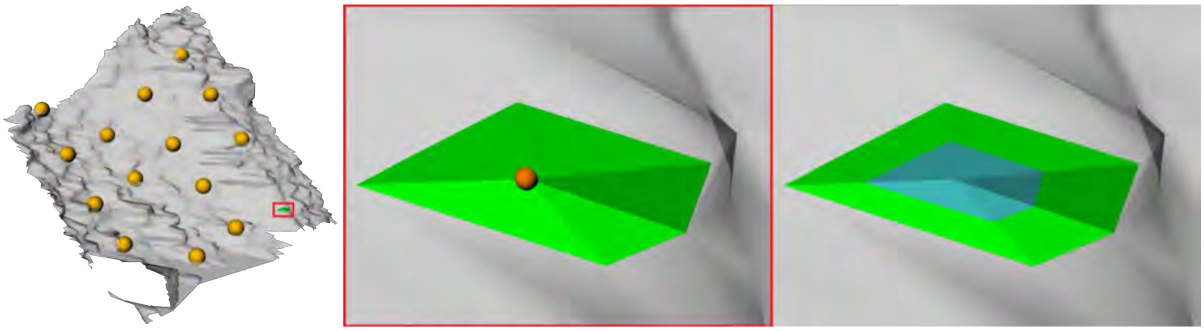

Figure 4.14: *Uniform sampling of candidates (left), area described by direct neighbours to a candidate (middle) and habitat (right)*

In the third and last step of the ICProx a series of n virtual transformations is computed based on different random combinations between candidates (yellow spheres in figure 4.15) and potential correspondences (pink spheres) that are located within the habitat (dark green region). Note that the term virtual has been used in this context due to the fact that the resulting transformation parameters are not applied to the datasets but strictly to derive uncertainty measures. For the computation of uncertainty measures the edges of the habitat are applied.

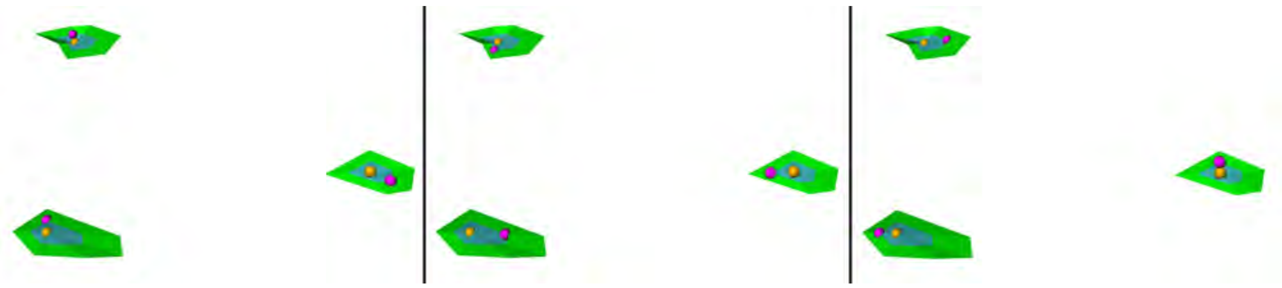

Figure 4.15: *Visualisation of three different combinations between candidates (yellow spheres) and corresponding points (pink spheres)*

As an outcome n different sets of transformation parameters result based on which uncertainty measures can be derived. In order to achieve this, the centroid of all candidates within an octree cell (yellow spheres in the left part of figure 4.16) is computed that is represented by the green sphere. By application of the previously computed n sets of transformation parameters ($n = 5$ in this example) the centroid is transformed into slightly different locations as illustrated by the red spheres in the middle part of the figure. The pink translucent box in the centre and right part of the figure depict the octree cell to which the uncertainty measures are assigned.

Finally a centroid C_i (large cyan sphere in the right part of the figure) of all transformed centroids is computed within a least squares adjustment. Apart from the location of this resulting centroid corresponding stochastic parameters σ_{C_i} arise from the adjustment. These parameters now reflect the uncertainty of the measurements and the applied matching process namely the ICP. Hence the ICProx also considers local geometric characteristics within each octree cell whose uncertainty will be applied for identification of congruency between cells as described under section 4.5.1.

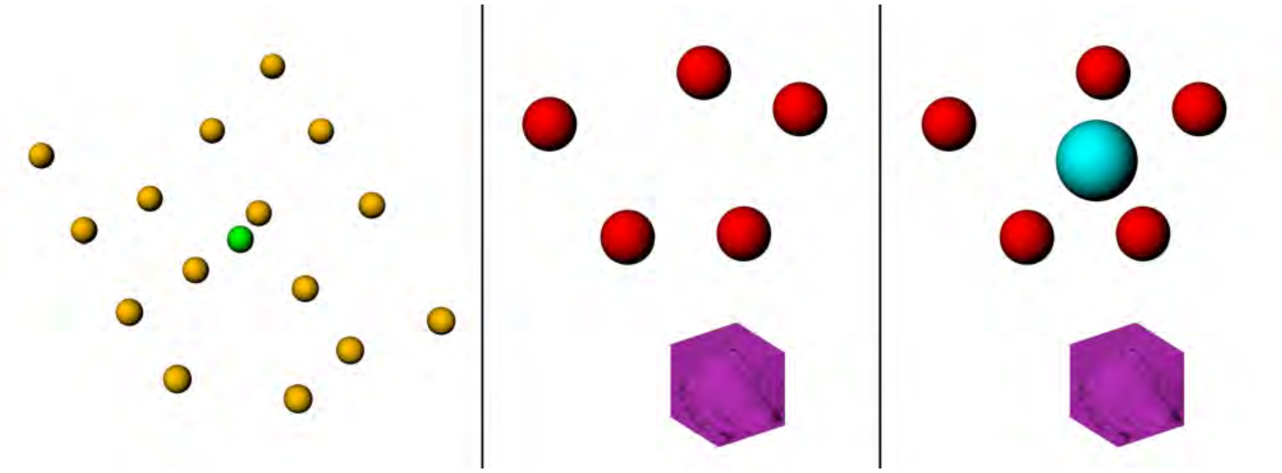

Figure 4.16: *Candidates within an octree cell (yellow spheres) and their centroid (green sphere) are depicted on the left. Application of n sets of transformation parameters (five in this example) leads to the red spheres (middle). As a final step the centroid of n transformed centroid points leads is adjusted (large cyan sphere on the right).*

Eventually all required information for congruence analysis, as discussed in subsection 4.5.1, is available namely centroids C and their stochastic measures σ_C derived by the ICProx-algorithm. Variance-covariance propagation has to be conducted in order to assign stochastic values to all compared distances Δ_{dist} between centroids referred to as $\sigma_{\Delta dist}$ in the equation below. By usage of the 3σ rule statistically significant differences between spans Δ_{dist} are detected. The applied test statistic is computed by

$$T = \frac{|\overline{C_b D_b} - \overline{C_a D_a}|}{\sigma_{\Delta dist}} = \frac{|\Delta_{dist}|}{\sigma_{\Delta dist}} \tag{4.5}$$

where C_b depicts the centroid of an octree cell before and C_a the centroid after application of transformation parameters while D_a and D_b describe the same for another octree cell. Hence the enumerator of equation (4.5) describes the comparable value that has been introduced before as well as in subsection 4.3. The null hypothesis follows

$$H_0: \quad T \leq 3 \tag{4.6}$$

and hence assumes that no deformation will be detected. The alternative hypothesis supposes

$$H_A: \quad T > 3 \tag{4.7}$$

By introduction of this procedure all required components for the identification of stable areas respectively deformation are given, that includes:

1. Comparable values: Comparison of spans between transformed focal points as presented in subsection 4.3.
2. Identification of congruent clusters: The maximum subsample method which has been presented in subsection 4.5.1.
3. Thresholds respectively stochastic measures: The ICProx-algorithm that was subject of this section.

Please note that the entire proposed algorithm will be named ICProx-algorithm in the following according to its key component.

4.5.3 Fully automatic deformation monitoring

In order to simulate deformation monitoring where two epochs have been captured from different positions the coordinate system of the successive epoch has been altered in a way that no overlap between the datasets was present. For coarse registration of the two scans (see section 4.1 for details) the 4PCS-algorithm has been applied that despite the existing deformation provided a sufficient pre-alignment. Subsequently the ICProx-algorithm has been applied in order to carry out fine matching while deformation monitoring may be the final procedure. The software has been set to decompose the point clouds into 2.5 m large octree cells while ten candidates should be sampled per cell on average. As a result 80 octree cells emerged from which only 28 have been used within the actual analysis. The reason for this at glance peculiar circumstance can be found in the relative orientation between object of interest and octree cells. Many cells were located on the outer boundaries of the scenario and did not feature enough candidates which is why they have been removed from processing. From the remaining 28 cells 378 distance combinations between octree cells have been established. For identification of deformation spans between difference vectors before and after application of locally derived transformation parameters within octree cells have been applied. The uncertainty for each cell has been derived by usage of the ICProx-algorithm. After testing of all distances 39% of them have been accepted that were assigned to 27 cells. It should be pointed out that the 3σ-rule is only used in this context to eliminate "impossible" combinations which hence reduces the computational effort. As a final step of the procedure the MSS-method identified 48% of these cells as the largest congruent subsample. The largest subsample is depicted by blue colour in the left part of figure 4.17. As a final step ICP matching is conducted solely based on stable areas as a whole after that the final outcome of deformation monitoring, a colour coded inspection map (unit is metres) as illustrated in the right half of the figure, can be generated. A closer look reveals that areas that were subject of deformation have been omitted from clustering. A detailed analysis of the algorithm's outcome will be given in subsection 4.5.5.

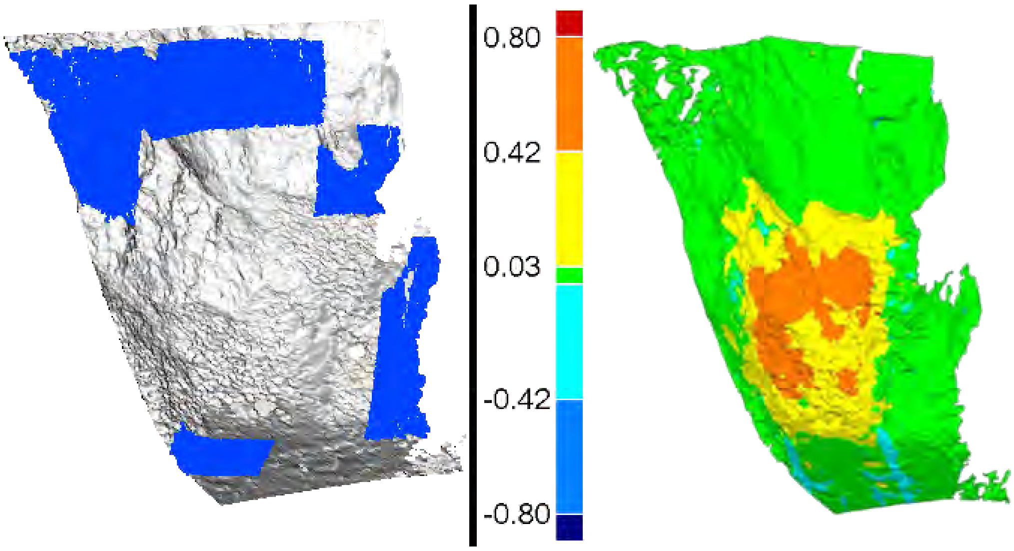

Figure 4.17: *Outcome of the ICProx (left) where stable areas are highlighted in blue. In comparison to the resulting inspection map (right; unit is metres) it can be seen that no areas where deformation occurred have been assigned to the cluster.*

In order to objectively assess the achieved result fine matching by use of a standard ICP has been carried out after coarse matching with the 4PCS-algorithm based on the entire dataset for comparative reasons. The transformed and previously modified successive epoch has been compared with itself in its original position by generating an inspection map. Hence the result describes how close a registration procedure can come to a known solution. The outcome for the standard ICP without rejection of deformation sums up to 10.3 mm on average for points that are located above the reference surface (triangulated successive epoch in its original coordinate system) and 12.9 mm for the respective points below. The standard deviation of residuals between target and actual outcome amounts to 20.3 mm. The according values for the ICProx are 3.2 mm (above the reference) and 3.9 mm (below) with a standard deviation of residuals of 4.0 mm.

4.5.4 Dealing with complexity – the combinatory wall

As already mentioned in subsection 4.5.1.2 and mathematically described by equation (4.1) it is obvious that the applied combinatory approach for the sake of congruence analysis rapidly leads to problems with an increasing number of octree cells. Figure 4.18 depicts two critical aspects of combinatorial strategies for identification of congruent groups. A set of ten points is assumed from which a group on n congruent points should be identified. It can notably be seen in the left part of the figure that a maximum of 252 combinations (represented by the vertical axis) need to be computed in order to assemble point groups (depicted by the horizontal axis) of $n/2$. Thus a series of point groups whose sizes are increasing has been simulated from which combinations of $n/2$ need to be identified. The outcome can be found in the right half of the figure where the size of the sets is described by the horizontal axis. The vertical axis – which features a logarithmic scale, shows the required amount of combinations that result. It is obvious that the required computational effort is rapidly increasing and hence not feasible. Consequently a method is described in this subsection that breaks down the complexity of the given problem into solvable pieces in order to determine a solution at an arguable amount of time.

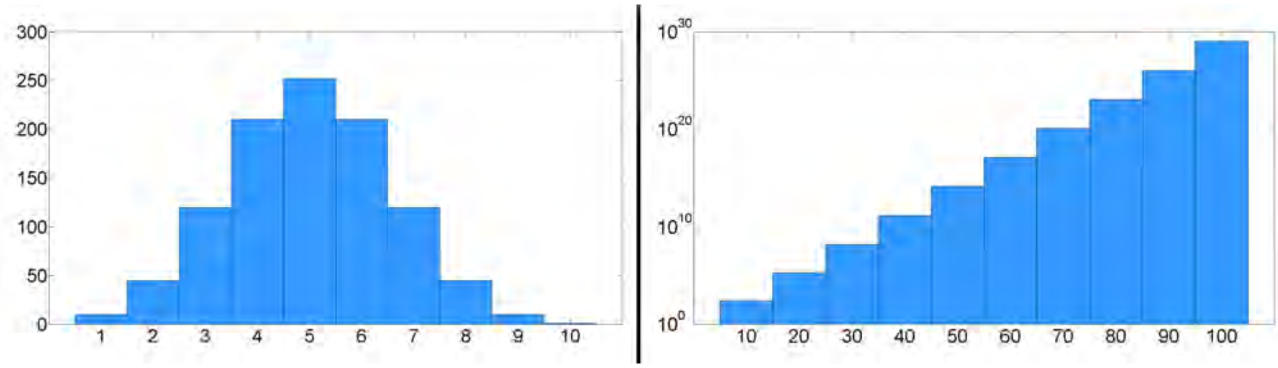

Figure 4.18: *The left part of the figure depicts the number of calculations (vertical axis) that are required to identify groups of n points (horizontal axis). The right part features different sizes of point sets on the horizontal axis while the required number of calculations can be seen on the vertical axis. Note that a logarithmic scale has been applied for the last mentioned axis.*

The chosen strategy decomposes the entire problem into manageable portions, 20 in our case, so that the maximum number of calculations is restricted. Assuming a point group of size $n = 20$ and a congruent set of 10 points which has to be identified then no more than 184,756 computation per portion are required according to equation (4.4). Note that the size of 20 cells per portion has been empirically defined as it revealed to be a good trade-off between acceptable run-time and meaningful set size for congruence analysis. In order to increase the probability of identifying preferably large congruent sets respectively to achieve similarity the octree cells are sorted according to their according lengths of transformation vectors. For each one of these groups, highlighted by red squares in figure 4.19, which are referred to as packages in the following the MSS-procedure is applied. The resulting maximum subsample is called congruent group and is depicted by yellow squares. The number within the square states by how many octree cells the maximum subsample is assembled. Subsequently new local transformation parameters are generated by means of ICP for which the content of all respective congruent groups is used. A problem that arises within this context is that the derived stochastic measures of all congruent groups are hardly comparable to each other as they are influenced by the spatial distribution of congruent octree cells in space. Hence the median or maximum uncertainty of a congruent group member is assigned to the whole group. As soon as the number of congruent groups falls below 20 a final run of the MSS is applied which yields to the desired result as illustrated by the green square. The numbers within the square indicate that the biggest congruent set consists of three groups which in total contain 30 octree cells (7, 11 and 12). The subsample denoted with a red flash consisting of five cells was not congruent to the other ones and hence was rejected. After determination of the largest congruent set the ICP is carried out where the content of all assigned octree cells is applied. In contrast to the local, cell-wise application during identification of stable areas the cells are now used as a whole. As a result a set of transformation parameters arises that is not falsified by deformed regions and hence allows conducting deformation monitoring.

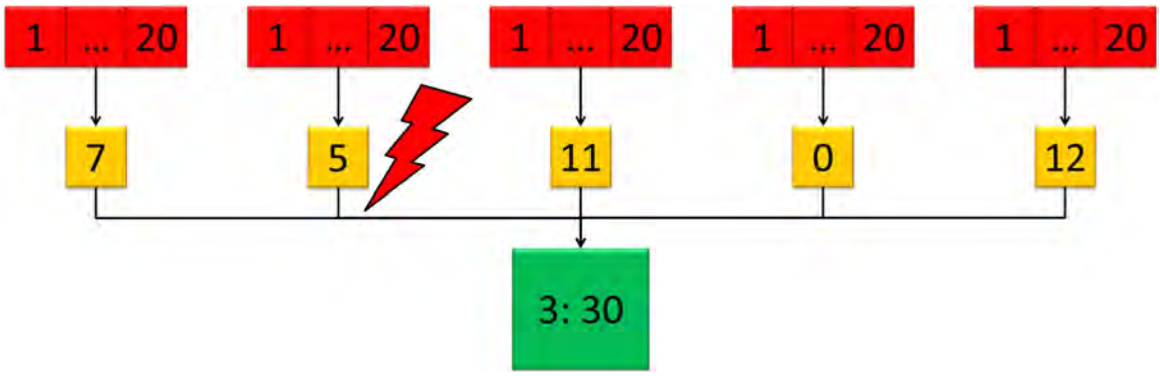

Figure 4.19: *Schematic visualisation of the procedure for a dataset with 100 octree cells that (depicted by red squares). At first the MSS is conducted for packages of 20 cells each, while the segments that describe the respective maximum subsample are merged into one group (yellow squares). The number within each square describes the size of the maximum subsample of each group.*

4.5.5 Impact of cell size, number of virtual transformations and degree of contamination

In order to analyse potential influences caused by tunable parameters and to demonstrate the robustness against deformed regions of the ICProx several tests have been conducted. At first the influence of varying octree cell sizes was of interest. Therefore three different settings have been processed where all datasets were already coarsely registered.

Figure 4.20 a) shows an inspection map where stable regions are coloured in green whereas deformed parts are tinted by yellow tones. The first test of the series has been conducted with an octree cell size of 2 m which led to 68 octree cells of which 53% have been declared as stable by the ICProx-algorithm as depicted in figure 4.20 b). A reduction of the cell size to 1 m leads to 232 cells from which 70% are considered stable as illustrated in figure 4.20 c). By processing the point clouds with octree cell sizes of 0.5 m 843 segments arise of which 67% have been assigned as being stable as shown in figure 4.20 d). Due to the fact that the identification of stable areas is a classification problem all potential cases have been colour coded in figure 4.20 b) to d) according to the following scheme:

- Blue: Area is stable, detected as stable (true positive).
- Cyan: Area is stable, detected as unstable (false negative).
- Red: Area is unstable, detected as stable (false positive).
- Orange: Area is unstable, detected as unstable (true negative).

In general the outcome has to be rated as satisfactory as the majority of regions in all cases has been classified correctly as highlighted by orange and blue tones. A comparative look at results b) to d) reveals that a smaller octree size leads to a higher degree of adaption to a stable region. On the other hand the likelihood increases that the geometric contrast within a cell may not be sufficient as seen in figure 4.20 d) where small cyan patches are notable within the stable region.

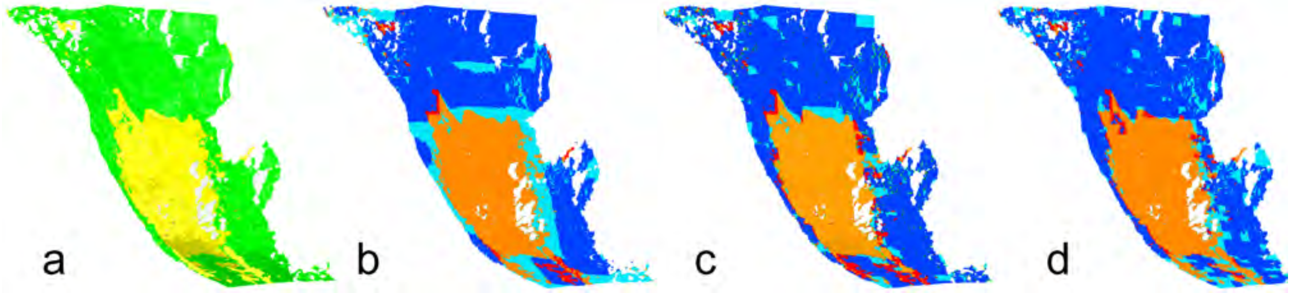

Figure 4.20: *An inspection map is illustrated for comparative reasons where stable regions are depicted by green while deformed areas are highlighted by yellow shades (a). Areas superimposed in blue indicate areas within the scene that have been declared stable by the ICProx-algorithm. The remaining figures have been processed with different octree segment sizes namely 2 m, 1 m and 0.5 m (b - d).*

In theory the perfect outcome of an algorithm for classification of stable and deformed regions should colourise the dataset exclusively in blue and orange. As this is not possible for the chosen strategy due to the decomposition of the object space via octree cells falsely assigned regions emerge as a consequence. Cyan regions – areas that are stable yet have been detected as unstable - are unfavourable as valid information remains unused. However, it has no falsifying effect onto the registration process such as the remaining case where deformed regions have been classified as stable which is highlighted by red tones. Table 4.9 gathers the according confusion matrices for the scenarios that are depicted in Figure 4.20 b - d. A comparison of the matrices reveals the most unfavourable result in the centre part of the table where 5% of all points have been falsely assigned as being stable. The outcome with the biggest loss of potential can be found on the outer left of the table where 21% of all points have been incorrectly interpreted as being subject of deformation. It should be mentioned that the listed confusion matrices only allow drawing conclusions concerning the achieved segmentation quality but not about the according influence onto the transformation parameters which depends on the geometrical degree of deformation.

Table 4.9: *Confusion matrices for the datasets from figure 4.20 b (left), figure 4.20 c (centre) and figure 4.20 d (right)*

56%	21%		60%	8%		57%	12%
2%	21%		5%	27%		2%	29%

Since the ICProx-algorithm has been developed to generate stochastic measures it is of importance to quantify potential influences that are caused by the number of virtual transformation between candidates and potential correspondences. Therefore the same dataset as mentioned above has been registered by three different settings including an octree size of 0.5 m as well as 5, 10 and 15 virtual transformations. A bar graph that displays the average spatial uncertainty as well as the according components which have been computed based on 843 octree cells can be found on the left of figure 4.21. Interestingly the number of virtual transformations doesn't appear to have a great impact onto the outcome at first glance which is also supported by the same according standard deviations that sum up to 6.9 mm, 7.5 mm and 7.2 mm. The right part of figure 4.21 illustrates colour coded spatial variances of all octree centroids for a dataset with 63 cells. It can be seen that a few notably larger uncertainties are present as indicated by e.g. the red sphere at the right bottom of the scene. The reason for this is caused by a comparatively low spatial resolution within these cells. As a consequence such octree segments are more "tolerant" against deformation which in consequence may lead to wrong segmentation results during congruence analysis.

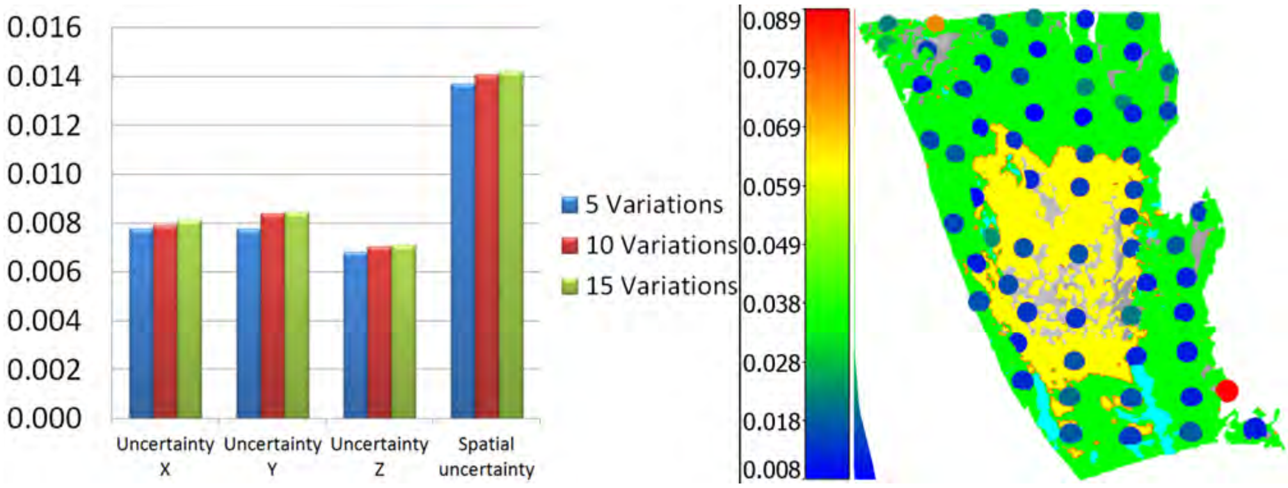

Figure 4.21: *Comparison of spatial uncertainty (left) and colour coded visualisation of spatial uncertainty (right). Note that the unit of all figures is metres*

The major motivation for this contribution was the aim to develop a potentially robust matching algorithm that is capable to process even highly contaminated datasets respectively scenes that were subject of significant geometric change. In order to simulate this effect stable parts of a successive epoch have been removed so that unfavourable ratios between unchanged and altered parts resulted. The according ratios are gathered in the third column from the left of table 4.10 and are referred to scenario A and B in the following as gathered in the outer left column. The second column from the left contains the area of all scenarios while the column right next to it contains the degree of contamination. The surface of scenario B for instance contains 65% of deformation so that only 35% of stable parts can be used for registration at best. For all scenarios the same coarse alignment has been used as computed by the 4PCS-algorithm based on the original dataset. The tunable parameters have been set to an octree size of 0.5 m, candidates were sampled in a 10 cm grid while ten virtual transformations were computed. After application of the ICProx-algorithm a registration has been conducted by using only the detected stable regions. The according average residuals after registration can be found in the second right column while the corresponding standard deviations are listed in the outer right column. It should be mentioned that for the last scenario the theoretical boundaries of robust estimators must be conquered or in other words: even the use of such estimators could not overcome the erroneous influence of deformation.

Table 4.10: *Used scenarios for robustness analysis*

Scenario	Area [m^2]	Stable portion [%]	Average residuals [mm]
A	167.47	56	8.0
B	114.82	35	8.5

The left part of figure 4.22 illustrates the scenarios for the test which have been compared to the reference epoch that is not depicted. It can notably be seen that the stable area has been reduced ranging from the original scenario (coloured in light grey), that has been previously used as depicted in figure 4.20, over scenario A in purple to scenario B in green. After classification of all scenarios with the ICProx-algorithm figures have been generated according to the colour scheme of figure 4.20 that assesses the outcome. A look at the centre of figure 4.22 reveals that the majority of stable respectively deformed regions have been assigned correctly. In total the algorithm classified 75% amongst 424 octree cells as being stable. However it can be seen that some cells located around the area of withdrawal were falsely assigned as highlighted by red colour. The reason for that may be caused by the fact that no or only a few candidates have been sampled in the transition between deformed and stable regions so that they haven't been uncovered. The outcome for scenario B as illustrated on the right of figure 4.22 features a narrow band of stable regions that has been detected despite the fact that extremely unfavourable and highly contaminated data has been processed. From a total number of 223 octree cells 36% were detected as stable. It can be seen that a significant amount of stable parts hasn't been correctly classified as highlighted by cyan. Apart from this very few red parts can be spotted that have been falsely classified as being stable.

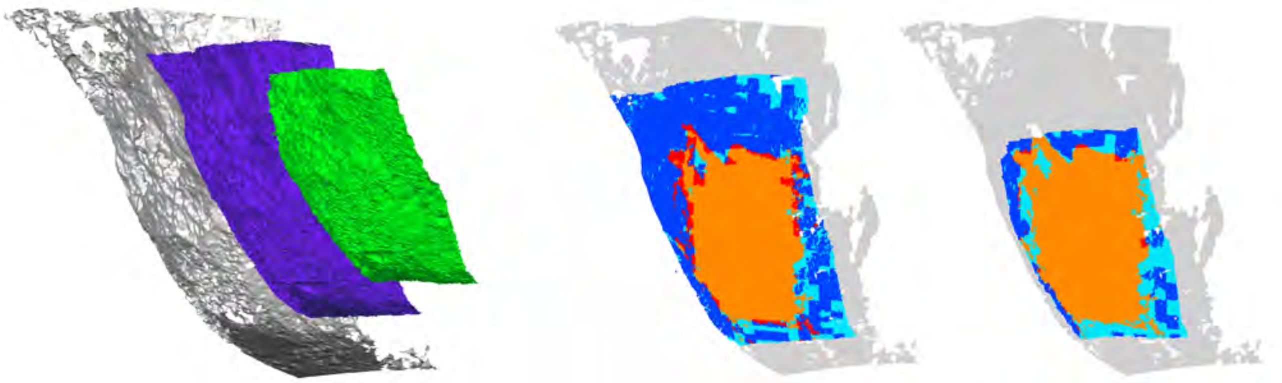

Figure 4.22: *Input scenarios for the robustness analysis (left). Colour coded confusion maps of processed scenarios A (centre) and B (right)*

Table 4.11 illustrates the according confusion matrices for the aforementioned scenarios. Scenario A features 5% of deformed regions which have been assigned as being stable while the outcome for the second case has to be rated as favourable as it only sums up to 1%. The compliance of detected deformation to the actual amount sums up to 89% for scenario A respectively 99% for scenario B. Finally it can be stated that the outcome has to be rated quite positive even though up to 20% of the dataset was falsely segmented.

Table 4.11: *Confusion matrices for scenario A (left) and scenario B (right)*

44%	12%
5%	39%

16%	19%
1%	64%

In order to compare the outcome between a standard ICP implementation and the ICProx-algorithm three inspection maps have been generated based on scenario B. For comparative purposes one inspection map served as a reference, depicted on the left of figure 4.23, where both datasets were acquired from one view point. In case of the ICP the altered successive epoch has been registered against the reference epoch. The according results are illustrated in the centre of figure 4.23. For the ICProx-algorithm only stable regions were used for matching, as illustrated on the right in figure 4.22, while the resulting transformation parameters have been applied to the complete and unaltered datasets. The outcome is depicted on the right of figure 4.23.

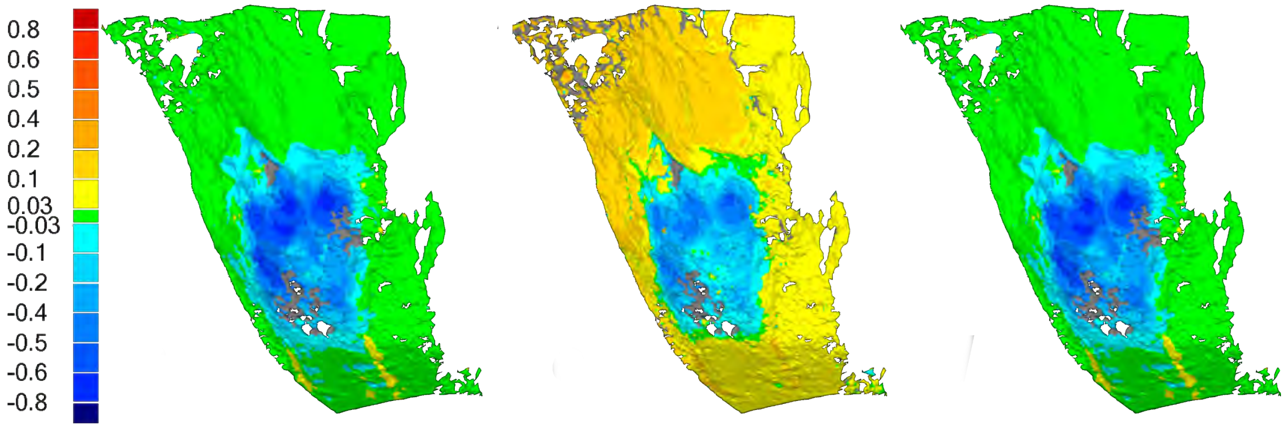

Figure 4.23: *Inspection map of the reference (left), after matching with a standard ICP (centre) respectively the ICProx-algorithm (right)*

A comparative look between left and centre of figure 4.23 immediately reveals large differences in the inspection maps so that very different conclusions must be drawn during analysis of the deformation pattern. The area of withdrawal has been roughly detected however differences in magnitude are notable. In addition it appears that the majority of the quarry was subject of filling. An explanation for this effect can be related to the method of least squares which has minimised the residuals between the datasets. As in between epochs material has been removed a notable shift of the successive epoch resulted.

As a visual comparison between reference and outcome of the ICProx depicted in left and right part of figure 4.23 is not feasible due to the similarity among themselves a numerical summary of all results can be found in table 4.12. The sign indicates whether points were located above or below the reference surface. A look at the middle column which gathers mean residuals between the epochs shows that the results generated by the ICProx are nearly in accordance to the reference values while the largest discrepancy of 15 mm can be related to the registration process itself. Similar conclusions can be drawn for the outer right column that contains the according standard deviations.

Table 4.12: *Statistical comparison of inspection maps*

Scenario | Algorithm	Average residuals [mm]	Standard deviation [mm]
Reference	+20 / -138	176
A | ICProx	+20 / -150	176
B | ICProx	+18 / -153	176

4.6 Results and discussion

Two novel diagnostic algorithms were subject of this section where different strategies for identification of deformation have been implemented. Both approaches share the idea of segmenting the object space by usage of octrees. By doing this a local amplification of geometric changes is achieved which eases identification of deformed regions that occurred in between successive epochs. The DefoScan++-algorithm uses correspondences between point clouds that have been computed by local application of the ICP within all octree cells as an input. As a result corresponding points arise while distances amongst them are compared in order to reveal deformed areas. For the last mentioned step a sequential procedure is used which has to be seen as a drawback as it involves the danger of interpreting deformed regions as stable. However for the tested dataset no cells were falsely segmented. Another downside is the enormous computational effort that is required.

In order to tackle the above mentioned problems two modifications have been introduced which resulted in the ICProx-algorithm. The first major improvement is that only one comparable measure is assigned to each cell while the second one focuses on congruency analysis which is conducted in a combinatorial fashion. First experimental results showed that the ICProx is capable to produce results of higher local resolution / smaller octree size in comparison to the DefoScan++-algorithm allowing it to detect a higher degree of stable areas for the final computation of transformation parameters. Additional tests analysed the influence of tunable parameters while surprisingly only one namely the octree size had a notable impact. Studies concerning the robustness of the approach against deformation showed that correct results can be achieved even if more than half of a scene was subject to geometrical change. In order to complete a fully automatic work flow for deformation monitoring without the necessity of using additional sensors as discussed under subsection 2.3.1.2, a robust coarse alignment algorithm has to be implemented. The reason for this necessity is caused by the exact same problem as in fine matching: existing deformation in between epochs falsifies the desired outcome especially in case of highly contaminated data.

5 On TLS based geodetic deformation monitoring

As previously discussed terrestrial laser scanning (TLS) can be seen as an established acquisition method for deformation monitoring of extensive surfaces. Based on captured data of at least two epochs registration needs to be carried out at first in order to define a common coordinate frame. Subsequently a so called inspection map can be generated that visualises deviations by colour coding distances between reference epoch and the successively captured epoch. Colour coding and hence the outcome can be influenced by setting certain margins that specify an “acceptable” deviation respectively the largest positive and negative deformation. This procedure is highly subjective since it is not known how large the “acceptable” deviation needs to be set in dependence to the applied instrument. Furthermore it is assumed that all points share the same theoretical accuracy, a fact that is well known not to be the case as demonstrated in section 3.1. In summary it can be established that an essential problem hasn’t been addressed up until now neither by commercial or scientific solutions namely: Has a deformation been significantly detected? In order to solve this issue a stochastic model has been developed for an applied Leica C10 TLS that is covering ranges as far as 120 m. This information is consequently used throughout a method which detects significant deformation by conducting variance-covariance propagation and statistical tests. The procedure is exemplified on the test case of section 4.1. A novel method for TLS based deformation monitoring is proposed in section 5.1.1 while its application on a practical dataset is shown under section 5.1.2. The content of this section complies to step 4 of the deformation monitoring processing chain. A novel method for visualisation of deformations on arbitrary surfaces is subject of section 5.2 and has already been published in Wujanz *et al.* (2011).

5.1 A rigorous method for C2M-deformation monitoring based on variance-covariance propagation

As the process chain of deformation monitoring via cloud-to-mesh (C2M) will be described in detail under section 5.1.1 a schematic description shall be given before:

1. Triangulation of the reference epoch **A**: Convert point cloud of **A** to mesh.
2. Assign points of the next epoch **B** to single triangles of **A**.
3. Compute distances from corresponding points to according triangles.
4. Visualisation: “Which distances are acceptable?”

The proposed methodology is a modified version of the previous procedure and contains the following steps:

1. Triangulation of the reference epoch **A**: Convert point cloud of **A** to mesh.
2. Assign points of the next epoch **B** to single triangles of **A**. In case that a point can be assigned to multiple triangles a correspondence to the closest one is established.
3. Compute distances from corresponding points to according triangles.
4. Conduct variance-covariance propagation in order to receive stochastic parameters for all distances.
5. Visualisation: “Which distances are of statistical significance?”

5.1.1 Schematic description of the proposed method

This section describes the mathematical relationships and procedures that need to be carried out in order to receive stochastic information for distances between points and associated planes according to the C2M-procedure. Let PC_0 and PC_1 be point clouds that contain spatial Cartesian coordinates within the instrument’s coordinate system while the following variables are used in the latter:

1. φ_{1-3}, λ_{1-3} and s_{1-3} depict polar elements for one triangle assembled by points P_{1-3} from reference epoch

PC_0.

2. φ_i, λ_i and s_i represent polar elements of points P_i from successive epoch PC_1 which have been assigned to a previously mentioned triangle.

3. x_{1-3}, y_{1-3} and z_{1-3} respectively x_i,y_i and z_i stand for the according Cartesian elements of PC_0 respectively PC_1,

4. $\vec{u}$ and $\vec{v}$ embody two vectors assembled by points P_{1-3} from epoch PC_0.

5. $\vec{n}$ stands for the face normal of the surface described by the two vectors introduced above.

6. $\vec{n}_0$ symbolises a standardised normal.

7. d is the perpendicular distance between origin of the coordinate system and plane from step 4 and 5.

8. μ represents a scaling factor that will be described later.

9. P_z stands for the foot point that results from a projection of P_i to the plane from steps 4 and 5,

10. while the distance between point P_i and P_z is depicted by $\overline{P_iP_z}$.

Figure 5.1 illustrates all parameters that have been mentioned above apart from scaling factor μ as there is no interpretable visualisation.

In order to assign stochastic information to each point spherical coordinates in the instrument's coordinate system have to be derived at first namely spatial distance

$$s_i = \sqrt{(x_i^2 + y_i^2 + z_i^2)}, \tag{5.1}$$

angle φ_i in the plane described by the X and Y axes

$$\varphi_i = \arctan(y_i, x_i) \tag{5.2}$$

and λ_i that represents the angle between Z axis and an arbitrary point

$$\lambda_i = \arccos\left(\frac{z_i}{s_i}\right). \tag{5.3}$$

Subsequently stochastic measures are assigned to each variable. For the stochastic behaviour of distance s_i a polynomial function has been used that follows

$$\sigma_{s_i}^2 = f \cdot s_i^3 - g \cdot s_i^2 + h \cdot s_i + j \tag{5.4}$$

where f = 9.97301E-10, g = -1.40861E-07, h = 8.64367E-06 and j = 1.49108E-03.

This experimentally derived model has been already used in Wujanz *et al.* (2013a) and needs to be obtained for every scanner. It has been derived as the applied instrument is capable to measure distances of up to 300 m whereas stochastic information is only given within a range of 50 m. The standard deviation for angles φ_i and λ_i have been chosen according to the manufacturer of the applied scanner (Leica 2013) namely 60 μrad respectively 12″. After stochastic information has been assigned to all points of both datasets respectively their polar elements the sequence of variance covariance propagations as illustrated in figure 5.2 has to be carried out. The sequence will now be described on example of three points from PC_0 namely P_{1-3} that assemble a triangle to which a point from PC_1 depicted by P_i is corresponding. In order to avoid datum dependent effects a centroid reduction has to be applied to all points based on the triangle's centre of gravity. All required steps are introduced in the following.

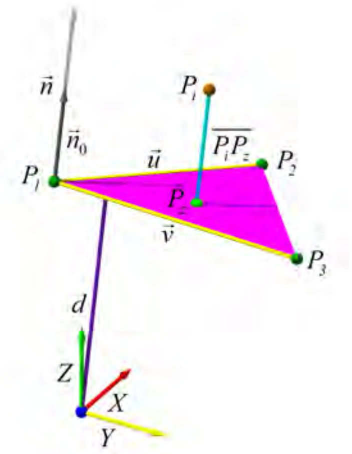

Figure 5.1: *Schematic illustration of parameters*

1. At first all previously computed polar elements have to be converted into Cartesian coordinates by applying the following equations:

$$x_i = s_i \cdot \cos(\varphi_i) \tag{5.5}$$
$$y_i = s_i \cdot \sin(\varphi_i) \tag{5.6}$$
$$z_i = s_i \cdot \cos(\lambda_i) \tag{5.7}$$

2. The aim of the second step is to assemble two vectors called $\vec{u}$ and $\vec{v}$ based on the Cartesian coordinates x_{1-3}, y_{1-3} and z_{1-3} from point cloud PC_0 for which the following equations needs to applied

$$\vec{u} = P_2 - P_1 \tag{5.8}$$

respectively

$$\vec{v} = P_3 - P_1 \tag{5.9}$$

3. Based on vectors $\vec{u}$ and $\vec{v}$ the respective face normal $\vec{n}$ of the resulting plane is computed via

$$\vec{n} = \vec{u} \times \vec{v} \tag{5.10}$$

4. The following step of the procedure generates a standardised face normal based on the previous outcome by conducting

$$\vec{n}_0 = \frac{\vec{n}}{\text{norm}(\vec{n})} \tag{5.11}$$

5. The last parameter that is missing to uniquely describe the location of a plane is d which describes the perpendicular distance between the plane and the origin of the coordinate system. Due to the previously conducted centroid reduction d sums up to null respectively very close to it. Even though this step appears to be somewhat redundant it is of importance for stochastic considerations that will be conducted in the following. Hence

$$d = \vec{n}_0 \cdot P_1 \tag{5.12}$$

is computed as indicated.

6. Within the next step μ is computed. For this a corresponding point P_i to the triangle from the successive epoch PC_1 is needed for the first time. This parameter can be interpreted as a scaling factor that brings the length of the standardised normal vector $\vec{n}_0$ in accordance to the span between P_i and foot point P_z with

$$\mu = \frac{d - \vec{n}_0 \cdot P_i}{\vec{n}_0^2} \tag{5.13}$$

7. Now the projection of P_i onto the plane described by $\vec{n}_0$ and d leads to foot point

$$P_z = P_i + \mu \cdot \vec{n}_0. \tag{5.14}$$

8. The last functional relationship computes the distance $\overline{P_iP_z}$ between P_i and foot point P_z by

$$\overline{P_iP_z} = \sqrt{(P_{z_x} - P_{i_x})^2 + (P_{z_y} - P_{i_y})^2 + (P_{z_z} - P_{i_z})^2}. \tag{5.15}$$

Now that all functional relationships have been defined variance-covariance propagation needs to be conducted, as discussed under section 3.1.2, in order to assign stochastic properties to all computed variables. Therefore partial derivatives with respect to observations respectively derived observations have to be computed based on the according functional relationships of the previously mentioned eight steps. These steps are in accordance to F_8 as depicted in figure 5.2. In order to avoid loss of co-variances a concatenated strategy has been chosen where

$$F = F_8 \cdot F_7 \cdot F_6 \cdot F_5 \cdot F_4 \cdot F_3 \cdot F_2 \cdot F_1 \tag{5.16}$$

gathers all partial derivatives. Input data of the procedure are polar coordinates as computed by equations (5.1) to (5.4) that are considered as derived observations. The corresponding stochastic model of these observations is represented by Σ_{ll}. Finally stochastic information for the distance between P_i and foot point P_z is calculated by

$$\Sigma_{xx} = F \cdot \Sigma_{ll} \cdot F^T \tag{5.17}$$

while in this case Σ_{xx} contains only one element namely $\sigma^2_{\overline{P_iP_z}}$.

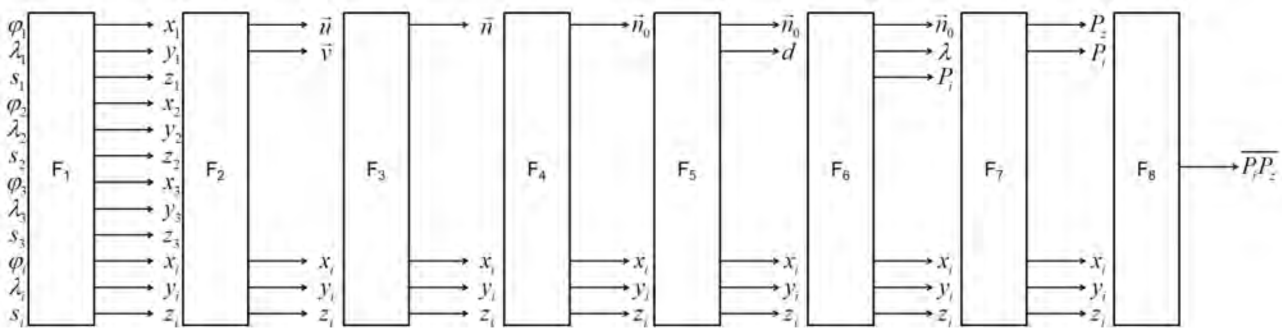

Figure 5.2: *Computational sequence for variance-covariance propagation in order to derive distance $\overline{P_iP_z}$ as well as its stochastic properties*

5.1.2 Practical application and influential impacts

This section presents results of the procedure based on synthetic data in order to identify influential parameters. Subsequently the outcome derived from a practical dataset is presented while finally theoretical considerations are raised concerning the influence of registration onto deformation monitoring.

5.1.2.1 Impact of the geometric configuration

Now that all required steps have been discussed influences onto the outcome such as the geometric configuration and the distance between a triangle and a corresponding point are analysed for which synthetic data is used. The first parameter of interest was simulated by generating differently sized equilateral triangles with side lengths of 1 cm, 5 cm and 20 cm. All geometric primitives have been virtually placed 45 m away from a simulated scanner. As a first step the precision of all points had to be computed which added up to 2.16 mm in x respectively

2.55 mm in y-direction while the z-component measured 2.67 mm. The results are gathered in table 5.1 while the left column contains the dimensions of equilateral triangles and the according distances to it. Columns two to four represent the precision of the standardised face normal, columns five to seven the according values for the foot point while the last one depicts the precision of the distance between corresponding point and foot point. The standardised face normals of all triangles point roughly towards $n_{0_x} = -0.685$, $n_{0_y} = -0.729$ and $n_{0_z} = 0.0000744$.

Table 5.1: *Stochastical measures of desired parameters derived by variance-covariance propagation*

Triangle dimensions | distance to plane	$\sigma_{n_{0_x}}$	$\sigma_{n_{0_y}}$	$\sigma_{n_{0_z}}$	$\sigma_{P_{z_x}}[m]$	$\sigma_{P_{z_y}}[m]$	$\sigma_{P_{z_z}}[m]$	$\sigma_{\overline{P_iP_z}}[m]$
1 cm | 3 cm	0.37546	0.34192	0.33861	0.34078	0.37414	0.01051	0.35941
5 cm | 3 cm	0.07509	0.06836	0.06773	0.06819	0.07489	0.00337	0.07197
20 cm | 3 cm	0.01877	0.01709	0.01694	0.01725	0.01896	0.00274	0.01836
1 cm | 1 m	0.36848	0.34604	0.33638	0.61183	0.62470	0.33640	0.61871
5 cm | 1 m	0.07365	0.06924	0.06728	0.12241	0.12495	0.06734	0.12379
20 cm | 1 m	0.01841	0.01730	0.01682	0.03071	0.03138	0.01704	0.03116

It can be notably seen that the surface area of the according triangles describes the most dominant impact onto the outcome which is then transferred to the variance of the standardised face normal and hence to all other quantities. Evidently the precision of the standardised face normal rises with increasing side lengths of triangles which hence boosts the chance of discretisation errors. It is also worth to mention that the precision of these parameters decreases in case of disadvantageous geometrical configurations such as unfavourable ratios between the sides which is why the triangulation plays a crucial role in C2M software. In addition it can be seen that the precision of the foot points is mainly influenced in planar direction of the according triangle that hence describes a limiting factor in terms of detectable deformation.

Finally the distance between triangle and corresponding point can be identified as the last influential source of the procedure. A comparison of foot point precisions between triangles of equal size but differing distance to corresponding triangles reveals this effect. This aspect is at first glance rather astonishing as the motivation for this procedure was to define the smallest statistically significant deformation while now it turns out that there may also be an upper margin that has to be taken into consideration. By usage of the 3σ rule statistically significant deformation is detected. The applied test statistic is computed by

$$T = \frac{\overline{P_iP_z}}{\sigma_{\overline{P_iP_z}}}.$$

The null hypothesis follows

$$H_0 : \overline{P_iP_z} = 0$$

and hence assumes that no deformation is present which applies if $T \leq 3$.

The alternative hypothesis supposes the inverse case, as illustrated in figure 5.1, namely

$$H_A : \overline{P_iP_z} > 0.$$

with $T > 3$.

Table elements coloured in green indicate that the null hypothesis has been accepted while red suggests that the alternative case occurred.

In summary it can be established that deformation monitoring based on C2M is highly dependent to the according geometric configuration which even prevails precision of the applied points. As the same procedure -

namely establishing point-triangle correspondences - is also applied in registration algorithms such as the ICP potential effects should be analysed in detail.

5.1.2.2 Application on a practical test case

The developed approach has been tested on the data that has been described in section 4.1 where approximately 34% of the scene was subject of deformation. As a first step the given information of the scanner manufacturer concerning the angular detectors needs to be combined with the stochastic model for the distance measurement which leads to the theoretical spatial precision of all Cartesian coordinates. Note that the stochastic information for observed distances has been derived similarly to the method described under section 3.1. It should be mentioned that the temporal conversion from Cartesian coordinates to polar coordinates and back describes the workaround as the available software does not allow exporting a polar point cloud with the original observations represented by two directional measurements and one distance. To the knowledge of the author there is no software or format on the market that is capable of achieving this. The flaw of this workaround is that the polar elements are correlated which can be seen in equation (5.1) to (5.3) as this information is not provided by any scanner manufacturer. A colour coded visualisation of the resulting standard deviations of 3D points based on the method described in the previous subsection can be found in figure 5.3.

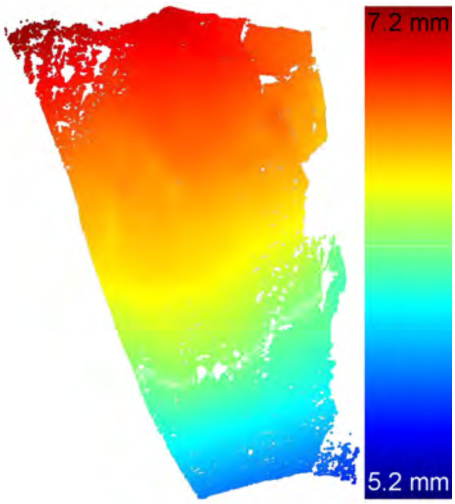

Figure 5.3: *Colour coded visualisation of the theoretical spatial point precision*

Subsequently a stochastic point cloud is present that then needs to be converted into a stochastic mesh. As soon as correspondences between triangles and points have been established according foot points as well as their stochastic properties can be generated. It has to be mentioned that the determination of correspondences is a critical task especially in convex regions such as the very bottom of a cliff where it is not clear to which triangle a point needs to be assigned. Usually a maximum distance needs to be defined by the user which requires *a priori* knowledge about the expectable deformation. In this case a value of 1 m has been set. The last step of the procedure determines the stochastic properties of the distance between point-triangle correspondences.

The reviewed datasets contained 96374 corresponding distances from which 15.5% have been declared as significant deformations. Note that the previously mentioned computed ratio of significant deformation is not directly comparable to the specified amount in relation to the entire surface area of 34%. Figure 5.4 illustrates the outcome.

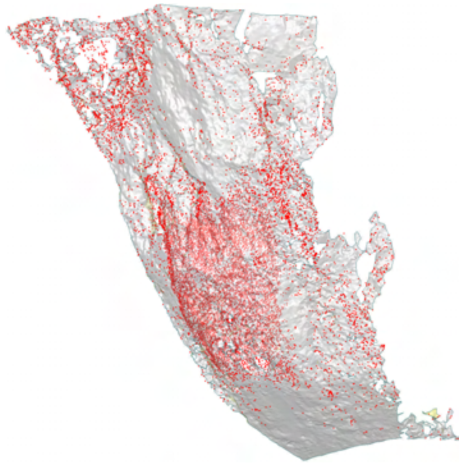

Figure 5.4: *Visualisation of points that feature statistically significant distances (red dots) to the triangulated mesh*

It can notably be seen that the majority of points lies, as expected, within the area where material has been removed. Interestingly clusters of comparatively high point density can be found left above the area of withdrawal as well as to its right. The reason for the occurrence in these regions can be explained by an unfavourable shape of the according triangles that are provoked by moving terrain respectively flat incidence angles. The smallest detected deformations have a distance to the mesh of 1.47 cm while the largest ones sum up to 99.97 cm. A histogram of all statistically significant deformations is depicted in figure 5.5 where the horizontal axis shows the distance between surface and points in metres while the vertical axis features the number of occurrences per class. The centre of the histogram shows the area of excavation while surprisingly many points measured less than five centimetres of deformation an effect mostly caused by large triangles in areas with low local point spacing.

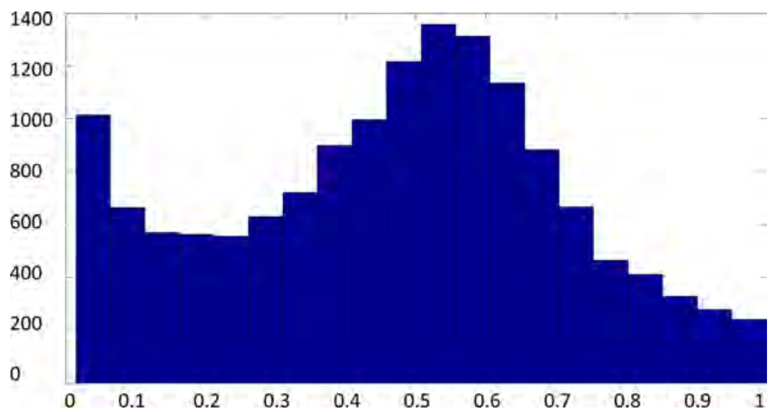

Figure 5.5: *Histogram of deformation vectors. The vertical axis counts the number of occurances per bin while the horizontal one depicts the distance to the surface in metres*

Finally a colour coded inspection map has been generated based solely on all statistically significant points that are depicted in figure 5.4. The outcome is illustrated in the left part of figure 5.6. Note that only colour coded points are shown according to their distance to the reference epoch. The dominating deformation can be found in the expected area where material has been withdrawn. However a close look at the figure reveals that the remaining points do not follow any systematic behaviour.

Another possibility to illustrate the outcome could be to use the smallest and largest statistically significant distances as boundaries for acceptable deformations on the complete dataset. The resulting inspection map can be found in the right half of figure 5.6 while this time the colour coding has been projected onto the reference mesh. An obvious difference to left half is that most of the scattered points can't be found in the other inspection map. The reason for this can be explained by a tunable parameter within the visualisation software (Raindrop Geomagic Qualify 12) that filters colours based on adjacent ones. The yellow areas below the withdrawal area are caused by compressed material that fell out the shovel of the digger previously. In comparison the outcome of both strategies can be rated as similar apart from the removal of scattered points by the visualisation software. Hence similar conclusions must be drawn from both results during deformation monitoring in this specific case. However it is not recommended to follow this strategy as it most probably visualises deformations that are not of statistical significance.

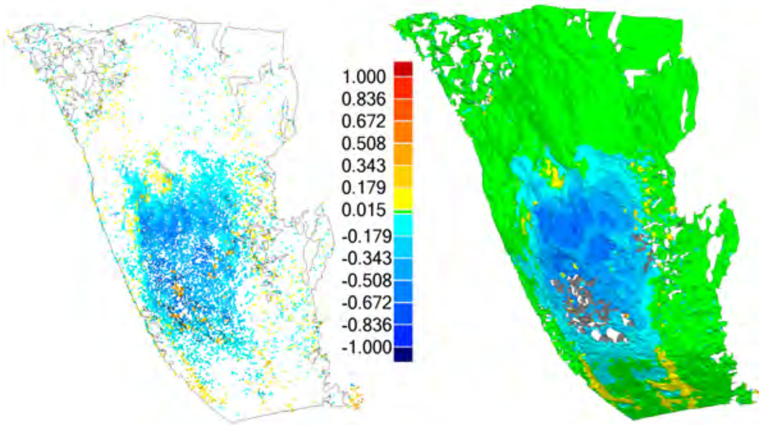

Figure 5.6: *Colour coded inspection map based only on statistically significant deformations in metres (left). Colour coded inspection map of the entire dataset (right) based on statistically significant boundaries in metres. Deviations between reference and successive epoch have been visualised on the triangulated mesh.*

After all results have been generated with the proposed C2M-approach the same data has been processed with LAGUE's *et al.* (2013) M3C2 algorithm. Several major differences of the M3C2 approach in comparison to the C2M can be identified:

1. Deformation monitoring is usually carried out at a quasi-regular spatial resolution in contrast to the full resolution that C2M uses.
2. Surface normal estimation is conducted on a larger selection of points while C2M applies a minimal configuration. Therefore no triangulation is required.
3. Stochastic information is derived based on the point cloud's local roughness.
4. A statistical test is carried out that determines whether deformation occurred or not.

At first glance it can be seen in the left half of figure 5.7 that a lot less scattered points have been interpreted as being deformed in contrast to the outcome depicted in figure 5.4. Furthermore the area of withdrawal features a considerably larger amount of detected points which can be rated as a better result in comparison to the procedure described within this contribution. Despite the fact that less disconnected points are visible the M3C2 rated 28.2% of all distances as statistically significant which is nearly twice as much compared to the other approach. A colour coded inspection map based on the outcome of the M3C2 is depicted in the right half of figure 5.7 where deviations are given in metres. The general pattern of the result in the area where material has been removed is comparable to the one computed with the C2M yet more statistically significant distances were detected. In summary the M3C2 produces results that correspond to the assumed outcome where nearly the entire area of withdrawal has been identified. Future work will analyse the capabilities of this algorithm in detail due to its promising outcome.

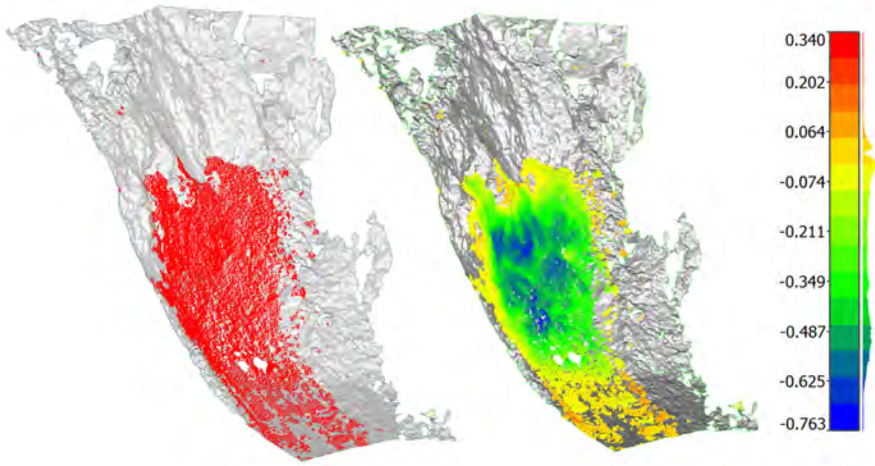

Figure 5.7: *Outcome generated by the M3C2 (left part) where red points represent stochastically significant deformation. It can clearly be seen that less scattered points have been detected. A colour coded inspection map generated by the M3C2 approach where deformations are given in metres is depicted on the right. A histogram of the deviations are located on the right of the colour bar.*

5.1.2.3 Influences due to registration

The major influence onto the outcome of deformation monitoring is caused by the registration process. Strictly speaking four factors may to be considered:

- Computation of transformation parameters that are falsified by deformation / outliers,
- accuracy of the registration,
- sampling of corresponding points between the epochs,
- parameterisation of the registration.

While the first aspect has already been discussed in detail by Wujanz (2012) and Wujanz *et al.* (2013b) the third one didn't raise great interest in the scientific community as most authors claim that the biggest impact is caused by the registration accuracy. In this section a simple numerical example exemplifies that the distribution of corresponding points is superior in terms of falsification onto the outcome of deformation monitoring than its accuracy. The crux concerning the registration accuracy is the fact that its quality measures can be easily manipulated in many ways for instance by tunable parameters (corresponding search radius in case of the ICP) or by omitting certain artificial tie points from the computation of transformation parameters. Hence the "best" solution can be found by identifying a minimal configuration of three point correspondences whose residuals are minimal. The danger in following this strategy is that the transformation parameters are computed presumably based on a local portion of the given dataset as exemplified in the following while an overview of the scenario is depicted in figure 5.8 from bird's eye view.

Three different sets of transformation parameters have been computed based on differently "sized" corresponding point sets. All sets consist of four points that are arranged in squared shape (in x- and y direction) while different heights have been assigned.

In order to simulate a second epoch the original dataset has been modified. Therefore Gaussian noise within the range of 1 cm has been added to points 1, 2, 5 and 8 which are referred to as the "red" dataset in the following. A larger portion of normally distributed noise of 2 cm was added to points 3, 6 and 9 that are named the "orange" dataset throughout this section. The "green" dataset which is assembled by points 4, 7 and 10 received the largest portion of noise namely 5 cm. Every dataset shares the cyan coloured sphere while the orthogonal distance between the points amounts to 50 m for the "red" scenario, 150 m between the vertices of

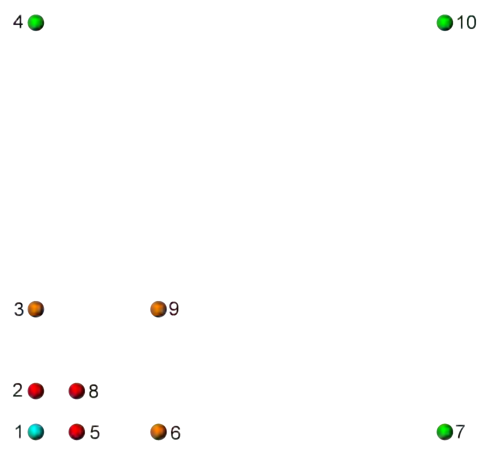

Figure 5.8: *Bird's eye view of the example - Orthogonal distances between points: 50 m (red spheres), 150 m (orange spheres) and 500 m (green spheres)*

the "orange" dataset and 500 m between the "green" points.

Table 5.2 gathers results for all calculated sets where different point sets have been used to compute transformation parameters. The "worst" result in terms of average residuals for applied tie points as well as average residuals over all points can be related to the "green" dataset. However this opinion needs to be revised after analysing the residuals of points 4, 7 and 10 where the order from best to worst results follows "green", "orange" and "red" which shows that the effect of tie point distribution is superior to registration accuracy. Further investigation has to analyse how the stochastic outcome of the registration process influences the stochastic properties of all points.

Finally it should be mentioned that parameterisation of the registration approach also has an impact yet hasn't been addressed thus far. In practice different functional models can be applied e.g. using a six degrees of freedom model describing the default case (translations t_x, t_y and t_z and rotations r_x, r_y and r_z) or a reduced functional model expressing only four degrees of freedom (translations t_x, t_y and t_z and rotation r_z) for scanners that set the rotation axis z of the scanner plumb.

Table 5.2: *Residuals after transformation for all three combinations*

	Average residuals: All points [mm]	Average residuals: applied tie points [mm]	Residuals: Points 4 | 7 | 10 [mm]
"Red" dataset: 1,2,5,8	29.7	7.6	92.6 | 53.3 | 67.1
"Orange" dataset: 1,3,6,9	25.4	11.2	41.1 | 44.4 | 46.1
"Green" dataset: 1,4,7,10	35.7	23.7	17.0 | 15.7 | 22.2

5.2 Visualisation of deformation on arbitrary surfaces

TLS, structured light scanners and other contactless surveying instruments are widely used for instance in alignment, as-built documentation, positioning, deformation monitoring or quality assurance. The outcome of these processes is usually presented in numeric form, through a raw point cloud or, for the last two cases, by a colour coded representation of the deviations (as discussed in section 2.5) respectively geometric alterations. The interpretation of colour coded 3D information that is displayed in 2D (inspection map) can be quite difficult depending on the geometric characteristics or extent of the surveyed object. In order to simplify this task approaches from augmented reality (AR) have been taken into consideration where the inspection map is projected onto the object itself.

In order to achieve this several problems have to be solved:

- Transformation of reference dataset (e.g. CAD) into the current sensor coordinate system.
- In order to receive the parameters of the interior orientation a calibration has to be carried out before usage of the projector unit. Alternatively they can be calculated by using homologues points as described in section 5.2.2.4.
- Determination of the relative orientation between projector unit and applied sensor coordinate system.
- Conversion of the inspection map into a 2D projector image.

Note that the projector image has to be resampled in a way that geometric properties of the object are taken into consideration. The problem of tie point signalisation for the use of TLS is presented in two ways. Amongst them is a novel approach referred to as virtual targets which uses the internal camera of the applied TLS and the projector unit in order to arbitrarily distribute simulated tie points around an object respectively within a scene of interest.

5.2.1 Related work

Heilig (1962) probably took the first steps towards mixed reality, which can be understood as a mixture between the real world and virtual components, by developing a multimodal arcade game called Sensorama based on a stereoscopic video. A classification of mixed reality categories and their distinctive features can be found in Milgram & Kishino (1994) while Milgram *et al.* (1994) give a theoretical overview specifically on augmented reality (AR). Raskar *et al.* (2001) apply several projectors in order to generate a virtual texture by projecting images onto a neutrally coloured object with arbitrary geometric properties. Note that the current implementation of our system does not apply a camera in order to correct the computed imagery against the given texture of an object as shown for instance by Bimber *et al.* (2005). A technical limitation of such a system is possibly given by insufficient resolution of the projector unit e.g. when the object is far away or its surface is comparatively large. This problem could be solved by sequentially projecting sub matrices of the inspection map by applying a motor controlled projector as described by Pinhanez (2001) or by using multiple projectors as proposed by Chen *et al.* (2000) in a simultaneous solution. Raskar *et al.* (2003) apply a handheld projector that uses a tilt sensor and a camera in order to compensate for keystone distortion and also present a self-configuring technique for several projector units. Lee *et al.* (2004) solve the problem of determining the relative orientation between projector and desired scanner coordinate system by embedding optical fibres into the object whose position can be captured by a structured light scanner. The proposed technique in this contribution does not apply active sensors for the mentioned purpose within the scene in order to being applicable in unreachable or untouchable areas, for instance in museums or on unstable surfaces.

5.2.2 Description of the system

One of the goals of this new approach was to make it adaptable and applicable to many different problem domains by using standard equipment that is usually available in every office. This section describes which components have been applied in order to establish the system. Furthermore a variation by applying another 3D measurement instrument and finally the mathematical background are presented.

The workflow of the proposed system can be divided into three major steps:

- Data preparation, which includes acquisition, transformation into a common coordinate system and comparison, is described in subsection 5.2.2.2,
- details concerning the relative orientation between the applied sensor systems are presented in subsection 5.2.2.3,
- and finally the transformation of the 3D content itself into a planar form is demonstrated in subsection 5.2.2.4.

5.2.2.1 Applied components

Two types of 3D measurement systems have been applied during the implementation of the approach. One being a Leica C10 terrestrial laser scanner with a maximum reach of 300 m the other being a GFaI structured light scanner (GFAI 2014) which can be adapted to different scenarios in terms of reach and spatial resolution. The off-the-shelf projection unit is fabricated by projectiondesign whereas the F1 model with a maximum sensor resolution of 1280 x 1024 pixels has been used.

5.2.2.2 Data preparation

The first step of this procedure is the data acquisition process in which the object of interest is captured. Subsequently this dataset has to be compared to a reference which can be a CAD or known geometric properties, for instance that an object is assumed to be planar. Figure 5.9 depicts how an inspection or deviation map is processed. In this figure both datasets are already correctly aligned, so that distances between the two geometries can be calculated. Afterwards these distances are converted into colours according to settings that can be adjusted by the user such as the acceptable spectrum of deviations. Various solutions are available on the market to fulfil this step such as Raindrop Geomagic Qualify or GFaI Final Surface (GFAI 2015).

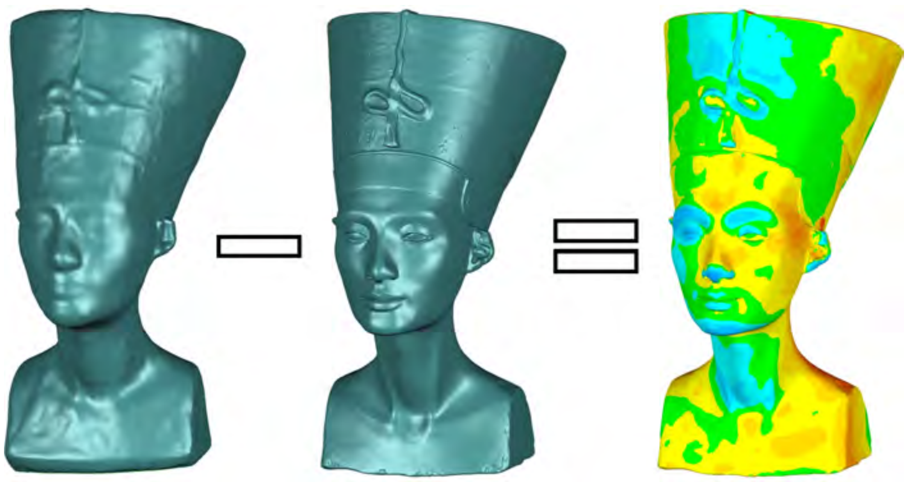

Figure 5.9: *Determination of an inspection map between measured values (left) and a CAD (middle). The outcome is shown on the right.*

In order to calculate correct deviations between reference dataset and measured values transformation parameters have to be determined which can e.g. be done by using Besl & McKay's (1992) iterative closest point algorithm (ICP) respectively Chen & Medioni's (1991) approach. Note that the superior coordinate system has got to be the one of the measurement instrument in which the reference dataset has to be transformed as the inspection map should be projected on to the measured object. It has to be mentioned that this transformation is a crucial step, which is of course also subject to falsification by the geometric quality of the measurements, as it directly influences the outcome of the deviation or inspection map which is computed afterwards. Bear in mind the necessity to reject deformed regions prior to computation of transformation parameters in order to avoid falsifications of the inspection map as extensively discussed in sections 2.3.4 and chapter 4.

5.2.2.3 Relative orientation

The aim of this step is to determine the relative orientation between the coordinate system of the measurement instrument and the projector unit which will be described in detail in the following section. Therefore tie- or homologous points have to be determined where six points are the minimal configuration as 11 parameters have to be determined. Six unknowns describe the exterior orientation while the remaining five represent the interior orientation. These points are measured in three dimensions in order to represent the scanner's location while two-dimensional coordinates are determined within the projector unit system. While the registration process influences the outcome of the inspection map the determination of tie points has its impact on how accurate the visual information can be projected onto the object. Therefore an established approach as well as a completely new solution for TLS have been analysed.

The first option for TLS usage applies physical targets that have been distributed around the area of interest. While the determination of the 3D coordinates within the measurement instrument coordinate system can be achieved automatically the 2D coordinates required human interaction. Therefore the centre had to be detected by manually pointing the mouse cursor into the middle of a target whose display coordinates were then stored in a coordinate file. Note that Leica's Cyclone software, which has been applied to determine the centre coordinates of all targets, works only on intensity data.

As physical targets such as spheres, paper print-outs or coded tilt and turn versions can be unpractical to distribute especially within larger scenes or hardly accessible areas it was opted for a more convenient solution. Motivated by these drawbacks a new approach called virtual targets has been developed where the projector and the internal camera of the TLS, which is calibrated to the scanner's coordinate system, have been applied. Another vital component of this system is software where coded targets can be placed interactively within the projectable region by moving the cursor into the designated position. In order to ensure sufficient local resolution, placed targets can be altered in size to adapt for decreasing resolution of optical sensors and TLS with preset point spacing.

In order to test the approach a scene including physical and virtual targets has been captured in terms of geometry and RGB imagery. As expected no distinguishable intensity information has been detected of the projected targets by the TLS so that a workaround had to be developed in order to solve this problem. Therefore the RGB imagery from the scanner's internal camera has been converted into a one channelled grey scale image. Subsequently these 8-bit values are then recomputed into a range between 0 and 1 and hence can be used to replace all captured intensity values for each according 3D point. Note that this approach assumes nearly planar projection surfaces as free form shapes would interfere with the automatic determination of the target centre.

Figure 5.10 illustrates several products captured from TLS that finally lead to usable targets. The left part shows a RGB image captured by the internal scanner camera. Six physical print-out targets are attached to the wall while the four slightly smaller targets on the outer left side are projected targets and hence virtual ones. These projected targets aren't visible in the intensity image which can be found in the middle section.

After conversion from RGB values into intensity values and its integration into the point cloud, the determination of target centres can be carried out as shown in the right part of the figure below.

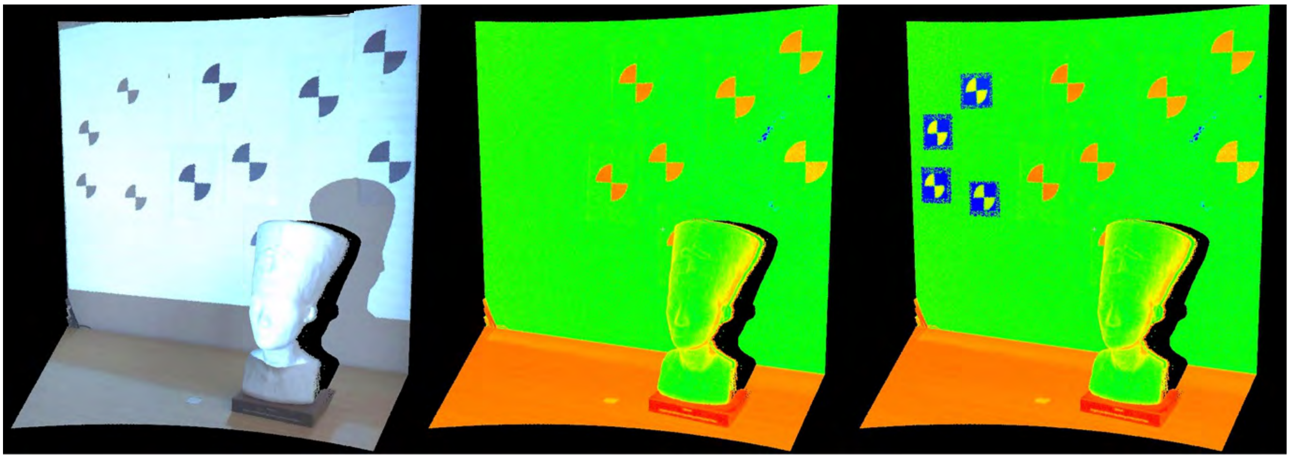

Figure 5.10: *RGB image captured by the internal camera of the scanner (left), measured intensity information (middle), virtual targets derived from RGB imagery and physical targets (right)*

It has to be mentioned that the problem simplifies significantly when structured light scanners are applied as the relative orientation between measurement system and projector has already been determined during calibration. Thus, this case applies the projection unit as an integral component of the measurement system itself. Another advantage of this system is that there is no parallax between measurement system and the projected information as they share the same optical path.

5.2.2.4 Transformation

Perspective mapping from an Euclidian three-dimensional space $\mathbb{R}^3$ to a two-dimensional space $\mathbb{R}^2$ can be, according to Hartley & Zisserman (2010 pp. 163), solved by introducing homogenous coordinates for object points (X, Y, Z) as well as image points (x, y). A major advantage of using homogenous coordinates is that rotation, translation and scaling can be applied to a set of points quite convenient as all necessary information is stored in one matrix. Homogeneous coordinates are composed by extending the Cartesian coordinates of the Euclidian space by an additional dimension. The relationship between Cartesian and homogeneous coordinates can be described by

$$\mathbf{x} = \lambda \cdot (x, y, 1)^T = (u, v, w)^T \tag{5.18}$$

respectively

$$\mathbf{X} = \lambda \cdot (X, Y, Z, 1)^T = (U, V, W, T)^T \tag{5.19}$$

where λ denotes an arbitrary scaling factor. Using homogeneous coordinates comprehends the possibility to describe a transformation between object and image points via projection matrix $\mathbf{P}$

$$\begin{bmatrix} x \\ y \\ 1 \end{bmatrix} = \mathbf{P} \begin{bmatrix} X \\ Y \\ Z \\ 1 \end{bmatrix} = \mathbf{KR} \begin{bmatrix} \mathbf{I} & -\mathbf{C} \end{bmatrix} \begin{bmatrix} X \\ Y \\ Z \\ 1 \end{bmatrix} \tag{5.20}$$

where $\mathbf{R}$ denotes the rotation matrix and $\mathbf{C}$ the translation vector between object and image coordinate system. Furthermore calibration matrix $\mathbf{K}$ represents the interior orientation of the used projector and only has to be determined once. In order to derive projection matrix $\mathbf{P}$ from given tie points, object as well as image coordinates for each point have to be normalised and reduced to the centroid by determining $\tilde{\mathbf{X}}_i = \mathbf{T} \cdot \mathbf{X}_i$ respectively

$\tilde{\mathbf{x}}_i = \mathbf{T}' \cdot \mathbf{x}_i$ with

$$\mathbf{T} = \begin{bmatrix} 1/X_{max} & 0 & 0 & -X_{centroid}/X_{max} \\ 0 & 1/Y_{max} & 0 & -Y_{centroid}/Y_{max} \\ 0 & 0 & 1/Z_{max} & -Z_{centroid}/Z_{max} \\ 0 & 0 & 0 & 1 \end{bmatrix} \tag{5.21}$$

and

$$\mathbf{T}' = \begin{bmatrix} 1/x_{max} & 0 & -x_{centroid}/x_{max} \\ 0 & 1/y_{max} & -y_{centroid}/y_{max} \\ 0 & 0 & 1 \end{bmatrix} \tag{5.22}$$

where X_{max}, Y_{max}, Z_{max} and x_{max}, y_{max} represent the absolute maximum value for object respectively image coordinates. For each one of the n tie points the following two rows of matrix $\mathbf{A}_i$ have to be set up

$$\mathbf{A}_i = \begin{bmatrix} -\tilde{w}_i\tilde{\mathbf{X}}_i^T & \mathbf{0}^T & \tilde{u}_i\tilde{\mathbf{X}}_i^T \\ \mathbf{0}^T & -\tilde{w}_i\tilde{\mathbf{X}}_i^T & \tilde{v}_i\tilde{\mathbf{X}}_i^T \end{bmatrix} \tag{5.23}$$

and finally combined to design matrix $\mathbf{A}$ which is containing $2n \times 12$ elements. An elegant way to solve the equation system

$$\mathbf{A}\mathbf{h} = 0$$

with $\mathbf{h} = \begin{pmatrix} h_1 & h_2 & \cdots & h_{12} \end{pmatrix}^T$ is to determine the right singular vector related to the smallest eigenvalue which can be achieved via Singular Value Decomposition (SVD) of $\mathbf{A}$. This vector $\mathbf{h}$ contains the 12 elements of the projection matrix $\tilde{\mathbf{P}}$ for normalised and reduced coordinates. Finally projection matrix $\mathbf{P}$ can be derived by

$$\mathbf{P} = \mathbf{T}'^{-1}\tilde{\mathbf{P}}\mathbf{T}. \tag{5.24}$$

which contains information on the interior orientation of the camera as well as the exterior orientation between object and image space. Due to the fact that $\mathbf{P}$ only depends on eleven parameters all elements have to be divided by its last entry p_{34}. For further information see Förstner (2000), Rodehorst (2004) or Hartley & Zisserman (2010). Figure 5.11 illustrates the workflow of the proposed system including all previously mentioned components.

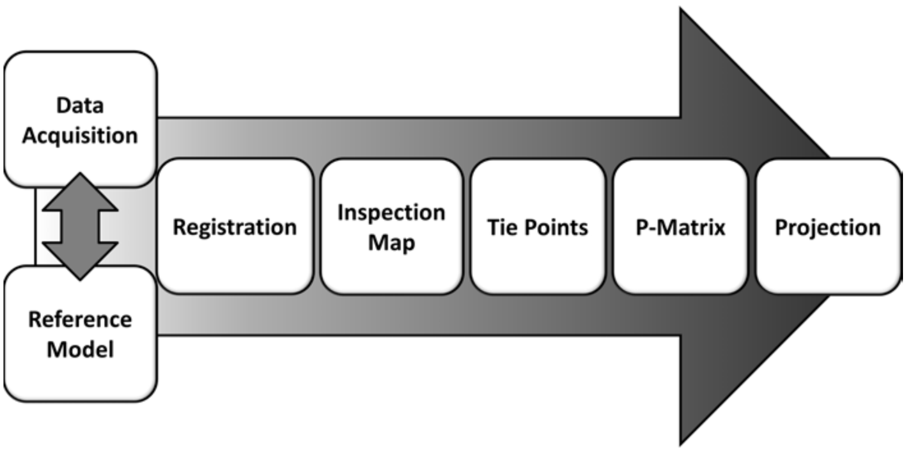

Figure 5.11: *Workflow of the presented approach*

5.2.3 Quality assurance and inspection

This section focuses on potential sample applications such as alignment and quality assurance. Before these examples are presented the workflow has been tested in order to verify its operational reliability. Therefore a checkerboard pattern has been mapped onto the three dimensional mesh of a surveyed bust by applying a parallel projection. After application of the technique described in section 5.2.2.4 the left part of figure 5.12 emerges. The silhouette of the bust is caused by the fact that projection direction and viewing angle of the projector differ. The same reason leads to effects that are visible in the right part of the illustration where a shade right next to and above the bust can be noticed. A close look at the image reveals imperfections in transition sections between bust and wall which can be simply explained by a parallax between projection direction and location in relation to the camera viewpoint and its alignment. In summary the quality of the outcome fulfils all expectations so that further applications have been explored.

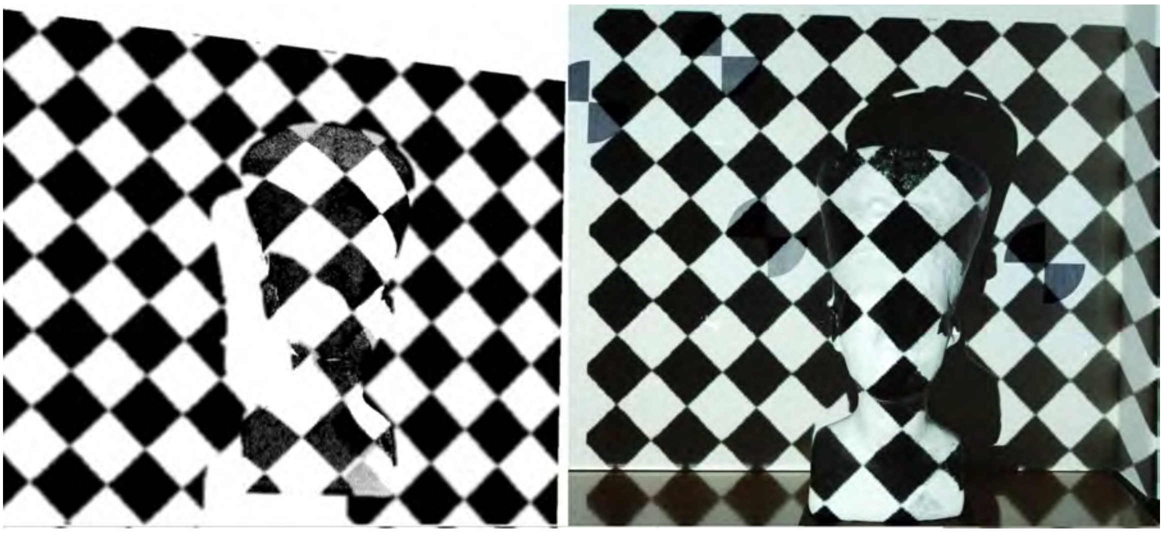

Figure 5.12: *Verification of the approach. Calculated image (left) and photography of the projected outcome (right).*

The main motivation of this project was to develop a more interactive and at the same time simpler way of how to present and communicate products that have been derived via 3D survey. The first idea for potential fields of applications was quality assurance, inspection of produced goods or of products within the manufacturing process. Hence the first example that has been tackled was a comparison between a CAD and a surveyed bust as depicted in figure 5.9 on the left. Note that the CAD has been derived from surveyed data by carrying out reverse engineering as well as removal of obvious dents.

After the survey has been carried out by TLS six tie-point coordinates have been determined within the coordinate system of the measurement instrument and of the projector unit. Subsequently the CAD has been registered into the coordinate system of the surveyed data whereas an average deviation of 2.3 mm between the two datasets resulted from ICP. Based on these datasets an inspection map has been computed which was then processed by the implemented software and projected onto a white coloured version of the bust as illustrated in figure 5.13. On closer inspection it can be seen that darker shades of blue, for instance located on the shin and on the nose of the bust, which are clearly noticeable in the left part of the image below, aren't visible on the right. This effect can be explained by the quality of the projector. Concluding the achieved geometric quality of the outcome can be rated quite positive as no apparent visible offsets occurred apart from the lack of contrast by the projector.

Another application where the proposed technique can be applied would be for alignment of laminar objects. To this day most alignment processes are carried out with discretely measuring sensors such as total stations which are quite time consuming to operate. Modern 3D scanners are able of capturing point clouds within very short periods of time, e.g. GFaI ScanMobile which takes about 1 s to 1.5 s. This capability opens possibilities for online systems where coordinates are captured continuously while deviations to a designated position are projected through colour coding onto the object of interest.

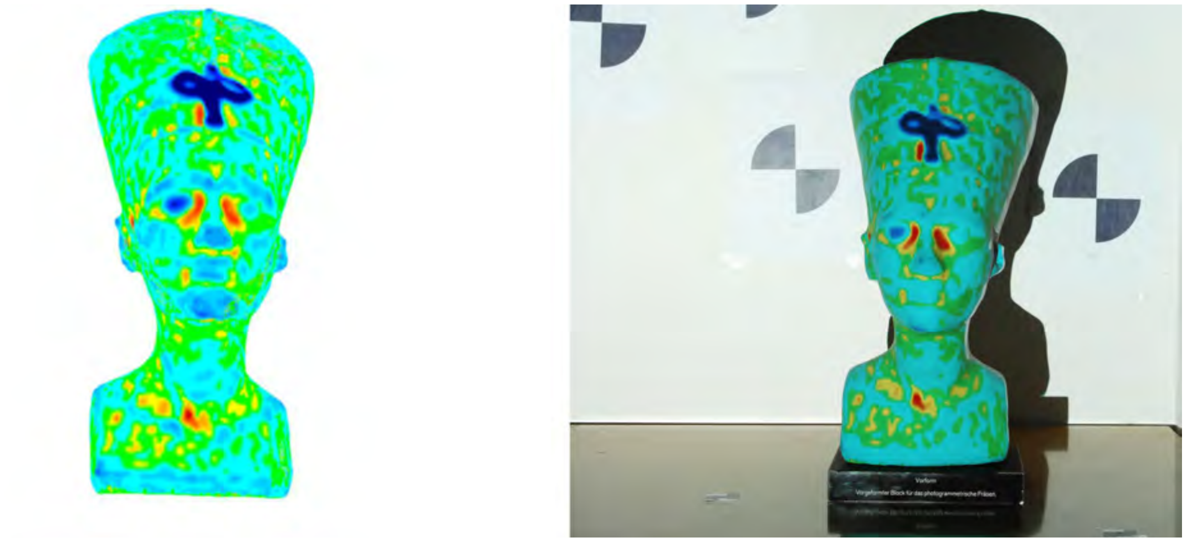

Figure 5.13: *Computed image (left) and and photography of the projected picture (right).*

A simple demonstration has been conducted by using two arbitrarily positioned cardboard boxes on which white sheets of paper have been attached in order to increase contrast. The goal of this test was to bring both boxes into a desired alignment. Therefore one of the boxes was declared to be the reference which has been established by approximating a plane through the according points. Subsequently the remaining points have been compared to the reference plane where colours were assigned to each point. After projection of the resulting pattern onto the box the position of it has been corrected, a new survey was conducted and a new projectable pattern has been determined. During this test a coarse to fine approach has been chosen so that the colour spectrum was tuned to the expected maximum deviation of the current position of the box.

Figure 5.14 illustrates how an alignment based on the proposed technique works. The left part of the image shows both boxes in their initial position whereas the left one has to be aligned parallel to the right green coloured box. A circular grey area visible on the last mentioned box is caused by a target that shielded the box against it. As this was the first position of the demonstration large deviations of up to +/- 30 cm have been set as acceptable while the colour spectrum was segmented in 5 cm steps. As the projected image shows step-like offsets a rotational misalignment apart from the translational offset can be spotted. The figure in the middle depicts the corrected position and alignment based on the previously mentioned pattern. Note that the colour spectrum has been refined in this step where different colours separate by 1 cm. After two iterations the image on the right emerges where both boxes are aligned to a satisfactory degree. The yellow spot in the left box is caused by a bulge of the attached paper which becomes visible as the tolerance between two colours is set to +/- 0.5 cm.

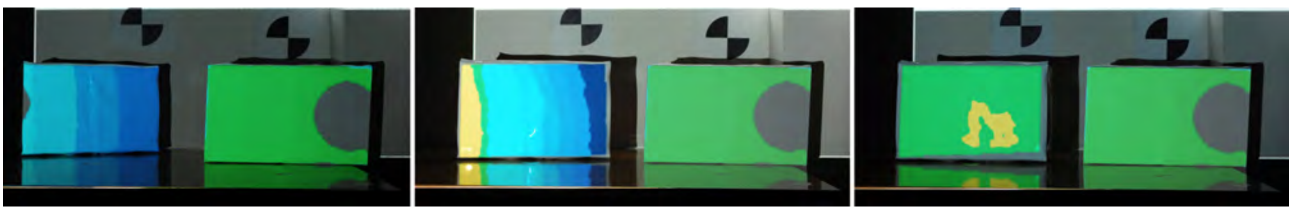

Figure 5.14: *Processing steps of the alignment: initial position of the boxes (left), corrected location according to projected colour coding (middle) and final alignment (right).*

5.3 Conclusions

This section presented a rigorous approach that determines boundaries respectively statistically significant distances for C2M inspection maps based on variance-covariance propagation. A synthetic example has clearly revealed that the detectability of the procedure drops with decreasing triangle size. In addition it can be established that the impact of the geometric configuration is superior to the accuracy of the applied points. This behaviour would demand an almost schizophrenic decision by the user in the field: Should one capture the region of interest at high local point spacing which leads to a lower detectability of statistically significant deformations or should one scan at a lower sampling rate so that smaller deformations may be sensed but the likelihood increases that these geometric changes are nothing else than resampling errors. The proposed procedure has then been used to compute two inspection maps one solely based on statistically significant distances respectively points while the other one applied only derived thresholds on the entire dataset. A first comparison among the modified C2M method and the M3C2-algorithm leads to the conclusion that the latter algorithm leads to results that rather comply with the assumed outcome.

Future work has to focus on the impact of registration onto the outcome of deformation monitoring, a problem that has not thoroughly been addressed. Furthermore the impact of the presented issue should be analysed within the context of ICP-based matching procedures. Another important question is how C2M deformation monitoring can be modified in order to stabilise the required face normals and to avoid wrong correspondences between epochs. In addition an extensive analysis of the M3C2-method has to be conducted.

A new visualisation technique for projecting inspection maps on to arbitrary surfaces with off-the-shelf projection units and application of different 3D measurement devices is presented. Furthermore the use of virtual targets for TLS is proposed, a convenient approach to interactively place simulated targets within a region of interest. After demonstration of the capabilities of the implemented system two primary fields of application, quality assurance and alignment are revealed on practical examples.

Apart from the demonstrated use of virtual targets they can be applied for connecting point clouds in inaccessible areas or where the ICP-Algorithm might fail such as planar surfaces. The presented projection technique can not only be useful within the geometric domain but also in other fields where problem specific information can be linked to spatial information for instance multispectral, thermal or acoustic information of objects that have been captured e.g. by sensor fusion or new developments.

Possible scenarios for the application of the presented system can be found in various fields of application for instance on construction sites where concrete slabs could be checked for planarity during casting. Free formed metal sheets, as used on shipyards, could be interactively aligned before welding. A variety of computer designed work pieces such as moulds from a technical perspective or products for instance manufactured by stone cutters to cover the artistic point of view are still handcrafted goods due to the low quantity of batches. By applying the proposed technique the manufacturing process could be controlled to by a much higher degree and could provide assistance during fabrication. Car rentals could introduce the system in combination with a camera to correct against object colour in order to locate damages after vehicles have been returned.

6 Practical application of the ICProx-algorithm

As the ICProx-algorithm proofed to be robust against large amounts of deformation within a scene its practical usability is under investigation for different problems in this section. The challenges in section 6.1 and 6.2 can be associated to the shear extend of the datasets where the movement of rock and ice glaciers was of interest. A rather unusual example from the field of dentistry is subject of section 6.3 while section 6.4 focuses on data acquired of a subsidence. Every methodology is subject to limitations and restrictions which is why section 6.5 tries to identify the boundaries of usability in presence of weak geometric contrast on example of datasets captured in crash testing.

6.1 Monitoring of a rock glacier

The ICProx is applied in this subsection on acquired data of a very active rock glacier located in the Hohe Tauern range of the Austrian Alps. Located between 2455 - 2720 m above sea level the Langkartal glacier features a width of 300 m and a length of 900 m. Notable changes of the rock glacier's surface have been detected by Avian *et al.* (2005) based on aerial photographs taken in 1997. In order to geometrically quantify these alterations a geodetic network has been established in 1998 which is since surveyed annually (Kienast & Kaufmann 2004). The glacier itself behaves differently in terms of its movement and can be categorised into a slower upper part and a rapidly moving lower part with maximum horizontal displacements of up to 2.5 m per year (Avian *et al.* 2009). On average the speed of horizontal movement varies between 0.10 – 0.18 m per year while maximum changes amount up to 3.6 m per year (Kaufmann & Ladstädter 2009). Delaloye *et al.* (2008) estimate this rock glacier to be one of the currently fastest moving one in Europe which underlines its importance for the scientific community. As already highlighted in subsection 2.5.1 terrestrial remote sensing techniques such as TLS are of enormous interest within the Geo-scientific community to compute:

- Extend of laminar changes,
- Volumetric variations,
- Deformation vectors,
- Alterations of slope / rock orientation.

Despite its popularity for monitoring of geomorphological processes, compare Oppikofer *et al.* (2008), TLS has seldom been used for analysis of periglacial effects such as rock glacier movement patterns. Hence annual TLS observations have been undertaken from the year 2000 onwards. For this subsection two epochs were of interest which have been captured in 2011 and 2013 by using a Riegl LMS Z620 scanner that applies a wavelength of 1550 nm and is capable to measure distances of up to 2 km. For registration of according epochs into a stable coordinate system the already mentioned geodetic network consisting of five points was used for computation of transformation parameters. Scanning of the scene was carried out from two known points of the superior coordinate system depicted as HLK and HLK_1. The lowest and highest ground sampling distance (GSD) for the 2011 campaign summed up to 6.6 cm respectively 41.8 cm while the according measures for the survey of 2013 are 4.8 cm and 33.1 cm. These measures have been computed based on the closest and furthest distance between scanner and scene. As every epoch is assembled of two scans registration is required before congruency analysis can be carried out while the according misclosures sum up to 2.63 cm for 2011 and 2.35 cm for 2013.

Figure 6.1 illustrates the two scanner locations which are depicted by red circles in the left part. In the centre of the figure all applied tie points are highlighted by green circles. It can notably be seen that the distribution is rather unfavourable from a geodetic point of view as the region of interest is not surrounded. This may lead to adulterant extrapolative respectively leverage effects. The right part of the figure illustrates the sectors of data acquisition (red dashed lines) while the active zone of the glacier is enclosed by a dotted white line.

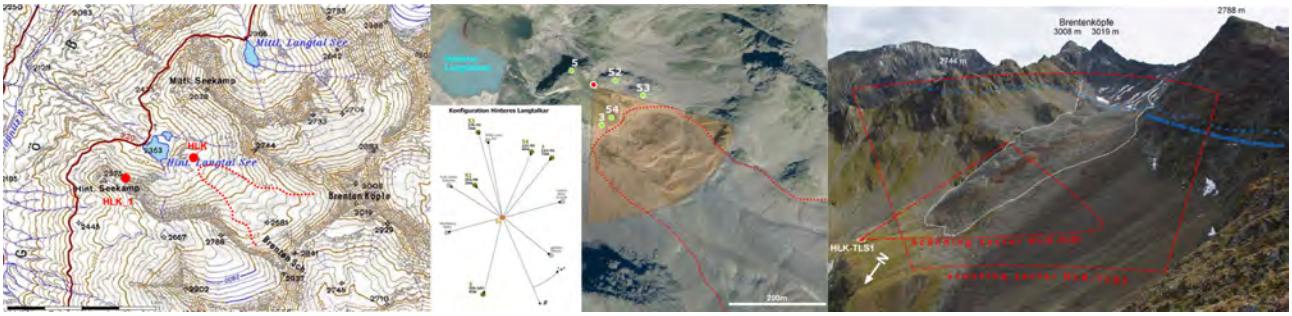

Figure 6.1: *Scanner locations HLK-TLS1 and HLK-TLS2 represented by red circles and rock glacier depicted by a red dashed line* (*left part of the figure,* ALPENVEREINSKARTE SCHOBERGRUPPE). *Distribution of applied tie points* (*centre,* © NATIONALPARK HOHE TAUERN). *The area of data acquisition from both viewpoints* (*red dashed lines*) *and active glacier zone* (*white line*) *is illustrated in the right part of the figure* (AVIAN).

The left part of figure 6.2 depicts a colour coded inspection map based on the mentioned two geo-referenced epochs. The glacier tongue can clearly be seen as it is highlighted by tones ranging from yellow to red featuring deformations of up to 2.5 m. Note that the according colour bar only ranges from +/- 1 m for illustrative reasons. Apart from this gain of material a narrow band coloured in cyan is visible, which is highlighted by a red rectangle, where single rocks with grain sizes between 20 cm and 36 cm came loose and rolled downhill. In order to demonstrate the capability of the ICProx-algorithm one epoch of the scenario has been significantly altered both in position and orientation. By doing this registration of two independent coordinate systems is simulated. Again the 4-PCS-algorithm has been used for pre-alignment of both epochs while subsequently the ICProx-algorithm was deployed in order to reveal regions that were subject of deformation. The centre part illustrates difference vectors that are the result from local application of the ICP within the ICProx-algorithm. Therefore the entire dataset has been segmented into octree cells of 30 m so that in total 661 cells emerged. In order to locally determine transformation parameters candidates have been sampled with 0.75 m on average. Despite the fact that difference vectors are datum dependent some peculiarities are notable. Apart from the glacier tongue where the vectors are significantly larger compared to its surroundings other regions can also be identified. The reason for this is caused by a low geometric contrast in the according cells. As a consequence the ICP converged into different local minima. The right part of the illustration shows the uncertainty which has been computed by the ICProx-algorithm. It is apparent that the uncertainty is very low for the according octree cells within the vicinity of the glacier tongue which is then increasing in the upper left and right parts. The reason for this is provoked by unfavourable perspectives during data acquisition which lead to a lower local sampling rate.

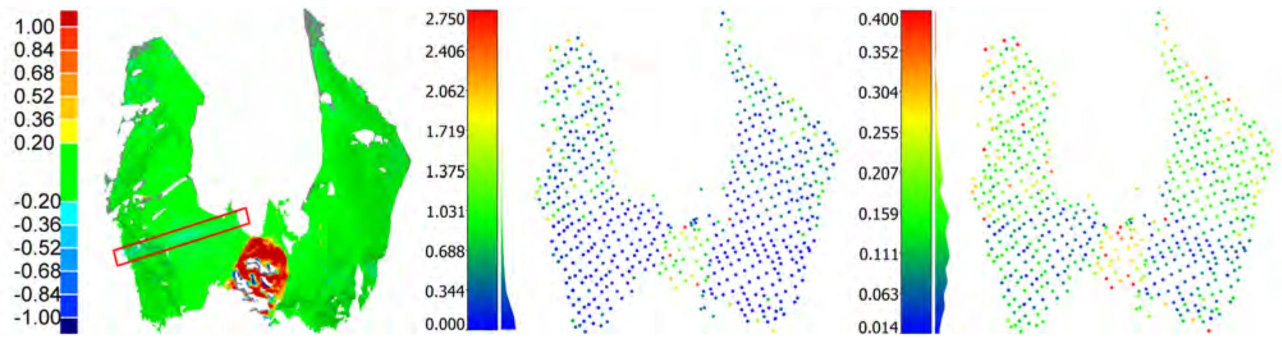

Figure 6.2: *Inspection map in metres based on georeferenced data (left), difference vectors for all centroids (centre) and uncertainty of all centroids (right)*

After congruence analysis the largest subset contains 441 cells that are considered as being stable. If one would naively approach the stated problem with exact knowledge of the amount of octree cells that were subject of deformation $1.38 \cdot 10^{181}$ combinations would arise. Hence, the computational demand of the stated problem is extensive which justifies the chosen cascading strategy that has been introduced in subsection 4.5.4. The left part of figure 6.3 shows a colour coded confusion map where the same colour scheme as in subsection 4.5.5 has been applied namely

- Blue: Area is stable, detected as stable (true positive).
- Cyan: Area is stable, detected as unstable (false negative).
- Red: Area is unstable, detected as stable (false positive).
- Orange: Area is unstable, detected as unstable (true negative).

The percentage of classes is depicted in table 6.1 and reveals that a comparably large part of stable areas has not been correctly assigned. The reason for this can be found in the weak geometric characteristic in the according cells.

Table 6.1: *Confusion matrix of the outcome*

55%	37%
3%	5%

A look at the glacier tongue in the left part of figure 6.3 shows that several octree cells partially reach into this region of deformation. This effect is caused by the comparably low amount of candidates within these areas that falsify locally derived transformation parameters within the statistical boundaries of uncertainty. The narrow band on the left side of the scene has been falsely assigned as being stable due to its limited spatial expansion. The remaining parts of figure 6.3 show inspection maps based on comparisons between the georeferenced epoch and their according versions which have been altered in position and orientation after application of the ICProx (centre) and ICP (right). Hence, the motivation for conducting this analysis is to reveal differences between the two surface based approaches against target based geo-referencing. A look at the centre part of figure 6.3 shows that the majority of the scene complies within +/- 5 cm while some parts feature deviations between 5 and 14 cm. These differences may be triggered by leverage effects due to an insufficient sampling of artificial targets for geo-referencing. This suspicion substantiates if one has a look at the centre part of figure 6.1 where it can be seen that all targets do not surround the glacier tongue and are only located in north-westerly direction (above the glacier tongue in the figure). On average the differences between reference and the result computed based on the ICProx sum up to 58 mm for points that are located above the reference surface and 45 mm for points below it while the standard deviation among the two datasets measures 57 mm. The right part of the figure again corroborates that the ICP is not an appropriate algorithm for registration of point clouds that were subject of deformation. Again the same statistical measures have been computed as before where the mean deviation among the datasets sum up to 174 mm for points above the reference respectively 239 mm for points below the reference. The according standard deviation of all residuals amounts to 242 mm. It has to be mentioned that the listed statistic measures are somewhat whitewashed due to the fact that only deviations within the specified range between +/- 50 cm have been considered but not the grey coloured areas where the discrepancies excess these boundaries.

6.2 Monitoring of an ice glacier

This subsection is focussing on monitoring Austria's largest glacier - the Pasterze. Just as the rock glacier, which was subject of the previous subsection, the Pasterze is located in the Hohe Tauern range of the Austrian Alps. The geometric behaviour of this glacier is of scientific interest since 1878, as reported by Wakonigg

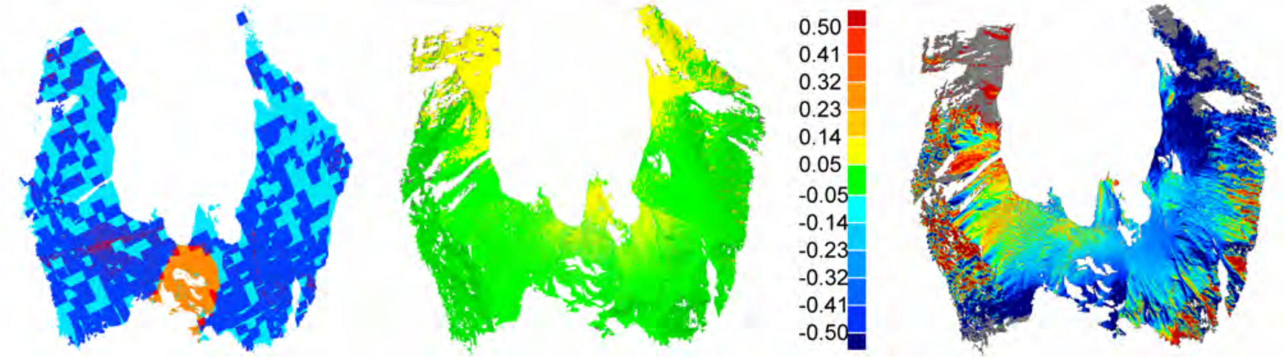

Figure 6.3: *Colour coded confusion map (left), inspection map in metres based on a comparison to the georeferenced outcome by usage of the ICProx (centre) and the ICP (right).*

& Lieb (1996), which makes it one of the longest documented glaciers in the world. The glacier spans over 17 km^2 while the tongue is divided into a clean ice part and a debris covered section with a visibly lower quotient of reflection. Since the little ice age the glacier has lost approximately 35% of its surface area as well as about 60% regarding its volume. The current retreat of ice masses on the earth provoked by changing climate conditions is also detectable in a study area that spans over 150 ha and has been monitored by TLS since 2001 under patronage of the University of Graz, Austria. All results presented in this subsection focus on detection of geometric changes within the period of 2010 and 2012 and have been captured by Michael Avian of the University of Graz, Austria. On average the annual elevation change within the debris covered part sums up to approximately 3.7 m while 6.3 m were detected in the clean ice section between 2011 and 2012. A detailed summary on the Geological situation of the glacier can be found in Avian (2015).

The left part of Figure 6.4 depicts an aerial image of the glacier's terminus (Avian 2015 p. 32) where a circle represents the study area. The red dotted line highlights the boundaries of the glacier. On the right of the figure a look into the valley is shown (Avian 2015 p. 33) where a red dot signifies the viewpoint of the scanner. Little white circles with red boundaries indicate target locations which have been placed for registration purposes. It has to be mentioned that the distribution of targets is very unfavourable as they are not surrounding the area of interest. As a consequence the computed transformation parameters can only be seen as an approximate solution as they are very likely to be subject of extrapolative effects and hence have to be refined by e.g. surface based registration. The necessity of revealing deformed regions prior to performing co-registration has already been extensively stated so that the ICProx-algorithm is deployed in the following to solve this task for a comparison among the datasets from 2010 and 2012.

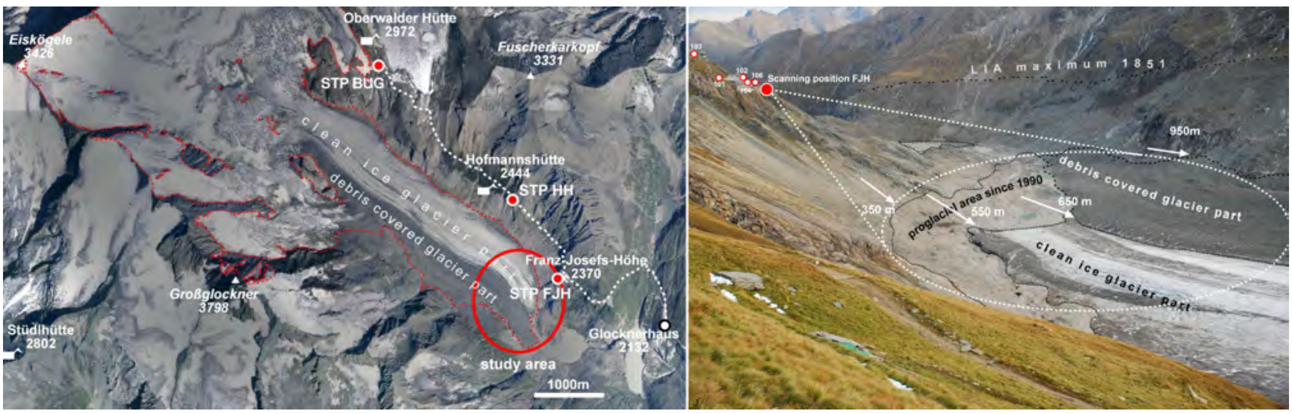

Figure 6.4: *The left part depicts a bird's eye view of the glacier's terminus* (Avian 2015 p. 32) *while the right part shows an oblique look into the valley* (Avian 2015 p. 33)

Data acquisition of the epochs has been carried out by usage of a RIEGL LSM Z620, a TLS that is capable to measure distances of up to 2000 m. Avian (2015 p. 84) specifies the ground sampling distance for object distances of 300 and 800 m, which denote the closest as well as the most remote regions in the study area. The dataset captured in 2010 serves as a reference epoch and features a GSD of 20 cm for an object distance of 300 m as well as 54 cm for points that are 800 m away from the scanner. The respective numbers for the 2012 epoch are 16 cm and 42 cm. In terms of captured points the reference epoch is described by 2.5 million points while the epoch of 2012 contains 3.6 million points due to a higher GSD.

After pre-alignment the ICProx-algorithm has been applied to register the epoch of 2012 into the reference epoch. It can be expected that deformation occurred predominantly directly at the glacier so that comparatively large octree cells can be defined. Based on a fraction of the point cloud's extent a cell size of 52.5 m has been set which resulted in 923 cells. On average candidates have been sampled every 6 m which lead to approximately 40700 candidates. After application of the algorithm a congruent set consisting of 536 octree cells emerged. The mean residuals after registration based on stable regions sum up to 44.1 cm. An explanation for this rather large quality measure can be found in the comparably low ground sampling distance in relation to the rugged terrain. Based on expert knowledge a set of reference transformation parameters has been computed based on undoubtedly stable areas. This course of action is very time consuming and leads to a rather pessimistic selection process so that large quantities of valid information are left out of the co-registration process. Subsequently the confusion matrix depicted in table 6.2 has been computed which shows that 79% of all cells have been correctly segmented. In total 31% of the stable regions have not been correctly detected by the algorithm which describes a loss of valid information. Only 2% have been assigned as being stable even though they were subject of deformation.

Table 6.2: *Confusion matrix of the outcome*

43%	19%
2%	36%

A look at the left part of Figure 6.5, which has been generated based on the colour scheme from section 4.5.5, shows that the majority of red coloured regions is located within the transition region between glacier tongue and bedrock.

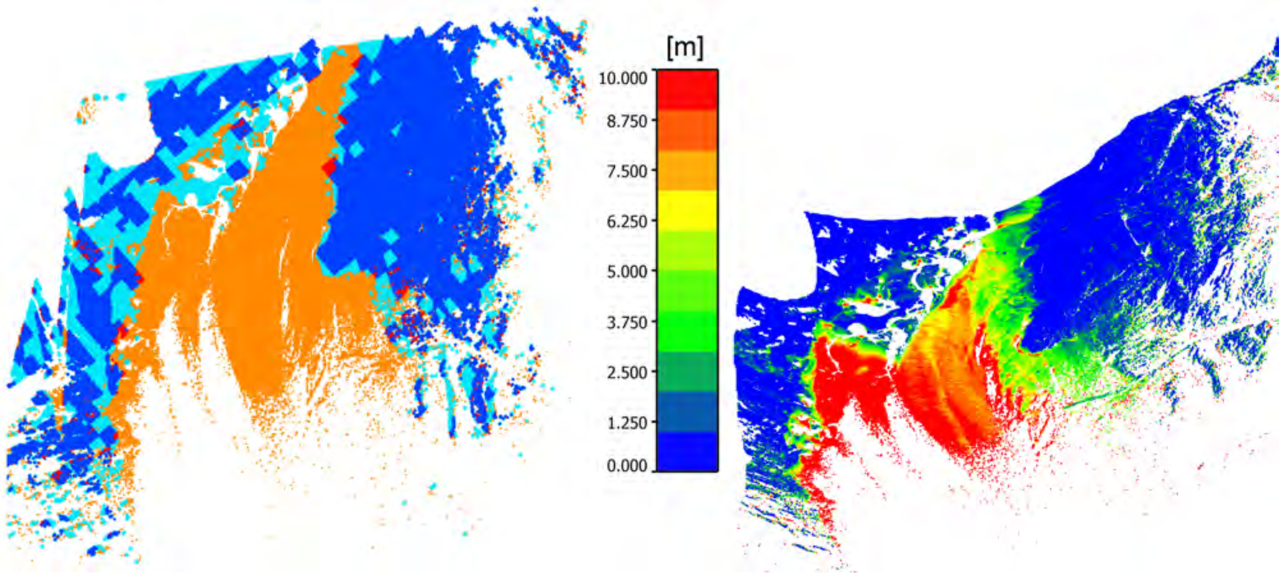

Figure 6.5: *Confusion map of the segmentation with the ICProx (left) and resulting inspection map (right)*

The right part of the figure shows an inspection map of the scene that has been generated based solely on detected stable regions. Note that the unit of the colour bar is given in metres. Tremendous elevation changes of up to 10 metres are visible on the glacier's tongue within just two years. The ICProx has again been successfully applied on a practical dataset while the challenge was twofold: the extent of the scene lead to almost 1000 octree cells and the magnitude of deformation surpassed all presented examples in this thesis.

6.3 Monitoring of tooth wear

The vast majority of fields of application for deformation monitoring can be associated to man-made structures or geo-related issues. This subsection covers an example related to the untrodden field of dentistry. In cooperation with the department of orthodontics, dentofacial orthopedics and pedodontics of Charité Berlin - Universitätsmedizin Berlin, Germany, two potential research questions have been identified. The first one is related to tooth alignment where a controlled tooth movement is activated by removable aligners (Kravitz *et al.* 2007) or braces. Optimisation of the biomechanical force system established between wires and brackets is supposed to avoid unwanted side-effects and accelerate tooth-movement. In order to achieve optimal results the aligner or wires are individualised for the purpose of establishing a requested force system in the periodontal ligaments. The research questions in this context are how precise the teeth follow their predefined trajectory and how well they are finally aligned. Based on magnetic resonance imaging (Ventura *et al.* 2013) or intraoral scanners (Cuperus *et al.* 2012) three-dimensional datasets can be acquired that form a potential base for monitoring tooth-movement.

A methodical hurdle of this task is the problem that a congruence model for quantification of deformation cannot be assumed. Thus, a novel deformation model has to be developed in order to overcome the stated issue. The second potential field of research in dentistry is associated to tooth wear monitoring. Park *et al.* (2014) define tooth wear as noncarious loss of tooth substance as a result of attrition, abrasion, and erosion. Hence, the task is to determine pre- and post-orthodontic volumetric differences of individual teeth between epochs which requires transformation of epochs into a common coordinate system. First studies on the subject have been conducted by Choi *et al.* (2010), Park *et al.* (2014) and An *et al.* (2015). The problem of rejecting deformed areas from the datasets prior to registration has been conducted manually, a course of action that should be implicitly avoided. Deformation between treatment stages can occur as a consequence of tooth wear but also very likely due to gingival recessions or hyperplasias. Since clinical studies always require a comparably large sample of patients in order to prove a scientific hypothesis, it is obvious that manual rejection of deformed regions have significant disadvantages.

Based on the aforementioned disadvantages a proof of concept has been carried out with the ICProx-algorithm. Therefore a plaster cast of a patient was used. In order to simulate tooth wear and gingival recession the model has been manipulated using a dental bur. As these manipulations have been defined by the executing dentist, a ground truth was known that is used for the sake of methodical assessment. The cast was digitised by using a GOM ATOS I structured light scanner before and after manipulation. Figure 6.6 illustrates the dataset of a patient's lower jaw on the left where grinding had been simulated in the lower left canine. Unaltered regions are tinted in green while manipulated areas are coloured in yellow. It can be seen that notable modifications to the original dataset have been introduced in the vicinity of the molar teeth as well as the incisors' gingival tissue. In order to see if small cavities, which are for instance caused by dental caries, can be detected by the algorithm, holes have been drilled into the incisors. These holes are represented by four small speckles in the figure. After pre-alignment the datasets have been decomposed into 584 octree cells with edge lengths of 2.2 mm which is a fraction of the denture's extent.

Application of the ICProx-algorithm lead to 390 octree cells which have been assigned as being stable. The mean residuals after registration summed up to 0.14 mm based on 14839 established correspondences. A comparison between outcome of the respective results and the ground truth lead to a confusion matrix that is depicted in table 6.3. Again the amount of critical false positive regions - an area is unstable yet is detected as being stable - is comparatively low with 2%. Nearly a third of all cells have been falsely assigned as being part of deformed regions even though they were in fact unaltered.

Table 6.3: *Confusion matrix of the outcome*

58%	30%
2%	10%

A look at the centre part of figure 6.6 shows that the small holes on top of the incisors have not been detected as deformation due to their comparatively small magnitude. It is also obvious that large quantities of stable regions have not been correctly segmented. Yet, in summary the outcome is quite encouraging as a very challenging dataset has been automatically processed that could be used in the future to process data within clinical studies. The right part of figure 6.6 shows the resulting inspection map based on stable regions detected by the algorithm. Note that the unit of the colour bar is given in millimetres.

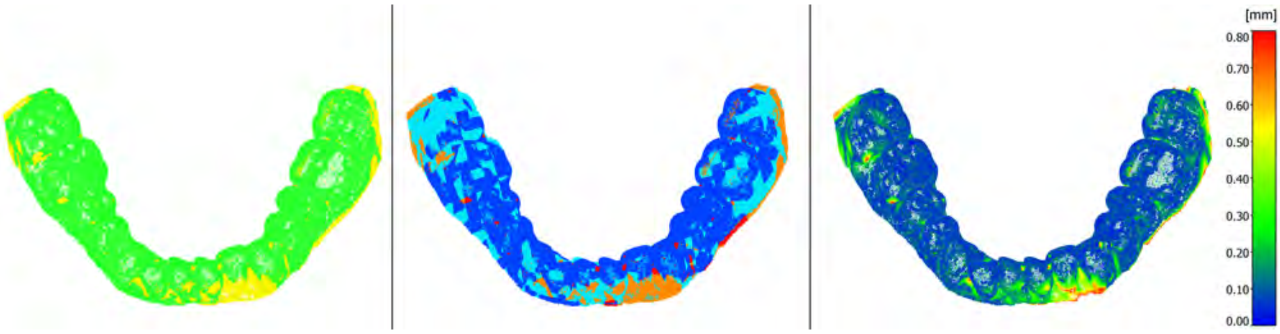

Figure 6.6: *Stable and deformed regions of the dataset (left), confusion map based on the outcome (centre) and resulting inspection map (right)*

6.4 Subsidence monitoring

Canada's province of Alberta has a long history in mining particularly in the town of Lethbridge where coal mining was initiated in 1872 and continued until 1965 (Sladen & Joshi 1988). Sladen & Joshi (1988) also raise concerns in their comprehensive article on potential hazards in form of subsidence as a cause of mining in Lethbridge - a relation that is well known (Bell *et al.* 1988). Another anthropogenic cause for morphological changes in Lethbridge is triggered by variations of the low groundwater level which potentially leads to subsidence, soil creep, slope failures or landslides (Ruban 1983). Berg *et al.* (1996) analyse the influence of lawn and garden irrigation onto the local water input. Hence, morphological changes need to be thoroughly monitored especially in vicinity to residential areas in order to prevent casualties and potential loss of homes.

In this subsection a subsidence which is regularly monitored by the University of Calgary, Canada is of interest. For data acquisition a camera equipped unmanned aerial vehicle (UAV) has been used (Neitzel & Klonowski 2011). Based on the captured imagery 3D-point clouds have been computed by means of semi-global dense matching (SGM) techniques (Wenzel *et al.* 2013). The successful application of this technique for monitoring of natural hazards has for instance been presented by Al-Rawabdeh *et al.* (2016). Figure 6.7 illustrates the boundary of the subsidence on the left that is highlighted by a pink line. The proximity to a residential area is apparent with a distance to the pictured road of approximately 50 m. The right part of the figure depicts the colour coded point cloud of the reference epoch from 2014, where the applied ground control points (GCP) for the sake of scaling are highlighted by pink circles. A successive epoch has been captured in 2015 in order to monitor the progression of the scarp and the subsidence.

In order to transform both epochs into a common coordinate system the ICProx-algorithm was used where the octree size has been set to 8 m which lead to 803 octree cells. This comparatively small octree cell size was

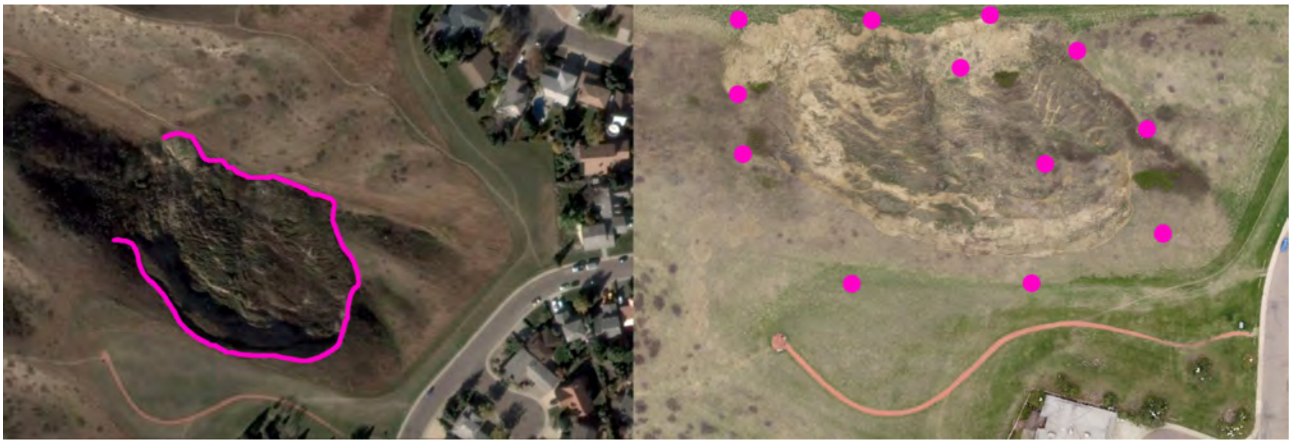

Figure 6.7: *Breaking edge of the subsidence (left figure based on Google Earth) and colour coded point cloud with control points (right)*

chosen due to the heterogeneous characteristic of the subsidence. As a result 318 cells have been recognised as being stable and were used for registration. The average misclosure between epochs sums up to 2.48 cm for 14740 correspondences. Based on a set of transformation parameters where deformation has been manually rejected a confusion matrix has been generated. A look at the matrix, that is depicted in table 6.4, shows that approximately 40% of stable regions have not been detected which is notably higher than in all previously presented cases.

Table 6.4: *Confusion matrix of the outcome*

40.2%	42.8%
0.2%	16.8%

Figure 6.8 illustrates the colour coded point clouds after registration on the left. The respective illustration is divided into two parts by a pink line where the left part shows the epoch from 2015 while the right part depicts the epoch captured in 2014. It can be seen that the breaking edge in the centre of the figure has expanded by about 10 m towards the residential area. In the centre of the illustration a confusion map visually rates the outcome of the segmentation process. One reason for the aforementioned high degree of undetected stable regions is the steady surface topography in some parts of the dataset which causes the ICP to converge into a local minimum. Another reason for this effect is provoked by the geometric characteristic of the subsidence which can be seen on the right of the figure. The depicted inspection map shows that the subsidence is heterogeneously sinking which leads to small stable islands. As octree cells in these regions are partially affected by deformation their rejection is inevitable.

6.5 Deformation monitoring in crash testing

The majority of registration problems in the context of deformation monitoring can be characterised as being “2.5D”. This term is used in analogy to geo-information science where it specifies that only one depth information respectively distance measurement can be assigned to a scanned direction of the TLS. In short it can be established that 2.5D-problems describe surfaces rather than complete 3D-objects. In order to see if the proposed ICProx-algorithm can successfully be applied to monitoring tasks in 3D an appropriate example will be processed in the following. Another difference to previously used test cases is the fact that each acquired epoch is assembled of eight scans which means that influences onto the outcome of the algorithm may be caused by the matching process that was required to compose every epoch. The chosen problem domain for this subsection can be

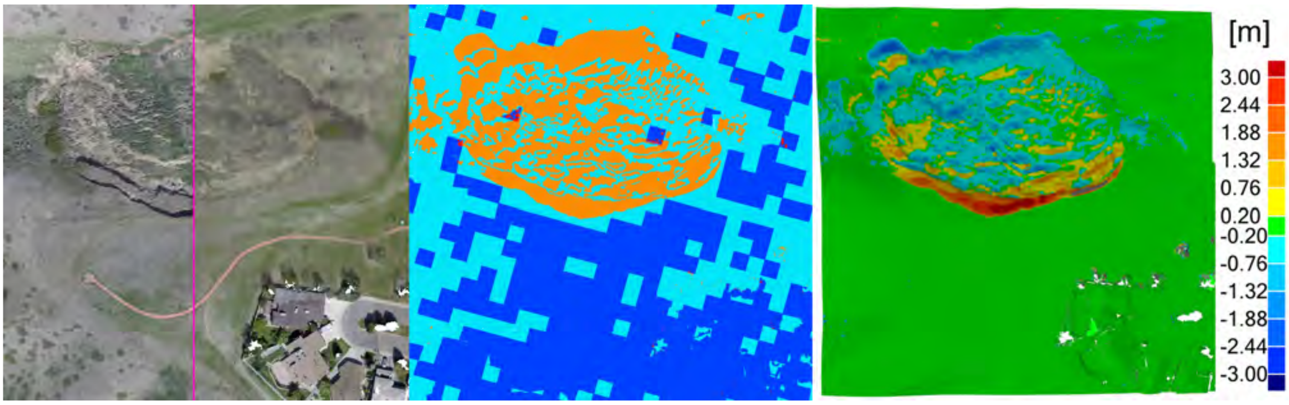

Figure 6.8: *Visual comparison of the two epochs (left), confusion map (centre) and inspection map (right)*

associated to accident research and hence features material documented in crash testing.

Despite the fact that the amount of fatalities in the German road traffic in steadily decreasing since the government introduced counteractive measures such as reducing the maximum speed on country roads to 100 km/h in 1973 or to introduce a stricter drink-drive-limit in 1998 the German authorities aim to reduce the number of annual casualties by 40% until 2020. From 387978 accidents that occurred in 2012 106606 victims were cyclists respectively pedestrians from which 919 are fatal casualties (Destatis 2012). Regardless of the outcome of an incident every single one of them has to be thoroughly documented either by police or accident assessors in order to clarify the question of guilt. A major question in this context is if all or which one of the involved parties broke the effective speed limit respectively disobeyed other effective traffic rules. Wagner & Rau (2000) revealed that even if outsiders witnessed an incident that their according travel speed estimation is always largely biased, regardless if the estimate came from laymen or professionals.

Hence current research focuses on collision speed estimation based on permanent deformation after an incident as reported by Pagounis *et al.* (2006) or Wood *et al.* (2009). The fundamentals for this field of research can be traced back to McHenry *et al.* (1967) or Campbell (1974) that showed the correlation between deformation and velocity of vehicles. This consequently allowed applying the energy theorem in this context which led to the equation for computation of the deformation energy (Burg & Moser 2009, pp. 261)

$$W_{def} = \frac{1}{2} \cdot m \cdot EES^2 \tag{6.1}$$

where m depicts the mass of a vehicle. The remaining parameter energy equivalent speed (EES) has been introduced by Burg & Zeidler (1980) and can be interpreted as an energy-equivalent measure for the deformation energy that was caused in a structure. In other words EES describes a velocity that a vehicle must have had during a collision with a rigid and static object to cause a resulting deformation. An advantage of EES is its direct applicability for accident reconstruction (Burg & Moser 2009, pp. 261). Even though it can't be measured it is derivable by several methods namely (Burg & Moser 2009, pp. 941):

- Execution of comparative crash tests: An identical or similar vehicle is subject of a collision under assumed circumstances. The EES is estimated by the collision speed for which the damage symptoms are comparable to the original vehicle.
- Raster field method: This method is also based on crash tests and decomposes deformed regions of a vehicle into laminar and planar segments. Deformations are assigned to segments based on which the EES is computed.
- By determination of volumetric changes caused by a collision. A prerequisite of this method is that the shape of an object has to be known prior to a crash.

In summary it can be established that only one procedure is not dependent to laborious crash tests which makes it quite attractive for current research even though information about a vehicle's shape has to be known in advance. Suitable sensors to capture the geometry of 3D-objects are TLS-systems as extensively outlined throughout this thesis while an undamaged reference 3D-model of the specific vehicle is required. Based on two states of an automobile an inspection or deviation map can be generated while the necessity arises to register the datasets strictly on stable or unchanged areas as discussed in chapter 4 in order to being able to compute the desired deformation volume. In combination with additional information such as materialistic properties and so called boundary conditions all required input sources are given in order to set up a so called finite element model (FEM). The interested reader is referred to textbooks such as Zienkiewicz (1971). Usually FEM's are used to compute displacement of a defined object under certain load while in accident research the question is posed from a slightly different perspective: Which forces must have been present that led to the observed deformation? Based on the calculated forces an estimation of the collision speed can be made. Hence this section undertakes the first steps towards the outlined long-term goal, namely computing the deformation volume, which has been generously supported by Dr. Michael Weyde respectively Priester und Weyde accident assessors who also hold all rights of the featured material.

Two experiments have been conducted while the first one simulated a pedestrian collision. As varnished or shiny surfaces lead to noisy datasets when captured with a TLS the used car in this crash test – a Pontiac Trans Sport – has been covered with a grey and dull base coat as depicted on the left of figure 6.9. An area of great interest for accident assessors within the context of pedestrian collisions are the windows as most of the forces during impact are absorbed by them. As translucent materials cannot be acquired by TLS a dulling spray has been applied – see centre part of figure 6.9 - that can easily be removed with a cloth if required. After completion of all preparing steps data acquisition of a reference epoch was carried out.

Figure 6.9: *Pontiac Trans Sport varnished in a base coat (left). Covering process of the windows with dulling spray (centre) and data acquisition with a Z+F Imager 5006h TLS (right).*

For the first crash test an 80 kg crash test dummy has been attached to a frame by using a rope. In order to avoid falsification by the fixation a light barrier, that was located 30 cm before the dummy, detached the rope. The collision speed was 80 km/h while a driver steered the vehicle. The left part of figure 6.10 shows the scene shortly after impact between car and dummy. It can be seen that torso and lower body of the dummy were detached an effect that can occur in reality as a consequence of the high speed. The centre part shows the car after the crash test while a notable deformation of the windscreen as well as a slight dent of the front lid can be seen. Note that the doors were opened manually for control purposes of internally placed sensors and not as a consequence of the impact. After the crash the wind screen has again been covered by dulling spray and a successive epoch was scanned as illustrated by the intensity image of the point cloud on the right of figure 6.10. Based on these two epochs the first experiment by usage of the ICProx-algorithm has been conducted.

The post processing part has been again initiated with a pre-alignment via 4PCS-algorithm while subsequently conducting the ICProx-algorithm. An amount of 28 octree cells with cube sizes of 1 m contained the dataset. It has to be mentioned that the chosen cell size is comparably large in relation to the vehicle's dimensions. However, this was necessary in order to ensure sufficient geometric contrast despite the laminar characteristic of the vehicle. The resolution for candidates has been set to 10 cm on average leading to 2965 points. As a result of the ICProx-algorithm 43% of all octree cells were declared stable containing 38% of the candidates.

Figure 6.10: *Dummy collision at 80 km/h (left), deformation of the wind screen (centre) and intensity image of the according point cloud (right).*

The average residuals after ICP-matching based on the detected stable areas sums up to 4.6 mm. Based on all detected stable areas transformation parameters have been computed and applied to the successive epoch as a whole. Subsequently an inspection map has been generated that is depicted on the left of figure 6.11. Notable deformations can be found on the windscreen, the number plate as well as the bonnet. A colour coded confusion map that assesses the outcome of the classification process can be seen in the right half of figure 6.11. Note that the colour scheme of the inspection map does not apply to the confusion map. It is interesting to see that not all stable areas were detected despite the fact that only 7% of the car's body have been subject of deformation. Reasons for this can be found by insufficient local geometric contrast that caused the locally applied ICP to converge into local minima. Additional effects may also be caused by the registration process of individual epochs. The reason why the mud guards have not been detected as stable even though the geometric contrast is sufficient is because the wheels were in a different steering respectively rotation angle in comparison to the reference epoch. Deformed regions that have been falsely classified as stable can be spotted on the left side of the bonnet and around the windscreen highlighted in red. The width of these areas measure between 10 and 20 cm so that only very few candidates have been sampled in it in relation to the rest of the cell. Hence their impact was comparably small during cell-wise determination of transformation parameters. Apart from the inspection map the volumetric change that was caused by the crash has been computed which sums up to 79 litres and hence describes the input parameter for EES-computation. In summary it can be stated that the generated results coincide with the ones of the accident assessors.

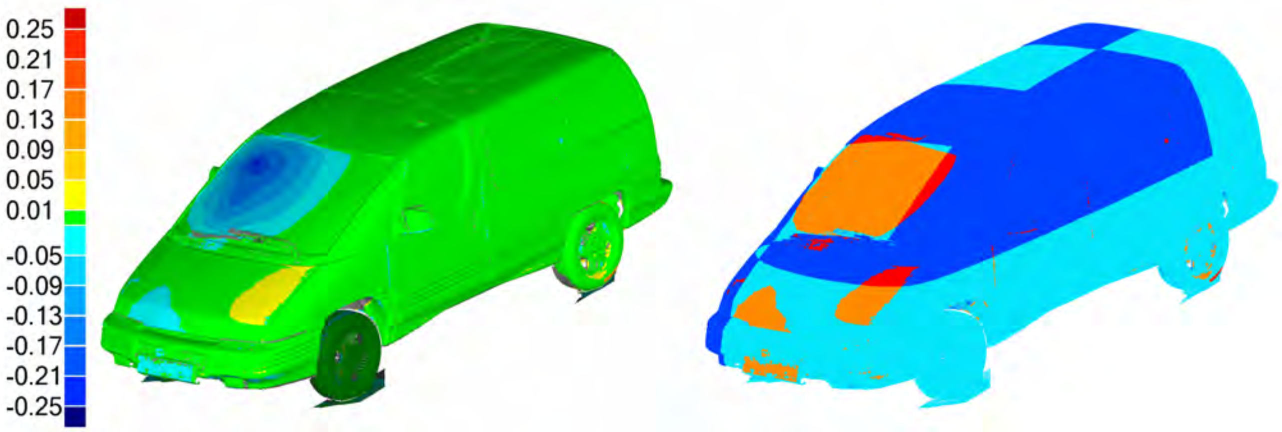

Figure 6.11: *Colour coded inspection map (left) and confusion map based on the ICProx's results (right)*

The second crash test simulated a collision to the tail end of a traffic jam. Therefore the remotely controlled Pontiac hit three identical Opel Corsa's at 96 km/h. The gearboxes of all static cars engaged the first gear while the handbrakes were pulled. The left part of figure 6.12 illustrates the first impact onto the first silver Opel. Apart from this impact three other ones occurred involving the red Opel at first, then the green one and finally a dirt pile. After the crash test the Pontiac was pulled back to a flat area in order to capture its deformed body by TLS. The right side of the vehicle is depicted in the centre part of figure 6.12. It can be notably seen that the mudguard as well as the front passenger's door were subject to substantial deformation while the sliding door slid out off its upper hinges. A look at the sliding door as well as the front lid reveals that larger areas of these parts have been torn apart as the Pontiac Trans Sport features a plastic body. The according left side can be found on the outer right of the same illustration. As this side was only exposed to a minor collision damages are only visible on the mudguard while the exterior rear view mirror was torn off. The occurred damages can be characterised as large in terms of surface area. Yet, the deformations only sum up to several centimetres.

Figure 6.12: *Moment of the first impact (left), right side of the test vehicle after the crash (centre) and according left side (right)*

Again the first step of post processing was a pre-alignment via 4PCS-algorithm. Subsequently the ICProx-algorithm has been used initialised with octree cell sizes of 0.5 m and an average distance between adjacent candidates of 5 cm. The comparably small size of octree segments bears the risk of low or non-existent geometric contrast within several cells e.g. on the rear side or the roof. Hence the given task can be categorised as the most challenging thus far. In total 9705 candidates have been distributed over the body of the car which was organised in 121 octree cells. The ICProx identified a congruent set of 31 octree cells that included 3114 candidates. Based on these points ICP matching transformed the point cloud of the third epoch into the reference epoch while the misclosures summed up to 3.9 mm on average. Finally, an inspection map was computed that revealed mean deformations of +35 mm / -44 mm. Due to the fact that an entire 3D-object is subject of this subsection two perspectives of the respective outcome are depicted from the front left side as well as from the rear right side. The illustration is grouped into inspection maps on the left of figure 6.13 as well as confusion maps on the right. As before the sign of the inspection map indicates if deformations occurred above or below the reference dataset. In contrast to all other featured examples a substantial amount of "growth" can be spotted. The reason for this is the skewed sliding door, which is depicted by a triangular shaped yellow area in the left part of figure 6.13, as a result of the significant impact. Furthermore it can be seen that large parts of the right side were compressed by several centimetres. Grey tones designate areas where the deformation was outside of the boundaries of the specified colour bar whose units are metres. The right part of figure 6.13 illustrates confusion maps of the vehicle based on the outcome of the ICProx-algorithm. In evaluative terms the result has to be rated quite positively even though a dataset with unfavourable characteristics has been processed. The area around the wheel guards have been not identified as being stable presumably due to the fact that the wheel was in a different position which may have left to falsification of the locally derived transformation parameters especially in the rotational components. Large stable regions of the car's carriage haven't been correctly detected which is caused by the low local geometric contrast within the according octree cells. Only few red parts are notable that describe an undesired outcome. Yet, it has to be said that these areas are located where the degree of deformation was comparably low so that no significant falsification of the transformation parameters can be assumed.

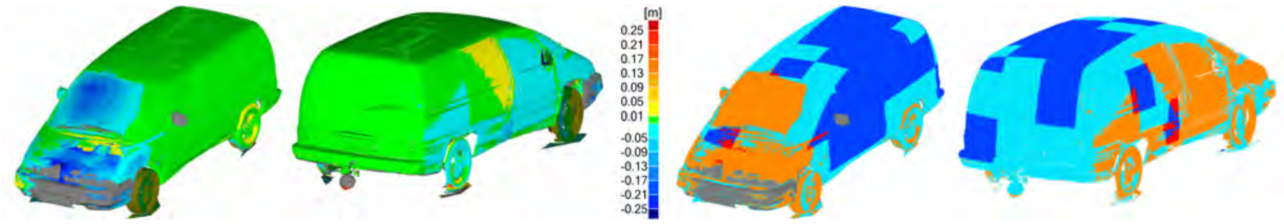

Figure 6.13: *Inspection maps of the car after the second crash test (left) according confusion maps based on the outcome of the ICProx (right).*

6.6 Concluding remarks

In summary all presented scenarios were challenging for the ICProx-algorithm in terms of extend and geometric characteristics. Regarding the first two scenarios that featured glaciers the cascading strategy proposed in subsection 4.5.4 enabled to process even very large datasets in terms of extend. A circumstance that was apparent in all shown examples is that weak local surface topography leads to unrecognised octree cells even though they haven't been subject to deformation. In order to avoid consideration of "weak" octree cells within congruency analysis - which also will reduce computational cost - an assessment scheme will be implemented in the future. A suitable scheme for this sake has already been introduced in subsection 3.2.4.2. On the other hand it is obvious that the chosen strategy of decomposing the object space has certain limits namely that it is not suitable for datasets that feature a smooth and steady surface such as dunes or snowy hills. In order to overcome this limitation a mixture of geometric and radiometric information will be pursued in the future. In order to adapt the ICProx-algorithm to the problem domain of section 6.3 several changes need to be implemented in the future. The first step would be to segment individual teeth from the original dataset rather than decompose the object space into octree cells. Subsequently individual teeth have to be dissected in order to being able to reveal tooth wear. A problem that occurred particularly in section 6.4 was related to numerous octree cells that were partially subject to deformation yet contained notable stable regions. Future works have to find ways of how to retrieve this information.

7 Conclusion and outlook

The thesis at hand extensively discussed well established and contemporary methods for deformation monitoring in chapter 2. In addition drawbacks and limitations of existing methods served as research questions respectively the motivation for novel developments in this thesis. Chapter 3 introduces a stochastic model for TLS where the observed intensity is used to estimate the theoretical precision of reflectorless distance measurements. Subsequently a combinatorial viewpoint planning algorithm is proposed that is used to determine the most economic acquisition configuration. An extension of the basic algorithm is also proposed where a sufficient overlap between scans has to be present so that a valid solution is connectable by surface based registration. In order to achieve this adjacency matrices have been applied that are usually used in the context of congruency analysis or routing. A beneficial side effect of introducing geometric criteria is an enormous reduction of the solution space that leads to a significant reduction of computational cost. The introduction of the second geometric criterion numerically assesses the given geometric contrast of an overlapping region between point clouds and hence allows to draw conclusions whether two point clouds can be reliably registered or not. The use of the previously mentioned stochastic model within the view point planning algorithm firstly allows receiving an estimate about the achievable precision of observations in dependence to one or several chosen viewpoints.

The main topic of this thesis was subject of chapter 4 where two algorithms for identification of deformation within point clouds captured in different epochs have been proposed. Both algorithms decompose the object space into spatial segments by using an octree structure. Subsequently different strategies are used to identify deformation and to compose the segments into congruent clusters. Finally transformation parameters are computed based on the largest congruent cluster which is assumed to be free of deformation. The DefoScan++-algorithm compared distances among corresponding points in order to reveal deformation, a procedure which showed to be very demanding in computational terms. A major drawback is caused by the sequential clustering process where the solution is dependent to the order of analysis. In addition effects induced by the chosen octree cell size revealed a significant influence onto the outcome. Yet this algorithm is the first one of its kind that models the uncertainty of a TLS in order to being capable to identify deformation within point clouds. As a predecessor the ICProx-algorithm has been developed that addressed the major drawbacks of the DefoScan++-algorithm. The first improvement is associated to the identification which is now based on locally derived transformation parameters. In order to define stochastic boundaries for the clustering process respectively the congruency analysis an advanced method has been proposed that models the uncertainty for an entire octree cell. In order to overcome issues caused by sequential methods NEITZEL's (2004) maximum subsample method has been adapted from point-wise measurements to quasi-laminar observations. A major hurdle of combinatorial approaches is its overwhelming complexity even for moderately sized networks of for instance 30 points. In order to tackle this significant problem a hierarchical procedure has been implemented that breaks the entire problem into manageable portions. Even though this approach led to satisfactory results future work will focus on alternative methods based on graph theory. Effects onto the outcome caused by tuneable parameters have been extensively investigated while the chosen octree size had the most significant impact. The robustness against deformation was a desired yet vital capability of the algorithm while the ICProx-algorithm was able to withstand a degree of more than 60% of contamination within the given data. Regarding data quality both algorithms require a sufficient geometric contrast as well as a satisfactory local resolution of the given point clouds. If the last-mentioned demand is not satisfied then deformation cannot be distinguished from noise.

The first part of chapter 5 conducts variance-covariance propagation on surface based deformation monitoring in order to clarify whether statistically significant geometric changes occurred in between epochs. It has been shown that the estimation of normal directions, respectively the determination of correspondences between epochs, plays the most influencing role in this context. Scientific efforts in the future should develop entirely novel methods for quantifying deformation. This can be justified by the most crucial step in the processing chain that is described by the determination of correspondences between points in one epoch to triangles in the other. This course of action is applied by all non-parameter based procedures that were described in 2.5. The problem of this perception is that correspondences are computed based on given data and not in regards of where an instrument was located at different epochs within the area under investigation. As a consequence the outcome of registration processes have to be taken into account. The second part of the section introduces a novel method for visualisation of deformation in form of inspection maps on arbitrary surfaces by usage of a projector. As discussed in chapter 4 the ICProx-algorithm proofed to be the superior algorithm for automatic identification of deformation within point clouds. Hence, chapter 6 applies the algorithm to different scenarios that are challenging in terms of geometric properties or extend.

Even though the ICProx-algorithm is already quite advanced in terms of robustness and computational efficiency even on large datasets some aspects require to be tackled in the future. As the process chain of fully automatic deformation monitoring still relies on Aiger's *et al.* (2008) 4PCS-algorithm for pre-alignment of point clouds issues concerning the robustness become obvious even at a considerably low degree of contamination. Hence, a combinatorial pre-registration algorithm has to be developed that models the uncertainty of features based on the idea described in the ICProx-algorithm. This novel algorithm should not only consider radiometric but also geometric features for registration in order to make use of all available information that is inherent. The current implementation of the ICProx only considers octree cells that are completely free of deformation. As a result valid information from cells that are only partially subject of deformation is neglected a circumstance that should be avoided.

Concerning the stochastic model described under section 3.1 the author sincerely hopes that other TLS manufacturers will adopt their specification sheets in a similar manner. The reason for that can be justified by the fact that all available specifications have to be rated as unsatisfactory from an engineering geodesist's perspective. While the developed procedure has been applied to a phase based instrument future research has to be adapted to time-of-flight scanners where distance measurements are not repeated several times. The most important aspects in engineering geodesy are accuracy and reliability yet they are barely addressed in any article. Prospective research has to enforce usage of these terms and their benefit to the user. The so called global test of the adjustment is another very important aspect within this context as it checks the functional as well as the stochastic model against imperfections. Future research will analyse how this vital check can be introduced into the processing chain of TLS. The existence of a stochastic model also allows weighing observations in relation to their theoretical precision yet section 5.1 revealed the fact that derived observations have to used and not measured quantities. This fact can again be associated to the varying point distribution on an object's surface in dependence to a chosen viewpoint and leads to unfavourable effects. Hence, it has to be clarified how observations can be weighted for instance in the context of the ICP-algorithm or within deformation monitoring.

The most popular model for deformation monitoring is the congruency model. A prerequisite for this model is that a portion of the area of interest remains unaltered respectively geometrically stable in order to being able to transform all epochs into a common coordinate frame. For the given case that point clouds serve as an input the stable regions within the scene have to provide a sufficient geometric contrast. If this precondition is not fulfilled the congruency model cannot be applied. Since several scenarios can't be stressed in these terms a novel deformation model has to be developed in the future as it is of vital importance for the field of engineering geodesy from a political point of view. This model has to describe surface changes based on alterations of a parametric description such as basis splines (de Boor 1978), a possibility which hasn't been addressed for this problem yet. A potential field of application for this novel deformation model is for instance monitoring of natural hazards. Due to climate change invoked 'secondary' effects such as avalanches and or rainfall-triggered landslides (Anderson & Bausch 2006) the urge for the development of a parametric deformation model becomes obvious as the impact of natural risks not only threatens the food supply chain (Schmidhuber & Tubiello 2007) but also the life of millions and their belongings. An example for the potential use of parametric deformation models can be associated to the field of maritime dynamics and ship building. According to the International Maritime Organization (IMO) 90% of the world's goods are hauled by ships while the annual loss of cargo ships sums up to more than 220 (Kaluza *et al.* 2010, IMO 2015). Apart from unforeseeable and hence uncontrollable reasons for loss of ships the distribution of containers has a major influence onto its maritime stability. Thus, the loading process should be monitored in order to verify if unacceptable deformations occurred. As the range of deformation for large cargo ships lies in between several decimetres up to a metre laser scanners can be considered as a suitable instrument to capture a ship before and after loading. For this purpose, first investigation with kinematic laser scanning for acquisition of ships in motion have already been conducted which led to promising results (Wujanz *et al.* 2013c).

Bibliography

Abellan, A., Jaboyedoff, M., Oppikofer, T., Vilaplana, J. M. (2009): Detection of millimetric deformation using a terrestrial laser scanner: experiment and application to a rockfall event. Nat. Hazards Earth Syst. Sci., 9, pp. 365-372

Abellan, A., Vilaplana, J. M., Calvet, J., Garcia-Selles, D., Asensio, E. (2011): Rockfall monitoring by Terrestrial Laser Scanning-case study of the basaltic rock face at Castellfollit de la Roca (Catalonia, Spain). Natural Hazards and Earth System Science, 11(3), pp. 829-841

Abmayr, T., Härtl, F., Hirzinger, G., Burschka, D., Fröhlich, C. (2008): A correlation based target finder for terrestrial laser scanning. Journal of Applied Geodesy, 2(3), pp. 131-137

Ackermann, F. (1984): Digital image correlation: performance and potential application in photogrammetry. The Photogrammetric Record, 11(64), pp. 429-439

Aiger, D., Mitra, N., Cohen-Or, D. (2008): 4-points congruent sets for robust pairwise surface registration. Proceedings of the ACM SIGGRAPH 2008 symposium, New York, United States of America, pp. 1-10

Akca, D. (2007a): Matching of 3D surfaces and their intensities. ISPRS Journal of Photogrammetry and Remote Sensing, 62(2), pp. 112-121

Akca, D. (2007b): Least Squares 3D Surface Matching. Ph.D. Thesis, Swiss Federal Institute of Technology Zurich

Alba, M., Fregonese, L., Prandi, F., Scaioni, M., Valgoi, P. (2006): Structural monitoring of a large dam by terrestrial laser scanning. International Archives of Photogrammetry, Remote Sensing and Spatial Information Sciences, 36(5)

Alba, M., Bernardini, G., Giussani, A., Rici, P., Roncoroni, F., Scaioni, M., Valgoi, P., Zhang, K., (2008a): Measurement of dam deformations by terrestrial interferometric techniques. International Archives of Photogrammetry and Remote Sensing: pp. 133-139

Alba, M., Roncoroni, F., Scaioni, M. (2008b): Investigations about the accuracy of target measurement for deformation monitoring. IASPRS, 37(B5), pp. 1053-1059

Alba, M., Roncoroni, F., Scaioni, M. (2009): Application of TLS for change detection in rock faces. Proc., Laserscanning09, pp. 99-104

Alba, M., Scaioni, M. (2010): Automatic detection of changes and deformation in rock faces by terrestrial laser scanning. In: Proceedings of the ISPRS Commission (Vol. 1501)

Al-Manasir, K., Fraser, C. S. (2006): Registration of terrestrial laser scanner data using imagery. The Photogrammetric Record, 21(115), pp. 255-268

Al-Rawabdeh, A., He, F., Mousaa, A., El-Sheimy, N., Habib, A. (2016): Using an Unmanned Aerial Vehicle-Based Digital Imaging System to Derive a 3D Point Cloud for Landslide Scarp Recognition. Remote Sensing

An, K., Jang, I., Choi, D. S., Jost-Brinkmann, P. G., Cha, B. K. (2015): Identification of a stable reference area for superimposing mandibular digital models. Journal of Orofacial Orthopedics/Fortschritte der Kieferorthopädie, 76(6), pp. 508-519

Anderson, J., Bausch, C. (2006): Climate Change and Natural Disasters: Scientific evidence of a possible relation between recent natural disasters and climate change. Requested study on behalf of the European Parliament's Environment, Public Health and Food Safety Committee

Appel, A. (1968): Some techniques for shading machine renderings of solids. In: Proceedings of the April 30-May 2, 1968, spring joint computer conference, pp. 37-45

AVIAN, M., LIEB, G.K., KAUFMANN, V. (2005): Recent and Holocene dynamics of a rock glacier system - the example of Langtalkar (Central Alps, Austria). Norsk Geografisk Tidsskrift - Norwegian Journal of Geography Vol. 59, Oslo, pp. 1-8

AVIAN, M., KELLERER-PIRKLBAUER, A., BAUER, A. (2009): LIDAR for monitoring mass movements in permafrost environments at the cirque Hinteres Langtal, Austria, between 2000 and 2008. Natural Hazards and Earth System Science, 9(4), pp. 1087-1094

AVIAN, M. (2015): Application of terrestrial laserscanning in the assessement of geomorphological processes in the Hohe Tauern Range Austria. Doctoral dissertation, Universität Graz, Austria

BAARDA, W. (1968): A testing procedure for use in geodetic networks, Netherlands Geodetic Commission, Publication on geodesy, vol 2, 841 no 5, Delft, Netherlands

BAARDA, W. (1973): S-transformations and Criterion Matrices. Netherlands Geodetic Commission, Publications on Geodesy, New Series, Vol. 5 (No. 1)

BAE, K.-H., BELTON, D., LICHTI, D. (2005): A framework for position uncertainty of unorganised three-dimensional point clouds from near-monostatic laser scanners using covariance analysis. International Archives of the Photogrammetry, Remote Sensing and Spatial Information Sciences 36 (Part 3/W19), pp. 7-12

BAE, K.-H. (2006): Automated registration of unorganised point clouds from terrestrial laser scanners. PhD thesis, Department of Spatial Sciences, Curtin University of Technology, Perth, Australia

BAE, K.-H., LICHTI, D. (2007): On-site self-calibration using planar features for terrestrial laser scanners. In: Proceedings of the ISPRS Workshop on Laser Scanning and SilviLaser

BAE, K.-H., LICHTI, D. (2008): A method for automated registration of unorganised point clouds. ISPRS Journal of Photogrammetry and Remote Sensing, 63(1), pp. 36-54

BAE, K.-H., BELTON, D., LICHTI, D. (2009): A closed-form expression of the positional uncertainty for 3d point clouds. Pattern Analysis and Machine Intelligence, IEEE Transactions on, 31(4), pp. 577-590

BARNHART, T. B., CROSBY, B. T. (2013): Comparing Two Methods of Surface Change Detection on an Evolving Thermokarst Using High-Temporal-Frequency Terrestrial Laser Scanning, Selawik River, Alaska. Remote Sensing, 5(6), pp. 2813-2837

BASELGA, S. (2010): Nonexistence of rigorous tests for multiple outlier detection in least-squares adjustment. Journal of Surveying Engineering, 137(3), pp. 109-112

BELL, F. G., CRIPPS, J. C., CULSHAW, M. G., LOVELL, M. A. (1988): A review of ground movements due to civil and mining engineering operations. Geological Society, London, Engineering Geology Special Publications, 5(1), pp. 3-31

BENTLEY, J. L. (1975): Multidimensional binary search trees used for associative searching. Communications of the ACM, 18(9), pp. 509-517

BERÉNYI, A., LOVAS, T., BARSI, Á., DUNAI, L. (2009): Potential of terrestrial laser scanning in load test measurements of bridges. Civil Engineering, 53(1), pp. 25-33

BERG, A., BYRNE, J., ROGERSON, R. (1996): An urban water balance study, Lethbridge, Alberta: Estimation of urban lawn overwatering and potential effects on local water tables , Canadian Water Resources Journal / Revue canadienne des ressources hydriques, 21:4, pp. 355-365

BESL, P., MCKAY, N. (1992): A method for registration of 3D shapes. IEEE Trans. Pattern Anal. Mach. Intell. 14, pp. 239-256

BIMBER, O., EMMERLING, A., KLEMMER, T. (2005): Embedded Entertainment with Smart Projectors. In: IEEE Computer, pp. 48-55

BJERHAMMAR, A. (1973): Theory of errors and generalized matrix inverses. Elsevier publishing

BÖDER, V., KERSTEN, T.P., HESSE, C., THIES, T., SAUER, A. (2010): Initial experience with the integration of a terrestrial laser scanner into the mobile hydrographic multi sensor system on a ship. ISPRS Workshop 2010 on Modeling of optical airborne and spaceborne Sensors, Istanbul, Turkey

BÖHLER, W., VICENT, M. B., MARBS, A. (2003): Investigating laser scanner accuracy. International Archives of Photogrammetry, Remote Sensing and Spatial Information Sciences, 34(Part 5), pp. 696-701

BÖHM, J., BECKER, S. (2007): Automatic marker-free registration of terrestrial laser scans using reflectance features. In: Proceedings of the 8th Conference on Optical 3D Measurement Techniques, Zurich, Switzerland, pp. 338-344

BRODU, N., LAGUE, D. (2012): 3D terrestrial lidar data classification of complex natural scenes using a multi-scale dimensionality criterion: applications in geomorphology. ISPRS Journal of Photogrammetry and Remote Sensing 68 (2), pp. 121-134

BUCKLEY, S. J., HOWELL, J. A., ENGE, H. D., KURZ, T. H. (2008): Terrestrial laser scanning in geology: data acquisition, processing and accuracy considerations. Journal of the Geological Society, 165(3), pp. 625-638

BUCKSCH, A., LINDENBERGH, R., VAN REE, J. (2007): Error budget of Terrestrial Laserscanning: Influence of the intensity remission on the scan quality. Proc. of GeoSiberia-2007, Novosibirsk, Russia

BURG, H. ZEIDLER, F. (1980): EES - Ein Hilfsmittel zur Unfallrekonstruktion und dessen Auswirkungen auf die Unfallforschung. Der Verkehrsunfall, Heft 4

BURG, H., MOSER, A. (2009): Handbuch Verkehrsunfallrekonstruktion: Unfallaufnahme, Fahrdynamik, Simulation (Vol. 10). Springer publishing

CAMPBELL, K. L. (1974): Energy basis for collision severity (No. 740565). SAE Technical Paper

CASPARY, W. (1996): Anmerkungen zum robusten Schätzen. Allgemeine Vermessungs-Nachrichten, 103, pp. 287-289

CHEBYSHEV, P. L. (1867): On mean values. J. de Math. Pures et Appliquées, 2(12), pp. 177-184

CHEN, Y., MEDIONI, G. (1991): Object Modeling by Registration of Multiple Range Images. Proceedings of the Intl. Conf. on Robotics and Automation, pp. 2724-2729, Sacramento, United States

CHEN, Y., GOTZ, D., HENSLEY, J., TOWLES, H., BROWN, M. (2000): Automatic Alignment of High Resolution Multi-Projector Displays Using an uncalibrated Camera. In: Proceedings of IEEE Visualization, IEEE CS Press, pp. 125-130

CHEN, Y., WANG, H., ROSEN, D. W., ROSSIGNAC, J. (2005): A point-based offsetting method of polygonal meshes. ASME Journal of Computing and Information Science in Engineering

CHMELINA, K., JANSA, J., HESINA, G., TRAXLER, C. (2012): A 3-d laser scanning system and scan data processing method for the monitoring of tunnel deformations. Journal of Applied Geodesy, Volume 6, pp. 177-185

CHOI, D. S., JEONG, Y. M., JANG, I., JOST-BRINKMANN, P. G., CHA, B. K. (2010): Accuracy and reliability of palatal superimposition of three-dimensional digital models. The Angle Orthodontist, 80(4), pp. 685-691

CHOW, J., EBELING, A., BESKEY, B. (2010): Low Cost Artificial Planar Target Measurement Techniques for Terrestrial Laser Scanning. Proceedings of the FIG Congress 2010 “Facing the Challenges - Building the Capacity” Sydney, Australia

Chuang, T. Y., Jaw, J. J. (2015): Automated 3d feature matching. The Photogrammetric Record, 30(149), pp. 8-29

Chvatal, V. (1979): A greedy heuristic for the set-covering problem. Mathematics of operations research, 4(3), pp. 233-235

Cignoni, P., Rocchini, C., Scopigno, R. (1998): Metro: measuring error on simplified surfaces. In: Computer Graphics Forum Vol. 17, No. 2, pp. 167-174

Cuperus, A. M. R., Harms, M. C., Rangel, F. A., Bronkhorst, E. M., Schols, J. G., Breuning, K. H. (2012): Dental models made with an intraoral scanner: a validation study. American Journal of Orthodontics and Dentofacial Orthopedics, 142(3), pp. 308-313

de Boor, C. (1978): A practical guide to splines. Number 27 in Applied Mathematical Sciences

Delaloye, R., Perruchoud, E., Avian, M., Kaufmann, V., Bodin, X., Hausmann, H., Ikeda, A., Kääb, A., Kellerer-Pirklbauer, Krainer, K., Lambiel, C., Mihajlovic, D., Staub, B., Roer, I., Thibert, E. (2008): Recent interannual variations of rock glacier creep in the European Alps. In: Proceedings of the Ninth International Conference on Permafrost (NICOP), University of Alaska, United States of America, pp. 343-348

Delaunay, B. N. (1934): Sur la sphère vide. In: Bulletin of Academy of Sciences of the USSR 7, Nr. 6, pp. 793-800

Destatis (2012): Unfallentwicklung auf deutschen Strassen 2012. Brochure of the German Federal Statistical Office

Dijkstra, E. W. (1959): A note on two problems in connexion with graphs. Numerische Mathematik, 1(1), pp. 269-271

Dirichlet, J. (1850): Über die Reduktion der positiven quadratischen Formen mit drei unbestimmten ganzen Zahlen. Journal für die Reine und Angewandte Mathematik 40, pp. 209-227

Dold, C. (2005): Extended Gaussian images for the registration of terrestrial scan data. ISPRS WG III/3, III/4, 3, pp. 12-14

Dold, C. (2010): Ebenenbasierte Verfahren für die automatische Registrierung terrestrischer Laserscans. German Geodetic Commission (DGK), Volume C, Nr. 646, Munich, Germany

Dold, C., Brenner, C. (2006): Registration of terrestrial laser scanning data using planar patches and image data. International Archives of Photogrammetry, Remote Sensing and Spatial Information Sciences, 36(5), pp. 78-83

Dold, C., Brenner, C. (2008): Analysis of Score Functions for the Automatic Registration of Terrestrial Laser Scans, International Archives of the Photogrammetry, Remote Sensing and Spatial Information Sciences, vol. XXXVII, Beijing, China

Eggert, D. W., Lorusso, A., Fisher, R. B. (1997): Estimating 3-D Rigid Body Transformations: A Comparison of Four Major Algorithms, MVA, Vol. 9, No. 5/6

Eling, D. (2009): Terrestrisches Laserscanning für die Bauwerksüberwachung. German Geodetic Commission (DGK), Volume C, Nr. 641, Munich, Germany

Elkhrachy, I., Niemeier, W. (2006): Stochastic assessment of terrestrial laser scanner measurements to improve data registration. ASPRS Annual Conference Reno, Nevada , United States of America

El-Sheimy, N. (2005): An Overview of Mobile Mapping Systems. FIG Working Week 2005. Cairo, Egypt

Esme, D. L., Bucksch, A., Beekman, W. H. (2009): Three-dimensional laser imaging as a valuable tool for specifying changes in breast shape after augmentation mammaplasty. Aesthetic plastic surgery, 33(2), pp. 191-195

Faig, W., Owolabi, K. (1988): Blunder detection in closeůrange photogrammetry using robust estimation. International Archives of the Photogrammetry, Remote Sensing and Spatial Information Sciences, Kyoto, Japan

Ferguson, T. S. (1961): On the rejection of outliers. In: Proceedings of the Fourth Berkeley Symposium on Mathematical Statistics and Probability (Vol. 1, pp. 253-287). University of California Press Berkeley

Fileformat (2015): Wavefront OBJ File Format Summary. http://www.fileformat.info/format/wavefrontobj/egff.htm (accessed 23.07.2015)

Fischler, M. A., Bolles, R. C. (1981): Random sample consensus: a paradigm for model fitting with applications to image analysis and automated cartography. Communications of the ACM, 24(6), pp. 381-395

Förstner, W. (1982): On the geometric precision of digital correlation. International Archives of Photogrammetry. Institut für Photogrammerrie der Universität Stuttgart. Schriftenreihe. 9: 24(3), pp. 231-243

Förstner, W. (1984): Quality assessment of object location and point transfer using digital image correlation techniques. International Archives of Photogrammetry, 25(3a), pp. 197-219

Förstner, W. (2000): Moderne Orientierungsverfahren. Photogrammetrie - Fernerkundung - Geoinformation, Heft 3/2000, pp. 163-176

Franke, J., Lichti, D., Stewart, M. (2006): MillMapper: A new tool for grinding mill thickness gauging. In: Proceedings International Autogenous and Semiautogenous Grinding Technology 2006, Volume III, pp III-75-III-87 (Department of Mining Engineering, University of British Columbia: Vancouver, Canada

Franke, J., Stewart, M., Lichti, D. (2013): System and method for measuring and mapping a surface relative to a reference. US patent Pub. No.: US 2013/0231892 A1

Ganz, J. (1914): Die Gipfelbewegung der Rosablanche, SAC-Jahrbuch Nr. 50 1914/15

Gauss, C. F. (1809): Theoria motus corporum coelestium in sectionibus conicis solem ambientium

Gauss, C. F. (1823): Theoria combinationis observationum erroribus minimis obnoxiae. Gottingae, Henricus Dieterich 1823. Henricus Dieterich

GFaI (2014): GFaI ScanMobile Datenblatt. http://www.gfai.de/deutsch/produkte/3d-datenverarbeitung-produkte/scan-mobile.html (accessed 04.12.2014)

GFaI (2015): Final Surfaceő product page, www.final-surface.com (accessed 10.03.2015)

Ghilani, C. D. (2010): Adjustment computations: spatial data analysis. John Wiley & Sons

Gielsdorf, F., Gründig, L., Milev, I., (2008): Deformation analysis with 3D laser scanning. In: Proceedings of the 13th FIG Symposium on Deformation Measurement and Analysis, Lisbon, Portugal

Gikas, V. (2012): Ambient vibration monitoring of slender structures by microwave interferometer remote sensing. Journal of Applied Geodesy, 6(3-4), pp. 167-176

Girardeau-Montaut, D., Roux, M., Marc, R., Thibault, G. (2005): Change detection on points cloud data acquired with a ground laser scanner. International Archives of Photogrammetry, Remote Sensing and Spatial Information Sciences, 36(part 3), W19

GORDON, S., LICHTI, D., FRANKE, J., STEWART, M. (2004): Measurement of structural deformation using terrestrial laser scanners. In: Proc. Of 1st FIG International Symposium on Engineering Surveys for Construction Works and Structural Engineering, Nottingham, United Kingdom

GOTTWALD, R. (2008): Field Procedures for Testing Terrestrial Laser Scanners (TLS). A Contribution to a Future ISO Standard. In: Proceedings of FIG Working Week, Stockholm, Sweden, pp. 14-19

GRANT, D. (2013): Cloud to cloud registration for 3D point data. Dissertation at Purdue University, West Lafayette, United States of America

GRANT, D., BETHEL, J., CRAWFORD, M. (2012a): Point-to-plane registration of terrestrial laser scans. ISPRS Journal of Photogrammetry and Remote Sensing, 72, pp. 16-26

GRANT, D., BETHEL, J., CRAWFORD, M. (2012b): Rigorous Point-to-Plane Registration of Terrestrial Laser Scans. In: ISPRS XXII Congress. 2012, Melbourne, Australia

GRIEGER, I. (2013): Graphische Datenverarbeitung: Mit einer Einführung in PHIGS und PHIGS-PLUS. Springer publishing

GROSSE-SCHWIEP, M., PIECHEL, J., LUHMANN, T. (2013): Measurement of rotor blade deformations of wind energy converters with laser scanners. Proceedings of the ISPRS Workshop on Laser Scanning, Antalya, Turkey

GRÜN, A. (1984): Adaptive least squares correlation - concept and first results. Intermediate Research Project Report to Heleva Associates, Inc., Ohio State University, Columbus, Ohio, pp. 1-13

GRÜN, A. (1985): Adaptive least squares correlation: a powerful image matching technique. South African Journal of Photogrammetry, Remote Sensing and Cartography, 14(3), pp. 175-187

GRÜN, A., AKCA, D. (2005): Least squares 3D surface and curve matching. ISPRS Journal of Photogrammetry and Remote Sensing, 59(3), pp. 151-174

GRÜNDIG, L. (1988): Datenverwaltungskonzepte für typische Aufgaben aus der Ingenieurgeodäsie. German Geodetic Commission (DGK), Volume C, Nr. 336, Munich, Germany

GÜLCH, E. (1984): Geometric calibration of two CCD-cameras used for digital image correlation on the Planicomp C100. Intl. Arch. Photogrammetry Remote Sens, 15, A3

HAKALA, T., SUOMALAINEN, J., KAASALAINEN, S., CHEN, Y. (2012): Full waveform hyperspectral LiDAR for terrestrial laser scanning. Optics express, 20(7), pp. 7119-7127

HAMPEL, F. R. (1968): Contributions to Theory of Robust Estimation. Unpublished Ph.D. Dissertation, Department of Statistics, University of California, Berkeley, United States of America

HAMPEL, F. R., RONCHETTI, E. M., ROUSSEEUW, P. J., STAHEL, W. A. (2011): Robust statistics: the approach based on influence functions (Vol. 114). John Wiley & Sons

HARTLEY, R., ZISSERMAN, A. (2010): Multiple View Geometry in Computer Vision, Cambridge University Press

HAUSDORFF, F. (1927): Mengenlehre. Berlin. Walter de Gruyter publishing

HE, W., MA, W., ZHA, H. (2005): Automatic registration of range images based on correspondence of complete plane patches. In: 3-D Digital Imaging and Modeling, pp. 470-475

HEILIG, M. L. (1962): Sensorama Simulator. U.S. Patent 3,050,870

HEJBUDZKA, K., LINDENBERGH, R., SOUDARISSANANE, S., HUMME, A. (2010): Influence of atmospheric conditions on the range distance and number of returned points in Leica ScanStation 2 point clouds. Int. Arch. Photogramm. Remote Sens. Spatial Inf. Sci, pp. 282-287

HEKIMOGLU, S. (2001): Local Reliability of the Least Median of Squares Method. First International Symposium on Robust Statistics and Fuzzy Techniques in Geodesy and GIS, Swiss Federal Institute of Technology Zurich (ETH), Institute of Geodesy and Photogrammetry, Zurich, Switzerland

HEKIMOGLU, S., KOCH, K. R. (2000): How can reliability of the test for outliers be measured? Allgemeine Vermessungs-Nachrichten, 107, pp. 247-252

HEKIMOGLU, S. (2005): Do robust methods identify outliers more reliably than conventional test for outlier. Zeitschrift für Vermessungwesen, 3, pp. 174-180

HELMERT, F. R. (1872): Die Ausgleichungsrechnung nach der Methode der kleinsten Quadrate: mit Anwendungen auf die Geodäsie und die Theorie der Messinstrumente. BG Teubner

HEMMLEB, M., WERITZ, F., MAIERHOFER, C. (2005): Multispektraler Laserscanner. Einsatz eines multispektralen Laserscanners zur Untersuchung von Bauwerksoberflächen. Project report. Fraunhofer IRB publishing

HESSE, C. (2007): Hochauflösende kinematische Objekterfassung mit terrestrischen Laserscannern. German Geodetic Commission (DGK), Volume C, Nr. 608, Munich, Germany

HEUNECKE, O., KUHLMANN, H., WELSCH, W., EICHHORN, A., NEUNER, H. (2013): Handbuch Ingenieurgeodäsie - Auswertung geodätischer Überwachungsmessungen. Wichmann publishing, Heidelberg, Germany

HÖFLE, B., PFEIFER, N. (2007): Correction of laser scanning intensity data: Data and model-driven approaches. ISPRS Journal of Photogrammetry and Remote Sensing, 62(6), pp. 415-433

HOLST, C., ZEIMETZ, P., NOTHNAGEL, A., SCHAUERTE, W., KUHLMANN, H. (2012): Estimation of Focal Length Variations of a 100-m Radio Telescope's Main Reflector by Laser Scanner Measurements. Journal of Surveying Engineering, 138(3), pp. 126-135

HOLST, C., NOTHNAGEL, A., BLOME, M., BECKER, P., EICHBORN, M., KUHLMANN, H. (2015): Improved area-based deformation analysis of a radio telescope's main reflector based on terrestrial laser scanning, J. Appl. Geodesy, 9 (1), pp. 1-14

HORN, B. K. (1987): Closed-form solution of absolute orientation using unit quaternions. JOSA A, pp. 629-642

HOUSHIAR, H., ELSEBERG, J., BORRMANN, D., NÜCHTER, A. (2013): A Study of Projections for Key Point Based Registration of Panoramic Terrestrial 3D Laser Scans. Accepted paper for publication in Journal of Geo-spatial Information Science

HUBER, P. J. (1964): Robust estimation of a location parameter. The Annals of Mathematical Statistics, 35(1), pp. 73-101

HUBER, P. J. (2011): Robust statistics. Springer Berlin Heidelberg, Germany

IMO (2015): Casualty statistics and investigations - Loss of life from 2006 to date. http://www.imo.org/KnowledgeCentre/ShipsAndShippingFactsAndFigures/Statisticalresources/Casualties/Documents/FSI%2020%20INF-17%20%20Casualty%20statistics%20-%20loss%20of%20life%20from%202006%20to%20date.pdf (accessed 25.02.2015)

IOANNIDIS, C., VALANI, A., GEORGOPOLOUS, A., TSILIGIRIS, E. (2006): 3D model generation for deformation analysis using laser scanning data of a cooling tower. In: The 3rd IAG Symposium on Geodesy for Geotechnical and Structural Engineering and 12th FIG Symposium on Deformation Measurement, Baden, Austria

ISO (2008): Evaluation of measurement data Guide to the Expression of Uncertainty in Measurement. JCGM 100:2008(E). Joint Committee for Guides in Meterology (JCGM)

JABOYEDOFF, M., OPPIKOFER, T., ABELLÁN, A., DERRON, M. H., LOYE, A., METZGER, R., PEDRAZZINI, A. (2012): Use of LIDAR in landslide investigations: a review. Natural Hazards, 61(1), pp. 5-28

JACOBS, G. (2006): Understanding spot size for laser scanning. Professional Surveyor Magazine, October issue

JAMES, M. R., PINKERTON, H., APPLEGARTH, L. J. (2009): Detecting the development of active lava flow fields with a very-long-range terrestrial laser scanner and thermal imagery. Geophysical Research Letters, 36(22)

JEUDY, L. M. (1988): Generalyzed variance-covariance propagation law formulae and application to explicit least-squares adjustments. Bulletin géodésique, 62(2), pp. 113-124

JOECKEL, R., STOBER, M. (1999): Elektronische Entfernungs- und Richtungsmessung. Konrad Wittwer publishing

JUTZI, B. (2007): Analyse der zeitlichen Signalform von rückgestreuten Laserpulsen. Dissertation, Technische Universität Munich, Germany

JUTZI, B., STILLA, U. (2003): Laser pulse analysis for reconstruction and classification of urban objects. International archives of photogrammetry remote sensing and spatial information sciences, 34(3/w8), pp. 151-156

JUTZI, B., STILLA, U. (2006): Precise range estimation on known surfaces by analysis of full-waveform laser. Proceedings of Photogrammetric Computer Vision PCV

KALUZA, P., KÖLZSCH, A., GASTNER, M. T., BLASIUS, B. (2010): The complex network of global cargo ship movements. Journal of the Royal Society Interface 7, pp. 1093-1103

KANANI, E. (2000): Robust Estimators for Geodetic Transformations and GIS. Institut für Geodäsie und Photo-grammetrie an der Eidgenössischen Technischen Hochschule Zürich, Mitteilungen Nr. 70

KANG, Z., LI, J., ZHANG, L., ZHAO, Q., ZLATANOVA, S. (2009): Automatic registration of terrestrial laser scanning point clouds using panoramic reflectance images. Sensors, 9(4), pp. 2621-2646

KARP, R. M. (1972): Reducibility among combinatorial problems. Springer US, pp. 85-103

KAUFMANN, V., LADSTÄDTER, R. (2009): Documentation and visualization of the morphodynamics of Hinteres Langtalkar rock glacier (Hohe Tauern Range, Austrian Alps) based on aerial photographs (1954-2006) and geodetic measurements (1999-2007). Proceedings of the 10th International Symposium on High Mountain Remote Sensing Cartography, Kathmandu, Nepal

KERSTEN, T. P., MECHELKE, K., LINDSTAEDT, M., STERNBERG, H. (2009): Methods for geometric accuracy investigations of terrestrial laser scanning systems. Photogrammetrie-Fernerkundung-Geoinformation, 2009(4), pp. 301-315

KIENAST, G., KAUFMANN, V. (2004): Geodetic measurements on glaciers and rock glaciers in the Hohe Tauern National park (Austria). Proceedings of the 4th ICA Mountain Cartography Workshop, Vall de Núria, Catalonia, Barcelona, Spain, pp. 101-108

KOCH, K. R. (1996): Robuste Parameterschätzung. Allgemeine Vermessungs-Nachrichten, 103: pp. 1-18

KUHLMANN, H., SCHWIEGER, V., WIESER, A., NIEMEIER, W. (2014): Engineering Geodesy-Definition and Core Competencies. Journal of Applied Geodesy, 8(4), pp. 327-334

KRAVITZ, N. D., KUSNOTO, B., BEGOLE, E., OBREZ, A., AGRAN, B. (2009): How well does Invisalign work? A prospective clinical study evaluating the efficacy of tooth movement with Invisalign. American Journal of Orthodontics and Dentofacial Orthopedics, 135(1), pp. 27-35

LAGUE, D., BRODU, N., LEROUX, J. (2013): Accurate 3D comparison of complex topography with terrestrial laser scanner: application to the Rangitikei canyon (NZ). ISPRS Journal of Photogrammetry and Remote Sensing, 82, pp. 10-26

LANE, S. N., WESTAWAY, R. M., MURRAY HICKS, D. (2003): Estimation of erosion and deposition volumes in a large, gravel-bed, braided river using synoptic remote sensing. Earth Surface Processes and Landforms, 28(3), pp. 249-271

LANG, W. (1929): Deformationsmessungen an Staumauern nach den Methoden der Geodäsie, Landestopographie, Bern, Switzerland

LAUTHER, U. (1981): An O (N log N) algorithm for Boolean mask operations. Proceedings of the 18th Design Automation Conference, pp. 555-562

LEE, J., DIETZ, P., MAYNES-AMINZADE, D., RASKAR, R., HUDSON, S. (2004): Automatic projector calibration with embedded light sensors. In: Proceedings of the 17th annual ACM symposium on user interface software and technology, United States of America

LEGENDRE, A. M. (1805): Nouvelles méthodes pour la détermination des orbites des cometes. F. Didot

LEHMANN, R. (2010): Normierte Verbesserungen - wie groSS ist zu groSS? Allgemeine Vermessungs-Nachrichten, 2, pp. 53-61

LEHMANN, R. (2013): 3 s-Rule for Outlier Detection from the Viewpoint of Geodetic Adjustment. Journal of Surveying Engineering, 139(4), pp. 157-165

LEICA (2013): Leica ScanStation C10 datasheet.
http://hds.leica-geosystems.com/downloads123/hds/hds/ScanStation%20C10/brochures-datasheet/Leica_ScanStation_C10_DS_us.pdf.
(accessed 30.05.2015)

LENZMANN, L., LENZMANN, E. (2004): Strenge Auswertung des nichtlinearen GauSS-Helmert- Modells. Allgemeine Vermessungs-Nachrichten, 111, pp. 68-73

LI, H., SUMNER, R. W., PAULY, M. (2008a): Global Correspondence Optimization for Non-Rigid Registration of Depth Scans. In: Computer graphics forum, Vol. 27, No. 5, Blackwell Publishing Ltd, pp. 1421-1430

LI, H., ADAMS, B., GUIBAS, L. J., PAULY, M. (2009): Robust single-view geometry and motion reconstruction. ACM Transactions on Graphics (TOG), 28(5), 175

LI, Z., CHEN, J., BALTSAVIAS, E. (2008b): Advances in photogrammetry, remote sensing and spatial information sciences: 2008 ISPRS congress book (Vol. 7). CRC Press

LICHTENSTEIN, M. (2011): Strukturbasierte Registrierung von Punktwolken unter Verwendung von Bild-und Laserscannerdaten. Doctoral dissertation, RWTH Aachen, Germany

LICHTENSTEIN, M., BENNING, W. (2009): Bestimmung räumlicher Transformationsparameter auf Grundlage von dreidimensionalen Geraden und projektiver Geometrie. In: Photogrammetrie - Laserscanning - optische 3D-Messtechnik, Beiträge der Oldenburger 3D-Tage. Herbert Wichmann publishing, pp. 66-73

LICHTENSTEIN, M., BENNING, W. (2010): Registrierung von Punktwolken auf der Grundlage von Objektprimitiven. In: T. Luhmann, C. Müller (editors), Photogrammetrie - Laserscanning - Optische 3D-Messtechnik, Herbert Wichmann Publishing, Heidelberg, Germany

LICHTI, D. (2007): Error modelling, calibration and analysis of an AM-CW terrestrial laser scanner system. ISPRS Journal of Photogrammetry and Remote Sensing, 61(5), pp. 307-324

LICHTI, D. (2010): A review of geometric models and self-calibration methods for terrestrial laser scanners. Boletim de Ciências Geodésicas, 16(1)

LICHTI, D., STEWART, M. P., TSAKIRI, M., SNOW, A. J. (2000): Calibration and testing of a terrestrial laser scanner. International archives of Photogrammetry and Remote sensing, 33(B5/2; PART 5), pp. 485-492

LICHTI, D., GORDON, S. J. (2004): Error propagation in directly georeferenced terrestrial laser scanner point clouds for cultural heritage recording. Proc. of FIG Working Week, Athens, Greece

LICHTI, D., LICHT, M. G. (2006): Experiences with terrestrial laser scanner modelling and accuracy assessment. Int. Arch. Photogramm. Remote Sens. Spat. Inf. Sci, 36(5), pp. 155-160

LINDENBERGH, R. (2002): Limits of Voronoi diagrams. arXiv preprint math/0210345

LINDENBERGH, R., PFEIFER, N. (2005): A statistical deformation analysis of two epochs of terrestrial laser data of a lock. Proc. of Optical 3D Measurement Techniques, 2, pp. 61-70

LINDENBERGH, R., PIETRZYK, P. (2015): Change detection and deformation analysis using static and mobile laser scanning. Applied Geomatics, 7(2), pp. 65-74

LINDSTAEDT, M., KERSTEN, T., MECHELKE, K., GRAEGER, T. (2012): Prüfverfahren für terrestrische Laserscanner - Gemeinsame geometrische Genauigkeitsuntersuchungen verschiedener Laserscanner an der HCU Hamburg. Beiträge der Oldenburger 3D-Tage. Herbert Wichmann publishing, pp. 264-275

LINKWITZ, K. (1999): About the generalised analysis of network-type entities. In: Krumm, F. and Schwarze, V. (Editor): Quo vadis geodesia ... ? Festschrift for Erik W. Grafarend on the occasion of his 60th birthday. University Stuttgart, Report Nr. 199.6, pp. 279-293

LITTLE, M. J. (2006): Slope monitoring strategy at PPRust open pit operation. In: Proceedings of the International Symposium on Stability of Rock Slopes in Open Pit Mining and Civil Engineering

LOVAS, T., BARSI, Á., DETREKOI, A., DUNAI, L., CSAK, Z., POLGAR, A., BERENYI, A., KIBEDY, Z., SZOCS, K. (2008): Terrestrial laser scanning in deformation measurements of structures. International Archives of Photogrammetry and Remote Sensing, 37(B5), pp. 527-531

LOWE, D. G. (2004): Distinctive image features from scale-invariant keypoints. International journal of computer vision, 60(2), pp. 91-110

LUHMANN, T., ROBSON, S., KYLE, S., HARLEY, I. (2011): Close range photogrammetry: Principles, methods and applications (pp. 1-531). Whittles publishing

MARTINEZ, F., RUEDA, A. J., FEITO, F. R. (2009): A new algorithm for computing Boolean operations on polygons. Computers & Geosciences, 35(6), pp. 1177-1185

MCHENRY, R., SEGAL, D. J., DELEYS, N. J. (1967). Computer simulation of single vehicle accidents. Stapp Car Crash Conference, Anaheim, California, United States of America

MEAGHER, D. (1982): Geometric modeling using octree encoding. Computer graphics and image processing, 19(2), pp. 129-147

METROPOLIS, N., ULAM, S. (1949): The monte carlo method. Journal of the American statistical association, 44(247), pp. 335-341

Mettenleiter, M., Oberteiber, N., Härtl, F., Ehm, M., Baur, J., Fröhlich, C. (2008): 3D laser scanner as part of kinematic measurement system. In: 1st International Conference on Machine Contol & Guidance. Zurich, Switzerland

Milgram, P., Kishino, F. (1994): A Taxonomy of Mixed Reality Visual Displays. In: Transactions on Information and Systems, Special issue on Networked Reality

Milgram, P., Takemura, H., Utsumi, A., Kishino, F. (1994): Augmented Reality: A class of displays on the reality-virtuality continuum. In: Telemanipulator and Telepresence Technologies, Vol. 2351, Boston, United States of America, pp. 282-292

Monserrat, O., Crosetto, M. (2008): Deformation measurement using terrestrial laser scanning data and least squares 3D surface matching. ISPRS Journal of Photogrammetry and Remote Sensing, 63(1), pp. 142-154.

Neitzel, F., (2004): Identifizierung konsistenter Datengruppen am Beispiel der Kongruenzuntersuchung geodätischer Netze, German Geodetic Commission (DGK), Volume C, Nr. 565, Munich, Germany

Neitzel, F. (2006): Investigations of axes errors of terrestrial laser scanners. 5th International Symposium Turkish-German Joint Geodetic Days, Berlin, Germany

Neitzel, F. (2015): Selected sections of adjustment calculation. Unpublished lecture notes, Technische Universität Berlin, Germany

Neitzel, F., Petrovic, S. (2008): Total least squares (TLS) im Kontext der Ausgleichung nach kleinsten Quadraten am Beispiel der ausgleichenden Geraden. ZfV, 133, pp. 141-148

Neitzel, F., Johannes, L. (2009): Anwendung des tachymetrischen Laserscannings in der Überwachung eines historischen Bauwerkes. In: Photogrammetrie - Laserscanning - optische 3D-Messtechnik, Beiträge der Oldenburger 3D-Tage. Herbert Wichmann publishing, pp. 127-136

Neitzel, F., Klonowski, J., Siebert, S., Dasbach, J. P. (2011): Mobile 3D mapping with a low-cost UAV system on example of a landfill survey. Int. Arch. Photogramm. Remote Sens. Spatial Inf. Sci.

Neitzel, F., Niemeier, W., Weisbrich, S., Lehmann, M. (2012): Investigation of Low-Cost Accelerometer, Terrestrial Laser Scanner and Ground-Based Radar Interferometer for Vibration Monitoring of Bridges. In: Proceedings of the 6th European Workshop on Structural Health Monitoring, pp. 542-551

Neumann, I., Kutterer, H. (2007): Congruence tests and outlier detection in deformation analysis with respect to observation imprecision. Journal of Applied Geodesy jag, 1(1), pp. 1-7

Nguyen, H. T., Fernandez-Steeger, T. M., Wiatr, T., Rodrigues, D., Azzam, R. (2011): Use of terrestrial laser scanning for engineering geological applications on volcanic rock slopes-An example from Madeira island (Portugal). Natural Hazards and Earth System Sciences, 11, pp. 807-817

Niemeier, W. (1976): Grundprinzip und Rechenformeln einer strengen Analyse geodätischer Deformationsmessungen. In: VII. Internationaler Kurs für Ingenieurmessungen hoher Präzision, Proceedings, Volume II. Darmstadt, 29.09.-08.10.1976. Technische Hochschule Darmstadt (Editors), THD Schriftenreihe Wissenschaft und Technik, Darmstadt, Germany 1977, pp. 465-482

Niemeier, W. (2008): Ausgleichungsrechnung. Walter de Gruyter, Berlin, New York

Nüchter, A., Elseberg, J., Schneider, P., Paulus, D. (2010): Study of parameterizations for the rigid body transformations of the scan registration problem. Computer Vision and Image Understanding, 114(8), pp. 963-980

Nurunnabi, A., Belton, D., West, G. (2012): Robust segmentation in laser scanning 3D point cloud data. In: International Conference on Digital Image Computing Techniques and Applications (DICTA) pp. 1-8

Nurunnabi, A., Belton, D., West, G. (2014): Robust statistical approaches for local planar surface fitting in 3D laser scanning data. ISPRS Journal of Photogrammetry and Remote Sensing, 96, pp. 106-122

Nyquist, H. (1928): Certain topics in telegraph transmission theory. American Institute of Electrical Engineers, Transactions of the, 47(2), pp. 617-644

Ohlmann-Lauber, J., Schäfer, T. (2011): Ansätze zur Ableitung von Deformationen aus TLS-Daten. Terrestrisches Laserscanning - TLS 2011, Fulda, Germany, pp. 147-157

Oppikofer, T., Jaboyedoff, M., Keusen, H. R. (2008): Collapse at the eastern Eiger flank in the Swiss Alps. Nature Geoscience, 1(8), pp. 531-535

Paffenholz, J.-A., Kutterer, H (2008): Direct Georeferencing of Static Terrestrial Laser Scans. Proceedings of the FIG Working Week -Integrating Generations, Stockholm, Sweden

Paffenholz, J.-A., Vennegeerts, H., Kutterer, H. (2008): High Frequency Terrestrial Laser Scans for Monitoring kinematic Processes. 4th International Conference on Engineering Surveying, Bratislava, Slovakia

Paffenholz, J. A., Alkhatib, H., Kutterer, H. (2010): Direct geo-referencing of a static terrestrial laser scanner. Journal of Applied Geodesy, 4(3), pp. 115-126

Paffenholz, J. A., Bae, K. H. (2012): Geo-referencing point clouds with transformational and positional uncertainties. Journal of Applied Geodesy, 6(1), pp. 33-46

Paffenholz, J.-A. (2012): Direct geo-referencing of 3D point clouds with 3D positioning sensors. German Geodetic Commission (DGK), Volume C, Nr. 689, Munich, Germany

Pagounis, V., Tsakiri, M., Palaskas, S., Biza, B., Zaloumi, E. (2006): 3D laser scanning for road safety and accident reconstruction. In: Proceedings of the 23rd FIG Congress, Munich, Germany

Park, J., Choi, D. S., Jang, I., Yook, H. T., Jost-Brinkmann, P. G., Cha, B. K. (2013): A novel method for volumetric assessment of tooth wear using three-dimensional reverse-engineering technology: A preliminary report. Angle Orthodontist, 84(4), pp. 687-692

Pathak, K., Vaskevicius, N., Poppinga, J., Pfingsthorn, M., Schwertfeger, S., Birk, A. (2009): Fast 3D mapping by matching planes extracted from range sensor point-clouds. In: Intelligent Robots and Systems, 2009, pp. 1150-1155

Pertl, A. (1984): Digital image correlation with the analytical plotter Planicomp C100. International Archives of Photogrammetry, 25(3b), pp. 876-882

Pesci, A., Teza, G., Bonali, E. (2011): Terrestrial laser scanner resolution: Numerical simulations and experiments on spatial sampling optimization. Remote Sensing, 3(1), pp. 167-184

Petrovic, S. (2003): Parameterschätzung für unvollständige funktionale Modelle in der Geodäsie. Verlag der Bayerischen Akademie der Wissenschaften in Kommission beim Verlags C.H. Beck

Pinhanez, C. (2001): The Everywhere Displays Projector: A Device to Create Ubiquitous Graphical Interfaces. In: Proceedings of the 3rd international conference on Ubiquitous Computing, Atlanta, United States of America, pp. 315-331

Pope, A. J. (1976): The statistics of residuals and the detection of outliers. NOAA technical report NOS 65

Pukelsheim, F. (1994): The three sigma rule. The American Statistician, 48(2), pp. 88-91

Pulli, K. (1999): Multiview registration for large data sets. In: Proceedings of the second International Conference on 3-D Digital Imaging and Modeling, pp. 160-168

Rabbani, T., van den Heuvel, F. (2005): Automatic point cloud registration using constrained search for corresponding objects. In: 7th Conference on Optical 3-D Measurement Techniques, pp. 3-5

Raskar R., Welch, G., Low K., Bandyopadhyay, D., (2001): Shader Lamps: Animating real objects with image-based illumination. In: Proceedings of the 12th Eurographics Workshop on Rendering Techniques, pp. 89-102

Raskar, R., van Baar, J., Beardsley, P., Willwacher, T., Rao, S., Forlines, C. (2003): iLamps: geometrically aware and self-configuring projectors. In: ACM Transactions on Graphics (TOG)

Rehr, I., Rinke, N., Kutterer, H., Berkhahn, V. (2011): MaSSnahmen zur Effizienzsteigerung bei der Durchführung tachymetrischer Netzmessungen. Allgemeine Vermessungs-Nachrichten 118, Nr. 1, pp. 2-14

Reshetyuk, Y. (2006a): Investigation and calibration of pulsed time-of-flight terrestrial laser scanners. Licentiate thesis in Geodesy, Royal Institute of Technology, Division of Geodesy, Stockholm, Sweden

Reshetyuk, Y. (2006b). Investigation of the influence of surface reflectance on the measurements with the terrestrial laser scanner Leica HDS 3000. Zeitschrift fur Geodasie, Geoinformation und Landmanagement, 131(2), pp. 96-103

Reshetyuk, Y. (2009): Self-calibration and direct georeferencing in terrestrial laser scanning, PhD thesis, Royal Institute of Technology, Stockholm

Reshetyuk, Y. (2010): Direct georeferencing with GPS in terrestrial laser scanning. ZfV-Zeitschrift für Geodäsie, Geoinformation und Landmanagement, 135(3), pp. 151-159

Rietdorf, A. (2005): Automatisierte Auswertung und Kalibrierung von scannenden Messsystemen mit tachymetrischem Messprinzip. German Geodetic Commission (DGK), Volume C, Nr. 582, Munich, Germany

Rietdorf, A., Gielsdorf, F., Gründig, L. (2004): A concept for the calibration of terrestrial laser scanners. In: Proceedings FIG Working Week, Athens, Greece, pp. 22-27

Rodehorst, V. (2004): Photogrammetrische 3D-Rekonstruktion im Nahbereich durch Auto-Kalibrierung mit projektiver Geometrie. wvb Wissenschaftlicher Verlag, Berlin, Germany

Roncat, A., Ghuffar, S., Székely, B., Dorninger, P., Rasztovits, S., Mittelberger, M., Pfeifer, N. (2013): A Natural Laboratory - Terrestrial Laser Scanning and auxiliary Measurements for studying an active Landslide. In: Proceedings of the JISDM conference, Nottingham, Great Britain

Rossignac, J. R., Requicha, A. A. (1986): Offsetting operations in solid modelling. Computer Aided Geometric Design, 3(2), pp. 129-148

Rousseeuw, P. J. (1984): Least median of squares regression. Journal of the American statistical association, 79(388), pp. 871-880

Rousseeuw, P. J., Leroy, A. M. (1987): Robust regression and outlier detection. John Wiley & Sons, New York, Chichester, Brisbane, Toronto, Singapore

Ruban, A.F. (1983): A report on slope instability along the Oldman river and tributaries in the vicinity of Lethbridge, Alberta. Master's thesis submitted to the faculty of graduate studies and research at the University of Alberta, Canada

Rusinkiewicz, S., Levoy, M. (2001): Efficient variants of the ICP algorithm. In: 3-D Digital Imaging and Modeling, 2001. Proceedings. Third International Conference on, pp. 145-152

RUSU, R. B., BLODOW, N., MARTON, Z. C., BEETZ, M. (2008): Aligning point cloud views using persistent feature histograms. In: Intelligent Robots and Systems, 2008. IROS 2008. pp. 3384-3391

RUSU, R. B., BLODOW, N., BEETZ, M. (2009): Fast point feature histograms (fpfh) for 3d registration. In: Robotics and Automation, 2009. ICRA'09. IEEE International Conference on pp. 3212-3217

SALO, P., JOKINEN, O., KUKKO, A. (2008): On the calibration of the distance measuring component of a Terrestrial Laser Scanner. In: Proc. in the XXIth ISPRS Congress, Silk Road for Information from Imagery (Vol. 37, p. B5)

SANSO, F. (1973): An exact solution of the roto-translation problem. Photogrammetria, 29(6), pp. 203-216

SCAIONI, M., ALBA, M. (2010): Understanding changes and deformations on multi-temporal rock face point clouds. The International Archives of Photogrammetry and Remote Sensing (IAPRS)

SCAIONI, M., RONCELLA, R., ALBA, M. I. (2013): Change Detection and Deformation Analysis in Point Clouds: Application to Rock Face Monitoring. In: Photogrammetric engineering and remote sensing, 79(5), pp. 441-455

SCHAER, P., SKALOUD, J., LANDTWING, S., LEGAT, K. (2007): Accuracy estimation for laser point cloud including scanning geometry. In: 5th International Symposium on Mobile Mapping Technology, Padua, Italy

SCHÄFER, T., WEBER, T., KYRINOVIC, P., ZÁMECNIKOVÁ, M. (2004): Deformation measurement using terrestrial laser scanning at the hydropower station of Gabcíkovo. In: INGEO 2004 and FIG Regional Central and Eastern European Conference on Engineering Surveying, Bratislava, Slovakia

SCHMIDHUBER, J., TUBIELLO, F. N. (2007): Global food security under climate change. Proceedings of the National Academy of Sciences, 104(50), pp. 19703-19708

SCHNEIDER, D. (2006): Terrestrial laser scanning for area based deformation analysis of towers and water damns. In: Proc. of 3rd IAG/12th FIG Symp., pp. 22-24, Baden, Austria

SCHUHMACHER, S. BÖHM, J. (2005): Georeferencing of terrestrial laserscanner data for applications in architectural modeling. IAPRS Vol. 36, PART 5/W17

SCHULZ, T. (2007): Calibration of a Terrestrial Laser Scanner for Engineering Geodesy. PhD thesis, ETH Zurich, Switzerland

SCHWARZ, K. P., EL-SHEIMY, N. (2004): Mobile Mapping Systems-State of the art and future trends. International Archives of Photogrammetry, Remote Sensing and Spatial Information Sciences, 35(Part B), 10

SCHWERMANN, R. (1995): Geradengestützte Bildorientierung in der Nahbereichsphotogrammetrie. Dissertation at the Geodetic institute of RWTH Aachen, Germany

SHANNON, C. E. (1949): Communication in the presence of noise. Proceedings of the IRE, 37(1), p. 10-21

SLADEN, J. A., JOSHI, R. C. (1988): Mining subsidence in Lethbridge, Alberta. Canadian Geotechnical Journal, 25(4), pp. 768-777

SLAVIK, P. (1996): A tight analysis of the greedy algorithm for set cover. In: Proceedings of the twenty-eighth annual ACM symposium on theory of computing, pp. 435-441

SOUDARISSANANE, S., LINDENBERGH, R. (2011): Optimizing terrestrial laser scanning measurement set-up. In: ISPRS Workshop Laser Scanning 2011, Calgary, Vol. XXXVIII, pp. 1-6

SOUDARISSANANE, S., VAN REE, J., BUCKSCH, A., LINDENBERGH, R. (2007): Error budget of terrestrial laser scanning: influence of the incidence angle on the scan quality. Proceedings 3D-NordOst, pp. 1-8

Soudarissanane, S., Lindenbergh, R., Gorte, B. (2008): Reducing the error in terrestrial laser scanning by optimizing the measurement set-up. Proceedings of International Archives of Photogrammetry, Remote Sensing and Spatial Information Sciences, pp. 3-11

Soudarissanane, S., Lindenbergh, R., Menenti, M., Teunissen, P. (2009): Incidence angle influence on the quality of terrestrial laser scanning points. In: ISPRS Workshop Laserscanning

Soudarissanane, S., Lindenbergh, R., Menenti, M., Teunissen, P. (2011): Scanning geometry: Influencing factor on the quality of terrestrial laser scanning points. ISPRS Journal of Photogrammetry and Remote Sensing, 66(4), pp. 389-399

Squid (2014): Shape Queries Using Image Databases. http://www.ee.surrey.ac.uk/CVSSP/demos/css/demo.html (accessed 17.03.2014)

Stahlberg, C. (1997): Eine vektorielle Darstellung des Einflusses von Ziel- und Kippachsenfehler auf die Winkelmessung. ZfV 122, Nr. 5, pp. 225-235

Staiger, R. (2005): The geometrical quality of terrestrial laser scanner (TLS). In: Proceedings of FIG Working Week, Cairo, Egypt

Staudte, R. G., Sheather, S. J. (1990): Robust estimation and testing. Wiley series in probability and mathematical statistics. New York, United States of America

Stöcker, H. (2000): Taschenbuch der Physik. Formeln, Tabellen, Übersichten. Harri Deutsch Publishing

Student, B. (1908): The probable error of a mean. Biometrika, 6(1), pp. 1-25

Technet (2014): Scantra - High-Precision Scan Registration without Targets. http://www.technet-gmbh.com/index.php?id=1051&L=1 (accessed 06.03.2014)

Teunissen, P. J. G. (1989): First and second moments of non-linear least-squares estimators. Bulletin géodésique, 63(3), pp. 253-262

Teunissen, P. J. G. (2000): Testing theory. An Introduction, VSSD publishing, Delft, The Netherlands

Teza, G., Galgaro, A., Zaltron, N., Genevois, R. (2007): Terrestrial laser scanner to detect landslide displacement fields: a new approach. International Journal of Remote Sensing, 28(16), pp. 3425-3446

Teza, G., Pesci, A., Genevois, R., Galgaro, A. (2008): Characterization of landslide ground surface kinematics from terrestrial laser scanning and strain field computation. Geomorphology, 97(3), pp. 424-437

Theiler, P. W., Wegner, J. D., Schindler, K. (2013): Markerless point cloud registration with keypoint-based 4-points congruent sets. Proceedings of the ISPRS Workshop on Laser Scanning, Antalya, Turkey

Theiler, P. W., Wegner, J. D., Schindler, K. (2014): Fast registration of laser scans with 4-points congruent sets-what works and what doesn't. ISPRS Annals of Photogrammetry, Remote Sensing and Spatial Information Sciences, 1, pp.149-156 Toor, P., Bird, M., Perkins, T., Powell, M., Franke, J. (2011): The Influence of Liner Wear on Milling Efficiency. In: MetPlant 2011, The Australasian Institute of Mining and Metallurgy, pp. 193-212

Torre-Ferrero, C., Llata, J. R., Alonso, L., Robla, S., Sarabia, E. G. (2012): 3D point cloud registration based on a purpose-designed similarity measure. EURASIP Journal on Advances in Signal Processing, 2012(1), pp. 1-15

van Gosliga, R., Lindenbergh, R., Pfeifer, N. (2006): Deformation analysis of a bored tunnel by means of terrestrial laser scanning. Image Engineering and Vision Metrology. pp. 167-172

VENNEGEERTS, H., MARTIN, J., BECKER, M., KUTTERER, H. (2008): Validation of a kinematic laserscanning system, Journal of Applied Geodesy, 2/2008, pp. 79-84

VENTURA, S. R., FREITAS, D. R., RAMOS, I. M., TAVARES, J. M. R. (2013): Three-dimensional visualization of teeth by magnetic resonance imaging during speech. Biodental Engineering

VÖGTLE, T., SCHWAB, I., LANDES, T. (2008): Influences of different materials on the measurements of a terrestrial laser scanner (TLS). In: Proc. of the XXI Congress, The International Society for Photogrammetry and Remote Sensing, ISPRS2008, Vol. 37, pp. 1061-1066

VON HANSEN, W. (2006): Robust automatic marker-free registration of terrestrial scan data. In: W. Förstner and R. Steffen (eds), Photogrammetric Computer Vision, IAPRS, Vol. XXXVI Part 3

VON HANSEN, W., MICHAELSEN, E., THONNESSEN, U. (2006): Cluster analysis and priority sorting in huge point clouds for building reconstruction. In: 18th International Conference on Pattern Recognition, (Vol. 1, pp. 23-26)

VON HANSEN, W., GROSS, H., THOENNESSEN, U. (2008): Line-based registration of terrestrial and airborne LIDAR data. International Archives of Photogrammetry and Remote Sensing, 37, pp. 161-166

VORONOI, G. (1908): Nouvelles applications des paramètres continus à la théorie des formes quadratiques. Journal für die Reine und Angewandte Mathematik 133 (133), pp. 97-178

VOSSELMAN, G., MAAS, H.G. (2010): Airborne and terrestrial laser scanning. CRC Press

WAGNER, O., RAU, H., (2000): Bandbreite bei der Unfallrekonstruktion - Studie über die Rekonstruktionsergebnisse von drei als Unfälle aufbereiteten Kollisionsversuchen. Proceedings of the 9th EVU conference, Berlin, Germany

WAKONIGG, H, LIEB, G.K. (1996): Die Pasterze und ihre Erforschung im Rahmen der Gletschermessungen. Wissenschaft im Nationalpark Hohe Tauern, Kärntner Nationalpark-Schriften 8, pp. 99115

WANG, G., PHILIPS, D., JOYCE, RIVERA, F. (2011): The integration of TLS and continuous GPS to study landslide deformation: A case study in Puerto Rico. Journal of Geodetic Science, volume 1, issue 1

WANG, J., KUTTERER, H., FANG, X. (2012): On the detection of systematic errors in terrestrial laser scanning data. Journal of Applied Geodesy, Volume 6, Issue 3-4, pp. 187-192

WEBER, T., HÄNSCH, R., HELLWICH, O. (2015): Automatic registration of unordered point clouds acquired by Kinect sensors using an overlap heuristic. ISPRS Journal of Photogrammetry and Remote Sensing, 102, pp. 96-109

WEHR, A., LOHR, U. (1999): Airborne laser scanning - an introduction and overview. ISPRS Journal of Photogrammetry and Remote Sensing, 54(2), pp. 68-82 WELSCH, W. (1979): Entwicklung der Analyse von Deformationsmessungen mit Hilfe geodätischer Netze. Deformationsanalysen, Schriftenr. Wiss. Studiengang Vermessungswes., HSBwM, 4, pp. 5-15

WENZEL, K., ROTHERMEL, M., FRITSCH, D., HAALA, N. (2013): Image acquisition and model selection for multi-view stereo. Int. Arch. Photogramm. Remote Sens. Spatial Inf. Sci, 40, pp. 251-258

WICKI, F. (1999): Robuste Schätzverfahren für die Parameterschätzung in geodätischen Netzen. Dissertation, ETH, Zurich, Switzerland

WILLIAMS, J., BENNAMOUN, M. (2001): Simultaneous registration of multiple corresponding point sets. Computer Vision and Image Understanding, 81(1), pp. 117-142

WOOD, D. P., GLYNN, C., WALSH, D. (2009): Motorcycle-to-car and scooter-to-car collisions: speed estimation from permanent deformation. Proceedings of the Institution of Mechanical Engineers, Part D: Journal of Automobile Engineering, 223(6), pp. 737-756

WUJANZ, D. (2009): Intensity calibration method for 3D laser scanners. New Zealand Surveyor, (299), pp. 7-13

WUJANZ, D. (2012): Towards transparent quality measures in surface based registration processes: Effects of deformation onto commercial and scientific implementations, Int. Arch. Photogramm. Remote Sens. Spatial Inf. Sci., XXXIX-B5, 251-256, doi:10.5194/isprsarchives-XXXIX-B5-251-2012

WUJANZ, D., NEITZEL, F., HEBEL, H. P., LINKE, J., BUSCH, W. (2013a): Terrestrial radar and laser scanning for deformation monitoring: first steps towards assisted radar scanning. Proceedings of the ISPRS Workshop on Laser Scanning, Antalya, Turkey

WUJANZ, D., KRUEGER, D., NEITZEL, F. (2013b): Defo Scan++: Surface based registration of terrestrial laser scans for deformation monitoring. 2nd Joint International Symposium on Deformation Monitoring (JISDM), Nottingham, United Kingdom

WUJANZ, D., RÖCKELEIN, S., NEITZEL, F., FRÖHLICH, C. (2013c): On data acquisition of moving objects via kinematic terrestrial laser scanning. Proceedings of the ISPRS Workshop on Laser Scanning, Antalya, Turkey

XU, P. (2005): Sign-constrained robust least squares, subjective breakdown point and the effect of weights of observations on robustness. Journal of Geodesy, 79(1-3), pp. 146-159

ZACZEK-PEPLINSKA, J., POPIELSKI, P. (2013): Utilisation of terrestrial laser scanning for verification of geometry of numerical models of hydrotechnical structures using the example of a section of the concrete besko dam. Accepted article for technical transactions on environmental engineering

ZAMECNIKOVA, M., WIESER, A., WOSCHITZ, H., RESSL, C., 2014: Influence of surface reflectivity on reflectorless electronic distance measurement and terrestrial laser scanning. Journal of Applied Geodesy, 8(4), pp. 311-326

ZHANG, Z. (1994): Iterative point matching for registration of free-form curves and surfaces. International journal of computer vision, 13(2), pp. 119-152

ZIENKIEWICZ, O. C. (1971): The finite element method in engineering science (Vol. 1977). London, England. McGraw-Hill publishing

ZOLLER & FRÖHLICH (2010): Z+F Imager 5006 h Owner's Manual

List of Figures

List of Tables